University of Zurich^UZH

Spatial and Temporal Patterns of Surface Elevation Change at Marine-Terminating Outlet Glacier Eqip Sermia, Western Greenland in Relation to Front Position, Flow Velocity and Climate

GEO 511 Master's Thesis

Author
Roger Honegger
14-734-495

Supervised by
Prof. Dr. Andreas Vieli

Faculty representative
Prof. Dr. Andreas Vieli

30.04.2020
Department of Geography, University of Zurich

Spatial and Temporal Patterns of

Surface Elevation Change

at Marine-Terminating Outlet Glacier

Eqip Sermia, Western Greenland

in Relation to Front Position, Flow Velocity and Climate

Author

Roger Honegger, 14-734-495
roger.honegger@uzh.ch

Supervisor & Faculty Member

Prof. Dr. Andreas Vieli
andreas.vieli@geo.uzh.ch

30th April 2020
Geo 511 Master's Thesis
Department of Geography

University of Zurich^{UZH}

Summary

Dynamic processes at marine-terminating outlet glaciers strongly control the mass balance of the *Greenland Ice Sheet* (GrIS). Thus, the understanding of the related processes is crucial for the assessment of the stability of these glaciers and inherently the future contribution of the GrIS to sea-level rise. The aim of this study is to investigate the temporal and spatial patterns of surface elevation change on small scale and in detail. The respective study object is Eqip Sermia, a marine-terminating outlet glacier in central Western Greenland. Eqip Sermia is chosen because this study site provides an exceptionally long time series of scientific data, covering more than a century. The analysis is based on the comparison of historic maps, digital elevation models (DEMs) derived from Structure-from-Motion processing of historic aerial imagery and image series from recent drone campaigns in the field, and modern satellite DEMs. The identified spatial and temporal patterns of surface elevation change are compared to additional parameters such as front position, flow velocity and temperature records, with the aim to qualitatively describe the dynamic inter-dependencies between these different factors.

Eqip Sermia underwent little changes from 1912 to 2003. From 2003 to 2014, Eqip Sermia was characterised by increasing rates of surface elevation lowering, acceleration and front retreat, which was unprecedented for the entire available data record. The surface geometry changes related to the dynamic retreat caused the downglacier slope to increase and the ice thickness to decrease. Analysis of spatial patterns reveal upstream propagation of thinning after large retreat of the front. The surface elevation close to the terminus stabilised shortly after, whereas the surface elevation lowering at higher elevations is persistent on the time-scale of multiple years. The surface elevation change is correlating well with length changes and changes of surface flow velocities. A seasonal pattern for surface elevation change is detected, which is in agreement with seasonal length and velocity oscillations.

A comparison of the surface elevation change with climate data from Ilulissat and from the *Swiss* Camp monitoring station reveals an earlier onset of increasing summer temperatures relative to the surface elevation response, which shows that the dynamic retreat was initially triggered by climate change but affected the glacier terminus through an indirect mechanism. The striking similarities of the temporal patterns of surface elevation change at the terminus and modelled surface melt rates indicate that the influence of atmospheric changes (namely temperature) is still important. According to a comparison of modelled melt rates and observed surface elevation change rates, dynamic mass loss accounts for ca. 80 percent of the total mass loss on the terminus of Eqip Sermia during the period from 1985 to 2017. The recent temporal pattern of surface elevation change on the low-dynamic margins at Eqip Sermia is largely explainable through temperature-dependent surface melt modelling. This pronounces the importance of the flow velocity as a control of the surface elevation change of high-dynamic marine-terminating outlet glaciers. A comparison of the temporal evolution of surface elevation change and front retreat at Eqip Sermia with other marine-terminating outlet glaciers emphasises that the changes at Eqip Sermia are strongly controlled by subglacial/submarine bedrock morphology.

Acknowledgements

With these words, I would like to thank the many people who supported me in the realisation of this thesis. Special thank goes out to my supervisor **Prof. Dr. Andreas Vieli** for his continuous and dedicated support throughout the entire year in the making. He always found the time to brainstorm, to feedback, to give valuable input and to keep in touch with me and my project even in times of difficult circumstances and working from home. Also, I would like to thank him and **Dr. Martin Lüthi** for making it possible to be part of the field campaign to Western Greenland in August 2019 and for their support in the field. Dr. Martin Lüthi also supported this thesis through providing numerous datasets and personal knowledge related to Eqip Sermia. Further, I would like underline the extremely valuable work, which has been realised by my predecessor **Simon Schudel** while working on his Master's Thesis in 2018 and 2019. His great effort to collect and organise a large amount of historic data was extremely helpful in the making of this study. Also, his excellent thesis served as a source of inspiration for my own thesis in many ways. In addition, I would like to point out the generous financial support of my fieldwork through the *Department of Geography of the University of Zurich* (GIUZ) and the *Gesellschaft für Schnee, Eis und Permafrost* (SEP).

The following list includes many other people who I want to thank for being part of this journey in many different ways. Andrea Walter, Christoph Rohner, Dr. Philip Rastner, Alessandro Cicoira, Dr. Frank Paul, Adrien Wehrlé, Prof. Dr. Michael Zemp and Dr. Jacqueline Bannwart for their scientific contributions in the form of provision of data, feedbacks and talks during and after coffee breaks. Further, I want to thank my dearest Sarah, Nina, Dario, Carmen, Philipp, Stefan, Armin, Andrew, Mathias, Manu, Flo 1st, Flo 2nd and all other members of the Greenland excursion, my loving parents, Patrick, Tamara, Cindy and everybody else for the distraction, patience, beers, ping-pong, walks, talks, mental support, cooking and card game evenings and everything else. Thank you!

Table of Contents

Table of Figures

List of Tables

1. Introduction

1.1. Motivation

Marine-terminating outlet glaciers have experienced acceleration, thinning and retreat around the entire *Greenland Ice Sheet* (GrIS) (Rignot & Kanagaratnam 2006; Pritchard et al. 2009). The dynamic retreat of marine-terminating outlet glaciers and related increase in mass-flux caused the mass loss of the GrIS to increase dramatically during the last two decades, which raised concerns about implications on future sea-level rise (e.g. Rignot & Kanagaratnam 2006; Shepherd et al. 2020). Several studies have tried to answer related questions through a GrIS-wide assessment of the mass balance (e.g. Kjeldsen et al. 2015; King et al. 2018; Shepherd et al. 2020). However, large spatial variability of the dynamic response of marine-terminating outlet glaciers to climate forcing has shown that these glaciers are sensitive to small-scale controls such as subglacial geometry or bathymetry (e.g. Felikson et al. 2017; Catania et al. 2018). Thus, a better understanding of dynamics of marine-terminating outlet glaciers related to their local controls is crucial for predictions of future sensitivity or resilience of the GrIS in the context of climate change.

Apart from acceleration, thinning and retreat at the front, mass loss at marine-terminating outlet glaciers has been observed to result from inland propagation of diffusive thinning (Felikson et al. 2017). However, only few studies have investigated surface elevation change on the scale of a single marine-terminating outlet glacier, despite the fact, that they are known to be able to show very large surface elevation change rates (Stearns & Hamilton 2007). The assessment of surface elevation change along profiles revealed correlations with terminus positions, flow velocities and temperature records (e.g. Howat et al. 2008; Joughin et al. 2008a; McFadden et al. 2011; Khan et al. 2014; Lüthi et al. 2016; Kehrl et al. 2017; Joughin et al. 2020). A distinctive pattern of surface geometry evolution has been identified by Howat el at. (2008). Studies by Kehrl et al. (2017) and Joughin et al. (2020) showed seasonal oscillations of surface elevation, flow velocity and front position on larger glaciers of Greenalnd.

However, a detailed investigation of temporal and spatial patterns of surface elevation change and their dynamic link to related parameters such as front position, velocity change as well as climate forcing has been missing. Further, studies, which determine the contribution of dynamic mass loss relative to the total mass loss are mostly focusing on long-term averages (i.e. Felikson et al. 2017) but never on the short-term. In this study, this research gap is targeted by the analysis of the changes at Eqip Sermia. This study site is chosen due to the availability of an exceptionally rich collection of scientific data, spanning over more than 100 years. This allows for an assessment of both larger-scale and small-scale as well as long-term and short-term surface elevation change and its connection to length change and flow velocity change.

1.2. Study Approach, Aim and Research Questions

In this study, spatial and temporal patterns of surface elevation change on Eqip Sermia, a medium-sized marine-terminating outlet glacier located in central Western Greenland, are identified based on a mostly qualitative and data-centred approach. This approach is based on the analysis of *digital elevation models* (DEMs) derived from historic aerial imagery from 1953-1964, modern high-resolution drone imagery from field campaigns in 2016-2019 and ready-to-use DEMs such as the new *ArcticDEM*.

Further, the observations of surface elevation change are interpreted by comparing them to a collection of front positions, flow velocity datasets and climate data from regional monitoring stations. The interplay of different processes is assessed through a comparison of the available datasets and qualitative interpretations. Collectively, the following research question and sub-questions are addressed:

- **How did the surface elevation of marine-terminating outlet glacier Eqip Sermia change from 1912 to 2019?**
  - **What spatial patterns of surface elevation change are observable? What is the magnitude? How does the surface geometry change?**
  - **What temporal patterns of surface elevation change are observable?**
  - **Is it possible to observe upstream propagation of surface elevation change signals? On what time scales?**
- **Do the observed surface elevation changes correlate with changes of the front position, the flow velocity and climate change?**
  - **What are the driving factors?**

The study is organised in logical order, similar to the workflow. The following chapter gives a brief summary of the knowledge related to marine-terminating outlet glaciers and the GrIS. Eventually, chapter 3 presents the datasets used for this study and chapter 4 describes the applied methods in detail. The method chapter outlines all steps including DEM generation, data pre-processing, DEM co-registration and post-processing as well as a description of the tools for the subsequent analysis. Chapter 5 presents all results obtained from the first analysis of the data, while chapter 6 contains the interpretation of the results, including additional results from further analysis to support the interpretations. Also, the results are compared to findings from other studies in related fields. Ultimately, chapter 7 concludes the main findings of this study by answering the research questions. Additionally, suggestions for a further improvement of the results as well as for further topic-related research are presented.

2. Background

This chapter gives an overview of the current state of scientific knowledge about the glaciology of Greenland, focusing the Greenland Ice Sheet and marine-terminating outlet glaciers. Subsequently, also a description of the study area and a brief summary of the local history of science is given. In addition, the principles of the methodology applied in this study, namely *Structure from Motion* (SfM) and *Digital Elevation Models* (DEMs) are briefly explained.

2.1. Glaciology

2.1.1. Greenland Ice Sheet

The *Greenland Ice Sheet* (hereafter: GrIS) covers an area of about 1’736’000 km^2, which makes about 81 percent of the area of Greenland. It extends for roughly 2’500 kilometres north to south and 1’000 kilometres from west to east. It is one of only two ice sheets in the world, the other one being the Antarctic Ice Sheet. The central eastern ice dome of the GrIS is peaking at an elevation of more than 3’200 metres. (Benn & Evans 2010)

The total volume is estimated to be 2.6 to 3.0 million km^3. (Benn & Evans 2010; Morlighem 2017). Thus, the average ice thickness of the GrIS measures 1’500-1’700 metres. Approximately 10 percent of the Earth’s freshwater is stored in the GrIS (Benn & Evans 2010). In a warming climate and with a temperature rise in Greenland by 3°C or more, the GrIS degenerates within the next few thousand years (Gregory et al. 2004). The ice mass of the GrIS yields a sea level equivalent of 6.5 to 7.4 metres (Benn & Evans 2010; Morlighem 2017).

Contributions to sea level rise are equivalent to the mass loss and inherently to changes of the extent and the surface elevation from the GrIS. The mass balance of the GrIS is driven by the balance of accumulation and ablation on the surface and ice loss through calving of marine-terminating outlet glaciers. Calving at numerous marine-terminating outlet glaciers all around Greenland accounts for approximately 50 percent of the ice loss of the GrIS, while the other 50 percent are lost through surface ablation. (Benn & Evans 2010) Thus, the mass balance of the ice sheet is highly sensitive to the flow velocities (Rignot & Kanagaratnam 2006).

Simultaneously with the annual accumulation-ablation cycle, the total mass of the GrIS varies within a range of ±150 Gt around the annual mean (Hall et al. 2008). Whether the marine-terminating outlet glacier dynamics or the surface mass balance (SMB) are the main driving factor determining the mass balance of the GrIS unclear. Rignot & Kanagaratnam (2006), Pritchard et al. (2009) and Mouginot et al. (2019) state that changes of the marine-terminating outlet glacier dynamics account for most of the SMB changes, while e.g. Kjeldsen et al. (2015) proclaim that, on the long-term, the SMB is more important. The accumulation on the GrIS is highly variable inter-annually but, according to reconstructions based on ice-cores, accumulation increased after 1995 and caused the ice in the interior of the GrIS to thicken (figure 1) (Pitchard et al. 2009; Noël et al. 2018). Nevertheless, contemporaneously, the total SMB is decreasing (Hanna et al. 2011), as the margins of the GrIS are affected by extensive dynamic ice mass loss through acceleration, thinning and retreat (Pritchard et al. 2009; Rignot & Kanagaratnam 2006).

Due to the small slope gradients on the ice sheet interior, the inter-annual temperature variability largely affects the area of occurring surface melt on the GrIS (Hall et al. 2008, 2013). Recently, the number of days with occurring melt has increased in the interior of the ice sheet (Hall et al. 2013). The *equilibrium line altitude* (ELA) is 1’000-1’500 metres a.s.l. in central Western Greenland (Reeh 1991;

Håkansson et al. 2014). In the GrIS ablation zone, numerous shallow meltwater lakes form on the ice sheet surface during the melt season. The large amount of meltwater resulting from summer surface melt (including the lake water) is known to drain through the ice sheet to the glacier bed, where the water triggers seasonal speed-ups of large areas in the ice sheet ablation zone. (Zwally et al. 2002; Box & Ski 2007; Benn & Evans 2010)

The average ice sheet flow velocities in the interior of the ice sheet typically range from 10 to 100 metres per year (Bamber et al. 2007). Several studies measured an increase of the background (winter) velocity by 25 (at the *Swiss Camp* near the equilibrium line in an elevation of 1149 metres) to 100 percent following the onset of the melt season (Zwally et al. 2002; Joughin et al. 2008a).

Zwally et al. (2002) show very slow flow velocities (slower than the winter values) just after the summer peak velocity. This observation coincides with the mechanism described by Vieli et al. (2004) according to which the flow velocities of a glacier are highest, when the water input is larger than the basal drainage capacity and a subglacial storage is built up. If the water pressures is large enough and discharge is increased, the drainage system becomes more efficient as conduits are enlarged by wall melting (Vieli et al. 2004; Benn & Evans 2010).

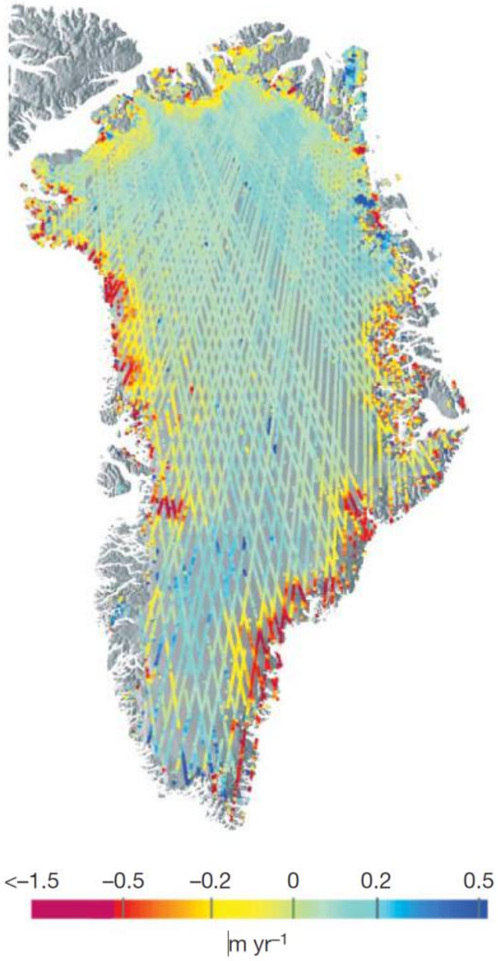

Figure 1: Surface elevation change rate of the GrIS over the period from 2003-2007. Note that the margins of the GrIS are thinning while the SMB in the interior is slightly positive. Figure from Pritchard et al. (2009: 973).

2.1.2. Marine-Terminating Outlet Glaciers

Benn & Evans (2010) distinguish marine- and land-terminating outlet glaciers, as they differ in flow velocities and size. The flow velocities of marine-terminating outlet glaciers range from a few hundred metres to several kilometres per year, whereas land-terminating outlet glaciers and ice margins flow much slower. Most prominent among marine-terminating outlet glaciers of Greenland and largest by ice-flux is *Sermeq Kujalleq* (Danish: *Jakobshavn Isbræ*), located east of Ilulissat in Western Greenland. It drains approximately 6.5 percent of the GrIS and has the largest ice-flux of all glaciers in Greenland. (Benn & Evans 2010) Due to the high flow velocities and a considerable ice-flux from the ice sheet interior to the ocean, marine-terminating outlet glaciers largely control the mass balance of the GrIS (Mouginot et al. 2019). Following the discovery of the dynamic mass loss through marine-terminating outlet glaciers at the onset of the 21st century, they have received much attention from researchers and media (Benn & Evans 2010; Catania et al. 2020).

Marine-terminating outlet glaciers dynamics are controlled by a multiple factors, which show variations on different time scales. Also, the mechanisms are often interdependent and spatially and temporally overlapping. The physical principles of the processes that are controlling the dynamic changes of marine-terminating outlet glaciers are difficult to assess and thus much debated. Accordingly, the current understanding of the related processes is limited and future predictions are difficult. Additionally, the continuous changes at the marine termini are directly affecting the ice sheet interior and thus, a holistic perspective is necessary. (Catania et al. 2020)

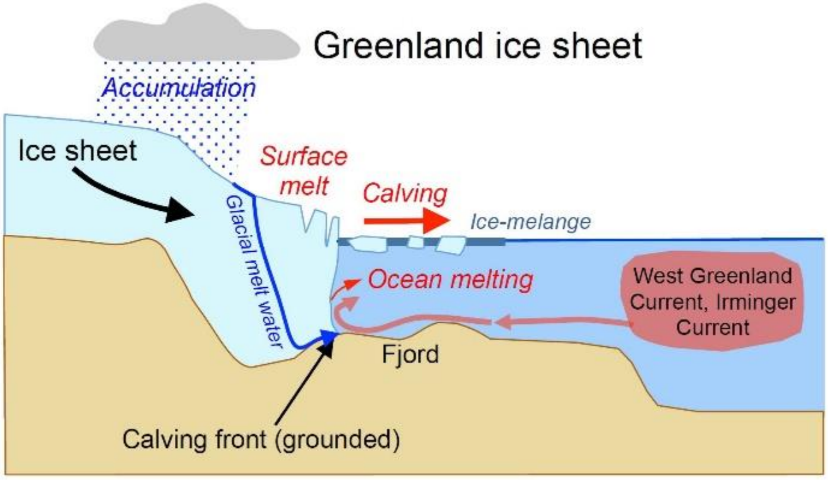

Figure 2: Simplified representation of processes governing the mass balance of marine-terminating outlet glaciers in Greenland. Figure from Vieli (2015).

A simplified representation of governing the mass balance at marine-terminating outlet glaciers is given in figure 2. Atmospheric conditions are controlling accumulation and ablation and inherently also the meltwater availability which determines the conditions at the glacier bed and the magnitude of subglacial discharge at the front. Other ocean-related controls such as the ocean temperature, the meltwater plume, the presence of ice mélange and the bathymetry at the glacier front and in the fjord are important. Ultimately, the morphology of the glacier surface and the bedrock properties are having an impact on the glacier dynamics. Accordingly, the observed dynamics and its changes are the result of multiple internal and external interwoven mechanisms. (Catania et al. 2020)

2.1.2.1. Morphological Controls

The morphological controls include the geometry of the glacier bed and its characteristics as well as the geometry of the ice surface (Catania et al. 2020). The bed of marine-terminating outlet glaciers is often located below sea level (Morlighem et al. 2017). The basal topography model *BedMachine v3* has lately been revised (Morlighem et al. 2017) and leads to the finding that the in-/stability of marine-terminating outlet glacier fronts is largely dependent on the local bedrock topography (Catania et al. 2018). Glacier fronts retreating from shallow submarine terminal moraines into deeper water are generally prone to fast and incessant further retreat until they reach areas with prograde slopes at the bed again (Catania et al. 2018). Apart from the depth, also the cross profile and its variation along the direction of advance and retreat influence the glacier dynamics. Where a front retreat causes the marine-terminating front to widen, glaciers are more sensitive to climate (Enderlin et al. 2013). Retreats of marine-terminating outlet glacier fronts are known to cause dynamic thinning and acceleration, which propagate upstream from the front towards the ice sheet interior (Price et al. 2011, Felikson et al. 2017). At steps in the bedrock with increased slope, inland propagation of dynamic thinning is slowed or restricted (Felikson et al. 2017). Further, the diffusive thinning strongly depends on the slope gradient of the glaciers, with largest thinning rates on steep marine-terminating outlet glaciers and decreasing rates towards the interior (Howat et al. 2008). Diffusive thinning is suggested to account for most of the GrIS mass loss, outweighing the mass loss from the front retreat (Price et al. 2011). Two prominent surface geometries are found to be prominent around the GrIS: (1) glaciers with a shallow- or reverse-slope terminus and increasing slope only after few kilometres from the front, and (2) glaciers with parabolic shaped termini, steepest at the front. Geometry (1) is observed to precede larger retreats. (Howat et al. 2008)

2.1.2.2. Oceanic Controls

Ocean forcing is mainly affecting marine-terminating outlet glaciers through the processes of calving and submarine melting. The calving volume-flux is controlled by buoyancy, buttressing and undercutting, which are highly variable in space and time due to the glacier geometry, the seasonality of ice mélange presence and corresponding stress balance as well as the ocean temperature at the terminus. (Catania et al. 2020)

The annual length oscillations of outlet glaciers terminating in deep fjords are larger than those of shallow-grounded outlet glaciers (Fried et al. 2018). In configurations with well-grounded calving fronts, undercutting controlled by submarine melting induces calving through sloughing of the overhanging ice (Bartholomaus et al. 2013) and the formation of temporal embayments in the sector of the subglacial meltwater outlets (Fried et al. 2018). Shallow-grounded glaciers are thus sensitive to the subglacial meltwater discharge (Fried et al. 2015, 2018). The effect of the meltwater plume on the submarine melting rate is expected to be large, as the buoyancy-induced turbulence is largely responsible for the advection of ocean heat to the submarine glacier front (Carroll et al. 2015). The rates of calving and submarine melting can vary within short distance along glacier fronts, depending on the local depth of the grounding line (Walter et al. 2020).

Subsurface ocean temperatures correlate with the front position, velocity and thickness of *Jakobshavn Isbræ* (Lloyd et al. 2011; Khazendar et al. 2019). The persistent thinning and retreat of marine-terminating outlet glaciers occurs simultaneously with a climate warming, which is favourable for an increase of submarine melt rates through higher ocean temperatures and more subglacial meltwater discharge (Rignot et al. 2016; Catania et al. 2018). Thus, the submarine melting is at least partly indirectly controlled by atmospheric conditions (Catania et al. 2020).

2.1.2.3. Atmospheric Controls

Starting in the mid-1990s, the summer temperatures and the melt extent on the GrIS started to increase drastically (Mernild et al. 2011; van Angelen et al. 2014; Ryan et al. 2019). Recently, the SMB of the entire GrIS has become increasingly negative (van de Broeck et al. 2016). The negative trend for the SMB driven by increasing surface melt rates causes increasing surface slope due to enhanced melt at lower elevations (Feliskon et al. 2017). For marine-terminating outlet glaciers, this can be the onset of a positive dynamic feedback, as the enhanced mass loss in lower areas triggers more ice to flow from higher to lower elevations (Catania et al. 2020). Apart from causing surface slope changes, surface melt is a driving factor of subglacial discharge and the meltwater distribution at the bedrock (Catania et al. 2020). As surface meltwater penetrates the ice sheet and contributes to rising subglacial water pressure, the effective pressure at the bed is reduced and basal velocities increase (Andrews et al. 2014). A correlation of surface melt and flow velocities at marine-terminating outlet glaciers was (Moon et al. 2014). However, as surface melt also contributes to the submarine melting and retreat at the front, also being a control over flow velocities, the exact relationship is uncertain (Fried et al. 2018).

2.1.3. Research Gap

The volume change of the GrIS is equivalent to its mass loss and thus, it is directly coupled to sea-level rise. The detection of dynamic mass loss through a highly dynamic cycle of acceleration, thinning and retreat on marine-terminating outlet glaciers and its implications for the total mass balance of the GrIS unveiled the importance of further investigation on these glaciers in order to better understand their role concerning future sea level rise. (Rignot & Kanagaratnam 2006; Pritchard et al. 2009)

Sole et al. (2008) showed that surface elevation changes on land-terminating outlet glaciers are principally the effect of in-situ ablation anomalies due to increased air temperatures, while the surface elevation lowering rates on marine-terminating outlet glaciers are much larger and therefore must be the effect of ice dynamics, and that ocean forcing must play an important role. However, several studies assess ice dynamics through measuring or model surface elevation/mass changes on the scale of the entire GrIS (i.e. Pritchard et al. 2009; Csatho et al. 2014; Shepherd et al. 2020; Bevis et al. 2019), entire regions (Felikson et al. 2017; Carr et al. 2017; Catania et al. 2018) or averaged per outlet glacier catchment (Catania et al. 2018; Mouginot et al. 2019). Price et al. (2011) and Felikson et al. (2017) use modelling approaches to assess the implications of dynamic thinning and related mass loss at the terminus and upslope propagation of the signal.

Research on the small scale of single marine-terminating outlet glaciers including surface elevation change analysis is being done (Kehrl et al. 2017; Joughin et al. 2020). However, the interplay of spatial and temporal patterns of surface elevation change on both short- and long-term time scales remains unassessed. Thus, this study is addressing this research gap by analysing an exceptionally extensive dataset covering a timespan of more than 100 years, which is available for the area of medium-sized marine-terminating outlet glacier Eqip Sermia. The results concerning surface elevation change are further compared to records of front positions, flow velocity and climate data as well as surface elevation changes assessed on the adjacent land-terminating GrIS margin by Schudel (2019).

2.2. Study Area

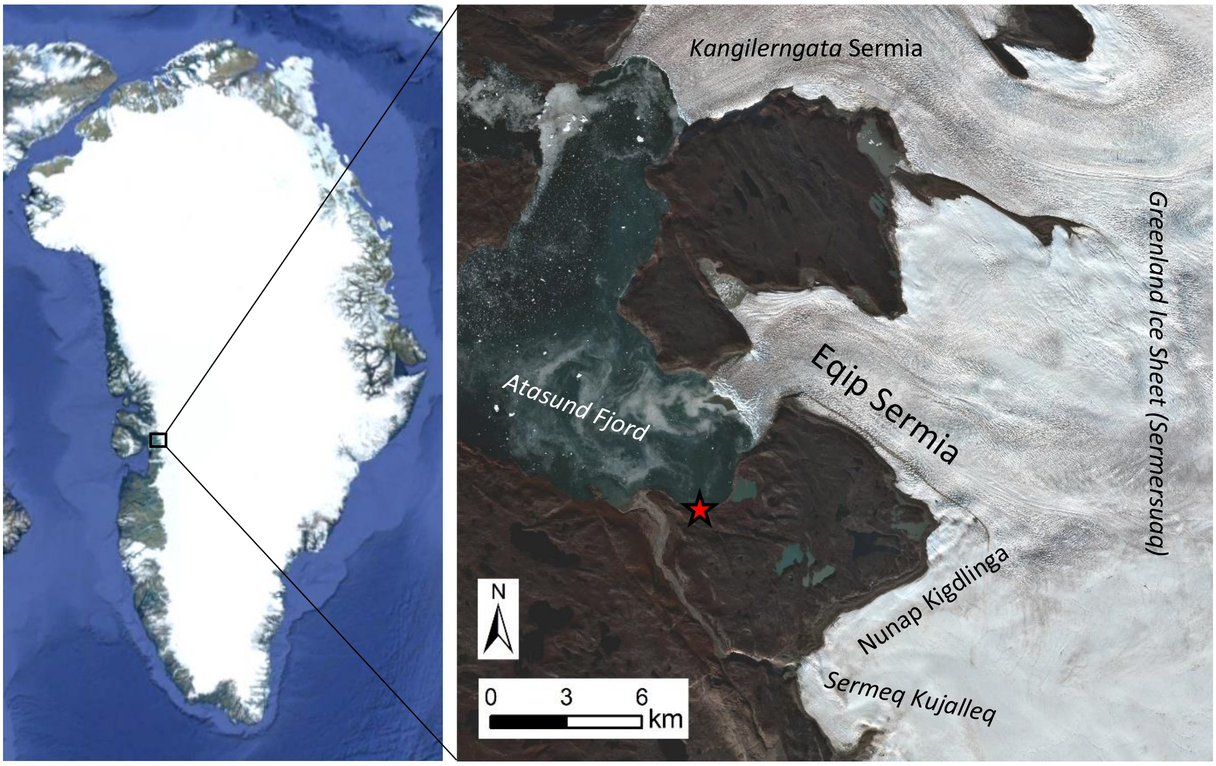

Figure 3: Eqip Sermia and adjacent land- and marine-terminating outlet glaciers. The red star marks the location of Camp Eqi, *base camp for the field campaign in 2019. Inset Map with data from Google Earth (2020). Background: Sentinel-2B, 30th August 2019, European Commission (2015).*

The subject of this study is the marine-terminating outlet glacier Eqip Sermia. It is located 69° 48’ N and 50° 12’ W in central Western Greenland and drains a part of the GrIS into the *Atasund Fjord* (figure 3). *Atasund Fjord* is a north extension of the *Disko Bay*, where Ilulissat, the largest town of the region and the touristic capital of Greenland, is located. In summer, Eqip Sermia can be reached by a boat trip of ca. 80 kilometres from Ilulissat, or alternatively by helicopter. On the southern shore of the fjord bay just in front of Eqip Sermia, the *Glacier Lodge Eqi* can host a small number of tourist. Next to the tourist accommodations, a relict wooden hut, informally called *Camp Eqi* and built by the *Expéditions Polaires Françaises* (EPF) (Kadded & Moreau 2013), serves as base camp for the scientific expeditions by the *Department of Geography of the University of Zurich* (GIUZ) to the area. From *Camp Eqi*, the orographic left moraine complex of Eqip Sermia marking the LIA maximum extent of ~1920 (Bauer 1953) as well as the land-terminating ice sheet margin (*Nunap Kigdlinga* and *Sermeq Kujalleq*) to the south of Eqip Sermia, can be accessed by a walk of a few-hours.

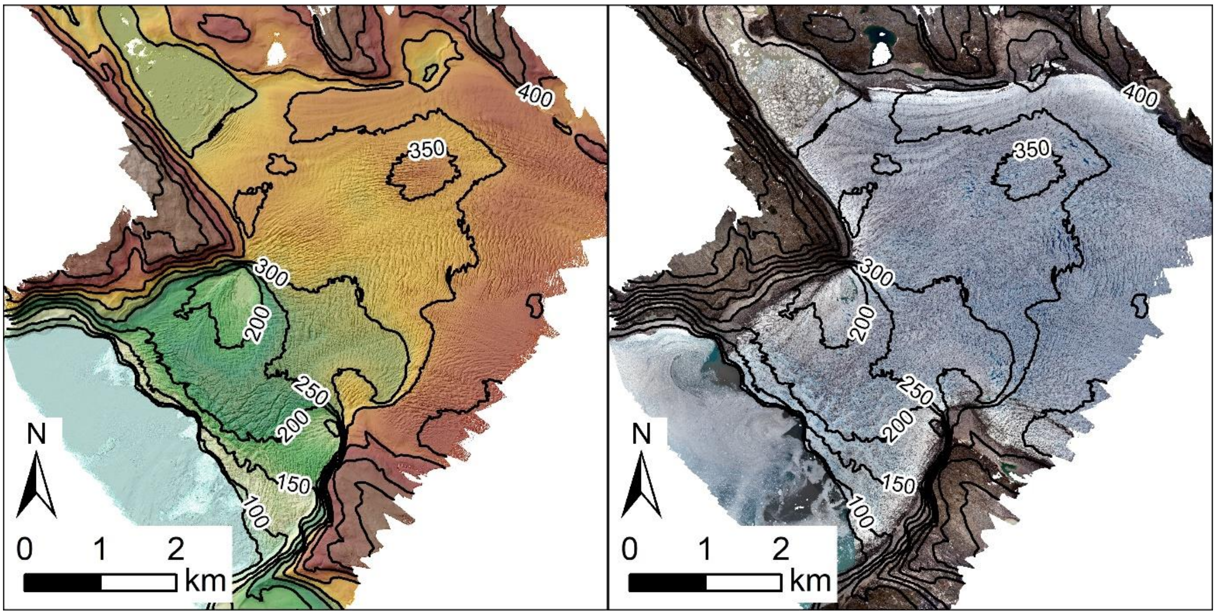

Figure 4: Topography (left) and orthomosaic (right) of the terminus of Eqip Sermia. The selected elevation contours (black) mark the elevation above the WGS84 ellipsoid. The orthomosaic dates to 11th July 2018. With data from Jouvet et al. (2019).

Eqip Sermia is one of ca. 280 marine-terminating outlet glaciers of Greenland, draining the GrIS in all cardinal directions (Catania et al. 2020). It is medium-sized (Lüthi et al. 2016), measuring a width of the calving front of approximately 3.2 kilometres in 2019. The calving front is highest in the centre and to the orographic right, where it reaches a height of ca. 150 metres above the water line (figures 4 and 5). To the orographic left, the front height above sea level measures ca. 50 metres. Located approximately 3 kilometres further out in the fjord, the front height in 1912 was only 30 metres (de Quervain & Mercanton 1925), while in 1955, a front with a height of 30 metres was described (Hansen 1968). Currently, the calving front is located in a relatively shallow zone of 0-20 metres (right) and 70-100 metres water depth (left) (Walter et al. 2020). The average depth of the grounding line was determined -25 metres in 2016. From 2015-2019, at times, bits of bedrock were uncovered at the bottom of the calving front (Walter et al. 2020). The long-term mean terminus flow velocity of ca. 3 m/day resulted in an average calving-flux of approximately 0.8 km^3/day during the past century (Bauer 1968a; Lüthi et al. 2016). However, Eqip Sermia is found to show a significant acceleration (Lüthi et al. 2016; Rohner et al. 2019) and velocities up to 10 metres close to the front more recently (Jouvet et al. 2019) (figure 7).

Figure 5: Orographic right part of the front of Eqip Sermia. Note the tourist boat for scale. The greyish moraine indicates the vertical extent of the LIA maximum of ca. 1920. Image by Roger Honegger (15th August 2019).

The hydrologic catchment of Eqip Sermia calculated based on the surface flow routine includes an extent of approximately 600 km^2 and extends approximately 50 kilometres inland (Walter 2016). As stated by Bauer (1953), the ice stream of Eqip Sermia itself is optically traceable all the way to the firn limit located 80 kilometres to the east. Catania et al. (2018) modelled the catchment based on the *GimpDEM* by Howat et al. (2014) and calculated an area of 300'000 km^2, assuming that it reaches all the way to the top of the ice sheet. From the ice sheet interior, the ice flows almost straight westwards before, about 15 kilometres from the front, it is deviated to northwest. Ca. 4 kilometres before the front, the ice-flow turns 90° to southwest before the glacier calves into the *Atasund Fjord*.

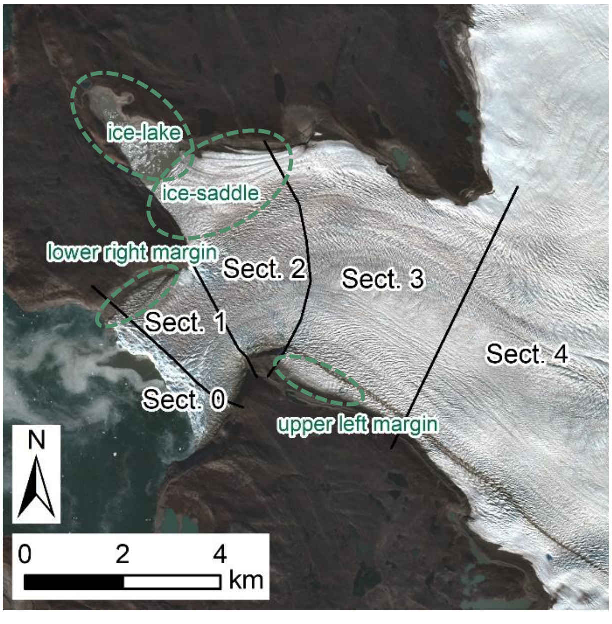

Figure 6: Sectors, sector limits (black lines) and margin areas (dashed green lines) of Eqip Sermia. Background: Sentinel-2B, 30th August 2019, European Commission (2015).

The surface structure in the higher elevated areas far from the terminus is almost completely even. Only as the ice approaches the terminus area, it accelerates and crevasses appear. The terminus area of Eqip Sermia has a very rough surface with abundant crevasses several dozens of metres deep and séracs towering just as high. The ice surface topography of the Eqip Sermia terminus area indicates that the ice flows over a first subglacial step in the bedrock ca. 4.3 kilometres from the front and another step ca. 1.8 kilometres before the front (figure 4). In the lowest section, the surface elevation is highest along the central flow line, whereas, especially below the lower step, towards the margins, significant depressions with a depth of more than 50 metres characterise the ice surface. The named steps in the bedrock are not strictly thought to extend across the entire cross-section of Eqip Sermia. Rather, according to the *BedMachine v3* (Morlighem et al. 2017) marginal rock shoulders partly form a step and partly just bottleneck-like narrow the ice-channel.

For the ease of description and analysis in this study, based on these observations, the terminus area of Eqip Sermia is divided into sectors (figure 6): (sector 0) the front, (1) the area below the lowest step, (2) the zone between the lower and the upper step, (3) the area above the upper step and (4) the smoother and more even upstream area. The surface elevation change patterns are poorly assessable in sector 4, as only few available datasets reach this far upstream. In this study, term *terminus area*

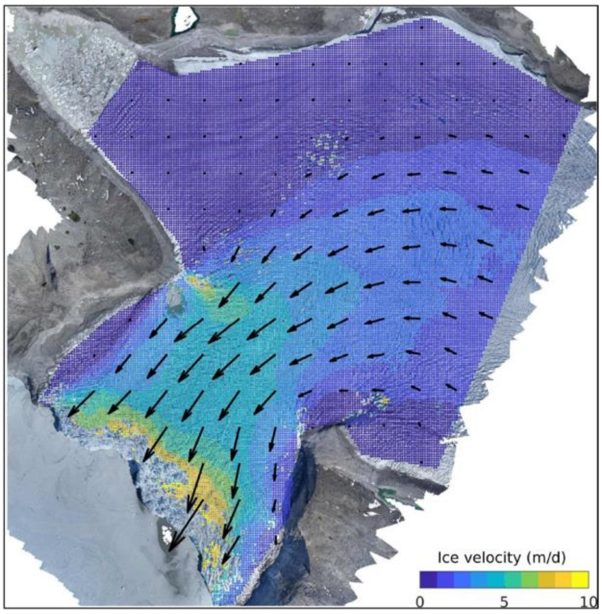

Figure 7: UAV-derived average surface flow velocity from 8th to 11th July 2018. Figure from Jouvet et al. (2019: 9).

includes the sectors 1-3. The surface elevation close to the front (in sector 0) is strongly affected by the front position variations and calving in recent years after 2013, as it is the area where the ice body of Eqip Sermia ultimately crumbles and disintegrates.

In contrast to the very rough surface in the centre of Eqip Sermia, especially the right margin in sector 1 and the left margin in sector 3 are charactervised by a rather smooth surface and inexistent crevasses. In accordance with a velocity field calculated by Jouvet el al. (2019, figure 7), hereafter, these areas are named *low-dynamic areas*. The same terminology is also used for the area of the ice-saddle, separating the main ice stream (hereafter: *high-dynamic centre*) from the ice-lake to the north of Eqip Sermia. The ice-lake has experienced a sudden and rapid subglacial drainage through the terminus are of Eqip Sermia in August 2014 (Vieli et al. 2018).

Despite the coarse resolution, *BedMachine v3* gives an impression of the 3D-dimensions of Eqip Sermia (figure 8). It reveals, that the glacier bed of Eqip Sermia is largely overdeepened, as the bedrock is composed of two troughs with bottoms well below current sea level. The extent of the overdeepened bedrock is modelled to reach 30 kilometres inland from the current front. The ice thickness along the main depression in the bedrock increases from approximately 250 metres in sector 1 to 400 metres in sector 2 and more than 600 metres in sector 3. 25 kilometres from the front, the ice thickness reaches ca. 1’200 metres (figure 9).

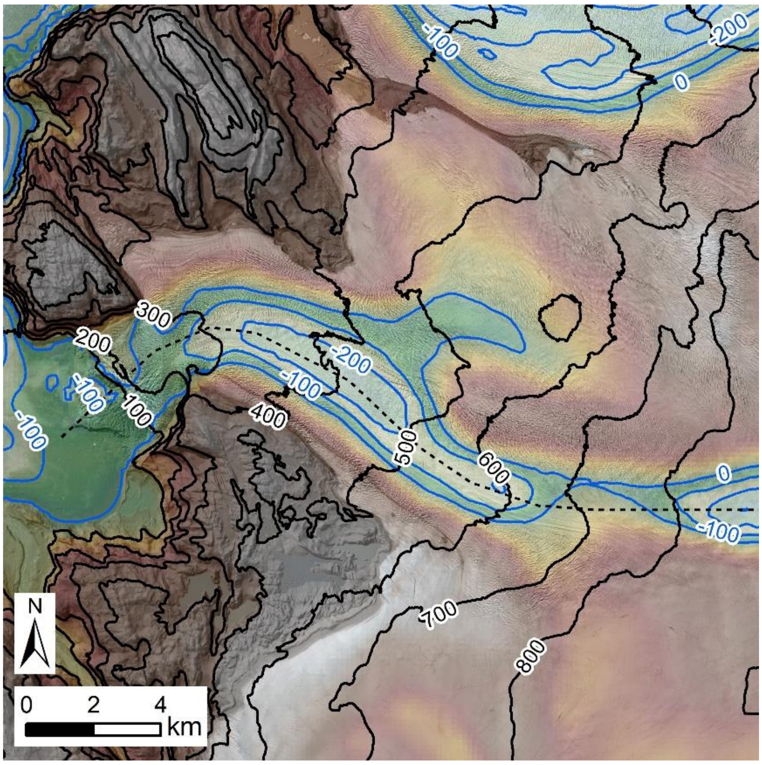

Figure 8: Surface and bedrock topography at Eqip Sermia. The surface contours (black) and the hillshade are derived from the ArcticDEM *composite. The submarine bedrock contours (blue) are derived from the* BedMachine v3 *bedrock topography (graded colours). The dashed black line marks the profile represented in figure 9. With data from Morlighem et al. (2017) and Porter et al. (2018).*

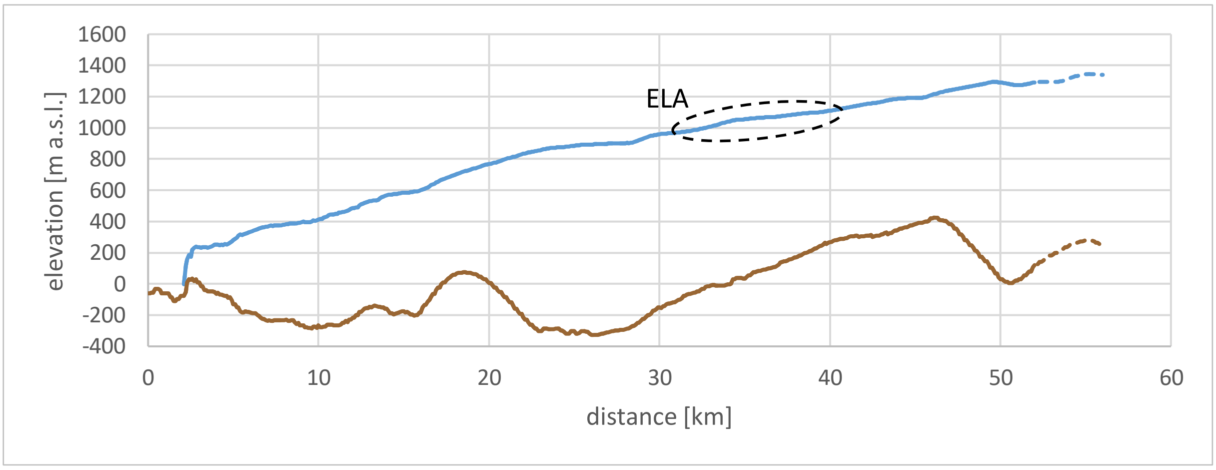

Figure 9: Surface and bedrock elevation along the central flow line of Eqip Sermia (dashed line in figure 8). The surface elevation profile is derived from the ArcticDEM *composite (Porter et al. 2018). The bedrock profile is derived from the* BedMachine v3 *(Morlighem et al. 2017). The dashed ellipse marks the approximate the regional equilibrium line altitude (ELA) (Håkansson et al. 2014).*

2.2.1. Exploration History

As mentioned above, the scientific exploration of Eqip Sermia and its adjacent area started over 100 years ago. Thanks to this long exploration history, the evolution of the terminus of Eqip Sermia is well documented (figure 10). A Swiss expedition arrived at Eqip Sermia in summer 1912. Alfred de Quervain, main leader of the expedition, together with three companions eventually succeeded in traversing the GrIS from west to east, being the second expedition ever to successfully cross the GrIS. Paul-Louis Mercanton, cartographer and leader of the remaining western group of the expedition, and his team stayed at Eqip Sermia and intensively investigated and mapped the area. (de Quervain & Mercanton 1925) One of the maps from this expedition, drawn by Mercanton and dated to 18.-19. VIII. 1912, is used in this study.

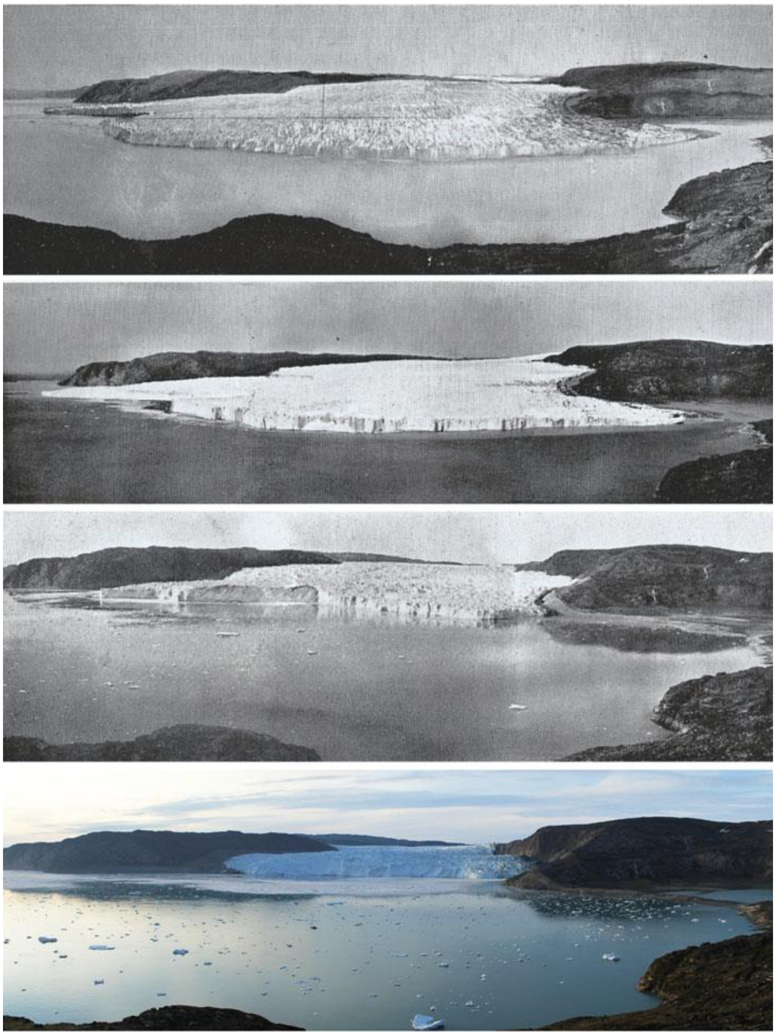

Figure 10: Evolution of the terminus of Eqip Sermia as seen from the opposite side of the fjord, close to Camp Eqi*. Year of image acquisition from top to bottom: 1912, 1929, 1953 and 2015. Figure from Lüthi et al. (2016: 643).*

Eventually, the area was revisited for scientific purposes by Wegener (1929-1931). (Lüthi et al. 2016) An old wooden hut, *Camp Eqi*, and remains of a funicular that was used to transport material for scientific work to the GrIS are relicts from a number of visits referred to as

Expéditions Polaires Françaises (EPF) in the years 1948-1953. These expeditions focused on the Eqip Sermia and the GrIS, where ice thickness was assessed for the first time. (Bauer 1953; LeSchack 1964) They were followed by the *Expéditions Glaciologiques Internationales au Groenland* (EGIG) from 1957-1960. These resulted in a topographic map of the terminus of Eqip Sermia dated to 1959 (Bauer 1968a) and aerial images from numerous flights, of which the resulting image series of the years 1953, 1957, 1959 (A. Bjørk (SDFE), Bauer 1968a/b) and 1964 (Bauer & Carbonell 1968) are used in this study. Eqip Sermia was again visited by Zick in 1971, when remeasurements of the results from the EGIG expeditions were made (Zick 1972). Ultimately, a project by the *Styrelsen for Dataforsyning og Effektivisering* (engl.: *Danish Agency for Data Supply and Efficiency*, SDFE) with the aim to obtain image series covering the entire ice-free areas of Greenland from 1978-1987 resulted in a valuable collection of high-quality aerial photographs, which later enabled the generation of the *AeroDEM*. (Korsgaard et al. 2016)

2.2.2. Greenland Ice Sheet

The GrIS manly consists of three different zones: (1) a large accumulation zone, which covers its entire interior part and is characterised by slow ice-flow, (2) ice streams leading the ice-flow towards the margins and (3) outlet glaciers (either land- or marine-terminating) that drain the GrIS (Benn & Evans 2010). Accordingly, Eqip Sermia incorporates all of the zones described above. The terminus area (sectors 1-3) corresponds to the outlet glacier, sector 4 and the area up to the ELA can roughly be considered as ice stream and the areas above the ELA mark the accumulation zone (compare: figure 9). This study mainly focuses on the Eqip Sermia outlet glacier below 800 metres a.s.l., which only represents a small, but however, the most dynamic fraction of the contributory area.

2.2.3. Neighbouring Outlet Glaciers and Ice Margins

Eqip Sermia is enclosed by marine-terminating outlet glacier *Kangilerngata Sermia* to the north and a sector of land-terminating ice including *Nunap Kigdlinga* and the ice lobe of *Sermeq Kujalleq* to the south (figure 3).

2.2.3.1. Kangilerngata Sermia

The terminus area of *Kangilerngata Sermia* is located approximately 13 kilometres north of Eqip Sermia. The accumulation zones of Eqip Sermia and Kangilerngata Sermia are located next to each other and the ice streams separate ca. 25 kilometres from the fronts. *Kangilerngata Sermia* experienced a velocity increase by factor three and fast retreat of 2.3 kilometres within 5 years from 2005 to 2010, during which the front retreated into deeper water. *Kangilerngata Sermia* is expected to retreat rapidly and continuously during the next decades as the glacier bed is strongly overdeepened all the way from the current front position to 30 kilometres further upstream. (Kane et al. 2016)

2.2.3.2. Sermeq Kujalleq and Nunap Kigdlinga

The land-terminating margin of the GrIS named *Nunap Kigdlinga* and the adjacent ice lobe *Sermeq Kujalleq* are located approximately 10 kilometres southeast of Eqip Sermia. The ice margin of *Nunap Kigdlinga* is located at an elevation of ca. 600m a.s.l., while the lobe of *Sermeq Kujalleq* reaches down into a valley to an elevation of 200m a.s.l. Together with Eqip Sermia, these two sites have been studied for more than 100 years, starting with the Swiss expedition of 1912 (de Quervain & Mercanton 1925). In contrast to fast-flowing Eqip Sermia, this area and especially *Nunap Kigdlinga* is characterised by slow ice flow. Its surface is easily accessible and therefore has been chosen as starting point for the ice sheet crossing by de Quervain in 1912 (de Quervain & Mercanton 1925). In a recent study, changes of the surface elevation, extent and flow velocity were investigated (Schudel 2019). Concerning surface elevation change, a long period from 1912 to 2003 of mostly stable surface elevation followed by a rapid surface lowering which is still ongoing. The observed surface elevation changes are strongly correlating with temperature records and modelled surface melt. (Schudel 2019)

2.3. Digital Elevation Models

Digital elevation models (DEMs) are representations of the elevation of a surface in three dimensions (Bhardwaj et al. 2016). While the x- and y-coordinates of DEMs are georeferencing the elevation values in the 2D-plane, the elevation values itself represent the z-coordinate. Usually, DEMs are grids with a regular grid size and equal grid cell dimensions in x- and y-direction. However, in some cases, DEMs can also have different x- and y-grid cell dimensions. For example, the *ASTER GDEM2* (Slater et al. 2011; Tachikawa et al. 2011) is provided with a resolution of 10x30 metres. The grid values of DEMs are displayed as raster in a GIS software.

In addition to the term *DEM*, other terms such as *digital surface model* (DSM) or *digital terrain model* (DTM) exist. Depending on the data acquisition technology, measured surfaces can appear layered. In case of high vegetation covering the survey area, the term *DSM* often refers to the top-of-vegetation elevation, representing the first-signal surface. The DTM accordingly represents the terrain surface disregarding signals from vegetation. (Bhardwaj et al. 2016) Due to the survey terrain conditions at Eqip Sermia, further consideration of terminology issues are of no avail, as no high obstacles such as vegetation or buildings are present in the study perimeter. Thus, the terms are useable interchangeably. All gridded elevation representations regarded in this study are referred to as *digital elevation models* (DEMs).

Different data acquisition methods enable the derivation of DEMs. The main advantage of active systems such as LiDAR and SAR is their independence of weather and light conditions, as they measure the reflection of self-emitted radiation. (Bhardwaj et al. 2016) However, SAR is known to be able to penetrate ice surfaces by multiple metres, which has to be considered in the generation of DEMs over glaciated terrain (Rignot et al. 2001). Optical sensors such as simple handheld digital cameras have the advantage, that they can be mounted on any UAV easily, as practiced for acquisition of the drone imagery used in this study.

A look at the *new high-resolution* DEM produced in the mid-1990s (Ekholm 1996) in retrospective, it appears that the technological achievements of the past two decades are immense. Whereas in 1996, a 2km-resolution DEM of Greenland was worth an announcement, nowadays, the *ArcticDEM* provides 2m-resolution DEM coverage of the entire Arctic landmasses in sub-annual temporal resolution. These latest developments are also the foundation of studies of temporal and spatial surface elevation change.

2.4. Structure-from-Motion

Structure-from-Motion (SfM) is a valuable tool to generate DEMs form images. According to the name, SfM derives the structure of the surveyed surface form data acquired by a moving sensor. Sensors are often optical or thermal cameras, whereas the motion is most practically obtained through mounting the respective sensor on either drones, airplanes or satellites. This way, series of overlapping images are acquired, which eventually, as the case in this study, are processed in digital SfM software in order to generate 3D models of the surveyed area. The 3D geolocation and 3D structure of surveyed objects is calculated based on the principle of photogrammetry, where the algorithm-based identification of identical points in overlapping images is used to triangulate their relative position.

Among other applications, SfM offers great opportunity for the detection and assessment of spatially distributed processes, which include surface elevation change. For instance, former glaciology related studies have used SfM derived elevation models to detect spatial patterns of downwasting of debris-covered ice (e.g. Midgley et al. 2018) or to assess melt dynamics of alpine glaciers (e.g. Rossini et al. 2018). Further, study site related, SfM derived orthomosaics have been used to investigate glacier flow velocities (Jouvet et al. 2019; Rohner et al. 2019). Therefore, SfM is very applicable for the purpose of this study. Except for the historic maps, all elevation data used in this study is derived from overlapping imagery by applying digital photogrammetry technologies (further explanation in chapter 3).

3. Data Description

3.1. Drone Data

Several high-resolution image series with a ground resolution of ca. 17 centimetres were acquired by an *eBee Sensefly* drone during three GIUZ field campaigns in the years 2016, 2017 and 2019 and are processed on behalf of this study (see chapter 4.1). Prof. Dr. A. Vieli und A. Walter were responsible for the planning and execution of all drone projects (both: GIUZ). During each of the 10 drone projects ca. 600 nadir images of the Eqip Sermia terminus were acquired. In the post-processing of the image series, the coordinates recorded by the drone GPS are assigned to the header of the images. The image series from these drone projects are used to generate high-resolution DEMs and orthomosaics to assess surface elevation change on Eqip Sermia. Table 1 gives an overview over all drone projects, whose image series were processed in this study.

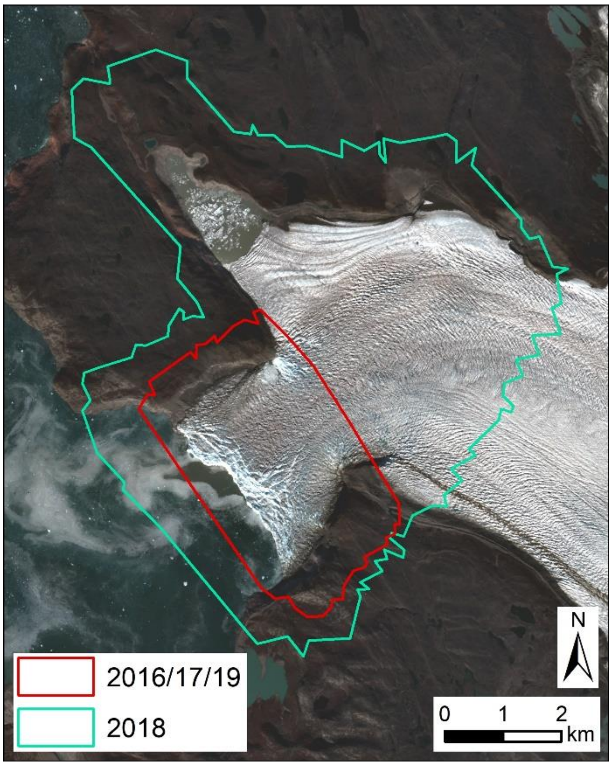

Figure 11: DEM and orthomosaic perimeters resulting from the drone projects in different years. Background: Sentinel-2B, 30th August 2019, European Commission (2015).

In 2018, Jouvet et al. (2019) acquired further aerial imagery of Eqip Sermia. Courtesy of Dr. G. Jouvet, he provides three already processed high-resolution (0.5m) DEMs and corresponding orthomosaics from drone projects executed on 6th, 8th and 11th July 2018. These projects were realised with the use of the *X8 Skywalker* drone. Due to the high endurance and flight speed of this drone, only one flight per drone project was necessary to cover an area of ca. 50 km^2 in 150 minutes (figure 11). No, GCPs were used, as the corresponding SfM projects were georeferenced directly through real-time recorded coordinates from the RTK GPS mounted on the drone. The resulting absolute position and elevation accuracy is in the range of 1-2 pixels or 0.25-0.5 metres. (Jouvet et al. 2019)

Table 1: Drone campaigns by the GIUZ and respective numbers of images, areas and flight altitudes. Note that the flight altitude is a rough average, as it varies depending on the flight line.

date	# images	area [km^2]	altitude [km]
30.06.2016	448	11.2	0.8
02.07.2016	626	13.0	0.8
21.08.2016	628	12.9	0.8
23.08.2016	214	7.1	0.8
25.08.2016	616	12.6	0.8
16.06.2017	620	12.7	0.8
20.06.2017	537	11.4	0.8
22.06.2017	625	12.4	0.8
18.08.2019	623	13.1	0.8
20.08.2019	613	12.8	0.8

3.2. Historic Aerial Imagery

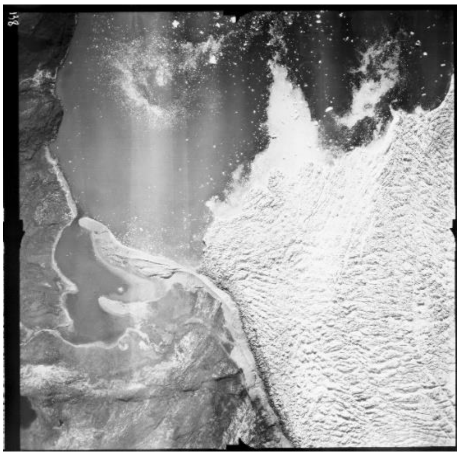
Figure 12: Example of a historic aerial image as used for the DEM generation. This image dates to 12thJuly 1957. Image from Bauer (1968b).

The history of aerial imagery of the area of Eqip Sermia started about 70 years ago. The earliest available aerial image was taken on 18th July 1949 by the then called *Geodætisk Institut* of Denmark (Hansen 1968, Schudel 2019), which is the predecessor of the SDFE. This agency runs the *AirBase* database, which archives a large catalogue of aerial imagery from all Danish expeditions to Greenland during the past decades (Korsgaard 2017).

In 1949, no sequence of overlapping nadir images in high resolution was acquired, which would be necessary for a potential DEM generation through SfM. However, in the following years, a number of projects including aerial photographs of the area were realised. Among these, overlapping aerial nadir image series from the years 1953 (A. Bjørk, SDFE) (figure 12), 1957 (Bauer 1968a), 1959 (Bauer 1968a) and 1964 (Bauer & Carbonell 1968) are available, originally obtained from A. Bjørk (SDFE) and provided for the purpose of this study by courtesy of Schudel (2019). All of these image series include a large enough number of high-resolution originally analogue photographs that have been digitalised by the SDFE. The set of historic images used in this study has already been pre-processed by Schudel (2019) by harmonising the images in brightness and contrast in order to support the SfM processing. In this study, the historic images serve as input data for DEM generation with SfM. All series of historic aerial images used in this study are listed in table 2. The according DEM and orthomosaic perimeters are visualised in figure 13.

Table 2: Historic aerial image campaigns and additional information. These corresponding image series are used for DEM and orthomosaic generation in this study. All images were imparted by courtesy of Schudel (2019). The original sources are listed. Note that the image series of 1953 was mentioned by Bauer (1968a) but no further reference is known.

date	**source**	**# images**	**area [km2]**	**altitude [km]**
03.07.1953	A. Bjørk, SDFE*	5	126	6.7
12.07.1957	Bauer (1968b)	14	31	3.8
25.06.1959	Bauer (1968a)	9	312	7.7
12.07.1964	Bauer & Carbonnell (1968)	8	220	9.3

Another survey campaign by the SDFE, covering the entire ice-free areas and marginal ice bodies of Greenland, took place in the years 1978, 1981, 1985 and 1987. The area of Western Greenland including the Eqip Sermia terminus area was covered in 1985. These images later served for the generation of the *AeroDEM* (see chapter 3.4.3). (Korsgaard et al. 2016)

3.3. Satellite Imagery

Open source satellite imagery is mostly limited in resolution and no overlapping image series are available which is why they cannot serve as SfM input data for the generation of additional DEMs. Therefore, in this study, satellite images are merely used for front position mapping (namely the false-colour images corresponding to the *AsterDEM* snapshots). Further, the Sentinel-2 scene from 30th August

2019 (European Commission 2015) was used as supplementary data for the mapping of the flow lines (and along-profiles) and for the production of maps.

3.4. Ready-to-Use DEMs

DEMs derived from space-borne data typically come as ready-to-use products and are provided online (i.e. *ArcticDEM*). Studying of surface elevation changes requires exact knowledge of the exact timestamps of all datasets. Therefore, the requirements for existing DEMs for this study include, that the data must represent a snapshot with a known timestamp. For composite DEMs, it often remains unclear how a resulting mosaic was generated and which point in time is represented in the dataset in different locations. Therefore, existing composite DEMs were mainly excluded from this study. The limitations of composites lead to the decision that only DEMs from four campaigns are considered, namely the *AeroDEM* (Korsgaard et al. 2016), *ArcticDEM* snapshots (Porter et al. 2018), *AsterDEM* snapshots (U.S./Japan ASTER Science Team 2007) and the *GimpDEM* composite (Howat et al. 2014). An explanation for the use of the *GimpDEM*, despite being a composite, is given in chapter 3.4.4.

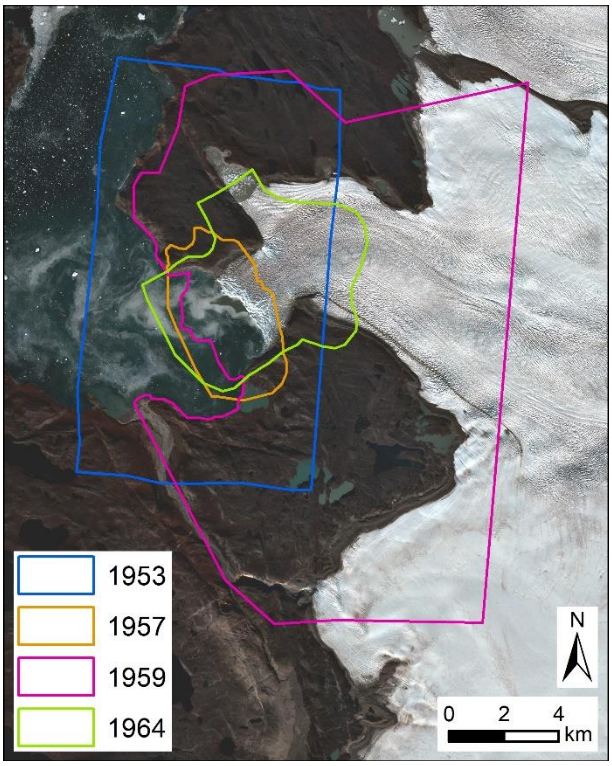

Figure 13: DEM and orthomosaic perimeters resulting from the historic aerial image series from 1953-1964. Background: Sentinel-2B, 30th August 2019, European Commission (2015).

3.4.1. ArcticDEM

The only high-resolution and high-quality area-wide ready-to-use elevation dataset covering the study area is the *ArcticDEM* (Porter et al. 2018). This open-source dataset results from a public-private initiative of the *National Geospatial-Intelligence Agency* (NGA) and the *National Science Foundation* (NSF) and aims for an automatic production of a DEM composite (and DEM strips) covering remote areas of the Arctic. The *ArcticDEM* is generated by processing overlapping pairs of high-resolution optical satellite images with *Surface Extraction from TIN-based Searchspace Minimization* (SETSM) software (Noh & Howat 2018; Morin et al. 2016; NGA & NSF 2019). The input optical images are acquired from 2010-2017, mostly by the commercial satellites *WorldView-1*, *-2* and *-3* and in few cases *GeoEye-1*, which belong to the *DigitalGlobe constellation* (NGA & NSF 2019).

The dataset is accessible through the *Polar Geospatial Center* (PGC) webpage (NGA & NSF 2019). The most recent *release 7* named *ArcticDEM v3.0* includes a mosaicked 2m-resolution DEM (hereafter: *ArcticDEM composite*) covering (almost) the entire land masses of the Arctic north of 60° latitude, complemented by the Kamchatka peninsula, the state of Alaska and

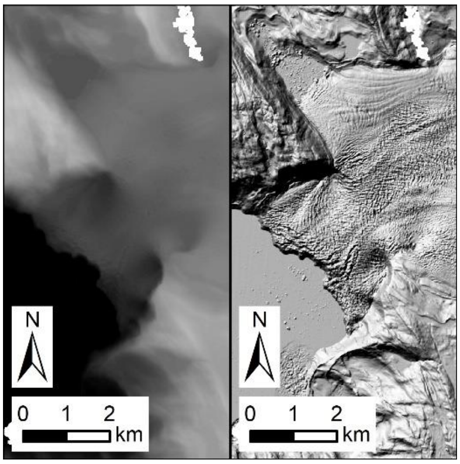

Figure 14: Example of a raw DEM (left) and hillshade (right) of an ArcticDEM *strip. This scene is dated to 24th October 2015. With data from Porter et al. (2018).*

the southern tip of Greenland. The unprecedented coverage and quality is of great advantage and essential for scientific investigations like in this study.

When studying temporal surface elevation changes, exact knowledge of the acquisition date of the elevation data used is crucial. Therefore, the *ArcticDEM composite* mosaicked from multiple datasets with different timestamps is not feasible for this study. However, the *ArcticDEM* dataset also includes a collection of more than 260’000 individual 2m-resolution *ArcticDEM* strips, including metadata information about the acquisition date of the data. Additionally, the metadata lists x, y- and z-offsets to *ICESat* altimetry data, to which also the *ArcticDEM composite* is georeferenced. Therefore, this data source is optimal for the purpose of this study. Further, hillshades are provided and, in the pre-processing, some low-quality areas on land and ice surfaces are already removed *ArcticDEM* strips (figure 14).

In total, 109 *ArcticDEM* strips were downloaded, of which 18 fulfil basic requirements considering coverage of the Eqip Sermia terminus area, stable terrain coverage and quality. The *ArcticDEM* strips used in this study enclose a time span from 19th April 2011 to 21st August 2017. In addition to the 18 *ArcticDEM* strips that cover stable terrain, a set of 11 *ArcticDEM* strips covering higher elevated areas of Eqip Sermia are downloaded of which two (28th May 2013 and 10th July 2015) area used for the assessment of surface elevation change further upstream (chapter 4.6 and 4.8.7). The name code of the *ArcticDEM* strips in this study is *AD*. A list of all *ArcticDEM* strips considered in this study is given in table 3.

Table 3: AcrticDEM strips considered in this study. The DEM names consist of the respective name code and the date in the form of YYMMDD. The DEMs marked with (*) are not co-registered regularly as they do not include enough stable terrain (see chapter 4.6).

DEM name	**date**
AD110419	19.04.2011
AD110613	13.06.2011
AD130325	25.03.2013
AD130423	23.04.2013
AD130512	12.05.2013
*AD130528**	28.05.2013
AD130811	11.08.2013
AD130927	27.09.2013
AD131028	28.10.2013
AD140528	28.05.2014
AD140704	04.07.2014
AD141015	15.10.2014
*AD150710**	10.07.2015
AD150815	15.08.2015
AD150921	21.09.2015
AD151024	24.10.2015
AD151105	05.11.2015
AD160311	11.03.2016
AD160515	15.05.2016
AD170821	21.08.2017

3.4.2. AsterDEM

Same as for the *ArcticDEM* composite, the *ASTER Global Digital Elevation Model (ASTER GDEM)* is a composite of data acquired on different dates (Slater et al. 2011; Tachikawa et al. 2011) and thus not suitable for the surface elevation change analysis in this study. It results from a collaboration of the *National Aeronautics and Space Administration* (NASA) and *Japan's Ministry of Economy, Trade, and Industry* (METI). However, the *EarthData* portal by NASA also provides on-demand *AsterDEM* snapshots and orthorectified images (U.S./Japan ASTER Science Team 2007). The *Advanced Spaceborne Thermal Emission and Reflection Radiometer* (*ASTER*) sensor is mounted on NASA's Terra satellite. The DEM snapshots are generated from *ASTER* stereo-pairs of nadir- and aft-looking NIR images. The developers specify an average vertical error of approximately 10-25 metres. (Tachikawa et al. 2011)

In contrary to the snapshots from the *ArcticDEM*, the *AsterDEM* snapshots are not checked for quality issues and include artefacts, mainly due to clouds and water bodies. Courtesy of Schudel (2019), a raw-version of masks for the clipping of artefacts of some *AsterDEM* snapshots was provided. The snapshots are accompanied by hillshade rasters that allow for a rough but rapid visual check of the quality of the single *AsterDEM* snapshots. From a pre-selection of 26 scenes that were downloaded, six scenes are used in this study. The name code of the *AsterDEM* snapshots in this study is *AS*. A list of all *AsterDEM* snapshots considered in this study is given in table 4.

Table 4: AsterDEM *snapshots considered in this study. The DEM names consist of the respective name code and the date in the form of YYMMDD. The grey entries are later disregarded for the analysis, as their quality is surpassed by other DEMs with similar timestamps.*

DEM name	**date**
AS030609	09.06.2003
AS060703	03.07.2006
AS100709	09.07.2009
AS140826	26.08.2014
AS160707	07.07.2016
AS160723	23.07.2016

3.4.3. AeroDEM

From the aerial imagery campaign by the SDFE in the period of 1978 to 1987, approximately 3500 high-resolution orthophotographs resulted, covering the entire ice-free terrain of Greenland as well as the marginal areas of the GrIS. Korsgaard et al. processed this dataset in order to obtain a large-scale DEM with a resolution of 25 metres (2016). Additionally, an orthophotograph with the same extent and a resolution of 2x2 metres was generated. For the triangulation of the aerial photographs, they made use of *BAE System's* digital photogrammetric application *SOCET SET 5.6*. The DEM and orthophotograph were co-registered through GCPs and altimetry data from the *Geoscience Laser Altimeter System* (GLAS), being part of the *ICESat* mission. They further provide a reliability mask for the *AeroDEM* with values ranging from 0-100. This so called *Figure-Of-Merit* (FOM) was calculated on the basis of processing information with the aim to classify whether DEM raster cell values were interpolated (2 < FOM

< 21) , manually edited (22 < FOM < 39) or automatically correlated (FOM ≥ 40). (Korsgaard et al. 2016) Thus, in this study, only *AeroDEM* elevation values with a FOM value ≥ 40 are used. The aerial photographs used for the generation of the DEM covering the study area were taken on 9th July 1985 (Korsgaard et al. 2016).

The *AeroDEM* is a crucial data source for this study, since it represents the only area-wide elevation dataset available of considerable quality in between 1959 and 2003. The *AeroDEM* also covers a large area of Eqip Sermia, reaching inland as far as 30 kilometres from the front along the central flow line. The name code of the *AeroDEM* in this study is *AE850709*.

3.4.4. GimpDEM

The *GimpDEM* by Howat et al. (2014) is a composite DEM and therefore an exception in the collection of used datasets in this study. The final *GimpDEM* includes elevation data from the *ASTER GDEM2* (Slater et al. 2011; Tachikawa et al. 2011) and *SPIRIT (SPOT 5 stereoscopic survey of Polar Ice: Reference Images and Topographies) DEM* (Korona et al. 2009) for the marginal areas of the GrIS and the *AVHRR photoclinometry enhanced Bamber DEM (PEB DEM)* (Bamber et al. 2001; Scambos & Haran 2002) for the ice sheet interior and far north. All elevation data of the *GimpDEM* is georeferenced to laser altimetry derived elevation data acquired by *ICESat/GLAS* between 2003 and 2009.

Despite the *GimpDEM* being a temporal composite, it is considered in this study due to a combination of the DEM quality and the timing of its data acquisition. According to Howat et al. (2014), the nominal date of the DEM is 2007, and this, for analysis, the decimal year timestamp 2007.5 was assigned to the *GimpDEM*. This timestamp is validated qualitatively by comparing the surface elevation to a *CReSIS* profile dated to 2008 (Gogineni 2012). The respective profile and comparison is shown in figure 77 (appendix I.). Except from the *AsterDEM* snapshots, the *GimpDEM* is the only available area-wide elevation data between 1985 (*AeroDEM*) and 2011 (*ArcticDEM*) for study area. Additionally, the vertical accuracy of the *GimpDEM* is smaller than the *AsterDEMs* uncertainties (chapter 5.2). The code name of the *GimpDEM* in this study is *GD07comp*.

3.5. Historic Maps

A collection of historic elevation information from Eqip Sermia resulted from several scientific expeditions in the 20th century. These include contours drawn in maps showing the dimensions of the terminus of Eqip Sermia in the years 1912 (de Quervain & Mercanton 1925), 1948 (Holtzscherer & Bauer 1954) and 1959 (Bauer 1968a) as well as three benchmarks from 1912 included in the respective map. Another set of points tracked for velocity measurements are measured by Zick (1972). Unfortunately, for the points measured on the terminus of Eqip Sermia, no elevation values are listed. The above-mentioned historic maps are georeferenced by Lüthi et al. (2016), making use of relocated and remeasured reference points included in the historic maps. The positional accuracy of the georeferenced maps is estimated to 50 metres (Lüthi et al. 2016).

3.6. Front Positions

A collection of front positions from 1912-2015 is provided by Lüthi et al. (2016). All of the mapped fronts before 1972 are based on maps produced by different scientific studies through the 20th century with an estimated accuracy of approximately 100 metres. All fronts from 1972 to 2015 are mapped either from Landsat or Sentinel satellite imagery and their position accuracy is better than 50 metres. (Lüthi et al. 2016) Additional front positions are mapped algorithm-based with Sentinel data from 2017 to 2019 and provided by Ch. Rohner (personal communication, Rohner et al. 2019). In total, together with the front positions specifically mapped for this study (chapter 4.9.1), 163 front positions are used.

A table with all timestamps of front positions and further information of the considered front positions is given in table 12 (appendix II).

3.7. Velocity Data

The *MEaSUREs Greenland Ice Sheet Velocity Map* by Joughin et al. (2015) provides gridded average winter surface flow velocities of the entire GrIS. The flow velocities are derived from data of the satellites *Radarsat-1*, *ALOS*, *TerraSAR-X/TanDEM-X* and *Sentinel-1A/-1B*. The dataset includes data for the winters of 2000/01, 2005-2010, 2012/13 (500m-resolution) and 2014-2018 (200m-resolution).

A velocity dataset produced by Ch. Rohner (personal communication, Rohner et al. 2019) provides average flow velocities of the terminus of Eqip Sermia from the time period of October 2014 to January 2020. The spatial resolution of the data is 15 metres. The values were calculated based on Sentinel-1 SAR scenes with a temporal resolution of 6 to 12 days ensuring continuous image correlation.

3.8. Climate Data

Climate data in the form of temperature series is used in this study for the purpose of modelling surface melt and assess the change of surface melt rates in the context of recent climate change. Therefore, temperature data from three different monitoring stations is used to assess surface elevation change in the terminus area of Eqip Sermia.

An automatic weather station (AWS) run by the GIUZ is located on the orographic left lateral moraine of Eqip Sermia at an elevation of 415 metres (hereafter: *AWS-ICE*) (Walter 2016). The horizontal distance to the current ice margin is approximately 100 metres. *AWS-ICE* was installed in 2014 and its data was already used by Walter (2016) to calibrate ablation measurements on the adjacent ice surface. A continuous temperature series with complete month coverage is available from July 2016 to July 2019.

The *Swiss Camp* marks the closest climate monitoring station on the GrIS. This station is part of the *Greenland Climate Network* (GC-NET) (Box & Steffen 2000) and is located ca. 40 kilometres southeast of Eqip Sermia at an elevation of 1149 metres. The distance from the *Swiss Camp* to the closest ice sheet margin measures approximately 30 kilometres. The Swiss camp is not located within the catchment of Eqip Sermia, but due to the geographic proximity, still a good representation of the climate conditions at the higher elevated areas of Eqip Sermia is given. Thus, the temperature data from this monitoring station is very valuable for this study, as it represents the conditions at the approximate regional equilibrium line altitude and (as revealed in further analysis) is helpful for the assessment of drastic changes concerning the melt season at this elevation. The continuous temperature data series of the *Swiss Camp* used in this study covers the period from 2009-2016.

Due to the short time period covered by the monitoring stations in the nearer surroundings of Eqip Sermia, additional data from the monitoring station in Ilulissat run by the *Danish Meteorological Institute* (DMI), is used (Cappelen 2020). This monitoring station is located ca. 70 kilometres SW on an elevation of 29 metres a.s.l. Its temperature series starts in the year 1807 and therefore covers more than 200 years. The temperature data series from Ilulissat is used for the reconstruction of long-term temperature series at the locations of the monitoring stations *AWS-ICE* and *Swiss Camp.*

3.9. BedMachine v3

The *BedMachine v3* dataset is a DEM of the entire subglacial bedrock topography under the GrIS (Morlighem et al. 2017), which is modelled based on spatially limited ice thickness data, seafloor bathymetry and the concept of mass conservation. It is available as a raster with a grid cell size of 150 metres. This dataset is helpful for a rough estimation of the ice thickness of Eqip Sermia and an supports the assessment of morphologic controls on the retreat (in-)stability of the front of Eqip Sermia. The ice thickness is further used to analyse the seasonal ice surface slope- and ice flow velocity-oscillations.

4. Methods

4.1. Drone Imagery

4.1.1. Drone Imagery Acquisition

The method applied for the drone imagery acquisition was largely identical for all the different campaigns and drone projects from 2016 (2 campaigns, 5 projects), 2017 (1 campaign, 3 projects) and 2019 (1 campaign, 2 projects). Prof. Dr. A. Vieli and A. Walter (both: GIUZ) were in charge of the planning and the realisation of all drone projects in the field.

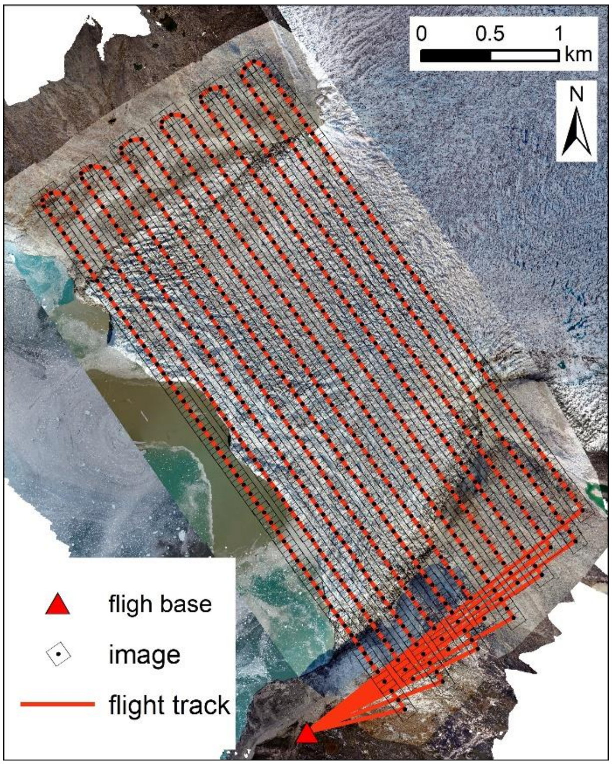

Figure 15: Drone flight base, flight track and image locations of the campaign on 20th August 2019. Background: Orthomosaics corresponding to DR190820 *and* DR180711*. With data from Jouvet et al. (2019).*

The procedure is described exemplarily for the drone projects of the field campaign in 2019. An *eBee Sensefly* drone owned by the *Department of Geography of the University of Zurich* (GIUZ) was used to obtain nadir images of the Eqip Sermia terminus area. The production of DEMs and orthoimages from the drone imagery works best with stable illumination of the study object. In order to minimise changes of light conditions (angle of sunshine, cloud coverage etc.) during one project, it is advisable to keep the time span of the flight projects as short as possible. Fixed wing drones such as the *eBee Sensefly* fly at higher speeds than copter drones, which both decreases the time span of taking pictures and increases the size of area that can be surveyed in a single project.

During the most recent GIUZ field campaign, two projects were realised on 18th and 20th August 2019 respectively. The *eBee Sensefly* drone projects were planned with the *eMotion* flight planning software and included six back-and-forth flights per project, which is equal to 12 flight lines roughly perpendicular to the ice flow direction or parallel to the glacier front (figure 15). One back-and-forth flight takes approximately 20-25 minutes, during which the drone covers ca. 10-14 kilometres of distance and the mounted camera (Sony DSC-WX220, Sony Lens G, 18 megapixels) takes ca. 100 nadir images. The image overlapping was set to 80 percent both in x- and y-direction. From the overlapping percentage and a coarse DEM loaded into the software, the flight altitude is calculated automatically for each traverse flight (ca. 800m a.s.l.). After each back-and-forth flight, the drone was landed to exchange the battery. To complete one flight project including six back-and-forth flights and resulting in a total of ca. 600 images, approximately 3 hours were required. During the project, sunlight angle therefore changed by approximately 45° from the first to the last image, which did not cause any issues during the later processing.

In 2018, the non-commercial *X8 Skywalker* drone was used to realise a larger-scale projects at Eqip Sermia and other glaciers in Greenland (Jouvet et al. 2019). Due to higher flight speeds and larger range of coverage, the area covered during the 2018 drone projects at Eqip Sermia was much larger (50 km^2

in 150 minutes) than the area of the *eBee Sensefly* projects (13km^2 in 180 minutes). The *X8 Skywalker* carries an RTK GPS, which has an uncertainty range of 0.25-0.5 metres. This allows for a very precise determination of the position and orientation of the drone during the flight and inherently the image locations, which straight forward translates into the quality of the resulting DEMs and orthomosaics. (Jouvet et al. 2019)

4.1.2. Ground Control Points for Drone Projects

For the exact georeferencing of drone projects with image series lacking RTK GPS-accuracy positional information, additional high accuracy ground control points (GCPs) well distributed over the entire study perimeter are needed. However, the local conditions did not allow for a measurement of a set of GCPs, as neither the land margin north of Eqip Sermia nor the terminus itself were accessible.

Therefore, in the field campaign of 2019, no GCPs were measured. Instead, the high-accuracy DEM and orthomosaic resulting from the project on 11th July 2018 by Jouvet et al. (2019) are used to define 10 optical GCPs on stable terrain and extract their 3D coordinates (figure 16). These GCPs are then used to georeferenced the *eBee Sensefly* drone projects of the field campaigns in 2016, 2017 and 2019. The accuracy of the reference DEM and orthomosaic are estimated 0.25-0.5 metres in in all dimensions (Jouvet et al. 2019).

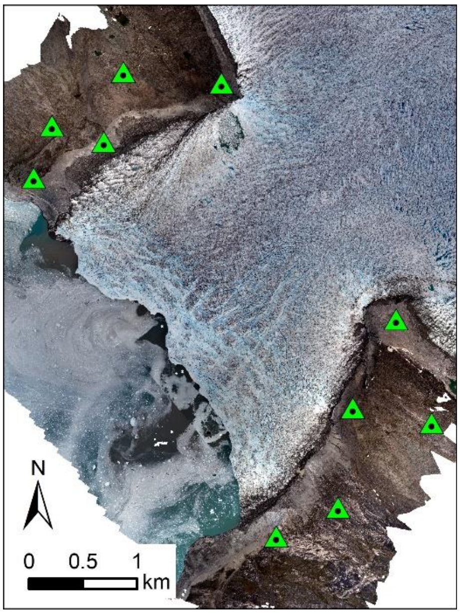

Figure 16: GCPs used for the SfM processing of the drone image series from 2016, 2017 and 2019. Background: Orthomosaic corresponding to DR180711*. With data from Jouvet et al. (2019).*

4.1.3. SfM on Drone Imagery in Pix4D

The drone image series acquired during the GIUZ field campaigns in 2016, 2017 and 2019 were all processed with *Pix4Dmapper (4.4.12)*, which is a photogrammetric *Structure-from-Motion* (SfM) software with the ability to generate 3D surfaces from overlapping images. The processing procedure of *Pix4Dmapper* mainly consists of three processing steps. During the initial processing, all loaded images are calibrated and aligned and a first set of *Tie Points* (equal points identified in multiple images by the algorithm) are calculated, resulting in a *Tie Point Cloud*. In a second step, the *Tie Point Cloud* is further densified into a *Dense Point Cloud*, consisting of all points identified in multiple images. From the *Dense Point Cloud*, the software eventually calculates a *Mesh*, which serves as basis for the *orthomosaic* generation. In the third processing step, based on the *Dense Point Cloud*, a *DSM* (hereafter: DEM) is produced. The calculation of the *DTM* is omitted, as the study area shows no high vegetation such as forest or higher bushes (further information: chapter 2.3). (Pix4D SA 2017)

In the case of the drone projects at Eqip Sermia, the dataset consists of a series of overlapping nadir images with GPS information (x-y-coordinates, accuracy of few metres) assigned to the images (during pre-processing). This GPS information in the header of the images supports the first alignment and calibration of the images in *Pix4Dmapper*. After the first processing step, the optical 3D GCPs are loaded to improve the georeferencing of the SfM project. Eventually, the GCPs are optically identified and manually marked in the images. After the adding of GCPs and before the calculation of the *Dense Point Cloud* and the *Mesh*, the SfM project are *reoptimized* in order to adjust internal and external camera parameters.

A test run with the highest possible quality settings did not notably improve the output quality and therefore not justify the much longer processing time (ca. 3h instead of >15h per project, excluding the manual tagging of GCPs). Therefore, the drone imagery based SfM projects are processed with medium quality settings to reduce processing time. All SfM projects based on drone imagery were processed in the *WGS84 / NSIDC Sea Ice Polar Stereographic North* coordinate system (EPSG: 3413) and the vertical coordinate system is, according to that of the GCPs, the height above the *WGS84 ellipsoid*. The name code of the DEMs derived from drone imagery is *DR*. All relevant processing details are listed in table 5.

Table 5: Processing details of the SfM projects based on drone imagery. The project and DEM names consist of the respective name code and the date in the form of YYMMDD. The grey entries are later disregarded for the analysis due to redundancy, as their timestamps only differ by a few days relative to other drone DEMs. The DEMs marked with (*) were processed by Jouvet et al. (2019).The respective coverage and no. of images per series are listed in table 1.

project & DEM name	**# GCPs**	**R^2 XYZ [m]**	**DEM resolution [m]**	**orthomosaic resolution [m]**
DR160630	9	0.318	0.171	0.171
DR160702	10	0.032	0.174	0.174
DR160821	10	0.025	0.174	0.174
DR160823	4	0.048	0.181	0.181
DR160825	10	0.022	0.174	0.174
DR170616	10	0.034	0.171	0.171
DR170620	10	0.033	0.169	0.169
DR170622	10	0.102	0.171	0.171
*DR180706**	-	-	0.500	0.250
*DR180708**	-	-	0.500	0.250
*DR180711**	-	-	0.500	0.250
DR190818	10	0.019	0.173	0.173
DR190820	10	0.048	0.174	0.174

4.2. Historic Aerial Imagery

SfM software offers the great opportunity to retrieve valuable elevation information not only from recent aerial projects but also from imagery of the past, if certain requirements regarding image overlapping and image quality are met. Exemplarily, continuously overlapping aerial imagery from 1978-1987 covering the entire ice-free areas of Western Greenland as well as the GrIS were used as input data for the production of the *AeroDEM* through digital photogrammetry (Korsgaard et al. 2016).

In addition to the modern drone imagery, digitised aerial imagery from Eqip Sermia of the years 1953, 1957, 1959 and 1964 is used for this study. The images of the respective image series are overlapping and available in considerably high-resolution (ground surface distance: 1.05-2.25 m). In this study, these image series are processed in the photogrammetric software *Agisoft Photoscan (1.4.4.6848)*, aiming for the extraction of area-wide digital elevation data from originally analogue historic photographs.

4.2.1. Ground Control Points for Historic Aerial Images

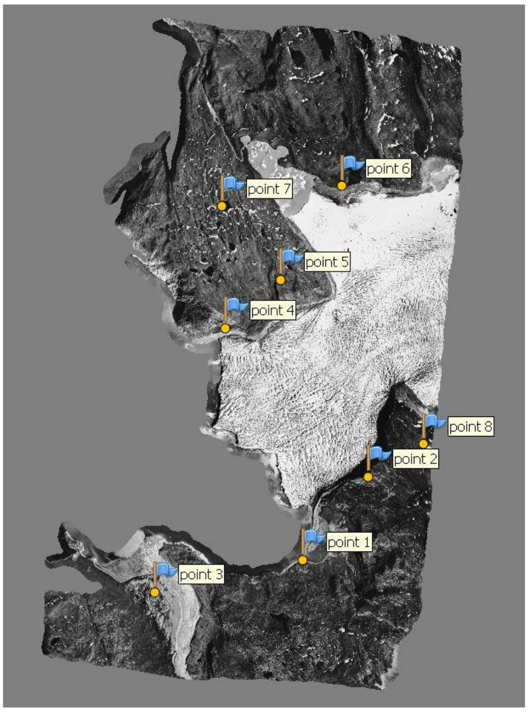

Figure 17: GCP configuration for the SfM processing of the historic aerial image series from 1953 in Agisoft Photoscan.

Due to larger extents of the old aerial imagery campaigns, the DEM from 11th July 2018 is not suitable for the georeferencing of these SFM projects. Here, optical GCPs are identified in the high-resolution orthomosaic from 1985, which corresponds to the *AeroDEM* and provides complete coverage of all historic SfM perimeters. The GCP elevation values are extracted from the 2m-resolution *ArcticDEM composite* rather than the 25m-resolution *AeroDEM*. Since all selected GCPs are located on supposedly stable terrain, the large temporal difference between the acquisition dates should not affect the results. Also, the output DEM resolution of the four SfM projects of the years 1953 to 1964 ranges from 2.0 to 4.5 metres and is therefore comparable to the *ArcticDEM composite* resolution. The 3D coordinates from the GCPs are extracted without prior x-y-correction of the 1985 *orthomosaic* to the *ArcticDEM composite*, which is a potential source of uncertainty. However, the x-y-bias of approximately 7 metres and the z-bias of roughly 0.5 metres between these two datasets both are much smaller than the uncertainties of the resulting DEMs, except for the SfM project of 1953 (chapter 5.2). Due to the varying extents covered by the different historic aerial campaigns, each SfM project was georeferenced by a specific set of GCPs (figure 17).

4.2.2. SfM on Historic Aerial Images in Agisoft Photoscan

From the user perspective, SfM software is largely a black box as the exact functionality of the underlying algorithms is not available. Only when trying to process historic aerial images, using the same input data, it turned out that *Agisoft Photoscan* was producing qualitatively better results than *Pix4Dmapper*, which offered some insuperable issues in the initial alignment and image calibration. Therefore, all historic aerial imagery is processed with *Agisoft Photoscan*. The general logic of the processing is comparable for both SfM software solutions (Agisoft LLC 2018; Pix4D SA 2017). Due to the unsatisfying quality of preliminary results, many different processing options and combinations of GCPs were used aiming for improvement. However, the main limiting factor supposedly is the contrast and colour quality of the input images. The quality of the resulting DEMs is discussed in chapters 5.2 and 6.5.

In comparison with the drone SfM projects, the SfM projects based on historic aerial imagery have very little images as input data, which largely affects the processing time. Therefore, *Agisoft Photoscan* projects were processed with *high/-est accuracy* settings. The output coordinate system is *WGS84 / NSIDC Sea Ice Polar Stereographic North* (EPSG: 3413) and the vertical coordinate system is, according to that of the GCPs, the height above the *WGS84 ellipsoid*. The name code of the DEMs derived from historic aerial image series is *SFM*, not to be confused with the SfM DEMs resulting from drone projects (name code: *DR*). All relevant processing details are listed in table 6.

Table 6: Processing details of the SfM projects based on historic aerial imagery. The project and DEM name consists of the name code and the date in the form of YYMMDD. The respective coverage and number of images per series are listed in table 2.

project & DEM name	**# GCPs**	**R sqrt XYZ[m]**	**DEM resolution [m]**	**orthomosaic resolution [m]**
SFM530703	7	0.4	3.2	1.6
SFM570712	16	37.7	1.0	1.0
SFM590625	14	44.5	4.5	2.3
SFM640712	8	4.4	4.2	2.1

4.3. DEM Co-Registration

If DEMs are used for the analysis of surface elevation changes, the co-registration process is crucial, as it assesses and corrects systematic shifts between the compared DEMs in x-, y- and z-direction. The co-registration process requires the selection of a *master DEM*, preferably of high quality, relative to which all other DEMs (*slave DEMs*) are corrected. Only elevation information from stable terrain is considered for the co-registration. This way, short-term surfaces changes like the targeted ice surface elevation changes of Eqip Sermia do not affect the quality of the co-registration results.

Nuth & Kääb (2011) propose a simple and easily applicable methodology for the co-registration process, which serves as guideline for the co-registration in this study. In a first step, referred to as 'a *universal* co-registration correction' by Nuth & Kääb (2011: 274), the 3D geolocation bias of the DEMs is assessed. Thereby, the translation vectors to be applied on the *slave DEM* are calculated based on the elevation difference of the *slave DEM* relative to the *master DEM* over stable terrain and in relation to the slope and aspect of the stable terrain of the *master DEM*. The underlying equations presented by Nuth & Kääb (2011) are:

$$\frac{dh}{\tan(\alpha)} = a * \cos(b - \psi) + c$$

where

$$c = \frac{\overline{dh}}{\tan(\bar{\alpha})}$$

with dh being the stable terrain elevation difference, α the slope and ψ the aspect. The parameters a and b are the magnitude and direction of the shift, while c equals the mean bias relative to the slope tangent. Eventually, the translation vectors Δx, Δy and Δz are defined as:

$$\Delta x = a * \sin(b)$$

$$\Delta y = a * \cos(b)$$

$$\Delta z = c * \tan(\bar{\alpha})$$

Nuth & Kääb (2011) provide an *Excel*-template which contains a model requiring the input values for dh, α and ψ of a large number (favourably at least a few thousand) of raster grid cells on stable terrain. The output consists of the translation vectors Δx, Δy and Δz. The corresponding shifts are applied to the *slave DEMs* in GIS software (here: *ArcMap*).

Further processing steps such as the identification and correction of elevation dependent biases and other 'biases related to the acquisition geometry of the data' as suggested by Nuth & Kääb (2011: 274) are considered out of scope.

4.3.1. Master DEM Selection

General requirements for a *master DEM* include a high quality of the elevation data and good coverage of the stable terrain in the study area. The latter includes the criteria that e.g. no snow should cover any stable terrain. For central Western Greenland, only a narrow time span from July to October is typically snow-free. Further, high spatial resolution is adjuvant.

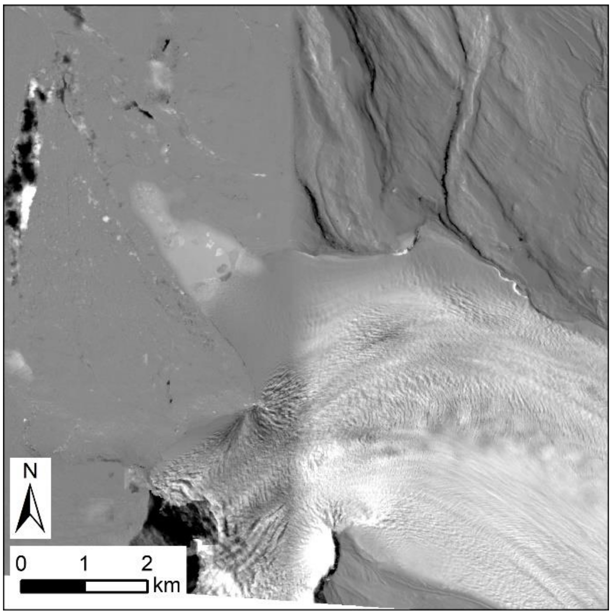

Figure 18: High-resolution difference raster resulting from the subtraction of AD130325 *from* ArcticDEM *composite. The different structure on the left and right indicates a mosaic artefact. With data from Porter et al. (2018).*

In a study by Schudel (2019) in the areas adjacent to Eqip Sermia, the *ArcticDEM composite* was chosen as *master DEM*. However, testing the quality of this composite on the terminus of Eqip Sermia revealed that it is composed of at least two scenes with a transition right across the centre of the area of interest, which is unfavourable. Since the stitching of the two parts of the composite along the transition was not most accurate, artefacts appear in high-resolution difference rasters (figure 18). Thus, an alternative *master DEM* is required to avoid the introduction of artefact-related uncertainties in the co-registration process.

Due to the above-mentioned requirements, after a pre-selection, only a handful of *ArcticDEM* strips could possibly serve as *master DEM*. Among those, a visual check of the corresponding hillshades unveiled the least surface noise and a complete coverage of the stable terrain for the *ArcticDEM* strip dated to 21st September 2015 (*AD150921*). The numerical testing of the absolute accuracy of the *master DEM* by Schudel (2019) was repeated for *AD150921*. Therefore, the differences of the *master DEM* to a set of 16 3D points, measured by a differential GPS with an accuracy of less than 0.001 metres in 2018, are calculated. Accordingly, the resulting mean (+0.27m) and median (+0.34m) of the differences as well as the standard deviation (±0.90m) all indicate that the quality of *AD150921* even surpasses the quality of the *ArcticDEM composite* (-0.10m, +0.52m, ±2.24m (Schudel 2019)). The spatial distribution of the test points was optimal for the study area investigated by Schudel (2019) and therefore suboptimal for this study. However, the elevation differences between the test points nearest to Eqip Sermia and the *AD150921* were smaller than the respective values for the *ArcticDEM composite* too.

4.3.2. DEM Pre-Processing

The co-registration process applied in this study requires the same resolution for the *master DEM* and the *slave DEMs* (Nuth & Kääb 2011). The original resolution of the *master DEM* is 2 metres, while the *slave DEMs* have different original resolutions ranging from 0.17 to 30 metres. In order to avoid upscaling before the co-registration and to preserve the highest quality possible, it was decided to co-register all *slave DEMs* in their original resolution, except for the drone DEMs and the SFM DEMs. The cell size of these DEMs is adjusted to a resolution of 2 metres to agree with the *master DEM*. Accordingly, for the co-registration process, a 25m-version and a 30m-version of the *master DEM* are generated. Table 7 gives an overview over the original resolution and co-registration resolution of the different DEMs.

Table 7: Original resolution of DEMs and resampled/aggregated resolution for the co-registration process.

DEMgroup	*original resolution [m]*	*co-registration resolution [m]*
drone DEMs	0.17-0.5	2
SFM DEMs	1.0-4.5	2
ArcticDEMs	2	2
AsterDEMs	30	30
GimpDEM	30	30
AeroDEM	25	25

To ensure that no information is lost during the adjustment of the cell size, upscaling (coarsening) of the rasters is done by cell aggregation, assigning the mean value of all parent cells to the aggregated cell. If the target cell size does not equal a multiple of the original cell size, an intermediate step to decrease the cell size to a common divisor is added. All downscaling of the cell sizes is done by resampling with the *nearest neighbour* method to avoid interpolation. For example, to change the cell size of the *master DEM* from 2 to 25 metres, first, the *master DEM* is resampled step from 2m- to 1m-resolution before aggregating 25x25 cells to the new 25m-resolution *master DEM*. After the adjustment of the cell sizes yet before the co-registration, all DEMs are clipped to the study perimeter.

The *AsterDEM* snapshots suffer from quality issues that have to be addressed in order to be able to properly use those datasets (figure 19). Artefacts do not only occur over ice or water surfaces, but also over stable terrain. Therefore, the affected areas were removed prior to the co-registration. The *AsterDEM* hillshades are used to manually mask areas in which elevation artefacts appear. Detailed masks for the clipping of the artefacts in this study area were drawn by hand in *ArcMap*. Courtesy of Schudel

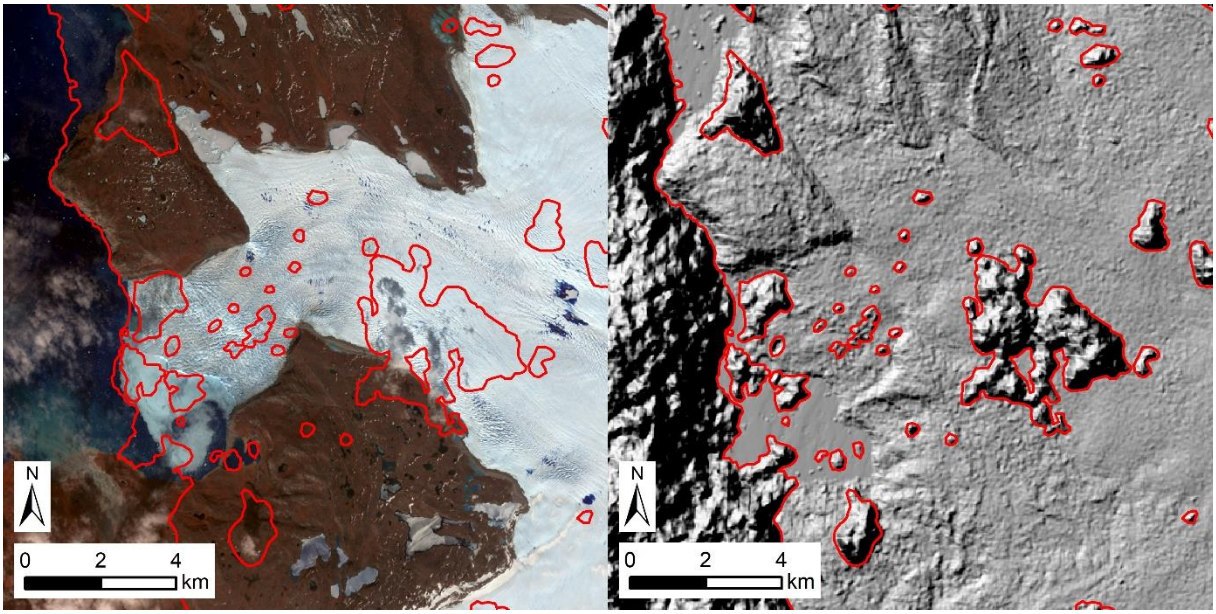

Figure 19: Manual mapping of masking outlines (red) for the masking of artefacts in AS030609*, exemplarily for all* AsterDEM *snapshots. Figure adapted from Schudel (2019: 43). With data from the U.S/Japan ASTER Science Team (2007).*

(2019), this processing step was partly based on a set of raw masks used in that study. A visual double check in the corresponding false-colour satellite image reveals that most of the artefacts in *AsterDEM* snapshots are caused by local cloud cover or low contrast surfaces.

4.3.3. Determination of Stable Terrain

In the co-registration process, only the elevation difference over stable terrain are considered to calculate the translation vectors. Short-term surface changes e.g. caused by ice flow or fluvial/gravitational processes could have a negative impact on the co-registration results. The stable terrain is determined based on a surface type dataset from the *Geological Survey of Denmark and Greenland* (GEUS) provided by Dr. P. Rastner (GIUZ). All surfaces classified as *lakes*, *ice-lakes*, *sea*, *ice* and *alluvial planes* are considered unstable. Additionally, LIA moraine complexes mapped by Prof. Dr. A. Vieli (GIUZ) (manually adjusted for the purpose of this study) are also disregarded. Older moraine complexes are partly covered by vegetation and therefore considered stable. Complementarily, all areas with slopes smaller than 10° are excluded to avoid higher uncertainties when calculating the aspect, and terrain steeper than 30° is also excluded, as it is more prone to erosive processes in general (figure 20).

Considering all limitations as described above, the stable terrain as well as the slope and aspect are calculated for all *master DEM* versions (three different resolutions). Based on the resulting three stable terrain-rasters, three point feature classes with one point per grid cell are generated, which are eventually used for the extraction of the raster values in the co-registration process.

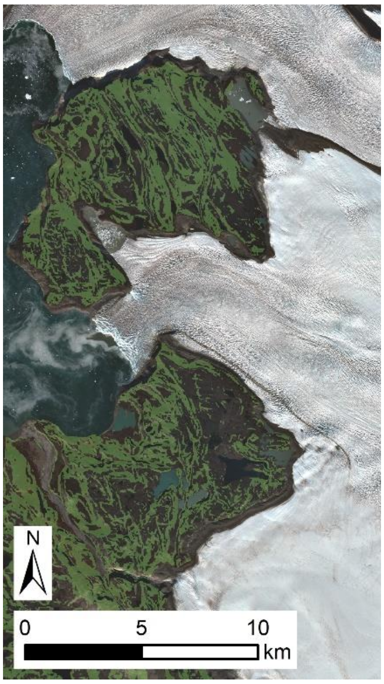

Figure 20: Stable terrain extent (green), which eventually serves a basis for the co-registration and the quality analysis of the DEMs. Background: Sentinel-2B, 30th August 2019, European Commission (2015).

4.3.4. Co-registration Workflow

All 43 DEMs with sufficient stable terrain coverage were co-registered according to the method presented by Nuth & Kääb (2011). The equations underlying the co-registration method are implemented in a model provided in an *Excel*-template. The model for the calculation of the translation vectors Δx, Δy and Δz requires sets of values for each the elevation difference Δh of the *slave DEM* relative to the *master DEM*, the slope α and the aspect ψ of the *master DEM*, all on stable terrain only. Δh, α and ψ are extracted from the respective rasters in *ArcMap*. Thus, the applied co-registration method consists of a combination of single steps executed in two different software applications. The steps reproduced for each dataset are the following:

Prior non-iterative step in *ArcMap*:

- *Extract Multi Values to Points*: extract α and ψ of *master DEM* with corresponding resolution (this step is non-iterative, as no changes are applied to *master DEM*)
- *Raster Calculator*: calculation of Δh-raster ($DEM_{slave} - DEM_{master}$)

ArcMap:

1. *Extract Multi Values to Points*: extract Δh-, copy values (incl. α- and ψ-values) to clipboard

Excel:

2. Paste Δh, α and ψ in *Excel*-template
3. *Excel-Solver*: calculate translation vectors Δx, Δy and Δz

ArcMap:

4. *Shift*: correction of *slave DEM* by Δx and Δy
5. *Raster Calculator*: correction of *slave DEM* by Δz
6. *Raster Calculator*: calculation of Δh-raster ($DEM_{slave(corr.)} - DEM_{master}$)

- Iterate until the mean of Δh and the standard deviation of Δh reach an optimum i.e. do not improve anymore

All changes applied to the s*lave DEMs* in the co-registration process are listed in table 13 (appendix III). The DEMs *AD110613* and *AD160515* are composites each mosaicked from two different *ArcticDEM* strips acquired on the same day. For this purpose, both strips are co-registered individually before being mosaicked. When mosaicking, for the overlapping areas, the values of the raster with the smaller mean Δh and standard deviation are translated into the final product.

4.4. Post-Processing

4.4.1. Pixel Size Adjustment

The surface of Eqip Sermia is very rough, as it is characterised by towering séracs and large crevasses, which cover most of the glacier extent. In order to reduce the local variability between different DEMs for a better surface elevation change assessment, after the co-registration, all DEMs are aggregated to 30 metres resolution for further analysis. For the cell aggregation, again the mean values of all parent cells are assigned to the aggregated cell, to avoid loss of elevation information, as no interpolation is done and no available information is omitted. For the aggregation of the 25m-resolution *AeroDEM* into the 30m-resolution, an intermediate step is added (compare to chapter 4.3.2). For the aggregation in *ArcMap*, the aggregated 30m-resolution version of the *master DEM* was set as snap grid in the *environment settings* to avoid *false hillshade* artefacts. The co-registered 30m-resolution DEMs are used for DEM differencing and the visualisation of the surface elevation along profiles (see chapters 5.3.1 and 5.3.2).

4.4.2. Surface Smoothing

Even with a 30m-resolution, in some areas of Eqip Sermia, the surface roughness is larger than the signal of changes between the DEMs, which is not suitable for the analysis of surface elevation changes in specific locations. Therefore, further smoothing of the DEMs is necessary. To assess this issue, focal statistics of the aggregated 30m-resolution DEMs calculated. This type of calculation includes all information from a specified number of neighbouring cells to calculate the value of the target cell without further increasing the grid cell size. To decrease the surface roughness but at the same time keep the local surface topography, the size of the focal statistics zone should be as large as necessary but as small as possible. In a test with a 3x3- a 5x5- and a 7x7-neighbourhood, the focal statistics neighbourhood of 5x5 cells (equal to 150x150 metres or 2.25ha) is found to be optimal, as in comparison to the 3x3-results, small-scale roughness is no longer visible. From the 5x5 to the 7x7 smoothed version, the improvements of the smoothing are negligible. When using the smoothed 30m-resolution DEMs, it has to be considered, that the elevation values of the raster cells less than 75 metres from the ice border are affected by the adjacent stable terrain elevation. The smoothed 30m-resolution DEMs are used to generate surface elevation point time series, which are especially prone to surface roughness (see chapter 5.3.3).

4.5. Quality and Uncertainty Assessment

After the co-registration, all *slave DEMs* are checked for quality measures by comparing them to the *master DEM*. The uncertainty is calculated based on the deviations of the DEMs over stable terrain only. Thus, all quality measures in this study refer to the stable terrain differences relative to the *master DEM*.

In a first step, the mean elevation difference and its standard deviation (STDV) before and after the co-registration are calculated for all DEMs (figure 30). The detection of non-normal distributions of the elevation difference values further leads to the calculation of the *normalized median absolute deviation* (NMAD). The NMAD as described by Höhle & Höhle (2009) serves as an alternate robust accuracy measure for non-normal distributions and is centred on the median, which is more robust to outliers than the (regular) mean. The NMAD is calculated as follows (Höhle & Höhle 2009):

$$NMAD = 1.4826 * median(|\Delta h - median_{\Delta h}|)$$

The NMAD values are expected to be maximum uncertainties for the aggregated DEMs, as they were originally calculated for the co-registration resolution and the method of aggregation was consistent relative to the *master DEM*. The resulting means, STDVs and NMADs are listed in table 9 (chapter 5.2.2)

4.6. Relative Georeferencing of Upstream DEMs

The assessment of the extent of dynamic surface elevation change with the regularly co-registered collection of DEMs is not possible due to coverage limitations. The lack of DEMs with a single acquisition date but a coverage of the areas further upstream or even coverage of the entire catchment of Eqip Sermia and stable terrain at the same time requires for an alternate methodology.

In this study, in addition to the already co-registered *ArcticDEM* strips*, two ArcticDEM* strips (*AD130528* and *AD150710*) that provide data further upstream of Eqip Sermia are selected for this purpose. These *upstream DEMs* do not cover stable terrain and thus cannot be co-registered according to the method presented in chapter 4.3. Therefore, in this study, the geolocation of the respective DEMs is corrected according to scene-specific 3D-translation vectors (quantifying the offsets of the DEMs to the *ICESat* altimetry data) provided in the metadata of the *ArcticDEM* strips. The described method and the lack of stable terrain of the *upstream DEMs* does not allow for a quality assessment of the 3D positioning accuracy like for the ordinarily co-registered DEMs and thus, these DEMs are not listed in table 9.

4.7. Elevation Extraction from Historic Maps

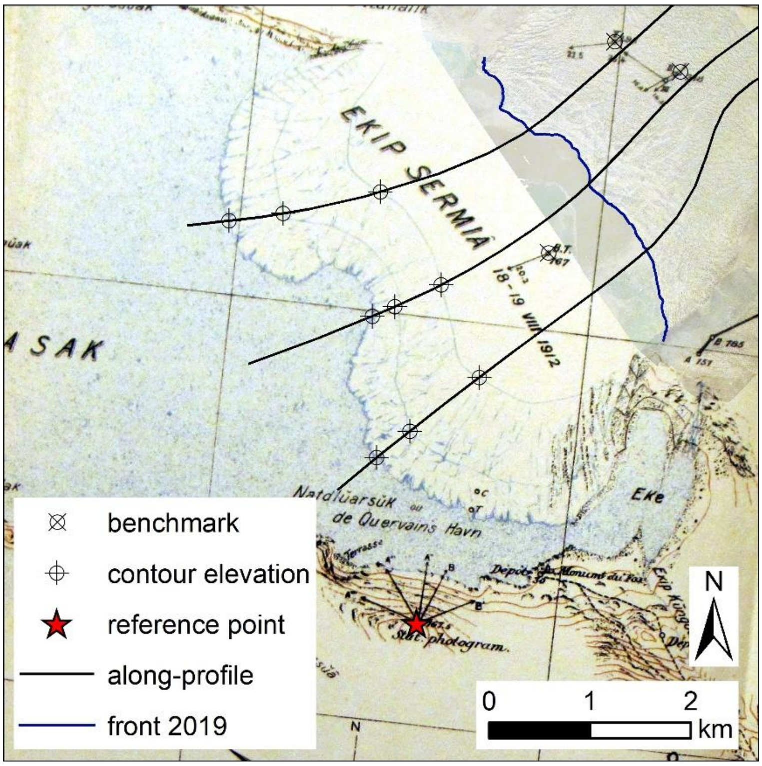

Figure 21: Retrieval of elevation information from historic maps, exemplarily illustrated with the map from 1912 by de Quervain & Mercanton (1925). The orthomosaic in the top-right corner corresponds to DR190820*.*

The existence of historic maps allows for the extraction of additional elevation information of the past. The maps of the Eqip Sermia terminus and front in 1912 (de Quervain & Mercanton 1925), 1948 (Holtzscherer & Bauer 1954) and in 1959 (Bauer 1968a) include a set of elevation contours on the glacier terminus. The map from 1912 additionally provides the elevation of three mapped benchmarks. Figure 21 demonstrates exemplarily, how the elevation information was extracted from the historic maps.

The intersection points of the along-profiles and the contours are used to identify the locations of the points with known elevation. The indicated elevations of mapped benchmarks are translated onto the adjacent along-profiles. As the contours in the maps mark the elevation above sea level, their values are adjusted by the difference to the height above the WGS84 ellipsoid (approximate site-specific sea level elevation: 26 metres above WGS84 ellipsoid). The elevation information extracted from the historic maps is included in the along-profile surface elevation figure (see chapter 5.3.2.1, figure 33).

4.8. Surface Elevation Change Analysis

For the purpose of surface elevation change analysis, 43 DEMs were co-registered. Out of this collection, 32 DEMs are considered in the analysis itself. 3 *AsterDEMs* are disregarded due to quality issues and high-quality DEMs with similar timestamps (table 4). Further, 8 drone DEMs are considered redundant, as from 2016-2019 multiple drone projects per field campaign were realised (table 5). A list of all DEMs co-registered for this study is given in chapter 5.2.2 (table 9). In addition, for the determination of the dynamic extent, two additional *upstream* DEMs were used (see chapter 4.8.7).

Several method for the quantification and analysis of the surface elevation change at Eqip Sermia are used. **DEM differencing** is used to detect spatial patterns of surface elevation change. Changes of the surface geometry of Eqip Sermia is investigated with **along- and across-profiles**. The along-profiles are also used for the investigation of length changes. Further, at the intersections of the profiles, a set of **analysis points** is created, to show the temporal evolution of the surface elevation in the form of point time series. Finally, the surface elevation change is also tracked **area-wide**, by assessing the surface elevation change averaged over the entire high-dynamic central part of Eqip Sermia except the margins.

Complementary to the investigations along the high-dynamic central ice stream, the low-dynamic **margin areas** of Eqip Sermia are further analysed. The spatial and temporal evolution of the surface elevation in these areas is mainly analysed with the help of analysis points placed in the areas and in adjacent locations. In addition, the right margin in sector 1 as well as the ice-saddle and ice-lake included in across-profiles.

4.8.1. DEM Differencing

In order to detect spatial patterns of surface elevation change, DEMs with different timestamps are subtracted from each other. According to the timespan between the timestamps of the chosen scenes, shorter- or longer-term spatial surface elevation change patterns can be detected. Depending on the scale of the target to be investigated, the quality of the differenced DEMs can be adjusted. Difference raster shows the change of the surface elevation per grid cell and are calculated as follows:

$$\Delta h = DEM_{new} - DEM_{old}$$

For this purpose, the aggregated 30m-resolution versions of the co-registered DEMs are used. As the resulting difference raster only covers the area where both input DEMs are overlapping, it is favourable to subtract DEMs with appropriate spatial extent from each other. In this study, except for the detection of the spatial patterns, this method is mostly used to get a first impression of the magnitude and extent of changes between two points in time.

The uncertainty of the difference raster resulting from DEM subtraction, according to Nuth & Kääb (2011), is equal to:

$$\sqrt{\sigma_1^2 + \sigma_2^2}$$

where, in this study, σ_n is the NMAD of a DEM. All plotted uncertainty ranges of DEM differencing values are calculated accordingly.

Further noteworthy is the fact that not the entire extent of Eqip Sermia is covered by DEMs used in this study. This does not allow for an assessment of the total mass or volume change of Eqip Sermia, as exhibited in other studies considering surface elevation change and mass balance on smaller glacial catchments (e.g. Mölg & Boch 2017; Huss et al. 2008).

4.8.2. Profile Analysis

Three along-profiles are roughly oriented along ice-flow lines and are manually defined by using flow directions from figure 7 (Jouvet et al. 2019) and optical information from a Sentinel-2 scene dated to 30th August 2019 (European Commission 2015). The centre (*C*) profile is accompanied by two lateral profiles, each located approximately 800 metres (at the ice-front) to the left (*L*) and right (*R*) of the centre profile, roughly dividing the glacier terminus in quarters. The along-profiles are named according to their relative orographic position (e.g. *P-L* for the along-profile to the left). Additionally, four across-profiles are defined. Their locations are chosen in respect of the sectors of Eqip Sermia, roughly cutting through their centre. The across-profiles are named according to the sector they are in (e.g. *P-S2* for the across-profile through sector 2) (figure 22).

Along all profiles, points with an interval distance of 30 metres were generated to extract elevation information for the analysis and visualisation. If multiple surface profiles of different years a plotted together, the long-term changes in the surface geometry along the profile can be assessed. The surface

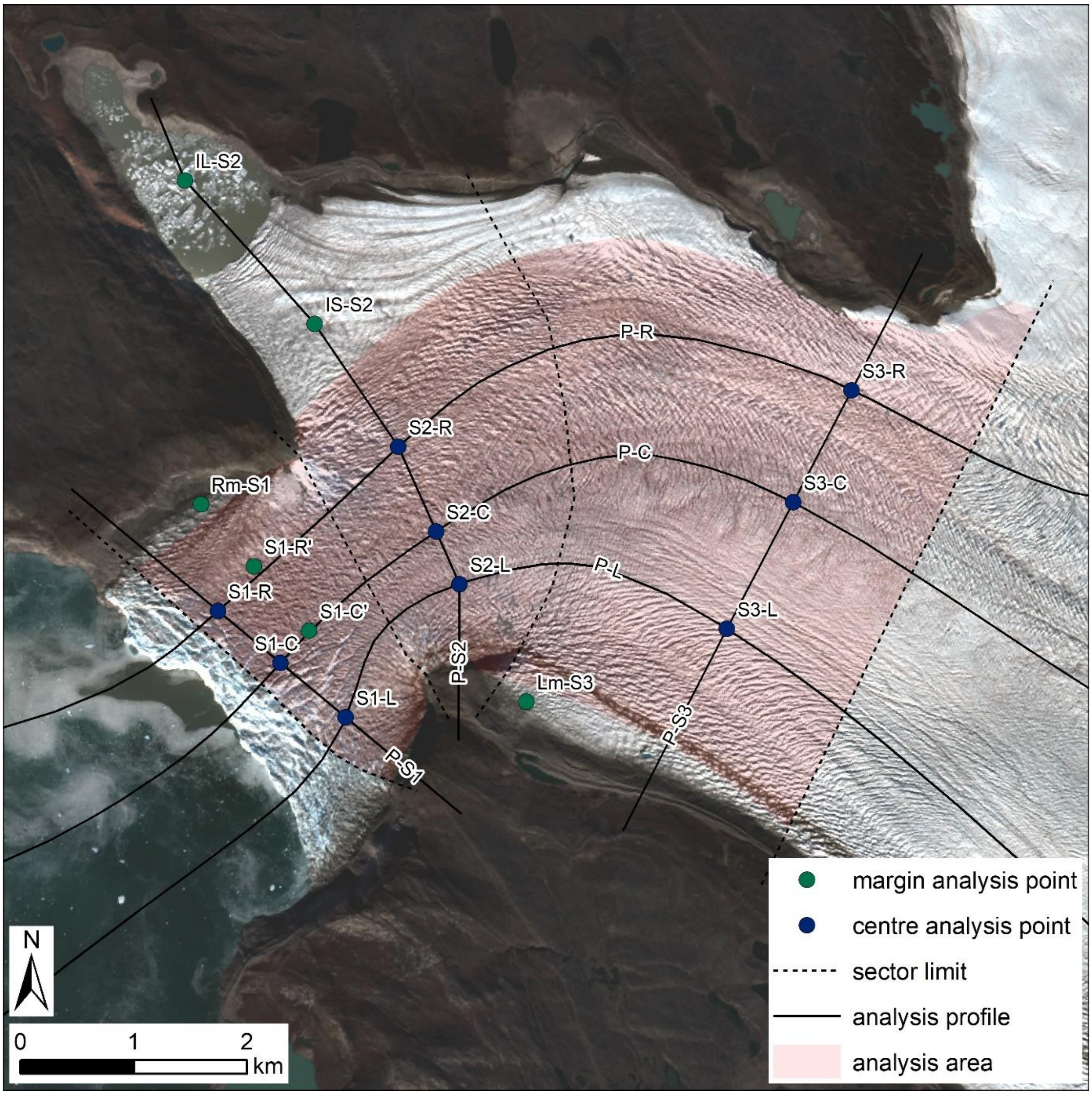

Figure 22: Analysis profiles, centre analysis points, margin analysis points and analysis area used for the investigation of surface elevation change and related parameters. The full versions of the abbreviated names in the figure are given in the text. Note that the points of sector 4 are not included, as they are located ca. 13.4 kilometres from the front. A full-scale overview map is attached in appendix IV. In addition, the sector margins are included. Background: Sentinel-2B, 30th August 2019, European Commission (2015).

profiles represent the elevation values of the 30m-resolution DEMs. The distance along the along-profiles is measured relative to the position of the front in 2019. The distances along the across-profiles is measured from left to right (south to north). The distances of the across-profiles (and the respective analysis points) to the front is measured along the central profile (*P-C*).

4.8.3. Point Analysis

In addition to the changes of the ice surface geometry, also surface elevation evolution in a single point location are of interest to get an impression of the temporal patterns of the changes. Analysis points for the extraction of values for the point time series are defined at the intersections of the along- and across-profiles. The analysis points are named according to their sector and relative orographic position (e.g. *S2-R* for the point at the intersection of the profiles *P-S2* and *P-R*).

Instead of geometrical changes of the ice surface, point time series allow for the detection of long-term temporal as well as seasonal patterns of surface elevation change, depending on the temporal resolution of the DEM collection available for the specific locations. Each elevation value is linked to a point in time (the timestamp of the corresponding DEM). Based on the timestamps, further investigations like a correlation analysis of e.g. surface elevation vs. glacier length are done. Because of the high sensitivity of this method to surface roughness, all point time series represent the values of the 5x5-focal-smoothed 30m-resolution DEMs. Hence, the elevation values of the data points represent the mean surface elevation of a squared area of 150x150 metres or 2.25 hectares respectively. The distances of the analysis points to the front is measured along the central profile (*P-C*).

4.8.4. Area-Wide Analysis

The area-wide surface elevation change analysis is limited to the high-dynamic centre of Eqip Sermia. It includes the sectors 1-3, which corresponds to the section between ca. 0.5 and 7.5 kilometres from the front of 2019. All marginal areas are excluded.

The area-wide surface elevation change series represents the area-wide mean elevation difference of the target DEM relative to reference DEM *AD170821*. All underlying subtractions use the DEMs of co-registration resolution as input data (SFM DEMs, drone DEMs & *ArcticDEMs*: 2m; *AeroDEM*: 25m; *AsterDEMs* & *GimpDEM*: 30m). The approach of considering averaged elevation differences relative to a single DEM is chosen because of the advantage, that the influence of limited coverage is smaller than for the comparison of the area-wide surface elevation. This statement is based on the assumption that the spatial variability of the surface elevation difference is smaller than that of the surface elevation itself. Considering the elevation difference therefore allows for a larger tolerance concerning the coverage percentage. However, for the analysis, only DEMs with a coverage of ≥70 percent are considered.

4.8.5. Low-Dynamic Margins

In addition to the high-dynamic central ice stream, the following areas are further looked at: (1) the low-dynamic right margin in sector 1 (map: *Rm-S1*), (2) the low dynamic left margin in sector 3 (*Lm-S3*) and (3) the low-dynamic saddle (*IS-S2*) separating the (4) marginal ice-lake (*IL-S2*) to the north of Eqip Sermia from the high-dynamic centre. The surface elevation evolution on the margins is studied for mainly two reasons: (1) to assess the changes on low-dynamic surfaces in contrast to the high-dynamic centre of Eqip Sermia and (2) to show the implications that can come with surface elevation changes at Eqip Sermia and other comparable sites.

The surface elevation change in *Rm-S1* is assessed in detail by three point time series; one representing the surface elevation change on the margin itself and two equivalent series from analysis points in the high-dynamic centre of sector 1 (*S1-R'* and *S1-C'*). Point time series are also generated for *Lm-S3*, *IS-S2* and *IL-S2*. Further, *Rm-S1* as well as *IS-S2* and *IL-S2* are traversed by *P-1S* and *P-S2*, respectively, which allows for an assessment of the surface geometry evolution.

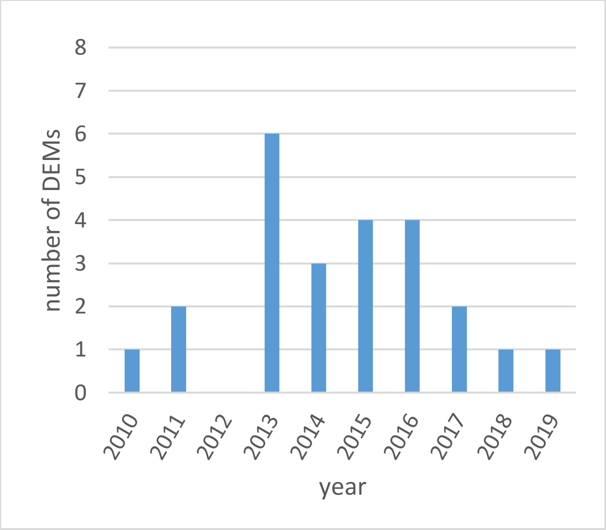

Figure 23: Number of DEMs per year from 2010 to 2019. Note that multiple drone DEMs of a single field campaign are counted as 1. The AsterDEMs *of the years 2014 and 2016 are excluded.*

4.8.6. Seasonality Analysis

Generally, the identification of the seasonal surface elevation changes requires a high temporal resolution of elevation data. Therefore, only sequences of the dataset with multiple DEMs per year with timestamps at least several weeks apart are useful to test the hypothesis of surface rise in winter and lowering in summer (figure 23). Thus, the seasonality analysis only focuses on the last decades, with sparse but most promising temporal resolution between 2013-2016.

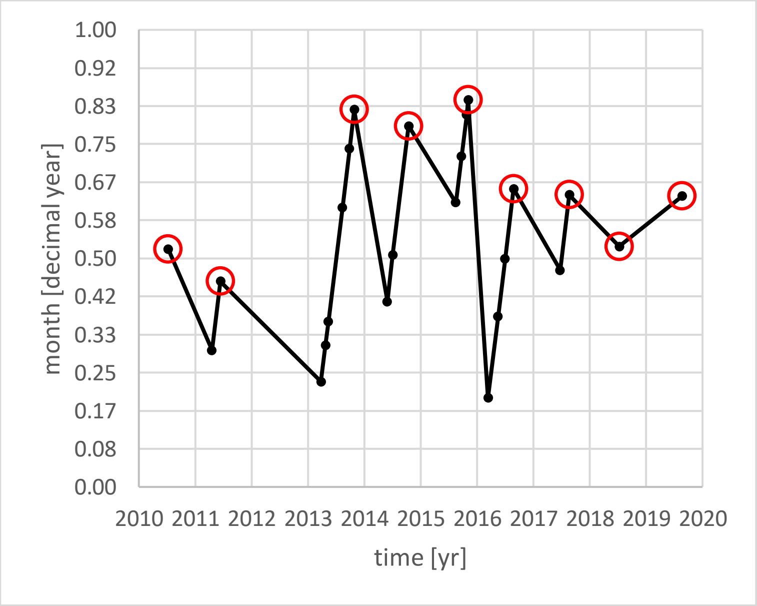

Figure 24: Visual representation of the end-of-season *(EoS) DEMs. The black line and dots mark the timeline of all available DEMs from 2010 to 2019. The red circles indicate the DEMs considered EoS. Note that the seasonal timing of the EoS DEMs is not always identical.*

To crystallise the seasonality pattern, time series of DEMs (where available) representing the end-of-season (EoS) state are produced (figure 24). A list of the selected EoS DEMs is given in table 8. Eventually, a linear interpolation of the elevation for the timestamps of the DEMs in between is made to reproduce a time series representing a *background* surface elevation change. After the subtraction of the linearly interpolated background elevations from the elevations extracted from DEMs in between, the remaining surface elevation deviations are interpreted as seasonal variations. The assessment of the seasonality pattern is based on values averaged among the three analysis points per sector (i.e. *S1-L*, *S1-C* and *S1-R* for sector 1). Thus, the 5x5-focal-smoothed 30m-resolution DEMs are considered.

Table 8: DEMs, which are considered EoS used for the calculation of the background *surface elevation change. The decimal year and decimal month values are corresponding to the x- and y-axis values in figure 24, respectively.*

DEM name	decimal year	decimal month
AS100709	2010.52	0.52
AD110613	2011.45	0.45
AD131028	2013.83	0.83
AD141015	2014.79	0.79
AD151105	2015.85	0.85
DR160825	2016.65	0.65
AD170821	2017.64	0.64
DR180711	2018.53	0.53
DR190820	2019.64	0.64

4.8.7. Dynamic Extent

A (*upstream*) difference raster of the two scenes *AD130528* and *AD150710* (no stable terrain, no-co-registration) is compared to a (*downstream*) difference raster of *AD130811* and *AD150921* (co-registered DEMs). This comparison is chosen because of the spatial overlapping and the relatively small difference of the acquisition dates of the *upstream* and *downstream* DEMs. The underlying assumption is that the surface elevation change in the low-dynamic areas to the lateral margins of Eqip Sermia in the meantime is negligible. The mean difference in those lateral (low-dynamic) areas of the overlapping zone of the two difference rasters is eventually used to determine an additional z-correction vector for the non-co-registered upstream DEMs. After that, the *downstream* difference raster and the (now x-y-z-corrected) *upstream* difference raster are mosaicked. The calculated contours of the mosaic represent the magnitude of and spatial extent of the surface elevation changes during the period from summer 2013 to summer 2015.

As the definition of the dynamic extent is based on the DEM difference contours, the above described methodology is executed using 5x5-focal-smoothed 30m-resolution versions of all involved DEMs to obtain relatively smooth contours. The definition of the margin of the dynamic extent representing the -3m contour is arbitrary. Although, this contour is the 'highest' integer contour that delineates an area closed to the north, east and south around the terminus of Eqip Sermia, whereas the shape of the -2m contours seems rather random, among other reasons probably because of surface elevation lowering through surface melt in this order of magnitude.

4.9. Front Positions

4.9.1. Front Position Mapping

In addition to the collection of front positions provided by others (chapter 3.6), for the purpose of this study, 42 front positions, corresponding to the DEM datasets used in this study, are mapped. The front positions are mapped by free hand in *ArcMap*, if available according to orthomosaics (SFM DEMs, drone DEMs) or satellite imagery (*AsterDEMs*). For the *ArcticDEMs*, no orthomosaics are available. Therefore, these front positions are mapped based on hillshades provided alongside with the DEMs. The front of the *GimpDEM* composite was not mapped due to limited knowledge about the acquisition date. The estimated uncertainties are mostly dependent on the corresponding DEM quality. At a rough estimate, they are in the range of 10 metres for the drone DEMs and *ArcticDEMs* and 50 metres the *AsterDEMs* and SFM DEMs.

4.9.2. Front Position Measuring

The front positions changes are observed in a 2D plane at sea level. For the translation of the mapped front positions into numbers, the changes of the front positions are measured in metres of retreat and advance along the along-profiles. Positive values indicate a larger glacier extent and negative values represent front positions behind the reference position of 20th August 2019 (= 0m). Therefore, at first, two approaches are chosen to measure the distances along the profile lines: length change determination based on (1) intersection points of the front positions and the profile lines (Lüthi et al. 2016) and (2) 150m-width averaged position change (Moon & Joughin 2008).

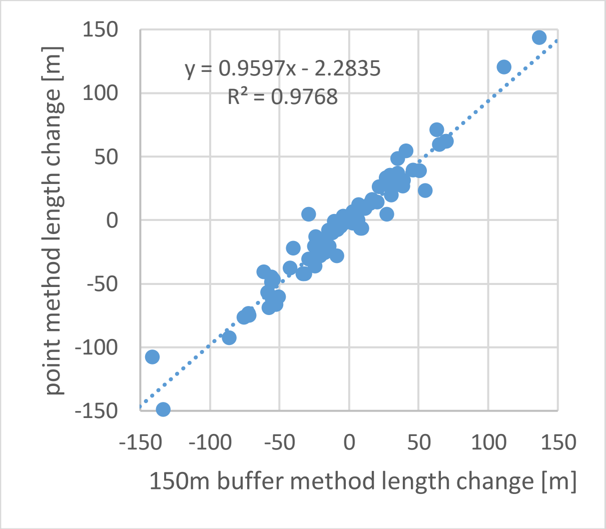

Figure 25: Comparison of intervals of front length change calculated with the point- and the buffer-method.

1. Point method: Calculation of intersection points of front positions and along-profiles Ą measuring distance between intersection points Ą cumulative length change
2. Buffer method: Calculation of buffer areas with a width of 150 metres around all along-profiles Ą cutting of buffers with front positions Ą calculation of buffer areas and division by buffer width Ą length relative to 20th August 2019 Ą cumulative length change

A comparison of the results for both methods, tested with all front positions corresponding to the DEMs, shows that the interval length change obtained from the two methods strongly correlate (figure 25). Therefore, the length changes resulting from the remaining front positions are calculated with the less time consuming point method.

4.9.3. Front Position Seasonality

The front position changes are further analysed in the same way as for the surface elevation, aiming for the crystallisation of the seasonal length oscillation resulting from retreat during the summer and advance during winter.

For most years, starting in 2000, at least one front position in June is available (figure 26). Thus, these front positions are defined to be the annual reference. All lengths for the timestamps in between are interpolated linearly and the resulting *background* length change is eventually subtracted from the original length values.

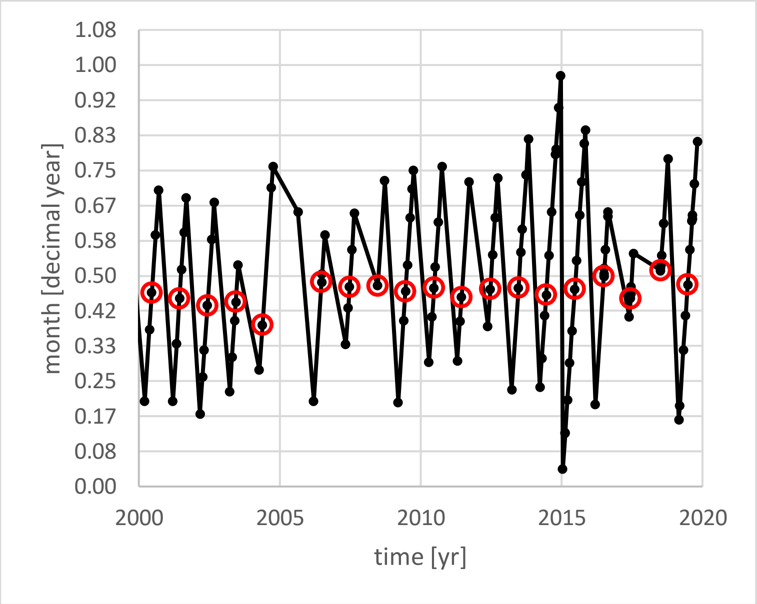

Figure 26: Visual representation of the reference *fronts for the determination of the front position seasonality. The black line and dots mark the timeline of all available front positions from 2000 to 2019. The red circles indicate the reference fronts.*

4.10. Slope, Ice Thickness and Surface Flow Velocity

The surface flow velocity u_s is the sum of basal sliding speed u_b and the contribution from ice deformation u_d, which in turn depend on the downglacier surface slope α as well as the ice thickness H. Thus, the surface flow velocity is determined by both the gravitational driving stress and the basal sheer stress. The surface flow velocity u_s in first approximation is given by the following equation (Cuffey & Paterson 2010):

$$u_s = u_b + u_d$$

where

$$u_b = \frac{(\rho g H \cdot \sin\alpha)^m}{\varphi}$$

and

$$u_d = \frac{2A}{n+1}(\rho g H \cdot \sin\alpha)^n$$

And ρ is the density of ice and g is the gravitational acceleration. For basal sliding, φ is a factor for taking into account basal lubrication, which is influenced by the bed material and the effective pressure at the bed (ice overburden minus water pressure), and the exponent is usually $m = 2 - 3$. For ice deformation, the rate factor A (depending on the ice temperature) and n are material constants, where usually $n = 3$. It follows for the basal siding contribution:

$$u_s \sim u_b \sim \alpha^{2-3}$$

$$u_s \sim u_b \sim H^{2-3}$$

and for the ice deformation contribution:

$$u_s \sim u_d \sim \alpha^3$$

$$u_s \sim u_d \sim H^4$$

Thus, the surface flow velocity u_s is strongly controlled by both the surface slope α and ice thickness H. Note that, for basal sliding, the velocity dependence has the same exponent for the slope and the thickness, whereas for the ice deformation the exponent for the thickness is slightly higher (4 vs. 3). The temporal evolution of α is dependent on the difference of surface elevation change along the ice-flow line. To investigate the change of the surface slope α, the average slope gradient on the lowest 5 kilometres of Eqip Sermia (between *S1-C* and *S3-C*) is calculated according to:

$$\alpha = \frac{h_{5km} - h_0}{\Delta L}$$

ΔL is ca. 5 kilometres, while h_0 is the surface elevation at the location of centre analysis point in sector 1 *S1-C* and h_{5km} is the surface elevation 5 kilometres upstream along the central flow line at *S3-C*. H is calculated as the average ice thickness along the central flow line in the respective section, based on the bedrock elevation from the *BedMachine v3* (Morlighem et al. 2017). A vertical correction of 36 metres has been applied to the underlying *BedMachine v3* raster dataset, which is equal to the approximate mean difference to the *master DEM* over stable terrain.

4.11. Melt Rates and Climate Change

4.11.1. Reconstruction of Temperature Series

The temporal coverage of the temperature data series from *AWS-ICE* (July 2016 to July 2019) and the *Swiss Camp* (2009-2016) is too short for a detailed long-term assessment of the surface melt during the period of surface elevation analysis in this study. Therefore, a relatively simple method is applied with the aim to reconstruct temperature data series for the respective location of the mentioned monitoring stations. The method is presented with the example of *AWS-ICE*.

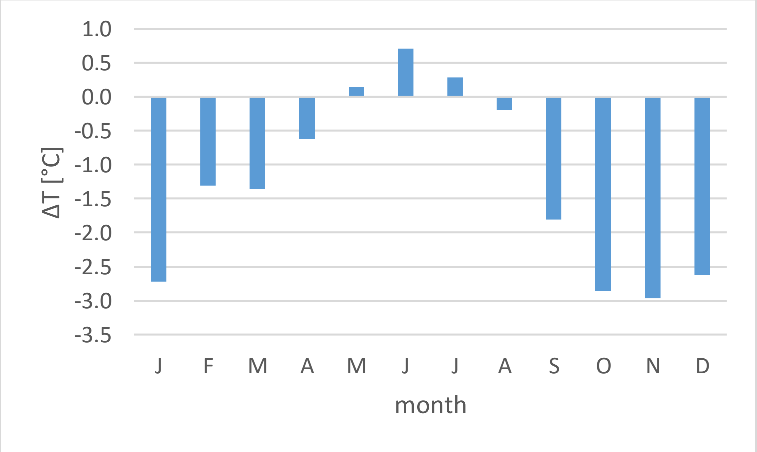

Figure 27: Monthly difference of the sir temperatures at AWS-ICE *and in Ilulissat. These differences are used to reconstruct a long-term temperature series for* AWS-ICE *from 1912-2019.*

The reconstruction of long-term temperature series is based on the comparison of the monthly mean temperatures measured at *AWS-ICE* and in Ilulissat, which results in a mean monthly temperature difference, as listed in figure 27. The seasonal temperature oscillation appears to show a slightly different timing with a delay of the temperatures at Ilulissat, what results in the minimum- and maximum-offsets in June and November. A correction of the temperature series from Ilulissat by the mean monthly deviations results in a *reconstructed* temperature series for *AWS-ICE* covering the entire study timespan of the study from 1912-2019 (figure 28). The same method is applied for the reconstruction of the long-term *Swiss Camp* temperature series. The standard deviation of the summer month (months with expected positive means) differences between the original and reconstructed temperature series is 0.71°C for *AWS-ICE* (months MJJAS) and 0.49°C for the *Swiss Camp* (months JJA) during the respective periods of overlapping data. Due to the limited data availablity, no independent validation of the temperature series is done.

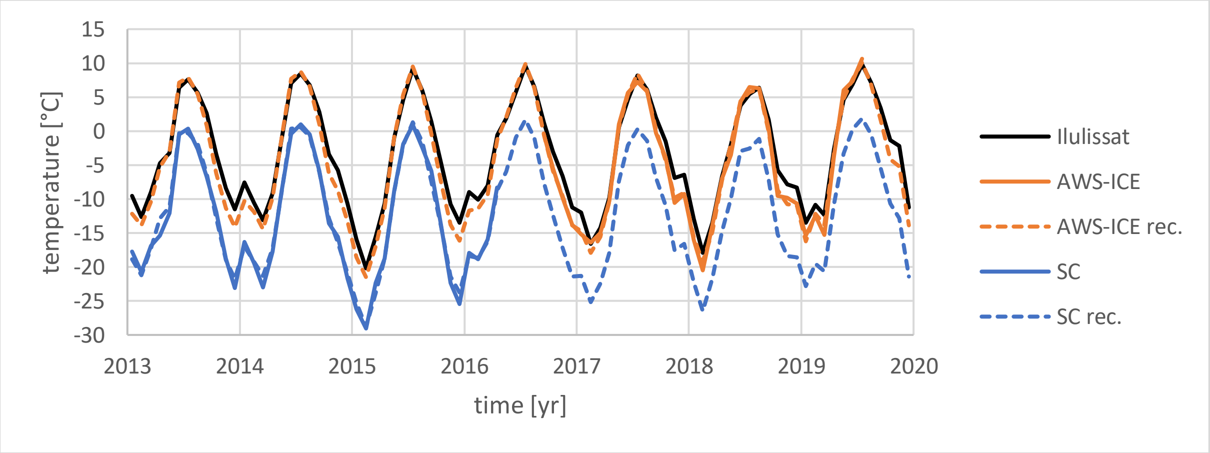

Figure 28: Comparison of reference temperature series (Ilulissat) and the original and reconstructed (rec.) temperature series for the monitoring stations AWS-ICE *and* Swiss Camp *(SC) during the period 2013-2019.*

4.11.2. Melt Rate and Surface Mass Balance Calculation

In a study by Walter (2016), data from the meteorological station *AWS-ICE* as well as ablation stakes installed on the adjacent ice margin (equivalent to *Rm-S3*) are used to determine a site-specific surface melt rate of 0.342mm/h/°C. The inclusion of temperature data from the *Swiss Camp* monitoring station and temperature data from other monitoring stations further resulted in a temperature lapse rate of -0.0072°C/m, determined to be typical for the area. (Walter 2016) The threshold air temperature for surface melt is set to 0°C. Based on these values and the reconstructed *AWS-ICE* temperature series, a model is developed to calculate the elevation dependent annual mean melt rate for the period 1912-2019. The underlying assumptions of the model are:

- Long-term temperature changes behave identical in Ilulissat and *AWS-ICE*
- Microclimate effects are negligible (consistent temperature lapse rate)
- Ice surface conditions are continuous (e.g. albedo, …)

The direct convolution from melt rates to surface elevation change is further based on the assumptions that accumulation (snowfall) and dynamic ice recharge is negligible. The model is eventually used to investigate the surface elevation changes on low-dynamic margins of Eqip Sermia, where the temporal patterns are different from those in the fast flowing centre.

4.11.3. Identification of Long-Term Trend and Recent Deviation

In an approach utilised by Schudel (2019), the surface melt and eventually the surface elevation change was modelled based on the assumption that during a period of stable glacier surface elevation, the surface melt rate and the rate of surface rise (through accumulation and ice-recharge) are in equilibrium. This approach further enables the calculation of the recharge rate itself and backward-modelling of the surface elevation. Schudel (2019)

In this study, a similar approach is chosen to assess the conditions at higher elevations and further away from the terminus, where the flow dynamics and thus the dynamic surface elevation changes are much smaller. The annually cumulated positive degrees (PD) at the *Swiss Camp* are calculated for the period of 1912-2019 based on (reconstructed) monthly mean temperatures. In doing so, the monthly means with T > 0°C are multiplied by the number of days of the respective month. Eventually, the annual sum of these values is calculated, yielding in the annual PD.

According to a period of stable surface elevation determined by Schudel (2019) on the adjacent land-terminating low-dynamic ice margin (1912-2003), the long-term PD trend is equal to the slope gradient of the trendline of the cumulative PD during the stable period. Accordingly, the deviation of the annual PD from the long-term PD trend at the *Swiss Camp* are calculated and summed up cumulatively, to calculate the magnitude of the recent warming relative to the long-term trend. This approach helps to interpret the role of climate change as a possible trigger for the dynamic changes further downstream at Eqip Sermia. Further, in lower elevations, the deviation of recent melt rates from the long-term mean is used to determine to what extent the surface elevation change at Eqip Sermia is controlled by surface melt and dynamic mass loss respectively.

5. Results

5.1. Co-Registration

The co-registration of all DEMs used in this study results in minimised vertical and horizontal biases relative to the *master DEM* (*AD150921*). The vertical shifts applied to the 2m-resolution *ArcticDEMs* and drone DEMs range from -6.1 to 3.7 metres and the horizontal corrections are between -7.7 and 2.3 metres. The corrections applied to the *AeroDEM* are in the same range, while the corrections for the *ASTER DEMs* and the SFM DEMs are much larger, with values up to +/- several dozens of metres. The fact that the shifts calculated for the SFM DEMs are this large, despite the fact that they were georeferenced to GCPs with 3D coordinates from the *ArcticDEM* hints at the relatively low quality of these products. A table with all translation vectors applied to the *slave DEMs* is provided in table 13 (appendix III).

5.2. Quality and Uncertainty of DEMs

The applied corrections as well as the resulting mean Δh and the respective standard deviations (STDVs) strongly depend on the type of dataset. As listed in table 9, after the co-registration, most elevation biases are smaller than 0.2 metres and the STDV of most of the *ArcticDEMs* (13 of 17) and all drone DEMs are no larger than 2 metres. The only *ArcticDEMs* with a STDV > 2m are from the years 2011-2014 and acquired in spring (April to mid-June). The STDVs of the *AeroDEM* and the *GimpDEM* are 6.5 and 8.1 metres and therefore slightly smaller than those of the *ASTER DEMs* (9.1 to 14.3 metres). The lowest quality based on the STDV measure are calculated for the SFM DEMs, with values ranging from 18.1 to 36.6 metres. Difference rasters calculated from the SFM DEMs and high-quality DEMs (figure 29) unveil sharp edges resulting in abrupt elevation changes of 10 metres and more as well as significant runaway effects towards the margins of all SFM DEMs, with least distinctive artefacts for *SFM530703*. *SFM590625* generally contains few artefacts too, but apparently suffers from an elevation dependent bias with an underestimation of surface elevation in high-elevated areas.

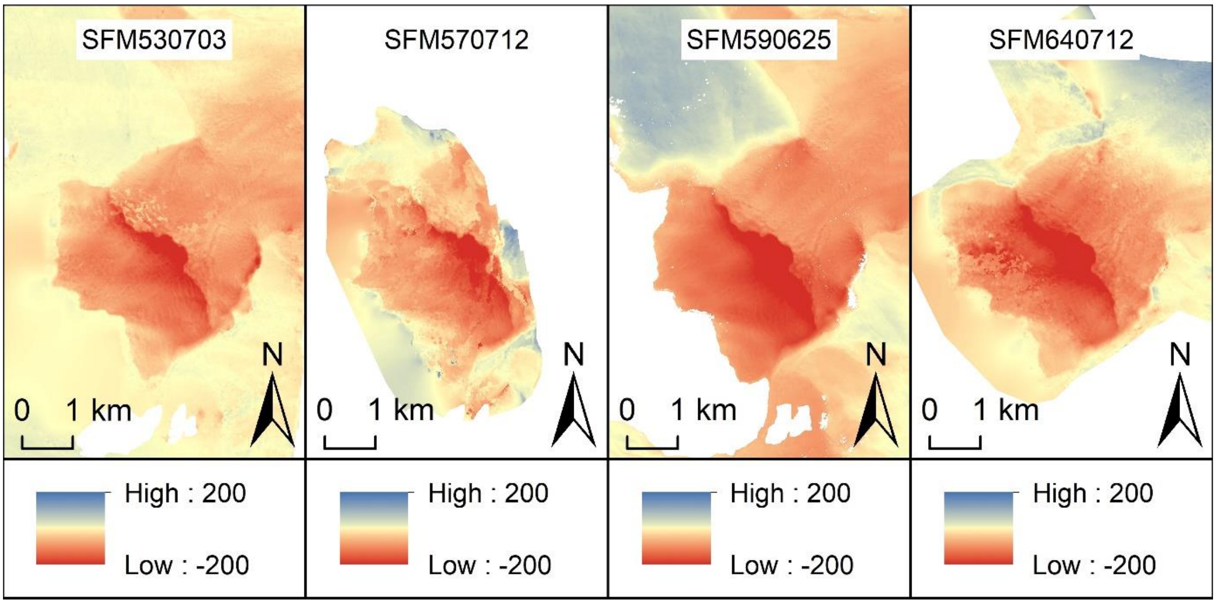

Figure 29: Elevation differences in metres of the SFM DEMs and high-quality reference DEM AD151024 *in the terminus area of Eqip Sermia. Note that in case of perfect quality, the difference in all areas except the outlet glacier would equal 0 metres (yellow). The differences of the reference DEM to* SFM590625 *and* SFM640712 *show signs of elevation dependent bias and tilt.*

5.2.1. Standard Deviation

Initially, the quality evaluation of the *slave DEMs* is centred on the standard deviations of the Δh-values above stable terrain relative to the *master DEM*. A visual check of the plots in figure 30 reveals, that the Δh-values are not normally distributed and most histograms reveal kurtosis. Accordingly, the normal STDV does not serve properly as a measure for the quality of the DEMs and thus, an alternate accuracy measure which is more robust to outliers is considered.

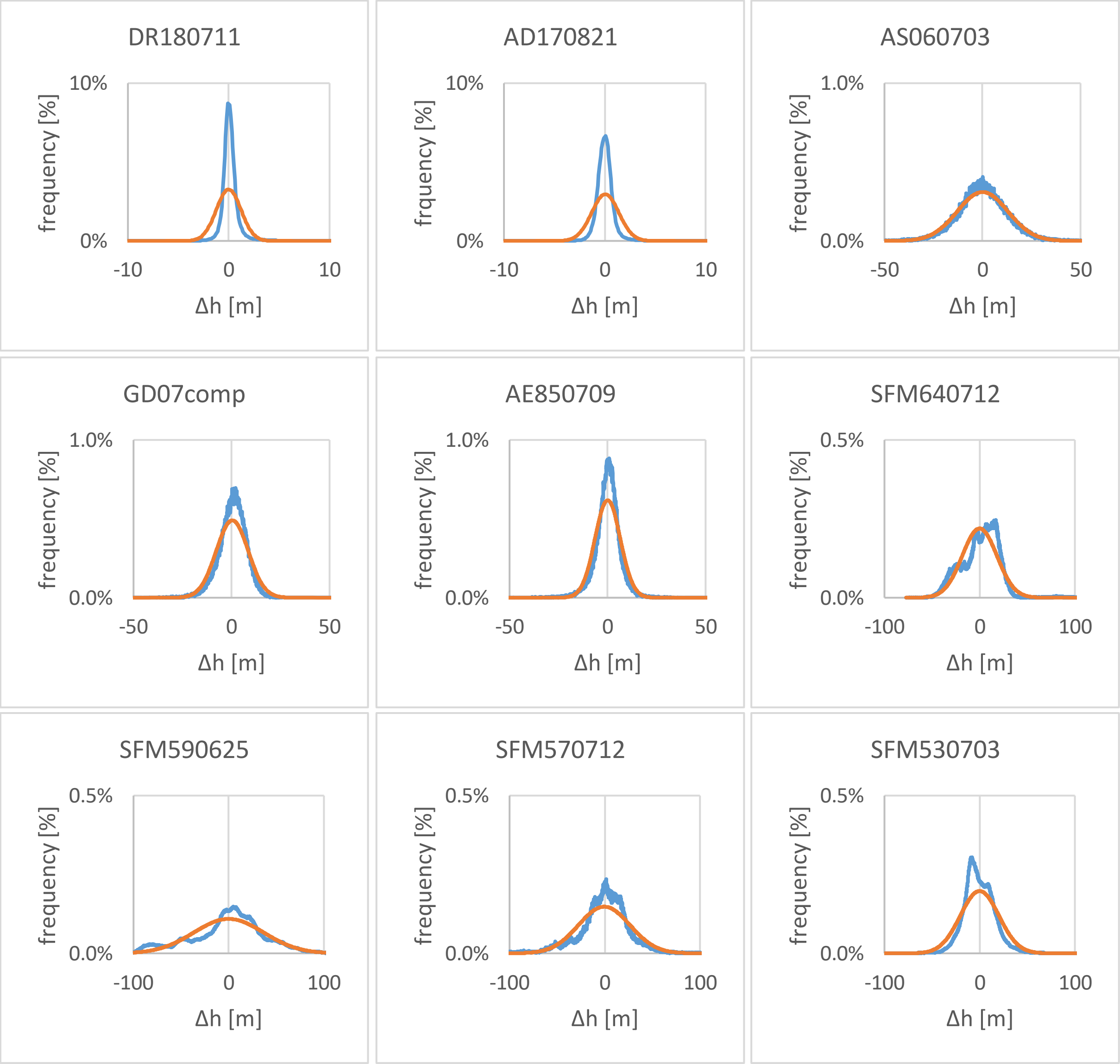

Figure 30: Error distribution histograms and respectively expected normal distribution histograms for different DEMs. The width of the classes for the histograms is 0.1 metre. Note that the x- and y-axes are varying, depending on the quality. The plotted distributions for the drone DEM, the ArcticDEM *and* AsterDEM *are representative for all other DEMs of the same group.*

5.2.2. Normalised Median Absolute Deviation

As suggested by Höhle & Höhle (2009), in case of a non-normal distribution in the form of kurtosis, the Normalised Median Absolute Deviation (NMAD) can serve as an alternate accuracy measure to estimate the scale of the Δh-distribution (see chapter 4.5). The resulting NMADs for all drone DEMs and *ArcticDEMs* except *AD110613* (1.17m) range from 0.37 to 0.82 metres. The *AeroDEM* (4.9m) and the *GimpDEM* (6.4m) have a smaller vertical uncertainty than the *AsterDEMs* (8.5-11.5m). Finally, the vertical errors of the SFM DEMs range from 15 to more than 30 metres. All vertical errors plotted in the following figures refer to the (propagated) NMAD. Further quality measures are given in table 14 (appendix V).

DEM name	**mean**	**STDV**	**NMAD**
SFM530703	0.04	20.21	15.33
SFM570712	-0.55	26.97	20.39
SFM590625	0.01	36.57	31.00
SFM640712	-0.06	18.19	18.45
AE850709	0.05	6.46	4.93
AS030609	0.12	14.32	10.91
AS060703	0.06	12.88	11.47
GD07comp	0.37	8.13	6.39
AS100709	0.61	9.15	9.17
AD110419	-0.06	2.47	0.82
AD110613	0.01	5.03	1.17
AD130325	-0.02	1.21	0.64
AD130423	0.00	0.70	0.37
AD130512	0.11	2.90	0.78
AD130811	-0.04	1.14	0.61
AD130927	-0.03	1.43	0.78
AD131028	0.02	1.62	0.40
AD140528	-0.02	2.78	0.76
AD140704	-0.01	0.88	0.50
AS140826	-0.35	9.27	8.90
AD141015	-0.01	1.00	0.56
AD150815	0.02	0.79	0.47
*AD150921**	0	0	0
AD151024	-0.02	0.89	0.50
AD151105	-0.01	0.85	0.54
AD160311	-0.03	1.10	0.63
AD160515	-0.02	1.23	0.68
DR160630	-0.01	1.54	0.41
DR160702	-0.05	1.51	0.42
AS160707	0.16	9.73	9.18
AS160723	0.10	9.66	8.48
DR160821	0.00	1.46	0.44
DR160823	0.00	0.93	0.41
DR160825	0.01	1.54	0.43
DR170616	0.02	1.59	0.54
DR170620	0.02	2.00	0.53
DR170622	-0.04	1.58	0.47
AD170821	0.05	1.35	0.69
DR180706	0.00	1.38	0.50
DR180708	-0.03	1.22	0.45
DR180711	-0.01	1.22	0.48
DR190818	0.00	1.48	0.47
DR190820	0.02	1.58	0.51

Table 9: DEMs and quality measures after the co-registration. The DEM marked with (*) was the master DEM for the co-registration process. The grey entries mark the DEMs, which are not considered for the analysis due to quality issues or redundancy.

5.3. Surface Elevation Change

5.3.1. Spatial Patterns of Surface Elevation Change

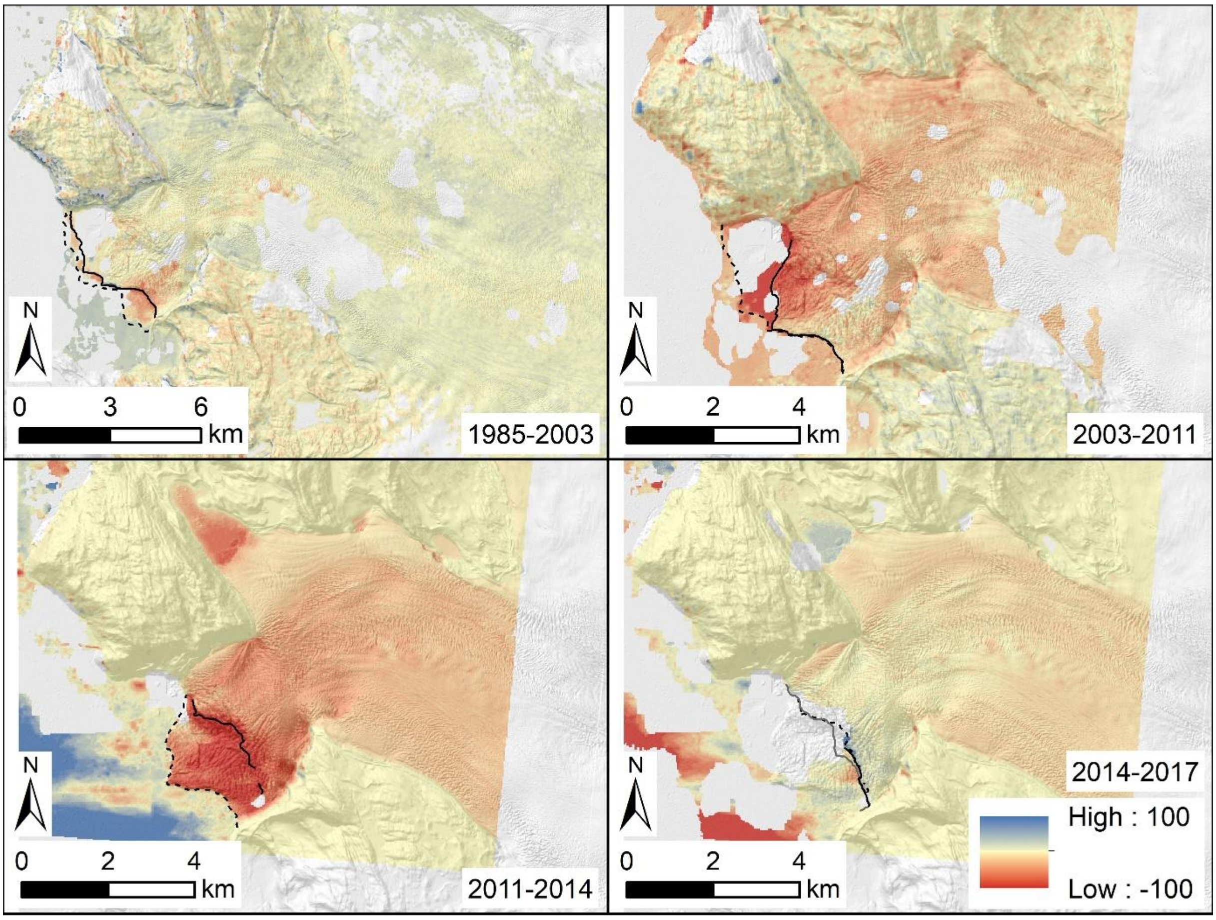

Figure 31: Surface elevation change in metres during different periods in the past decades. The years are represented by the following DEMs: AE850709, AS030609, AD110613, *and* AD141015 *and* AD170821*. The dashed black lines mark the glacier front position at the start of the period and the solid black lines at the end, respectively. Due to limited coverage of the respective DEM, the DEM front in 2017 is complemented by the front from 21st July 2017 (grey). The background hillshade is from the* ArcticDEM *composite.*

The results from DEM differencing reveal interesting spatial patterns. From 1985 to 2003, the observed surface elevation changes are very small and except for the lowering close to the left front, where also the retreat was the largest, no clearly identifiable changes occurred (figure 31). Eventually, in the period from 2003 to 2011, a distinct surface lowering is observable with the largest changes occurring centre-right close to the front. Again, this correlates spatially with the largest frontal retreat. During the said period, the front to the left remained in the exact same position. Accordingly, the surface elevation change in the left part of sector 1 is small. However, a few hundred metres upstream of left front, the surface elevation change is slightly negative.

Eventually, between 2011 and 2014, the situation is very different. The spike of the front formerly protruding far out into the fjord as well as a large area of the centre and left front disintegrated and the front retreated strongly. The entire terminus area of Eqip Sermia experienced surface lowering, with highest rates right very closely behind the new front. The area-wide lowering during the respective 3 years is roughly equal to the lowering during the former 8 years from 2003-2011. Also, the ice-lake has drained in the mean-time.

The 3 years of large changes were followed by 3 years with a completely different pattern (2014-2017). Now, the surface elevation in the areas close to the front (formerly most affected by surface elevation change) seems to have stabilised. The area of little to no distinct surface elevation change does not only include the largest parts of sector 1 but, especially in the centre of Eqip Sermia, expands several kilometres upstream. Interestingly, further upstream, the thinning seems to persist, however, at a smaller rate than from 2011 to 2014.

Also, most clearly noticeable in the period of 2011-2014 but also from 2014-2017, the low-dynamic margins are characterised by a different behaviour in terms of surface elevation change. Unaffected by the large variations of the surface lowering rates in the high-dynamic centre of Eqip Sermia, the margins seem to lower at roughly constant rate throughout the entire 6 years.

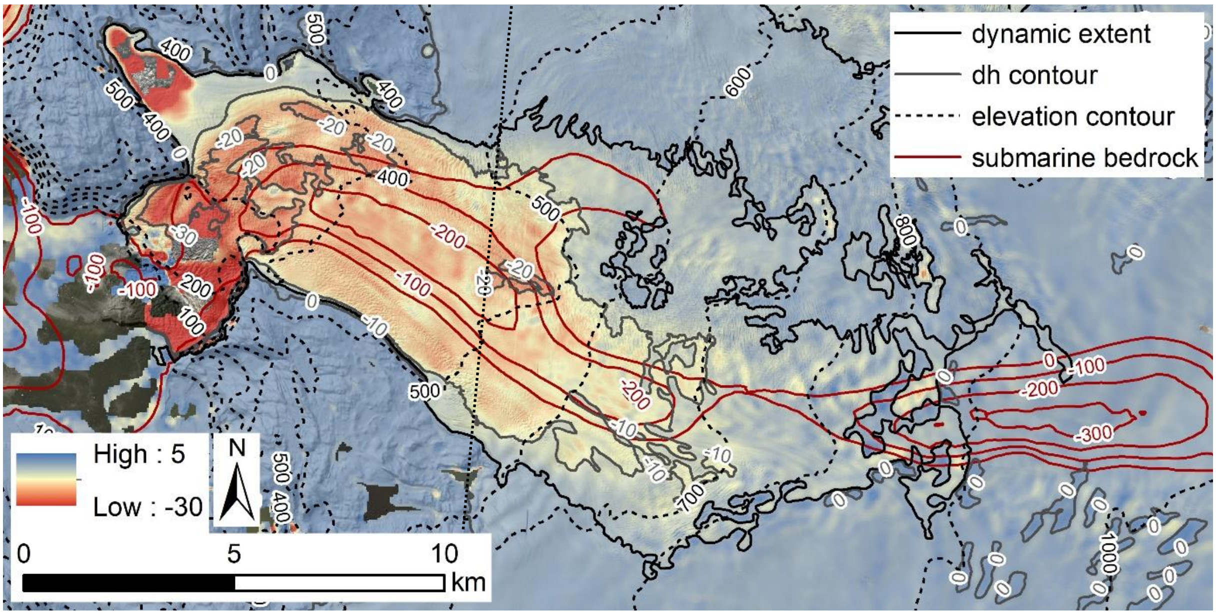

Figure 32: Upstream thinning of Eqip Sermia from 2013 to 2015. The underlying DEMs are AD130528 *and* AD150710*. The dynamic extent is equal to the -3m surface elevation change contour line, based on a differencing of the underlying DEMs. The dotted line marks the stitching line of the mosaicking of the underlying* downstream *(co-registered) and* upstream *difference rasters. The background hillshade is from the* ArcticDEM *composite.*

The dynamics of Eqip Sermia seem to largely affect the surface elevation change far upstream (figure 32). The area with a surface elevation lowering by three metres or more from May 2013 to July 2015 extends more than 20 kilometres upstream from the front, while the surface elevation change further upstream and in the adjacent glaciated areas to the north and south of the ice stream are smaller. As the ice approaches the terminus, the onset of the area with increased surface lowering is located at the end of a subglacial overdeepened trough.

5.3.2. Surface Geometry Change

5.3.2.1. Along-Profiles

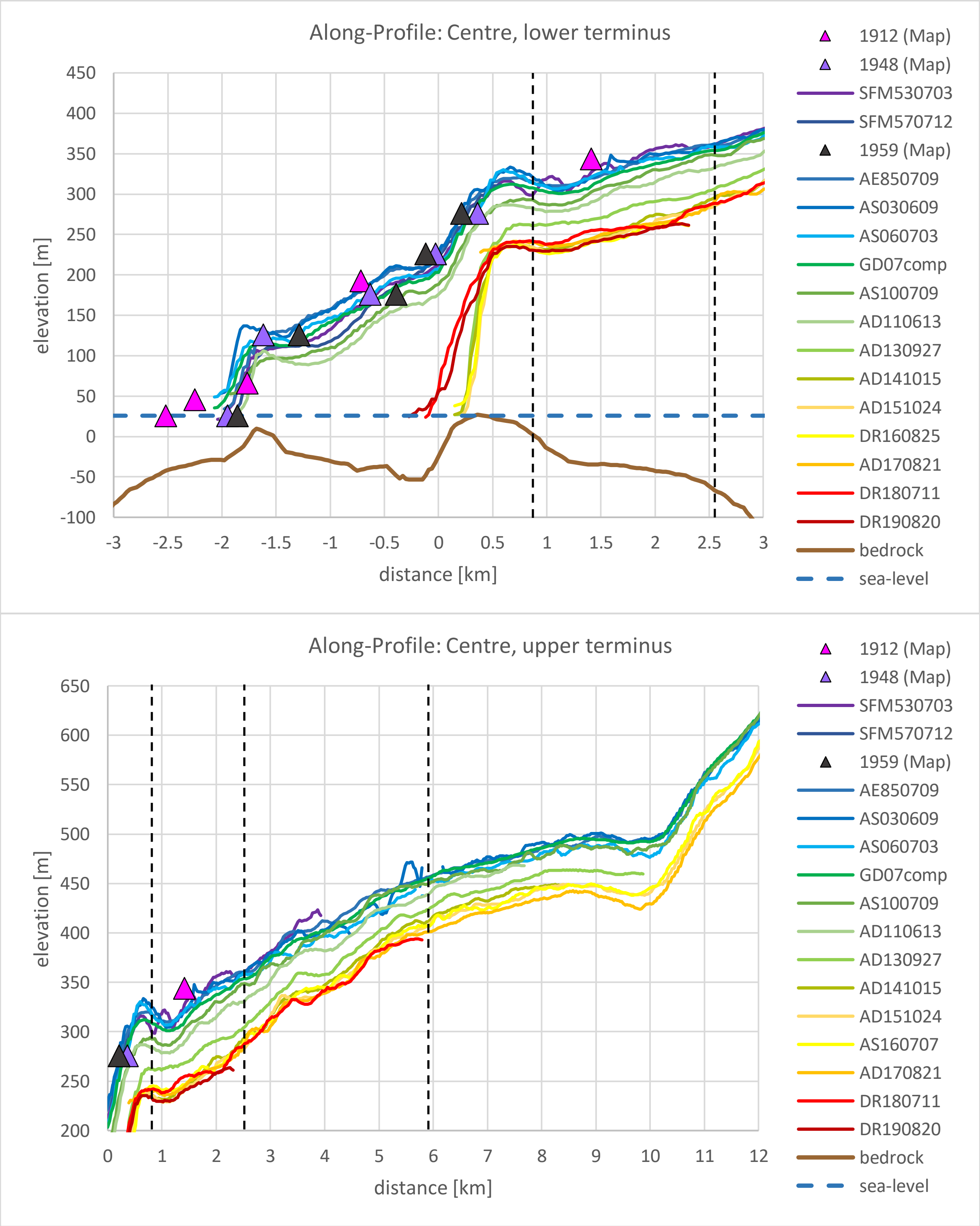

Figure 33: Surface geometry of the central along-profile; top: lower section (km -3 – 3) and bottom: upper terminus (km 0 – 12). Note that not all DEMs are represented. After 2010, (if available) one DEM per year is included. Further excluded due to quality issues are the profiles resulting from the SFM DEMs of 1959 and 1964. Triangles represent elevations of contours and benchmarks of historic maps. The distance reference (0 km) is the front of 20th August 2019. The bedrock elevation is extracted from the BedMachine v3 *by Morlighem et al. (2017). The vertical black dashed lines indicate the location, where the analysis points* S1-C, S2-C *and* S3-C *are located, respectively, where the across-profiles* P-S1, P-S2 *and* P-S3 *intersect.*

A collection of profiles along the central flow line reveals the characteristics of surface geometry changes of Eqip Sermia during the past century (figure 33). The shape of the terminus area is dominated by a *bump* located at km 0.5, present at all times with continuous elevation information after 1953. The bump is not represented in the data from the single benchmark and contour elevations from the historic maps, as they either not provide enough information in the respective area (1912) or do not cover the area at all (1948 & 1959). The surface profiles confirm that the geometry and extent of the terminus were largely unchanged from the 1950s until 2007. Eventually, the surface elevation along the central flow line started to decrease suddenly between 2007 and 2011. The thinning was largest in the section between the front position at the time and the current front, but also occurred in the area above the bump. Within short time, the entire relatively shallow frontal section degenerated completely and the front in the centre of Eqip Sermia rapidly retreated, only stopping a few hundred metres beyond the front position of August 2019. The retreat caused the front to rise from a height of ca. 100 to more than 200 metres above the waterline. From 2013 to 2014, the surface above the new calving front continued to lower by another 25 metres, whereas from late 2014 to August 2019, the surface elevation along the central flow showed no large changes. Concurrently, the front appears to have advanced slightly by 0.5 kilometres after 2016, while the steepness of the front is becoming slightly lower.

Worth mentioning is the bedrock geometry in the terminus area of Eqip Sermia. It shows two shallow zones along the central flow line; a submarine bump in a depth of less than 20 metres below sea level, just beneath the long-term steady front from 1948-2011, and another shallow zone where the fast central retreat stopped in 2013. At this location, temporarily, the calving front even uncovers bits of bedrock above the water line in recent years. Approximately 1 kilometre further inland of the contemporary front position, the bedrock is deepening again.

A look at the along-profile further upstream shows a similar timing of changes as the lower terminus of Eqip Sermia. The thinning preceding the state of 2011 seems to be larger from km 0 to km 3 than further upstream. The following dramatic thinning by ca. 15-25 metres within one year from autumn 2013 to autumn 2014 is traceable all the way up to km 10, where *AD130927* coverage ends. More moderate thinning persists until at least 2017 at higher elevations up to km 8 from the front. Additional along-profiles of the surface geometry and bedrock are included in figures 79 (left) and 80 (right) (appendix VI).

5.3.2.2. *Across-Profiles*

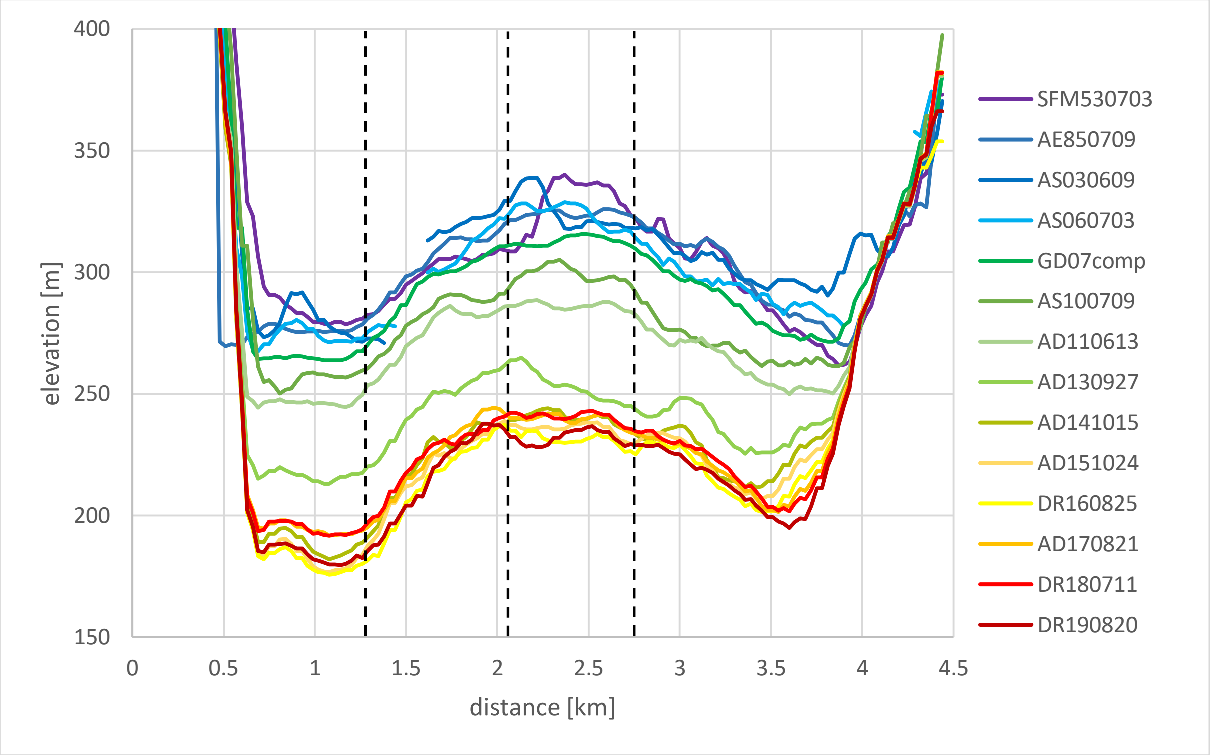

Figure 34: Across-profile through sector 1 (P-S1). Note that not all DEMs are represented. After 2010, (if available) one DEM per year is included. Further excluded due to quality issues are the profiles resulting from the SFM DEMs of 1957, 1959 and 1964. The distance is measured along the profile from orographic left to right (south to north). The vertical black dashed lines indicate the location, where the analysis points S1-L, S1-C *and* S1-R *are located, respectively, where the along-profiles* P-L, P-C *and* P-R *intersect.*

A look at the surface geometry in a cross-section though sector 1 reveals that, in this sector, the surface of Eqip Sermia is higher elevated in the centre than at the margins (figure 34). This pattern is roughly continuous through the entire timespan covered by the dataset. The depression to the left has lowered stepwise, with large surface elevation changes between 2011 and 2014, which is equal to the behaviour in the elevated central part. The right margin in sector 1 of Eqip Sermia seems to have experienced a more steady surface lowering (further comments: see chapter 5.3.6). The surface elevation in the centre of the cross-section was around 325 metres until 2007, and eventually rapidly sank by roughly 85 metres to 240 metres in 2014. Eventually, the surface elevation across the front remained more or less stable. From 2018 to 2019, a small but continuous lowering across the entire sector 1 is observed.

Further upstream, in the sector 2 of the terminus area of Eqip Sermia, an interesting surface geometry exists (figure 35). While the across-profile through sector 1 shows an elevated area in the centre of Eqip Sermia, here, the surface is lower in the centre and rises towards the margins. The temporal pattern is again identical with the one described for the profile across sector 1. The elevated section between km 2.5 and 4.5 is not only the right margin of the fast-flowing centre of Eqip Sermia, but also marks an ice-saddle, which separates the ice flow. The surface elevation to the right of the ice-saddle again decreases and ultimately leads into the ice-lake (km 5-6). The surface in the area of the ice-saddle has lowered at higher rates with a maximum from 2007-2014 closer to the main ice-flow of Eqip Sermia (ca. km 3), whereas the surface lowering further away from the main ice-flow occurred by mostly constant rates from 2007-2017 (ca. km 4). From 2017 to 2018, the surface geometry along the entire profile underwent no changes. The summit of the ice-saddle has been dislocated by ca. 800 metres to the right.

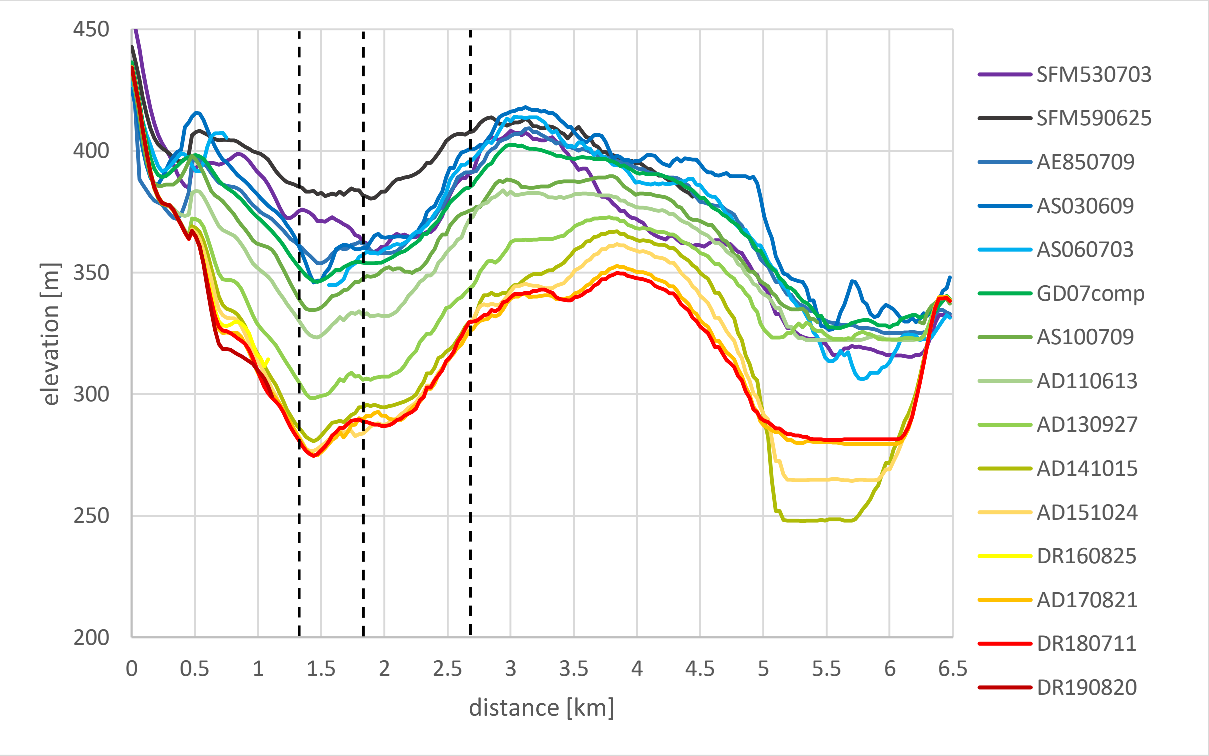

Figure 35: Across-profile through sector 2 (P-S2). Note that not all DEMs are represented. After 2010, (if available) one DEM per year is included. Further excluded due to quality issues are the profiles resulting from the SFM DEMs of 1957 and 1964. The distance is measured along the profile from orographic left to right (south to north). The vertical black dashed lines indicate the location, where the analysis points S2-L, S2-C *and* S2-R *are located, respectively, where the along-profiles* P-L, P-C *and* P-R *intersect.*

The ice-lake water level shows a more or less constant elevation of ca. 325 metres until 2013, to suddenly drop to 250 metres during a subglacial drainage event before October 2014. More recently, the water level increased again, reaching a water level of 280 metres in 2018. The across-profile through sector 3 (*P-S3*) is included in figure 81 (appendix VI).

5.3.3. Temporal Patterns and Magnitude of Surface Elevation Change

The tracing of surface elevation change in point locations allows for a more precise assessment of temporal patterns. In general, the following figures are including the elevation information of all available DEMs, except the *AsterDEMs* of 2014 and 2016 (due to quality issues) as well as redundant drone DEMs.

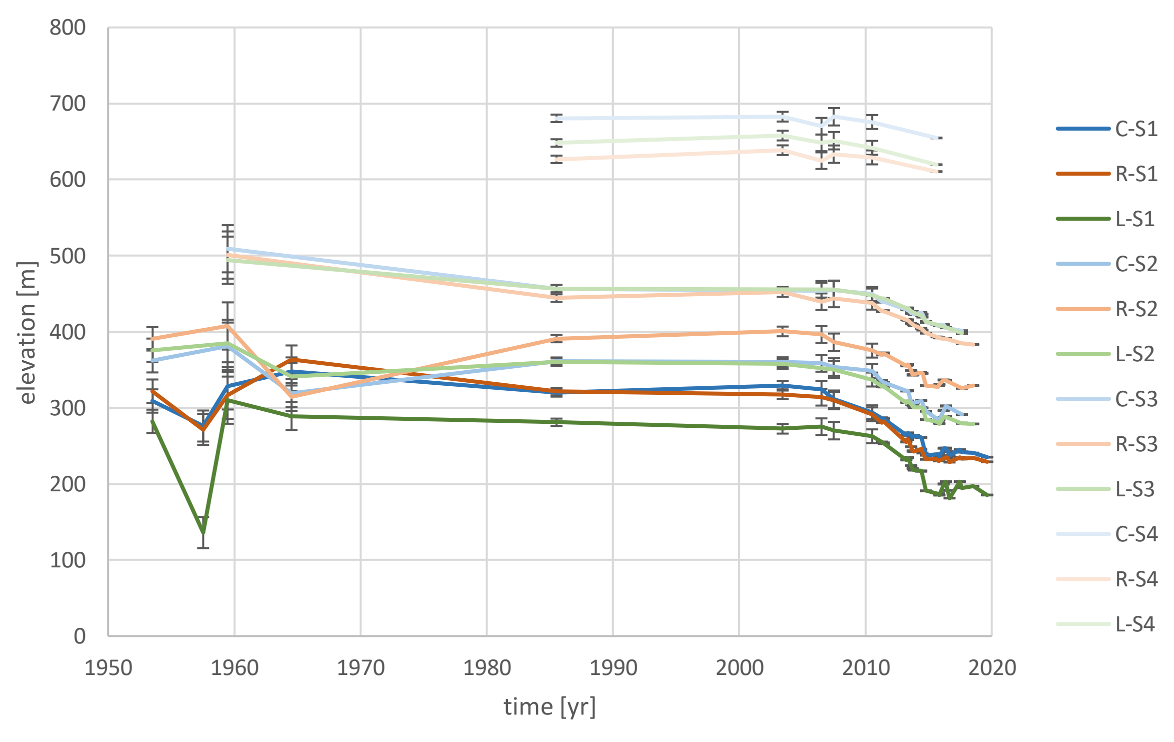

Figure 36: Point time series of the surface elevation of Eqip Sermia. Note that the uncertainties of the values from 1957, 1959 and 1964 are probably larger than the respective error bars indicate. Note that the points *represent average surface elevations of an area of 150x150 metres. The approximate distances of sectors to the front of 20th August 2019 are 0.75 km for S1, 2.5 km for S2, 6 km for S3 and 13 km for S4. The exact locations of the analysis points is included in figures 22 and 78.*

Figure 36 shows the temporal evolution of surface elevation at the locations of 12 analysis points located at the intersections of the along-profiles and the across-profiles. Note that the large fluctuations around 1953 to 1964 represent data from DEMs with relatively large uncertainties exceeding the visualised error bars. The point time series (PTS) show that the surface elevation remained largely unchanged in all sectors during the second half of the 20th century and until 2003. Eventually, a period of gradually increasing rates of surface lowering commenced, which lasted until the end of summer 2014. In the centre and to the right, the timing of the surface elevation changes is similar. Only the left part of sector 1 shows a slight delay.

Also, the timing of the onset of the surface lowering among the sectors is comparable in all sectors. Further, it can be observed that the magnitude of the surface elevation changes is highest in sector 1 and decreases further upstream. This observation is even more pronounced when all PTS are visualised averaged per sector and translated (vertically corrected) to an identical starting point of 0 metres in 1985 (figure 37). From 1985 to 2003, the surface elevation in sector 4 even experienced a slight increase, whereas ultimately after 2006/07 the surface pronouncedly lowered in all sectors. By the end of 2014, sector 4 has lowered by ca. 12, sector 3 by 45, sector 2 by 70 and sector 1 by 85 metres. The further evolution in the years 2015-2019 indicates a stabilisation of the surface elevation in sector 1

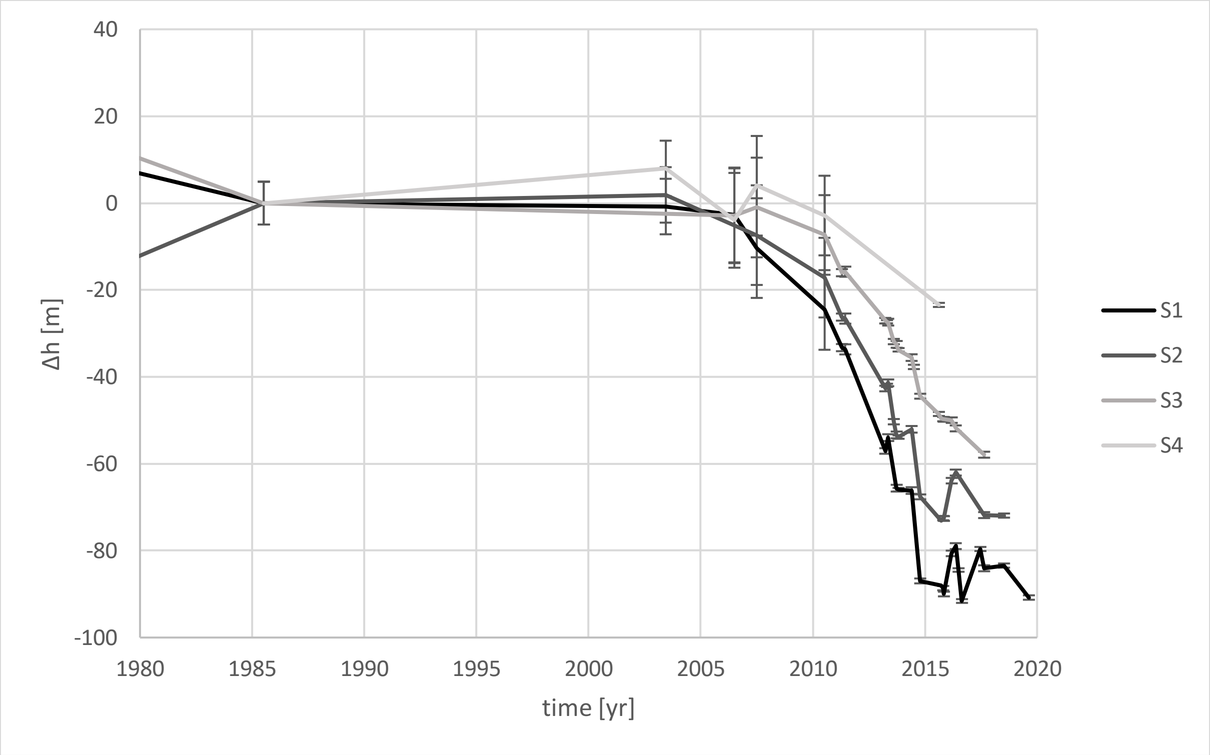

Figure 37: Surface elevation relative to AE850709. The values are averaged among the three analysis points per sector. The approximate distances of sectors to the front of 20th August 2019 are 0.75 km for S1, 2.5 km for S2, 6 km for S3 and 13 km for S4. The exact locations of the underlying analysis points is included in figures 22 and 78.

and 2, while lowering seems to be ongoing (though at lower change rates) in sector 3. The data availability at the analysis points in sector 4 is limited after 2015.

In sector 1 and sector 2, the shape of the PTS in the recent years indicates a seasonal pattern of surface elevation change which is most pronounced in the years after 2014 but is already recognisable in 2013. Before, 2013, low temporal resolution of the dataset makes the detection of a seasonal pattern impossible.

5.3.4. End-of-Season Surface Elevation Change and Seasonality

Figure 38 shows the seasonal deviations of the surface elevation from the *background* surface elevation trend averaged for the three analysis points in sector 1. As the EoS surface elevation is expected to mark the annual minimum surface elevation of Eqip Sermia, the *true* surface elevation change is found to be increasing (and decreasing) above (and below) it, showing a maximum offset in late spring/early summer.

A subtraction of the EoS from the *true* surface elevation reveals that seasonal surface elevation changes of up to 12 metres occur between the seasonal minimum and maximum in sector 1 (figure 38, bottom). In general, the maximum surface elevation is reached before the end of June. The negative value for 2011 marks the elevation of *AD110419*, which shows lower elevation values in sector 1 than *AD110613* (considered EoS DEM due to the lack of temporal resolution in this period). In 2018 and 2019, only DEMs from one single campaign each year are available, which does not allow for the detection of a seasonality pattern.

The pronounced peak in 2014 is synchronous with a generally large surface elevation lowering during that year. A look at the corresponding period in figure 38 (top) reveals that the surface elevation itself

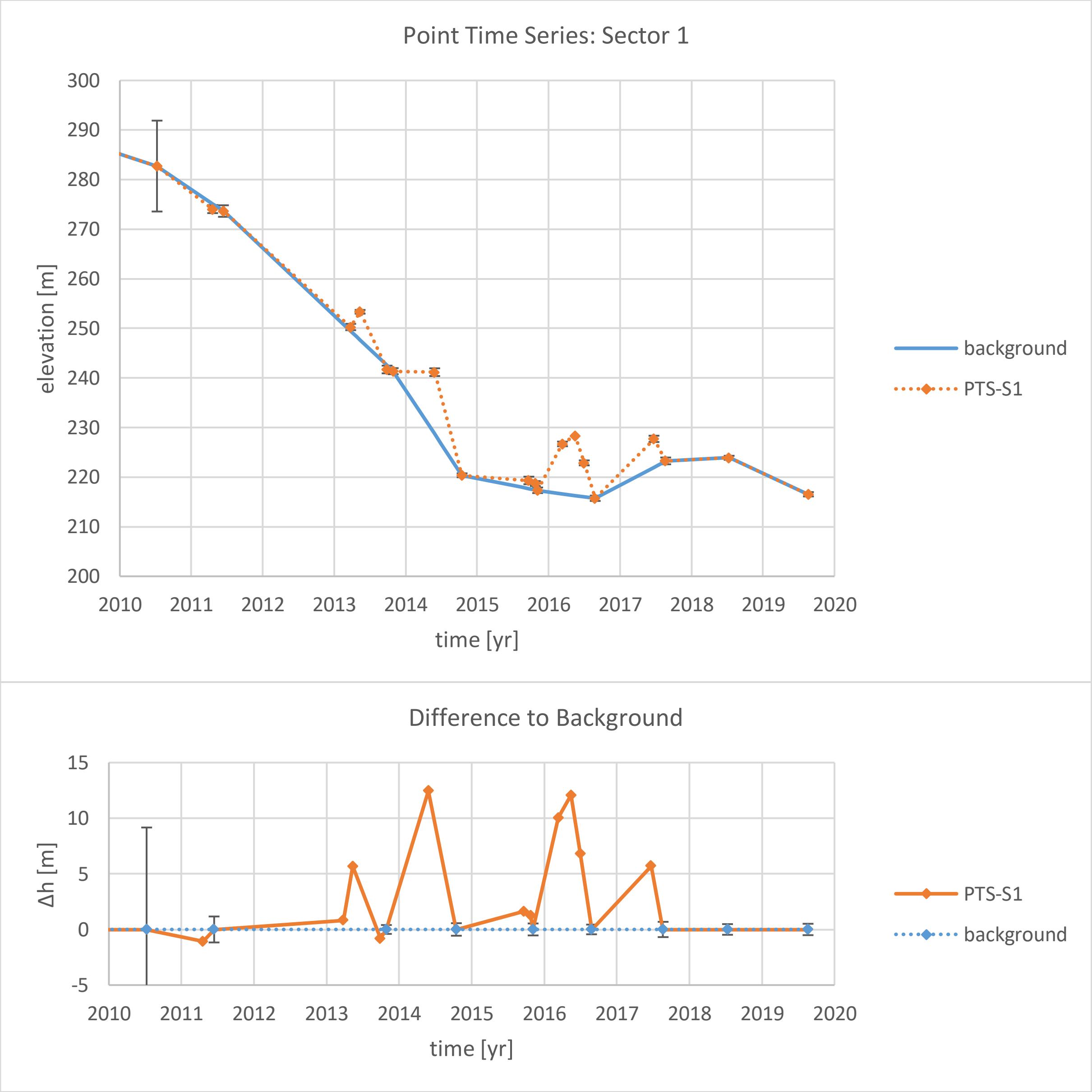

Figure 38: Background surface elevation change and seasonal pattern in sector 1. The values are averaged among the three analysis points in the sector. The reference DEMs for the background change determination are given in table 8. Note that the temporal coverage before 2013 and after 2017 is not high enough for the detection of a seasonal pattern.

did not change between autumn 2013 and July 2014 and the entire *seasonal peak* stems from the difference between the two EoS reference DEMs. In general, the magnitudes of the observed seasonal oscillations have to be interpreted accounting for the generally rather poor temporal resolution of the dataset (at least for seasonality assessment). A possible shift between the timing of the DEM acquisition and the seasonal maximum surface elevation affects the magnitude presented here. Thus, statements about inter-annual variabilities of the seasonal surface elevation change pattern and magnitude are not possible.

While the identified magnitude of the seasonality pattern in sector 2 are practically identical with that of sector 1, the seasonal surface elevation increase is limited to no more than 2-5 metres further upstream in sector 3. The respective figure 82 is included in appendix VII.

5.3.5. Area-Wide Surface Elevation Change and Seasonality

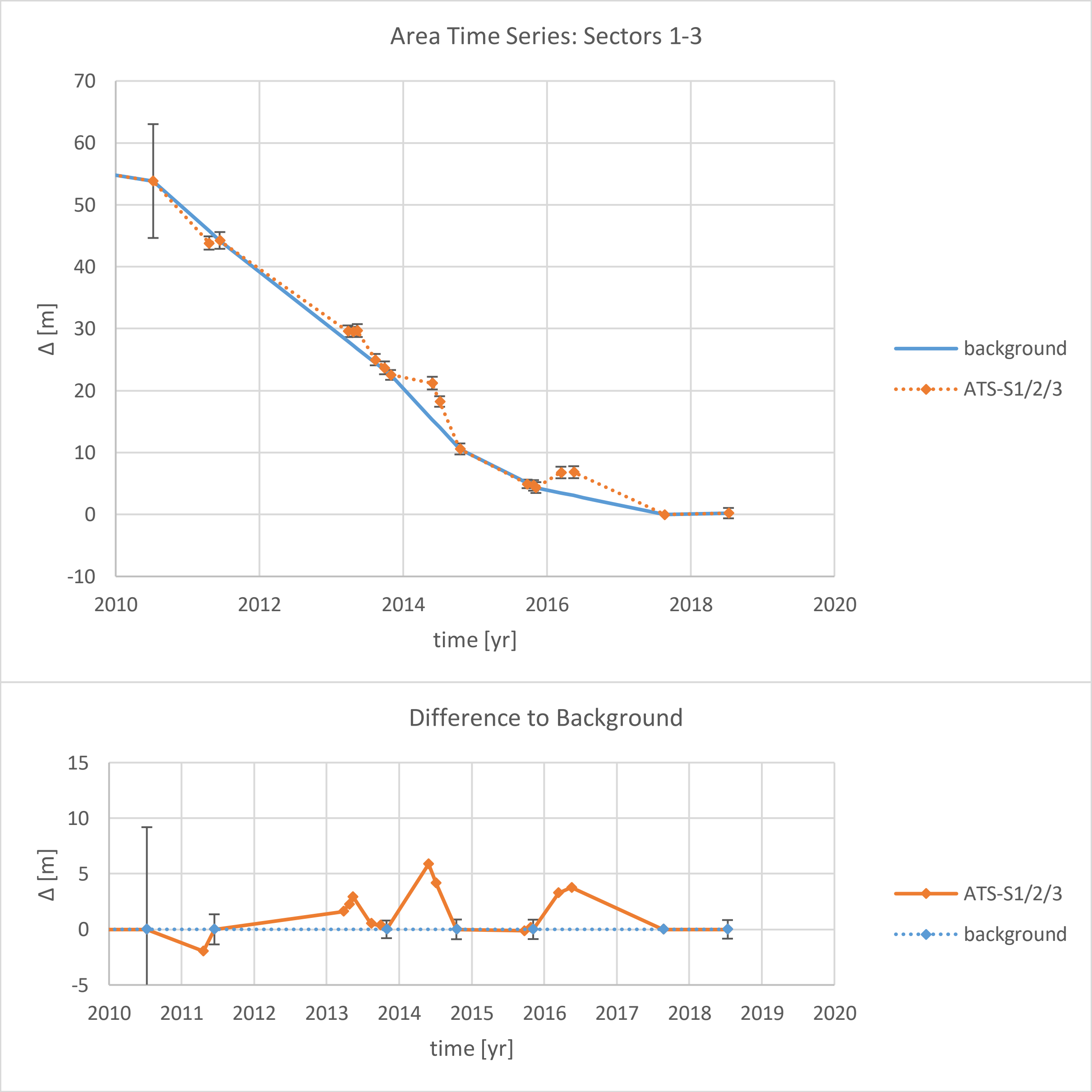

Figure 39: Background surface elevation change and seasonal pattern averaged area-wide for sectors 1-3. All values are relative to the area-wide elevation of AD170821*. The reference DEMs for the background change determination are given in table 8. Note that the temporal coverage before 2013 and after 2017 is not high enough for the detection of a seasonal pattern.*

The knowledge of a distinct seasonal pattern of surface elevation change close to the front in sector 1, and decreasing magnitudes with increasing vertical and horizontal distance from the front raises the question what surface elevation change and seasonal pattern characterises the terminus on an area-wide scale (sectors 1-3, excluding marginal zones). The considered area includes ca. 24 km^2 and roughly corresponds to the fast flowing central part of the terminus of Eqip Sermia.

In figure 39, all presented values are relative differences to *AD170821*. The area-wide surface elevation change is larger than 50 metres during the last decade. In comparison to the sector-wise analysis, where especially the lower sector 1 and 2 showed a drastic lowering until 2014 and then a sudden stabilisation, the area-wide surface lowering curve is smoother, with slowly decreasing surface lowering rates until 2017. Between 2017 and 2018, on an area-wide scale, the surface elevation is stable.

The magnitude of the seasonal surface elevation change pattern appears to be lower as in sector 1 and more similar to that of sector 3 (figure 82, appendix VII), which also marks the largest part of the represented area. The magnitude of the seasonal surface elevation change roughly lies between 3-5 metres, again with a maximum in 2014.

5.3.6. Surface Elevation Change on Low-dynamic Margins

According to the results presented concerning the temporal patterns of the surface elevation change, it can be stated, that the highest surface lowering rates as well as the largest magnitude of seasonality can be observed in sector 1. This sector also stabilised at first (after 2014), while the surface lowering persists at higher elevations (sector 3). Area-wide analysis reveals that the average surface elevation of the dynamic central parts of Eqip Sermia in sectors 1-3 seems to have stabilised after 2017.

However, after a look at an elevation difference raster of two DEMs (figure 31), a velocity map (figure 7) or the surface geometry changes (figures 34 and 35) reveals, that the evolution of the surface elevation of the marginal areas behaves different from the centre of the ice stream. In this chapter, these areas are further investigated.

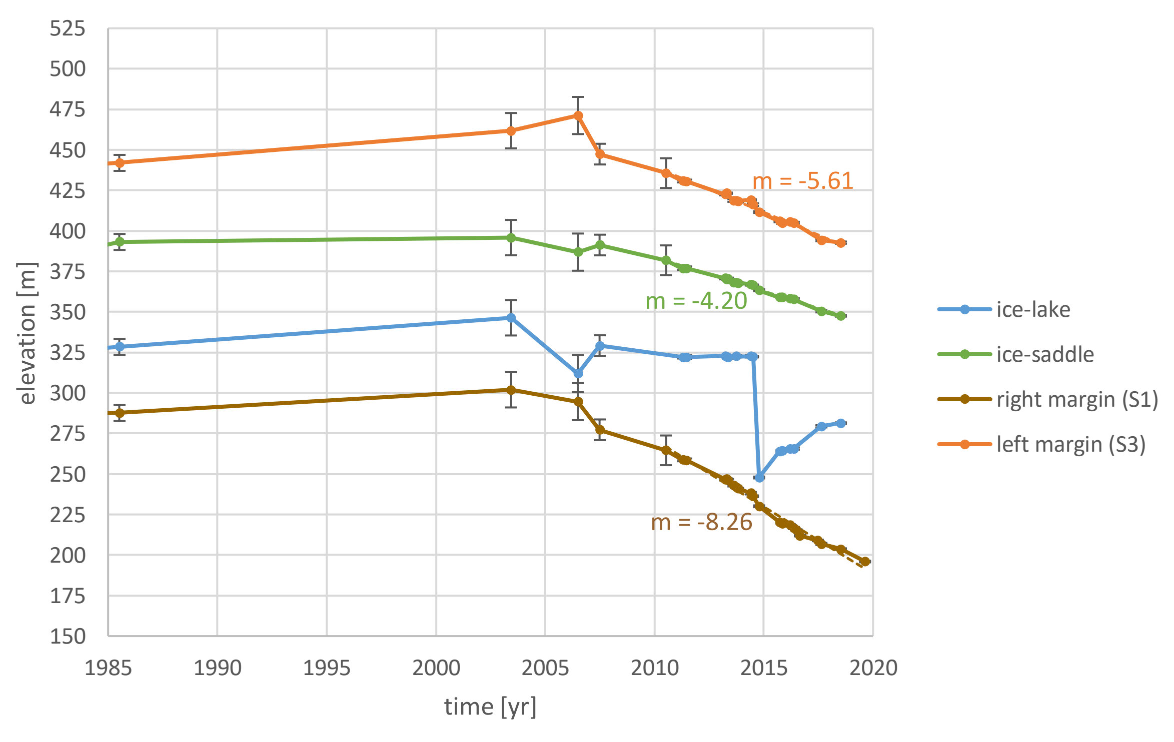

Figure 40: Point time series of the surface elevation on the low-dynamic margins of Eqip Sermia. In addition, the temporal evolution of the water level of the ice-lake is included. The numbers indicate the rate of surface elevation change in m/yr (= slope of the trendline) in the respective areas from 2010 to 2019.

As figure 40 shows, all PTSs of the marginal areas show very little surface elevation change with a slight increase between 1985 and 2003. After 2007, the rates of surface elevation change (i.e. lowering) are nearly constant, being larger at the lower right margin in sector 1 (2007-2019: -8.26 m/yr) and the left margin in sector 3 (2007-2018: -5.61 m/yr) in comparison the ice-saddle on sector 2 (2007-2018: -4.20 m/yr). A closer look at the change rates hints at a clear seasonal pattern with strong surface lowering in summer and almost stable conditions in winter, most pronounced at the right margin in sector 1. The water-level of the ice-lake was constant from 2007- July 2014 and then suddenly dropped by 75 metres during the lake-drainage event. From October 2014 until 2018, the water level rose again by almost 30 metres. The rise of the water level occurs stepwise with little to no increase during winter.

Figure 41 analyses the situation on the right margin in sector 1 in more detail. Here, exemplarily, the strong contrast between the temporal surface elevation change pattern in the marginal areas and the fast flowing central part of Eqip Sermia becomes visible. While the surface elevation at the margin mostly lowers at constant rate after 2010, the rate of surface lowering is higher towards the centre from 2010 to 2014. Eventually, the rapid lowering in the centre practically stops and the surface elevation remains unchanged except from the seasonal pattern. This has an impact on the surface geometry of the area (figure 41, right). The centre of Eqip Sermia (represented by analysis point *S1-C'* was approximately 20 metres higher than the right margin in 2010 and eventually, the elevation difference diminished and reached close to 0 metres by the end of 2014. From 2015 to 2019, the elevation difference increased again, measuring ca. 35 metres in 2019. In the meantime, the elevation difference between the right margin and the depression to the right of the high-dynamic centre (*S1-R'*) reached -35 metres in 2014 and is recently approaching 0 metres again.

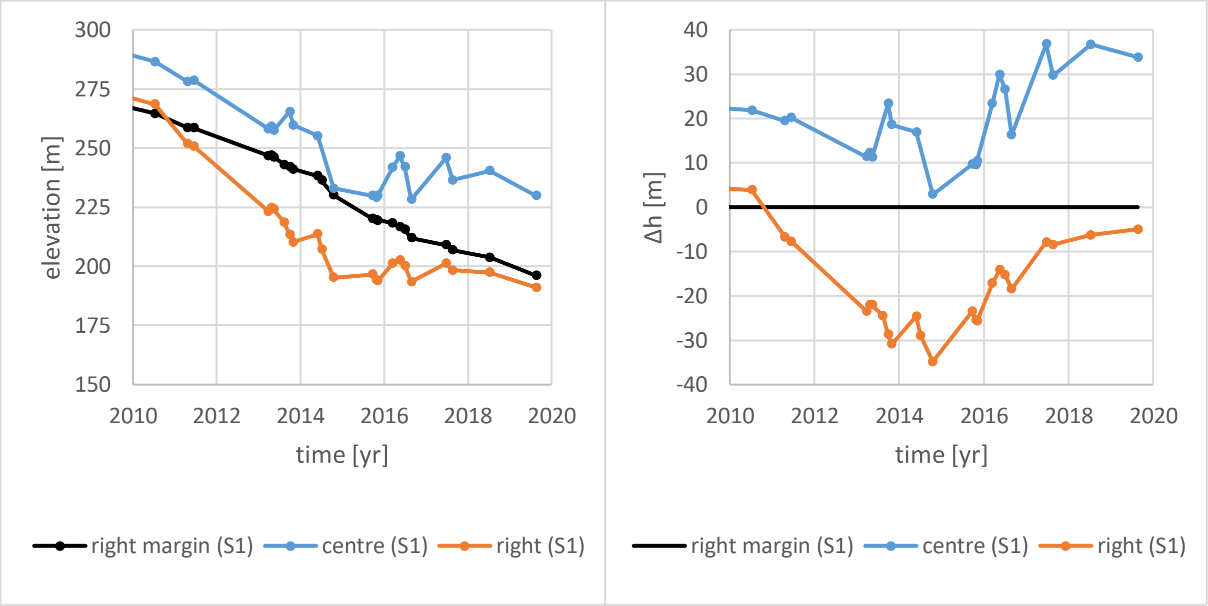

*Figure 41: Point time series of surface elevation on the low-dynamic right margin in sector 1 and analysis points to the right (*S1-R'*) and in the centre (*S1-C'*) of high-dynamic Eqip Sermia. Left: original elevations; right: elevation difference relative to the right margin.*

5.4. Slope and Ice Thickness Change

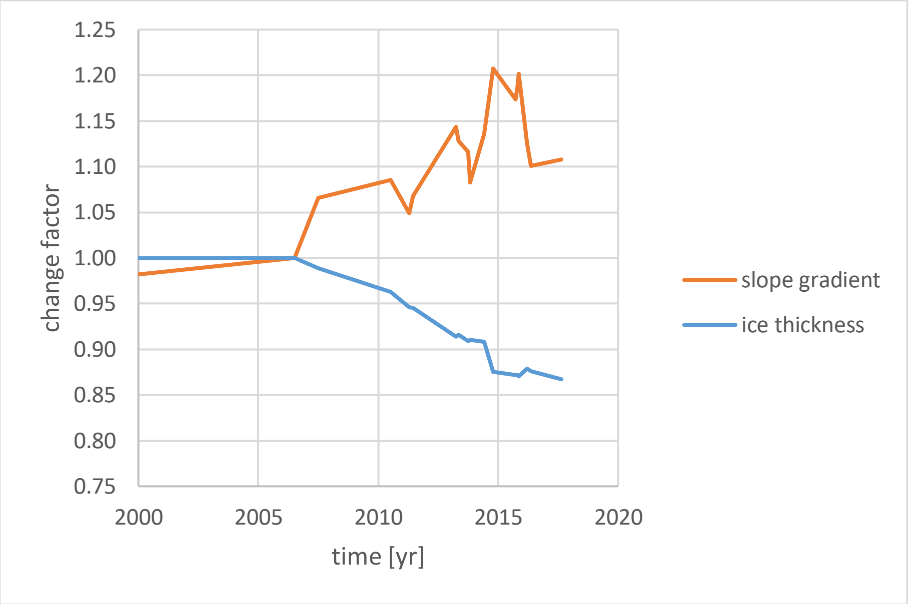

Figure 42: Implications of the surface elevation change on the slope and ice thickness averaged along the central profile between S1-C *and* S3-C*. The change factors of the slope gradient and the ice thickness are given relative to* AS060703*.*

As shown in figure 37, the magnitude of surface elevation change is larger in lower elevations and less pronounced in higher elevations. This, of course, has implications on the surface slope gradient, which accordingly changes over time. Also, resulting from the general surface lowering trend, the ice thickness changes.

The average slope gradient along the central flow line of the lowest 5 kilometres between *S1-C* and *S3-C* was equal in 1985 and 2006. Eventually, it has increased by 30 percent between 2006 and the end of 2014 (figure 42). After this peak, the slope gradient decreased again, being 18 percent steeper in 2017 than in 2006. Simultaneously, the average ice thickness in the corresponding section of Eqip Sermia has decreased by 12.5 percent from 2006 to October 2014. The decrease is followed by a period with nearly stable ice thickness. Implications of the changes of the slope gradient and the ice thickness on the flow velocities are discussed in chapter 6.2.1.

5.5. Front Position and Length Change

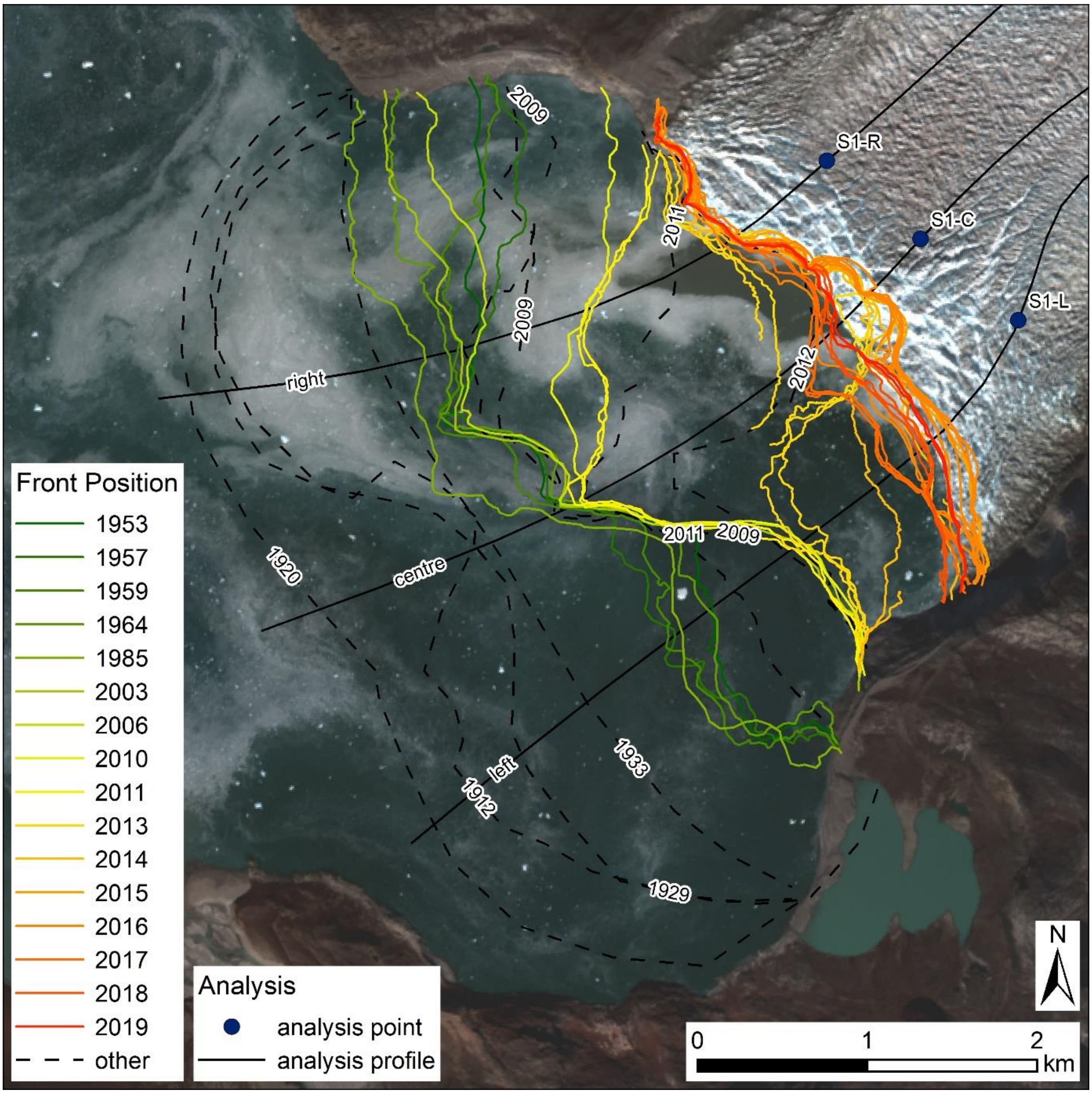

Figure 43: Front position change at Eqip Sermia in the period from 1912 to 2019. The coloured lines mark the front positions according to the timestamps of the analysed DEMs. The dashed black lines mark selected additional front positions from Lüthi et al. (2016). The solid black lines are the along-profiles used for the analysis of the length change. The length changes are compared to the average elevation change from the analysis points in sector 1 (blue dots). Background: Sentinel-2B, 30th August 2019, European Commission (2015).

The terminus extent of Eqip Sermia decreased by approximately 16 km^2 during the last century. The LIA maximum extent was reached ca. 1920. While the frontal extent has changed by roughly 3.5 kilometres, due to the steep topography curtailing the terminus area, the narrowing only measures about 50 to 300 metres maximally.

The front position of Eqip Sermia was advancing from 1912 to 1920 and eventually retreated by approximately 1.5 kilometres from 1920 to 1950 (figure 43 and 44). The period of 1950 to 2000 is generally characterised by a slight advance of the front position, except for a retreat and readvance of the left part of the front. In 1994, the left and right parts of the front reached their largest extent since the 1930s. From 2000 to 2003, the left front retreated by a ca. 1 kilometre, while the right sector only

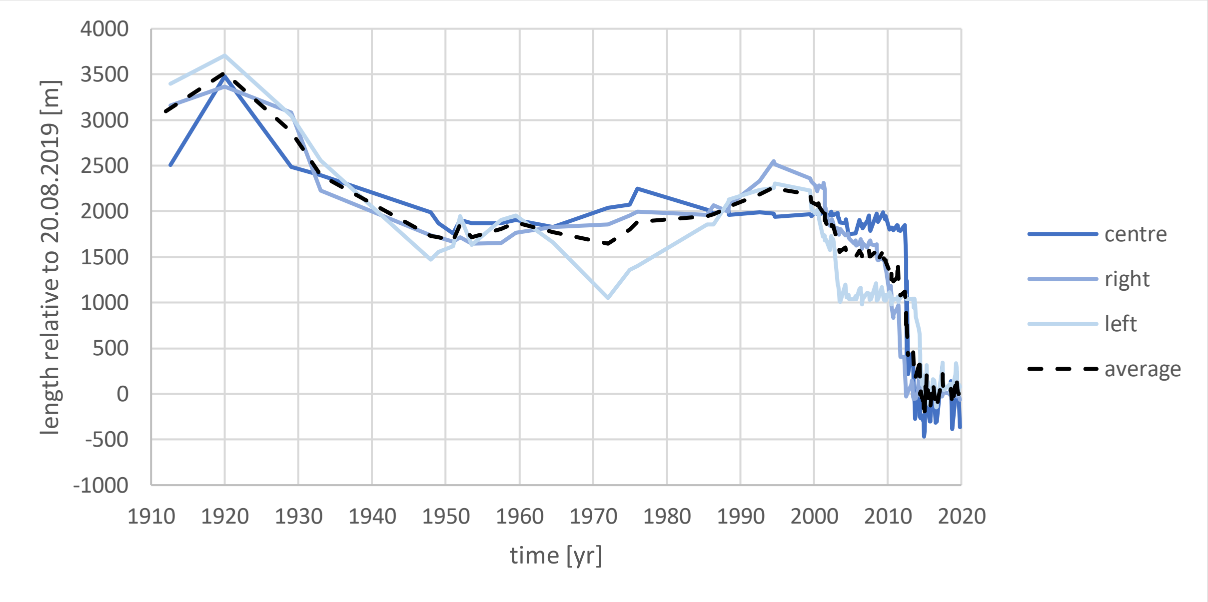

Figure 44: Length change of Eqip Sermia form 1912 to 2019. The length is measured relative to the front position on 20th August 2019. With data from Lüthi et al. (2016) and Rohner (personal communication, Rohner et al. 2019).

retreated slowly and the front position in the centre remained unchanged. The right sector started to retreat at increased rate in 2008 and the centre finally retreated extremely rapidly in 2012. Both sectors, the right and centre, continued they retreat until 2013, when they reached the approximate position of the current front. Interestingly, the front position of the left sector was almost stable from 2003 to the end of 2013, when it suddenly retreated by 1 kilometre within the following year 2014.

After 2014, no large changes of the front position were observed. However, a clear seasonal pattern of advance in summer and retreat in winter is visible. This seasonal pattern and its magnitude are further looked at in the following chapter.

5.5.1. Front Position Seasonality

The seasonality of the front position is assessed in the same way as the surface elevation seasonality (see chapter 5.3.4). The reference date for the length difference calculation is mostly between end of May and End of June, depending on the data availability (figure 26). A clear seasonal pattern is visible during the entire period from 2000 to 2019 (figure 44). Accordingly, the mostly negative ΔL-values indicate that the front of Eqip Sermia at that time of the year is usually in an advanced position, just before the onset of the summer retreat. The largest magnitudes are recorded between 2012 and 2014. However, in these years, large geometry changes and a strong front retreat occurred, what might negatively influence the expressiveness of the respective values. In general, it can be observed that the magnitude of the seasonal length oscillation increased from ca. 200 metres before 2011 to approximately 400 metres more recently.

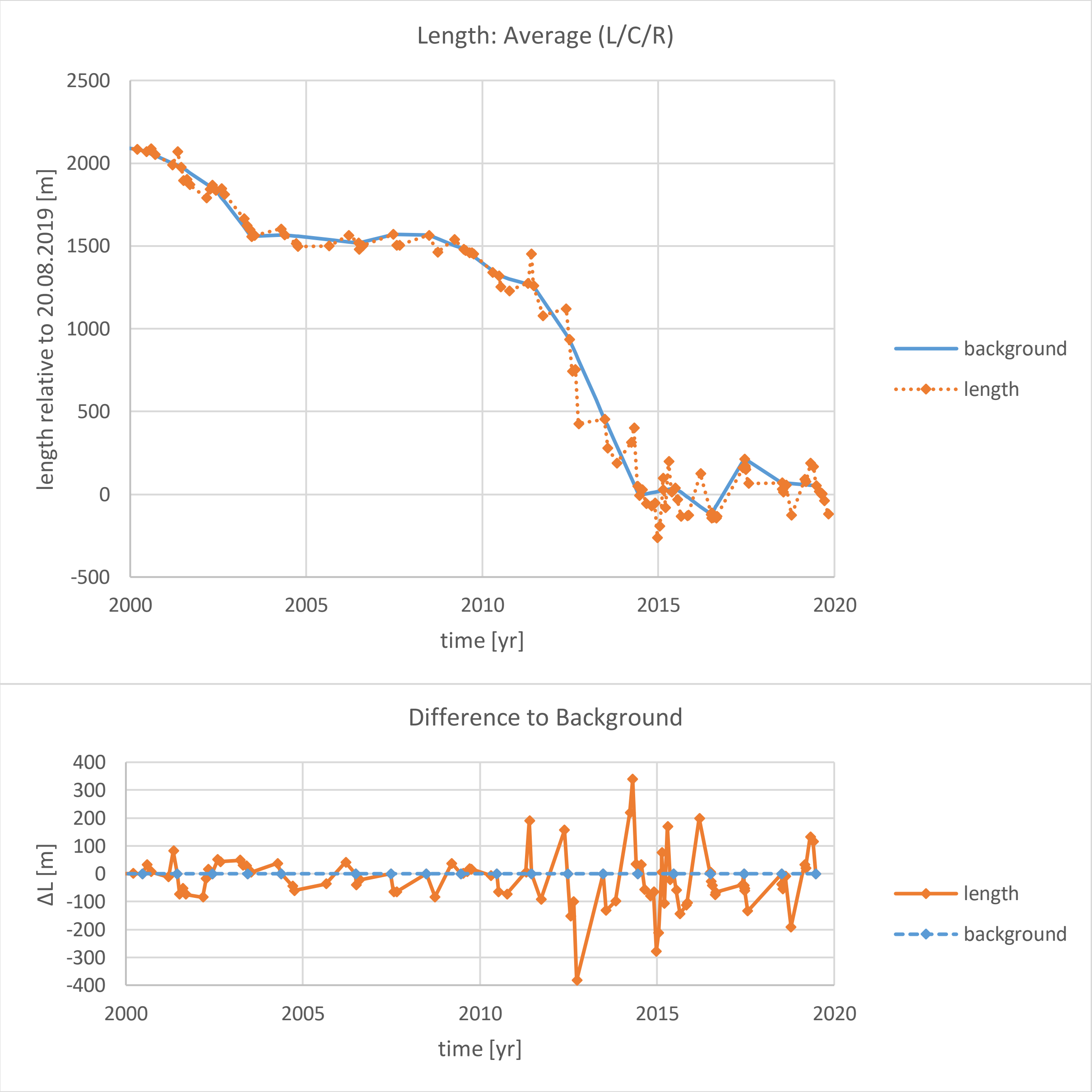

Figure 45: Time series of background length change and seasonal pattern. The values are averaged among the three profiles. A visualisation of the timestamps of the reference fronts for the background change determination is provided in figure 26. Note that the temporal resolution of the front dataset does not allow for a front position seasonality analysis before 2000.

5.6. Climate Forcing

5.6.1. Elevation Dependent Melt Rate

The long-term reconstructed temperature series of *AWS-ICE*, a site specific temperature lapse rate of 0.0072°/m and a temperature dependent melt rate of -0.342mm/h/°C are used to calculate the occurring melt on the margins in different elevations. Figure 46 shows the resulting elevation dependent melt rate expected for different elevations in the surroundings of *AWS-ICE*. At 0 metres, the average melt rate was ca. -9 m/yr on the long-term and increased by ca. 12 percent, reaching almost 10 m/yr during the last 15 years.

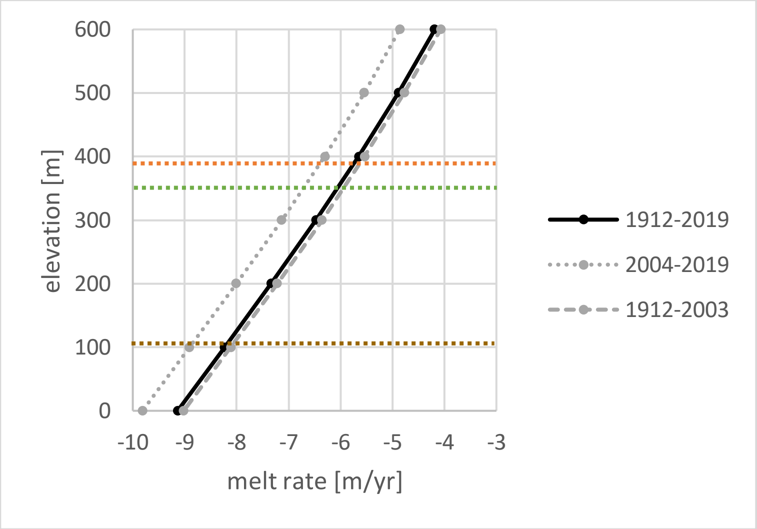

Figure 46: Elevation dependent surface melt rates for the periods 1912-2003 (= stable period), 2004-2019 and 1912-2019. The dashed lines mark the elevations of the low-dynamic margins in figure 40 (identical colours).

5.6.2. Elevation Dependent Positive Degree Change

The modelled surface melt rates between the period with stable conditions (1912-2003) and the recent years (2004-2019) are compared in figure 47. It appears that the increase of the melt rate is larger at higher elevations due to the fact that the hitherto annual positive degree sum is much smaller than in lower regions. According to extrapolation of the melt model towards the GrIS interior, the melt rate at the *Swiss Camp* increased by 57 percent recently.

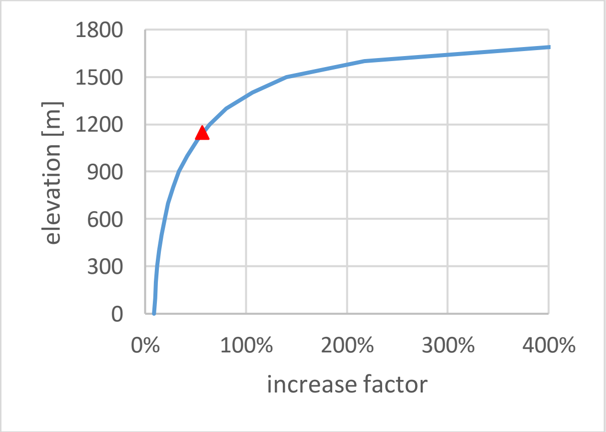

Figure 47: Elevation dependent increase of annual melt rate based on the modelled elevation dependent melt rates (figure 46). The red triangle marks the elevation of the Swiss Camp*.*

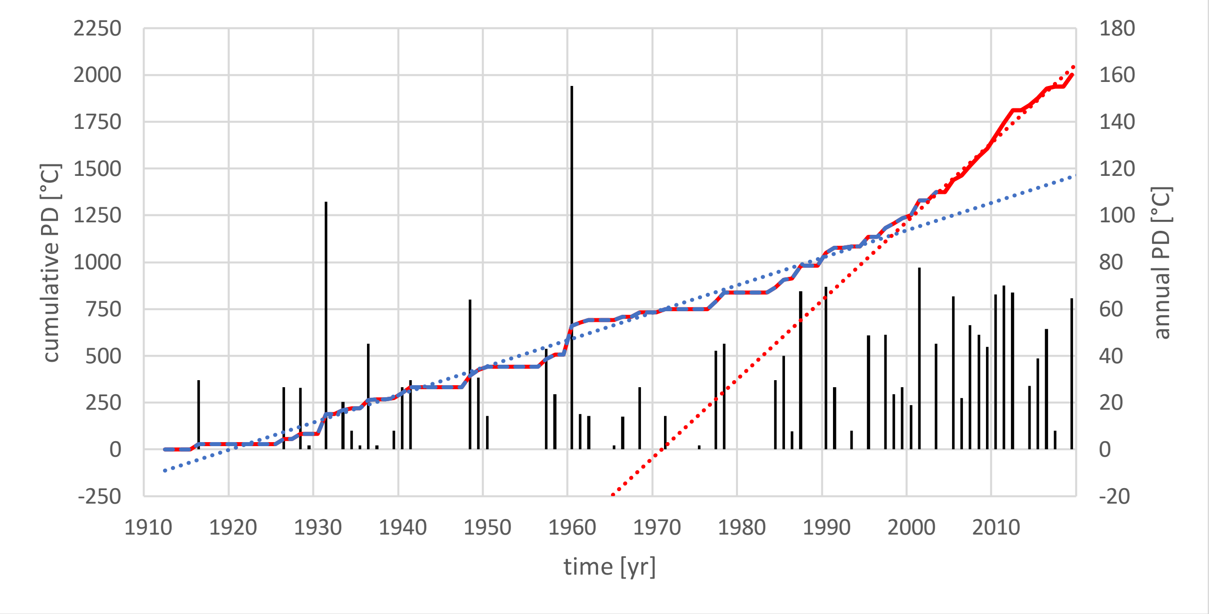

Figure 48: Annual positive degrees (PD) and cumulative PD from 1912-2019 at the Swiss Camp*. The black columns show the annual PD. The dashed blue cumulative PD and dotted blue trendline mark the trend of the stable period 1912-2003. The red line shows the cumulative PD from 1912-2019 and the dotted red line is the cumulative PD trendline from 2004-2019. Note that the underlying temperature data series is reconstructed based on the temperature series of Ilulissat.*

The (reconstructed) temperature series the *Swiss Camp* shows a drastic trend towards more positive-degree-days (figure 48). From 1912 to 1990, only in 2 out of 5 years, positive monthly mean temperatures were measured. After 1990, positive monthly mean temperatures occurred in 75 percent of all years.

The cumulative trend of the period 1912-2003 is strongly exceeded by the temperatures in the period 2004-2019. The slope gradients of the trendlines of the two periods shown an increase of PD by 187 percent. According to the above presented melt model, the resulting cumulative PD excess (figure 49) accounts for additional surface lowering through melt. This indicates that higher areas in the area of the equilibrium line altitude experience drastic changes in the SMB.

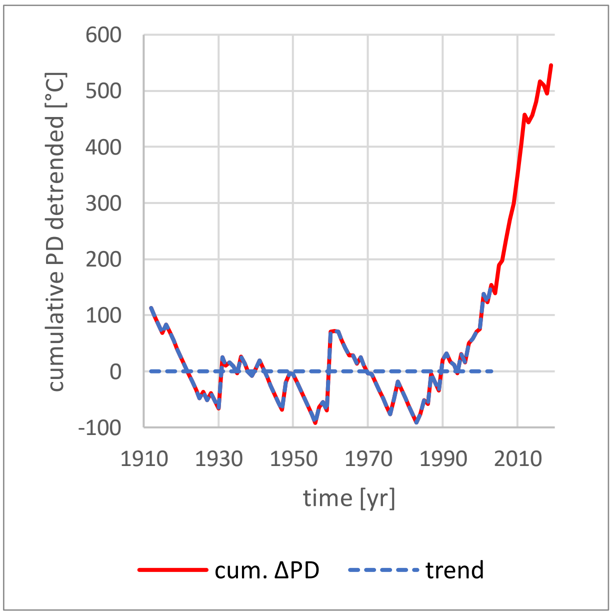

Figure 49: Detrended cumulative PD at the Swiss Camp*. The dashed blue detrended cumulative PD and dotted blue trendline represent the stable period from 1912-2003. The red line shows the temperature anomaly in respect to the stable period.*

5.6.3. Simulated Melt Rates on Low-Dynamic Margins

According to the melt model presented above and with utilisation of the reconstructed temperature series from *AWS-ICE*, the annual melt rates of the low-dynamic margins of Eqip Sermia can be determined. The respective melt rates modelled for the corresponding elevations in 2018 are listed in table 10, accompanied by the observed surface lowering rates. According to the assumption, that no dynamics or accumulation affects the surface elevation change on the low-dynamic margins of Eqip Sermia, these surface melt rates are not detrended.

The (*modelled*) annual melt rates for the ice-saddle and the left margin in sector 3 exceed the (*observed*) surface lowering during the corresponding period 2010-2019. Contrastingly, the modelled surface melt for the right margin in sector 1 is smaller than the observed value. According to the model, the surface melt in the terminus area of Eqip Sermia has increased recently by ca. 12 percent from 1912-2003 to 2004-2019.

Table 10: Modelled annual melt rates on the low-dynamic margins for different periods, complemented by the (observed (DEM-derived) surface change rate from 2010-2019. The increase refers to the periods 1912-2003 and 2004-2019. All listed values are calculated based on the reconstructed temperature series of AWS-ICE*.*

		modelled					**observed**
area	*elevation 20.08.2019 [m]*	**1912-2019 [m/yr]**	**1912-2003 [m/yr]**	**2004-2019 [m/yr]**	**increase [%]**	**2010-2019 [m/yr]**	**2010-2019 [m/yr]**
right margin, S1	*204*	-7.3	-7.2	-8.0	11	-7.9	-8.3
left margin, S3	*393*	-5.7	-5.6	-6.4	14	-6.3	-5.6
ice-saddle	*348*	-6.1	-6.0	-6.7	13	-6.6	-4.2
Swiss Camp	*1149*	-1.2	-1.1	-1.7	57	-1.6	

6. Discussion

6.1. Spatial Patterns

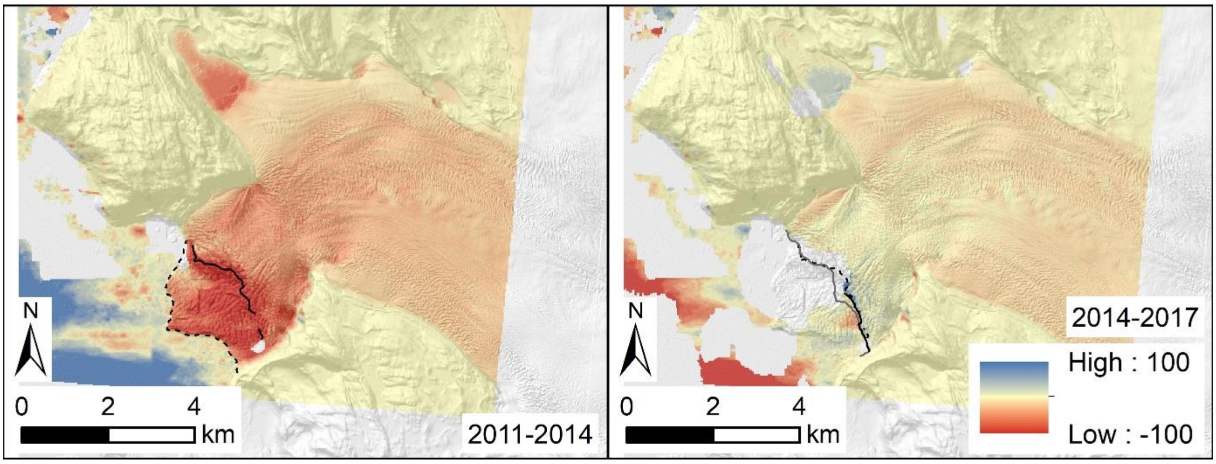

Figure 50: Surface elevation change in metres from 011-2014 and 2014-2017. These years are represented by the following DEMs: AD110613, AD141015 *and* AD170821*. The dashed black lines mark the glacier front position at the start of the period and the solid black lines at the end, respectively. Due to limited coverage of the respective DEM, the DEM front in 2017 is complemented by the front from 21st July 2017 (grey). The background hillshade is from the* ArcticDEM *composite.*

The analysis of spatial patterns of surface elevation change results in the identification of rapid surface elevation adjustment that follows large changes of the geometry of the terminus in sector 1. For example, already the retreat of parts of the front of Eqip Sermia resulted in a surface lowering of the area behind (i.e. upstream of) the affected location (see chapter 5.3.1). The largest changes monitored by the collection of data investigated in this study occurred from 2011 to 2014 and had a major impact on the surface elevation of Eqip Sermia in sector 1 (figure 50: left). However, the fact that already shortly after (during the period from 2014-2017) no further changes of the surface elevation at the front are recorded, indicates that the surface elevation adjustment is highly dynamic and occurs on relatively short time scales. In contrast, the surface elevation during the period 2014-2017 in higher elevations shows a persistent lowering signal (figure 50: right). At the same time, the smallest surface lowering rates (which indicate nearly completed surface elevation adjustment) seem to extend in the area with largest flow-velocities i.e. in sector 1 and the central part of Eqip Sermia in sector 2 (figure 7). This observation is supported by figure 37, showing a continuing surface elevation lowering in sector 3, while apparently the surface elevation already stabilised at lower elevations.

Thus, it can be assumed, that the time necessary for a complete surface elevation adjustment after large changes at the front is dependent on the flow velocity. This hypothesis is supported by Felikson et al. (2017) who modelled the implications of diffusive thinning on the mass balance of the GrIS. They find, that the inland propagation of surface elevation lowering at marine-terminating outlet glaciers is dependent on the ice thickness and surface slope gradient, which are dynamically intertwined with the flow velocity.

6.1.1. Dynamic Extent

Further analysis of spatial patterns of surface lowering at higher elevations revealed that the extent of surface elevation change from supposedly dynamic thinning reaches as far as 20 kilometres inland (figure 32). However, the datasets chosen for this purpose only frame a relatively short period of merely 2 years from May 2013 to July 2015. It remains unassessed what the exact causes of the observed thinning at higher elevations of Eqip Sermia are and whether the signal from the large changes of the period from 2011-2014 already propagated this far upstream. Nevertheless, the outline of the supposedly dynamic extent is probably robust as it marks a minimum. It is defined based on the -3 metre contour of the elevation difference raster (3 metres of surface elevation lowering in the respective period) and marks the largest surface elevation change contour that encircles the terminus area of Eqip Sermia completely. Therefore, all ice mass equivalent to the surface lowering within this outline most probably has been lost through Eqip Sermia (except for evaporation).

One alternative method to determine the extent of dynamic thinning would be, to calculate the thinning rate and compare it to a modelled SMB. However, the conditions at *AWS-ICE* and the *Swiss Camp* are supposedly affected (warmed/cooled) by microclimate effects and thus, upwards/downwards extrapolation of the temperatures and melt rates would introduce large uncertainties (further comments in chapter 6.3.7). After all, it has to be considered that the effects of diffusive thinning continuously lower and asymptotically approach zero with increasing distance to the front and thus, all definitions of dynamic extent limits can only be arbitrary. Nevertheless, the distance of the upper limit of the dynamic at 20 kilometres is roughly agreeing with the value of 16 kilometres obtained by Felikson et al. (2017), calculated based on a numerical approach.

The dynamic extent also correlates strongly with measured winter surface flow velocities (Joughin et al. 2015). The upper limit of the dynamic extent corresponds to an area, which is characterised by an increase of the flow velocities from 300 to 400 metres per year within relatively short distance (figure 51). This acceleration occurs ca. 2-3 kilometres upstream of a sector, where the bedrock again lowers below sea level and the ice flows through a large subglacial overdeepening (compare to figure 32), which correlates with the acceleration. Also, towards the low-dynamic areas to the north and south of Eqip Sermia, the dynamic extent is roughly delimited by the surface flow velocity contour marking 100 metres per year.

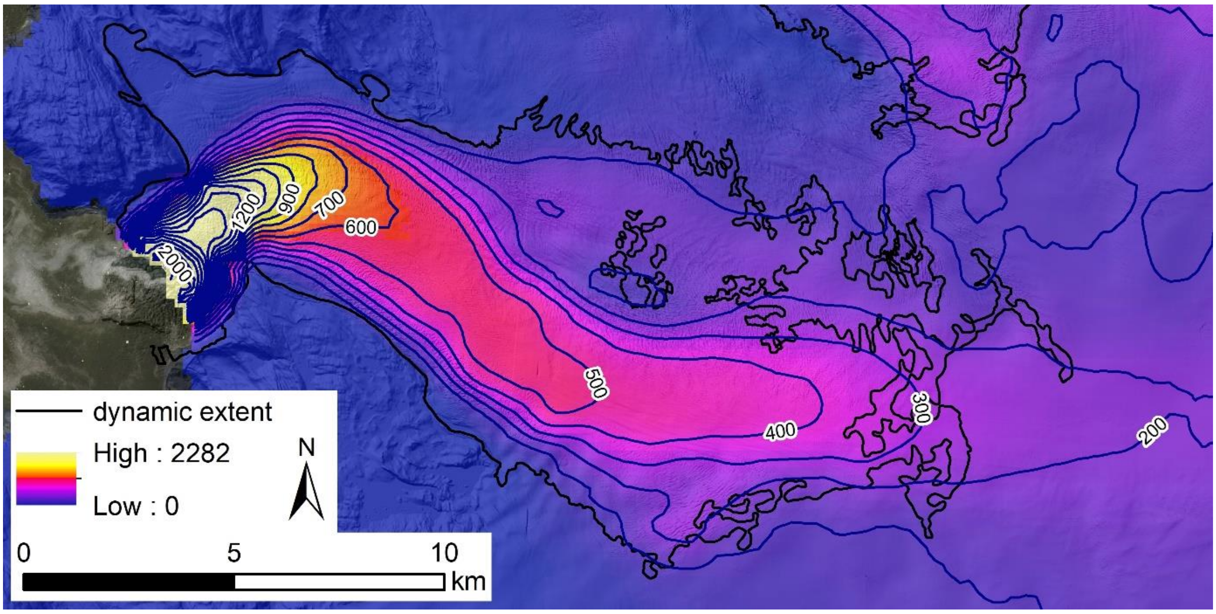

Figure 51: Dynamic extent (figure 32) and winter flow velocities in m/yr. The background hillshade corresponds to the ArcticDEM *composite. With data from Joughin et al. (2015). Background: Sentinel-2B, 30th August 2019, European Commission (2015).*

6.1.2. Spatial Retreat Pattern

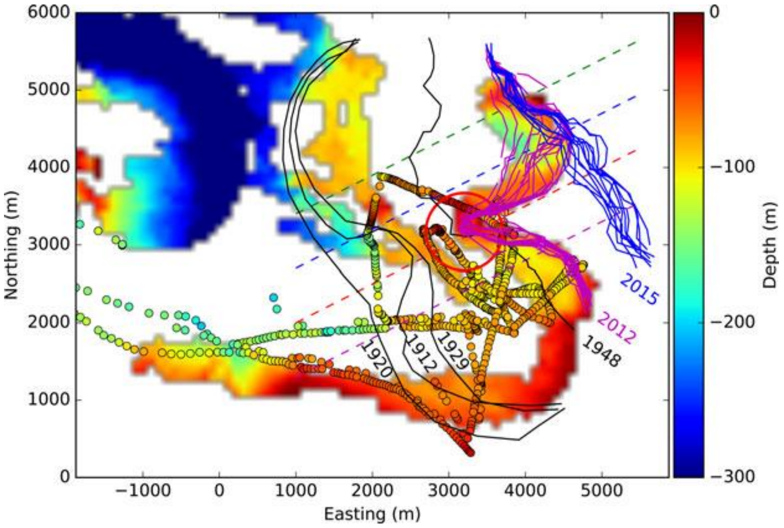

Figure 52: Bathymetry in the Atasund Fjord*. The figure combines swath bathymetry data from Rignot et al. (2015) and measurements from Lüthi et al. (2016). Further included is a selection of front positions. Figure from Lüthi et al. (2016: 648).*

The bird view of the retreat history of Eqip Sermia reveals interesting spatial patterns that are non-linear in every sense. According to the bathymetry data collected by Lüthi et al. (2016), the area of the bay, in which Eqip Sermia terminates is characterised by relatively shallow water with depths often smaller than 100 metres (figure 52). The location of a very shallow area coincides with the location of the central front from at least 1988 to 2011. Among others, Catania et al. (2018) describe a typical behaviour according to which marine-terminating outlet glaciers tend to persist in shallow areas of the fjord. Only if their terminus lowers enough and their front is not sustained anymore, they rapidly retreat through the deeper sector and only stabilise again in zones of prograde slope at the bed. This mechanism at hand, the interpretation of the non-linear retreat of Eqip Sermia is more obvious.

At the current front position, the depth of the grounding line again is relatively shallow (further comments in chapter 6.4.1). Among other factors, this explains to a large extent, why the fast retreat before 2014 came to stop at the current front position and why the front of Eqip Sermia has been mostly stable for several years since then. Further interesting is the fact that in the past, Eqip Sermia was often characterised by one-sided retreat. This provides additional support for strong morphologic control on the retreat pattern of Eqip Sermia and further hints at the properties of the bedrock topography, even if no directly measured bathymetry data is available. The spatial patterns of the retreat of Eqip Sermia emphasise the importance of knowledge of the subglacial bedrock topography to understand past and predict future front changes of marine-terminating outlet glaciers.

6.2. Surface Geometry

The analysis of the surface elevation profile evolution along the central flow line of Eqip Sermia allows for the detection of a characteristic profile evolution during retreat (figure 53). The profile from 1985 shows a prominent bump at kilometre 0.5, below which the surface slope is very steep. Closer to the front, the slope is more gentle (but steeper than above the bump), leading directly to the front. In 2011, few months before the large retreat in the centre, the surface elevation along the profile is much lower than in 1985 and behind the front, even a sector with reversed slope has formed. After the retreat, a very high front has formed and the surface continues to lower (2013-2014), presumably in order to find a new stable geometry. Once, the front geometry is adjusted, the surface elevation shows no further changes, and in the case of Eqip Sermia, even a small readvance of the front is documented.

According to Howat et al. (2008), among a larger variability, the geometries of Eqip Sermia precisely represent the two *end members* of geometry. They explain, that many observed glaciers at first had a geometry more similar to Eqip Sermia in 1985 (or 2018) with constant or increasing slope towards the front (type 1). Eventually, multiple glaciers started to form shallow frontal sectors, in cases even with prograde slope like Eqip Sermia in 2011 (type 2). The formation of type 2 surface geometries was found to often precede large frontal retreats. These findings strongly agree with the observed surface profile evolution pattern at Eqip Sermia. Further, if zoomed out, the state of Eqip Sermia can be interpreted as type 2, which under respective environmental conditions could slowly transform into a type 1 in the future.

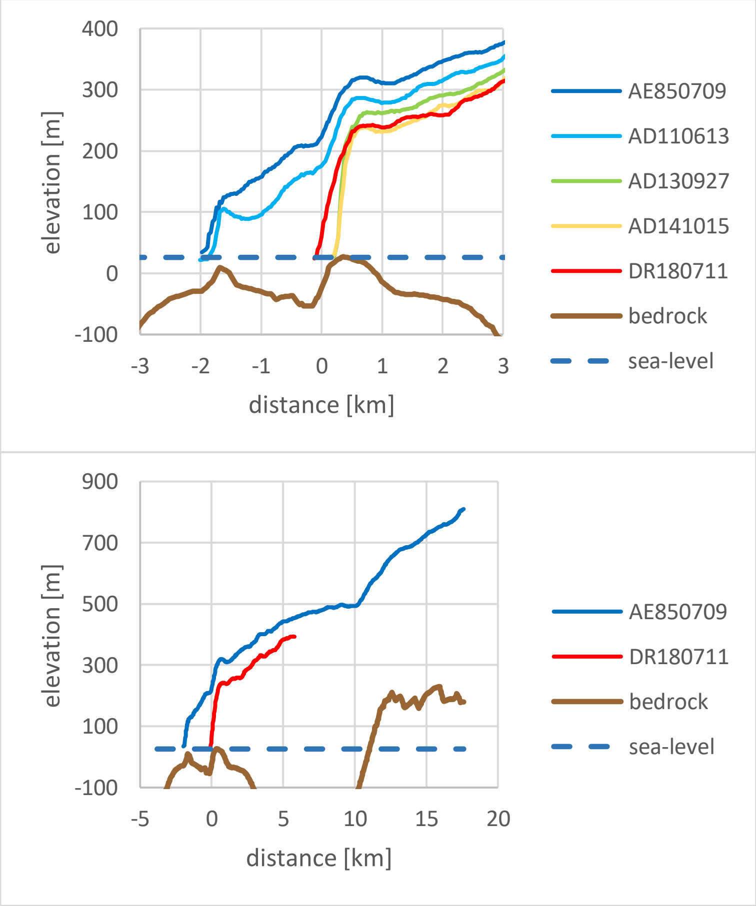

Figure 53: Selection of surface profiles along the central profile P-C, *showing the characteristic profile evolution before, during and after the retreat.*

6.2.1. Slope, Ice Thickness and Velocity

In accordance with the changes of the surface elevation and the surface geometry, also the surface slope gradient and the ice thickness are affected. According to the equations in chapter 4.10, the surface flow velocity is dependent on both, slope gradient and ice thickness. As presented in figure 54, assuming $m = 3$ and $n = 3$, the effects of the slope gradient increase and the ice thickness decrease on the surface flow velocity are almost in balance at Eqip Sermia. Accordingly, the solely geometry-deduced surface flow velocity for sectors 1-3 would have increased by 30 percent after 2006, while from 2011-2015, it had ranged around the value from 2006 (±20%). After 2015, the velocity would have decreased strongly to values clearly lower than those of 2006.

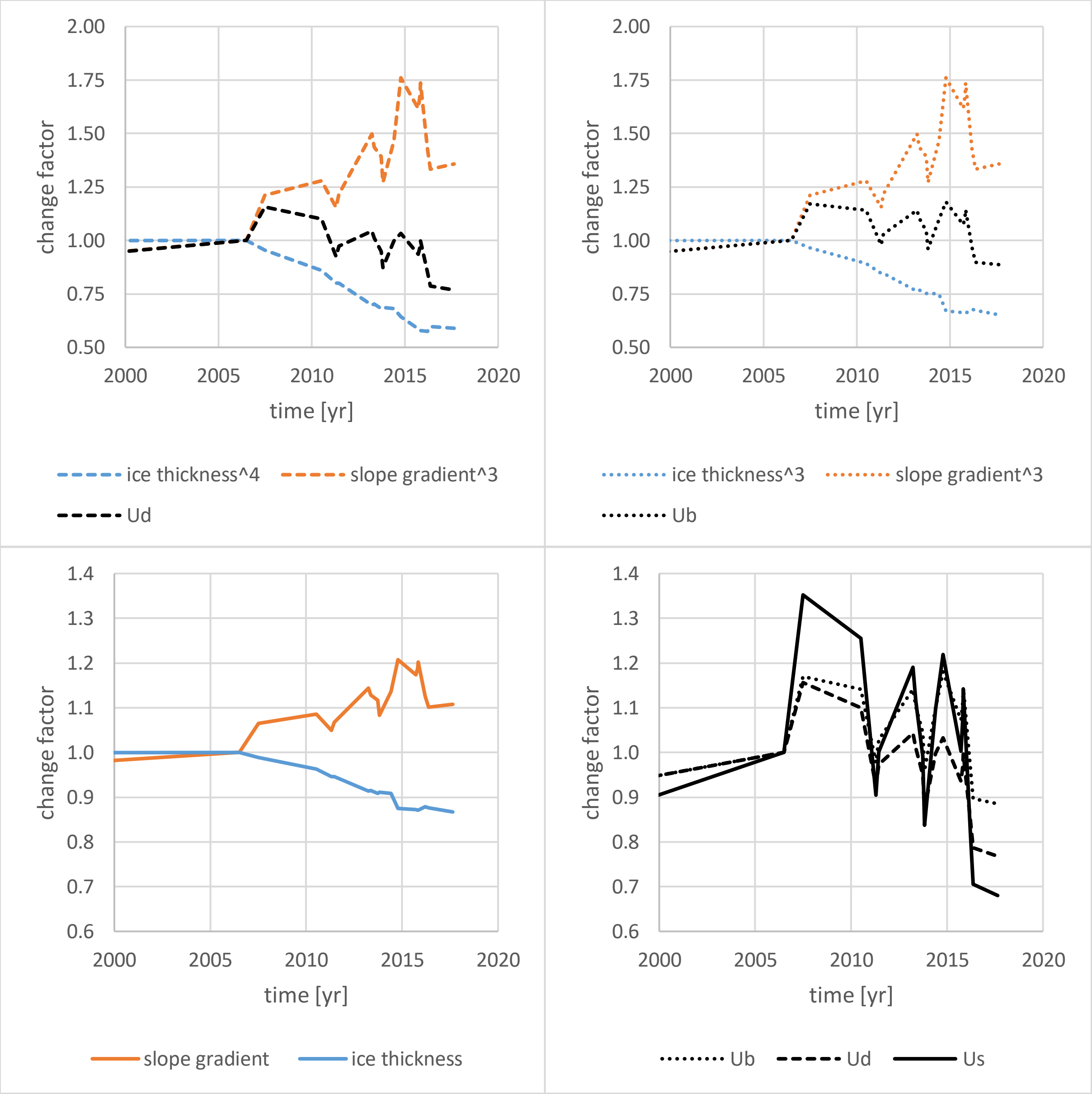

Figure 54: Implications of changes of the surface slope gradient and the ice thickness on the gravitational driving stress (GDS) and accordingly the ice deformation U_d (top left) as well as on the basal sheer stress (BSS) and accordingly the basal sliding velocity U_b (top right). The relative changes of the surface geometry lead to a changing slope gradient and ice thickness (bottom left), which results in a (minor) change of the surface flow velocity U_s (bottom right).

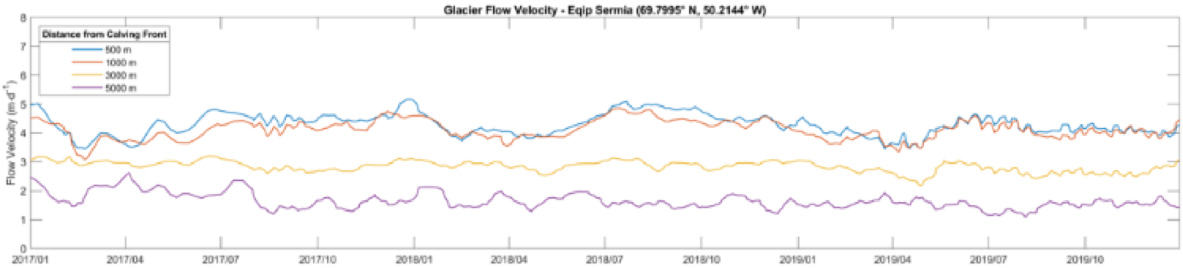

Figure 55: Seasonal variation of the surface flow velocity at Eqip Sermia from 2017-2019. Figure from Rohner (personal communication, Rohner et al. 2019).

This result contradicts with the observed changes of surface flow velocities in the terminus area of Eqip Sermia (Joughin et al. 2015; Rohner et al. 2019). As the longer-term time series by Joughin et al. (2015) represent the average *winter* flow velocities (mostly from September to May), they have to be interpreted in the context of seasonal changes. Figure 55 shows that the average surface flow velocity between 2017 and 2019 shows a minor seasonality with summer velocities ca. 1.25x higher than winter velocities (personal communication, Rohner et al. 2019). In 2006 and 2007, the relative summer speedups were roughly in the same range (Lüthi et al. 2016). Year-round, the flow velocities roughly range between 3.75 and 4.75 metres 0.5-1 kilometres from the front (personal communication, Rohner et al. 2019). Rohner et al. (2019) further determined UAV-derived 5-day average surface flow velocities of ca. 5 metres per day in the sector of 0.5-2 kilometres from the front in August 2016. A long-term velocity calculation (October 2014 to January 2020) based on satellite data resulted in an average surface flow velocity of ca. 4.5 metres per day at km 1.5 (personal communication, Rohner et al. 2019).

The winter velocity measurements by Joughin et al. (2015) show a clear increase by factor 2.2 (km 1.5) and 1.9 (km 5) from 2005/06 to 2014/15 (figure 56). Thus, from the comparison of the geometry-deduced velocities and the measured winter velocities, it can be interpreted, that the observed changes in the winter flow velocity are the result of other mechanisms than the geometry of the investigated section from *S1-C* to *S3-C*. The most prominent velocity increase close at the front (figure 83, appendix VIII) hints at a strong influence of the conditions at the front itself.

For instance, after the strong retreat from 2011 to 2013, the calving front was reaching a height of 200 metres in the central part of the front (Lüthi et al. 2016). According to Mercenier et al. (2019), close to the calving front, the acceleration

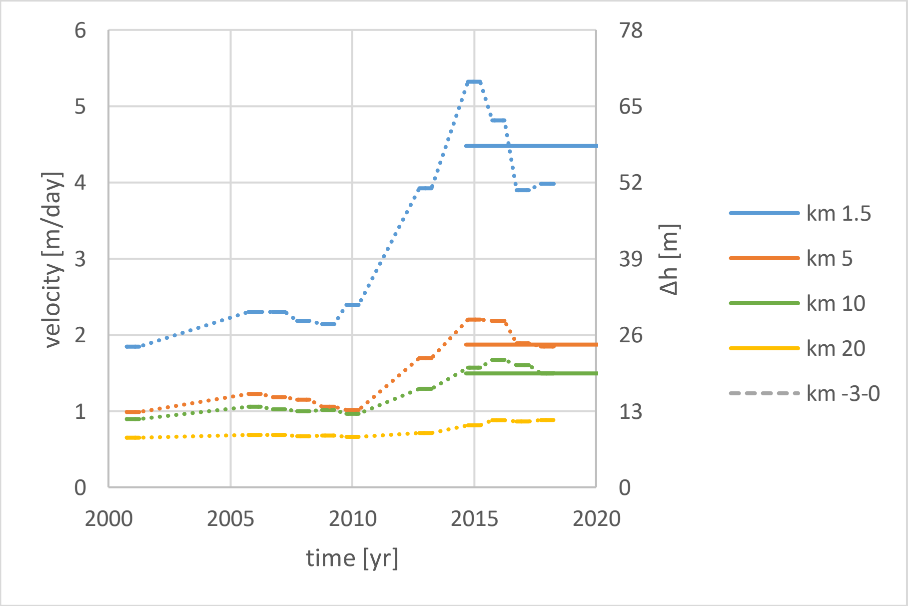

Figure 56: Temporal evolution of surface flow velocities at Eqip Sermia from 2000-2020 in different distances to the front. The short plateaus represent average winter flow velocities from Joughin et al. (2015). The dashed lines are linking them accordingly. The long plateaus form October 2014 to January 2020 show 5-year average velocities from Rohner (personal communication, Rohner et al. 2019).

towards the front is strongly controlled by the height of the front itself. Bassis & Walker (2011), state that there is an upper limit of the ice-cliff height of calving glaciers, which is higher for deeper grounded glaciers and lower for shallow-grounded glaciers. Eqip Sermia retreated into a very shallow zone, and thus, shortly after the retreat, the height of the calving front supposedly was above than the upper limit of stability. As the stable surface elevation and front position from 2014-2017 indicates, the front reached a new stable geometry within short time.

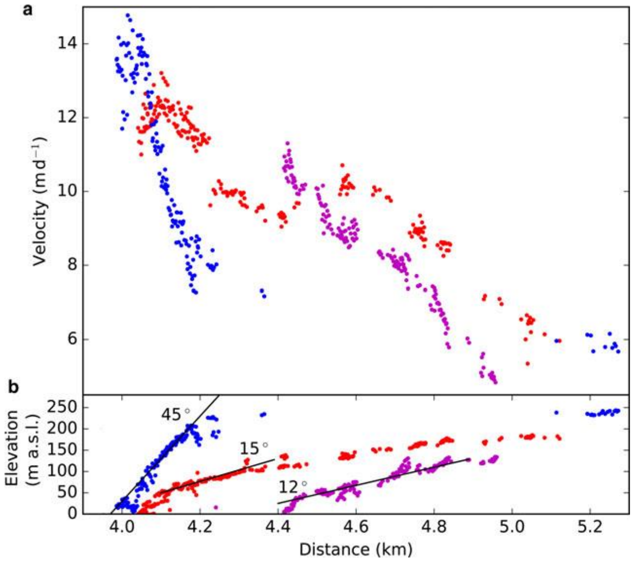

Figure 57: Radar measurements of flow velocities and front geometry at Eqip Sermia on 2nd July 2014. The blue dots are measured in the centre of Eqip Sermia, while the purple and red dots are measured to the left. Figure from Lüthi et al. (2016: 647).

Thus, in addition to the spatial pattern of acceleration, also the timing of the acceleration (increase in surface velocity during the time when the front was highest and the geometry was supposedly unstable, as well as the eventual deceleration after 2015) agree with the assumption that the front geometry has a strong impact on the dynamics and inherently the flow velocities in the terminus area. This assumption is also supported by radar velocity measurements in different sectors of the front of Eqip Sermia in 2014 (Lüthi et al. 2016, figure 57). Also, the thinning, which can be observed simultaneously with the acceleration during the geometry adjustment additionally decreased the mass of the ice body and thus the effective pressure at the glacier bed. This mechanism can contribute to the persistently higher surface flow velocities even years after the large retreat.

6.3. Temporal Patterns

As shown in figure 37, the surface elevation lowering is persistent at higher elevations (i.e. sector 3) even years after the large changes at the terminus. This is in agreement with Price et al. (2011), who show that the mass loss from dynamic thinning after perturbations at the front (in the form of a large retreat) can persist for multiple decades, however with decreasing mass loss rates. In fact, on the long-term, the mass loss form diffusive thinning is expected to outnumber the mass loss from the actual short-term changes at the front (Price et al. 2011).

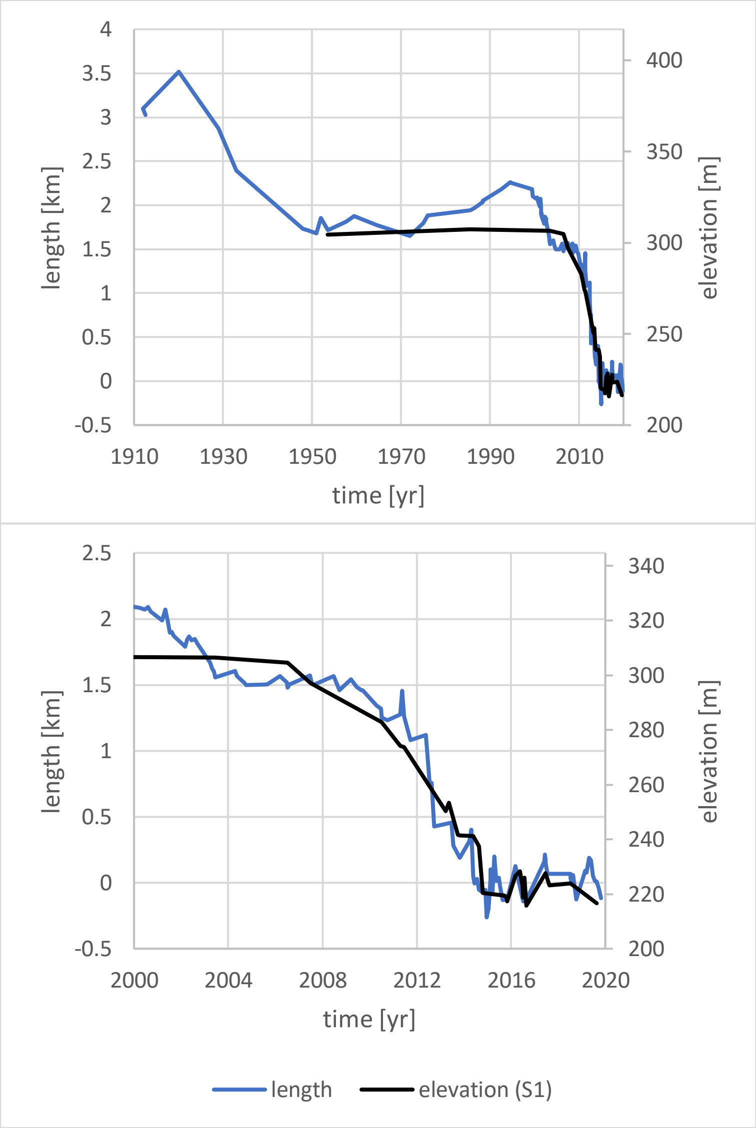

Figure 58: Surface elevation in sector 1 and length relative to 20th August 2019 at Eqip Sermia. Top: 1912-2019; bottom: 2000-2019.

6.3.1. Surface Elevation and Length

As plotted in figure 58, the temporal patterns of surface elevation and length (both averaged among centre, left and right) are very similar. The front retreat starts slightly before the onset of the surface elevation lowering, indicating at the marine conditions as possible trigger. Eventually, both the surface elevation and the length show a strong decrease until 2014 followed by a stabilisation. Also, the seasonal pattern is identifiable in both variables. The temporal resolution of elevation data only allows for the detection of a seasonal pattern 2011 onwards. The very simultaneous surface elevation lowering in sector 1 and retreat show that, at least during the past 10 years, both parameters strongly depend on each other.

Despite the slightly different timing in the beginning of the new millennium, a linear regression shows that, overall, there is a good correlation between the surface elevation and the length (figure 59). This accounts for all sectors (1-3), with correlation coefficients ranging from 0.76 to 0.79. Accordingly, in sector 1, the surface elevation lowers by 43 metres if the front retreats by 1 kilometre. With increasing distance from the front, this elevation dependent length change decreases (35m in S2, 32m in S3). This is good evidence supporting the hypothesis of diffusive thinning affecting the glacier surface elevation far upstream but with smaller magnitude. Due to the expected signal delay at higher elevations, the correlation coefficients could be expected to lower with increasing distance to the front. However, such a lowering is not apparent in the presented data. One possible explanation is that the temporal resolution of the elevation dataset is not high enough for precise correlation assessment, considering that the analysed timespan in figure 59 includes more than 30 years and only 20 data points per sector (limited by the elevation data availability).

6.3.2. Surface Elevation and Climate

A visual comparison of the detrended cumulative positive degrees (PD) from the reconstructed temperature series of the Swiss Camp with the surface elevation evolution reveals a generally good agreement (figure 60). The recent increase of detrended cumulative PD can be interpreted as evidence for the recent climate change to affect the SMB, as the proxy for the determination of the stable period is the surface elevation of a long-term stable low-dynamic land-terminating GrIS margin, which after the stable period showed significant lowering (Schudel 2019).

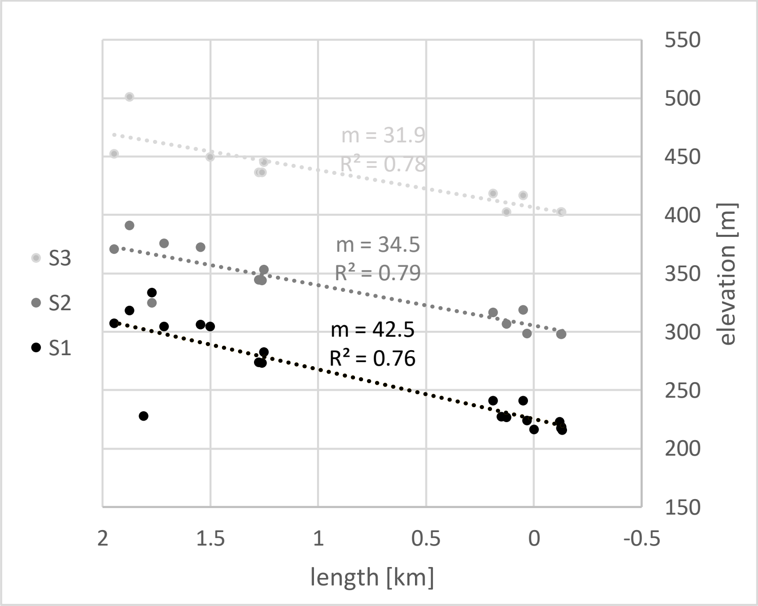

Figure 59: Elevation-length-relation for measurements from 1985-2019 in sectors 1, 2 and 3. Note that the length values on the x-axis are in reverse order. The correlation coefficients (R^2) and the slope gradients (m) are given in the respective colours.

The strong temporal correlation is further interesting, as the detrended cumulative PD is roughly equivalent to the SMB anomaly because of very small snow accumulation in the area (Moreau, personal communication, Lüthi et al. 2016). Accordingly, the cumulative PD trend marks the background melt, which on the long-term continuously melts the ice recharge from the ice sheet interior. The detrended cumulative PD thus can be considered as the exceeding temperature directly accounting for further surface melt. The accordingly expected signal of surface lowering is confirmed by a measured SMB of -1.31 metres per year at the *Swiss* Camp for the period 2011-2014 (Stober et al. 2015). If this surface elevation deficit at higher elevations is thought to translate downstream through mass conservation, this would result in an amplified signal at the terminus.

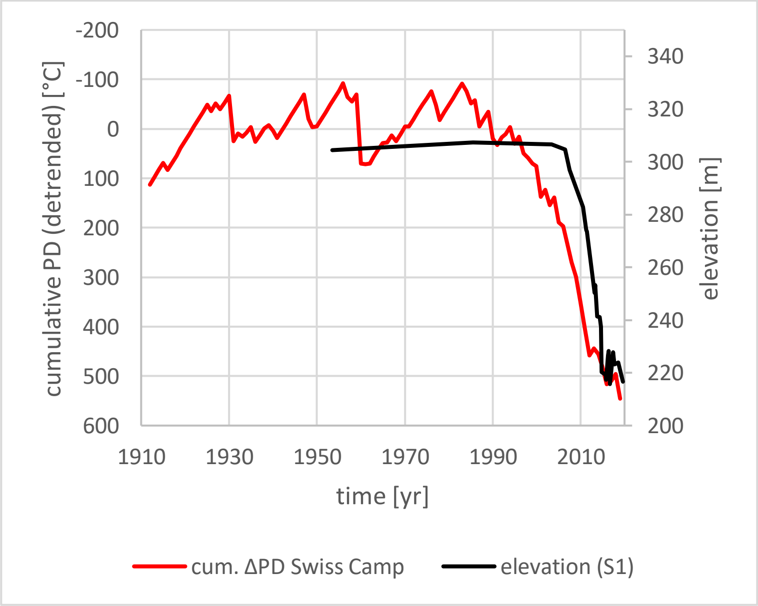

Figure 60: Surface elevation in sector 1 and cumulative PD excess relative to the stable period from 1912-2003. Note that the temperature axis is inverted to represent the interconnection of the two parameters.

The recent increase in temperatures clearly precedes the observed surface elevation change, as it started already in the 1990s. This is a strong indication, that the onset of the dynamic changes at Eqip

Sermia are initially triggered by changing climate. However, whether the climate change induced the surface elevation change directly (through increasing surface melt, …) or indirectly (through enhanced subglacial meltwater discharge, enhanced plume driven submarine melting, enhanced submarine melting through ocean warming, …) is not assessable from this observation.

Straneo & Heimbach (2013) found a strong increase of water temperatures in the subpolar North Atlantic after 1995, which correlates with the widespread retreat of marine-terminating outlet glaciers. After 2016, a cooling of ocean temperatures has been observed in Disko Bay, which is thought to have triggered the recent advance and thickening of *Jakobshavn Isbræ* (Khazendar et al. 2019). The warm Atlantic waters are typically overlain by a layer of cold and less saline freshwater. Thus, the access of warm Atlantic water to the fjords with marine-terminating outlet glaciers is partly controlled by the minimal depth of sills between the fjords and the open sea. (Straneo et al. 2013) Accordingly, the relatively shallow bathymetry in the fjord before Eqip Sermia could potentially reduce the site-specific influence of ocean forcing. However, a more detailed assessment of ocean forcing and related calving and submarine melting is considered out of scope for this study.

It has to be considered that the temperature evolution at the *Swiss Camp* in figure 60 is based on a reconstruction of the temperatures according to the differences to Ilulissat. As the reconstruction considers the mean monthly temperature differences, effects of climatic regime differences (e.g. continental-maritime condition differences) are accounted for. Additionally, no (uncertain) temperature lapse rate (potentially disturbed by microclimate effects) is used. Therefore, the largest remaining uncertainty arises from possibly different long-term climatic changes at the two compared locations. However, according to Hanna et al. (2012), the summer warming (JJA) in Ilulissat and at the *Swiss Camp* shows a similar order of magnitude. The original temperature series from the *Swiss Camp* shows that positive monthly mean temperatures at the *Swiss Camp* are generally rare and only occur during the summer months (JJA). Thus it can be concluded, that the temperature reconstruction is appropriate for the assessment of the changes of PD.

On the long-term, ice sheet runoff and SMB correlate with the temperatures in the Northern Hemisphere (Hanna et al. 2011). The slight slowdown of the cumulative PD at the *Swiss Camp* is in agreement with recent findings by Ruan et al. (2019) who observe a deceleration of the surface melt on the GrIS since 2013 due to a more positive North Atlantic Oscillation in summer.

For the terminus area of Eqip Sermia on an elevation of 300 metres, the temporal pattern of the cumulative detrended surface melt based on the stable period 1912-2003 interestingly shows a very good correlation with the surface elevation and length evolution (figure 61 with figures 36 and 44). However, the magnitude of the cumulative detrended surface melt

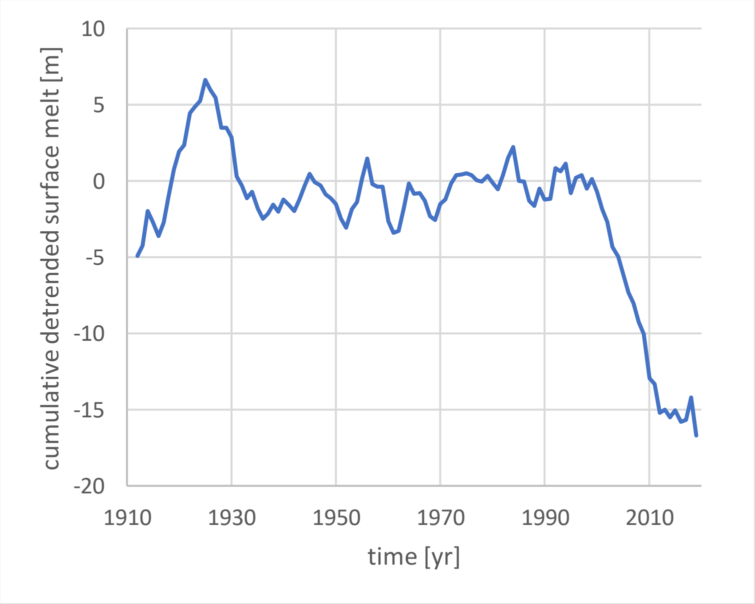

Figure 61: Cumulative detrended surface melt for an elevation of 300 metres from 1912-2019, exemplarily for the entire area of the terminus of Eqip Sermia. The reference stable period is 1912-2003.

is much lower than that of the observed surface elevation lowering. As discussed already and underlined by findings from e.g. Sole et al. (2008), the surface elevation on the terminus is surely not controlled entirely by the in-situ surface melt. Thus, the striking similarity including a recent decrease of the surface lowering rate is though to be at least partly coincident, considering the strong topographic control on and dynamic feedback of changes at the front of Eqip Sermia.

6.3.3. Surface Elevation and Velocity

The changes of surface elevation during the 20th century occurred slowly and were of small magnitude after 1950, as far as assessable. This agrees well with a collection of historic velocity information by Lüthi et al. (2016). Accordingly, historic surface flow velocities, always measured during summer, mostly ranged from 2 to 4 metres per day, with slightly higher values in 1948, 1959 and 1971 and lower values in 1912 and 1964 (Lüthi et al. 2016). Therefore, it can be concluded that little changes of the flow velocities correlate with little changes in the surface elevation and extent.

As already presented in figure 56, the recent temporal pattern of the velocity does only partly (negatively) correlate with the temporal pattern of the surface elevation itself. No strong surface elevation rise is observed complementary to the deceleration of Eqip Sermia after 2015.

If the velocity is compared to the surface lowering *rate*, the patterns are very similar (figure 62). The rise and peak of both velocity and lowering rate occur simultaneously, as well as the sudden deceleration and a drop of the lowering rate to 0 metres per year (stabilisation of the surface elevation). Thus, it can be concluded, that a direct link between the surface flow velocity and the surface elevation change rate exists.

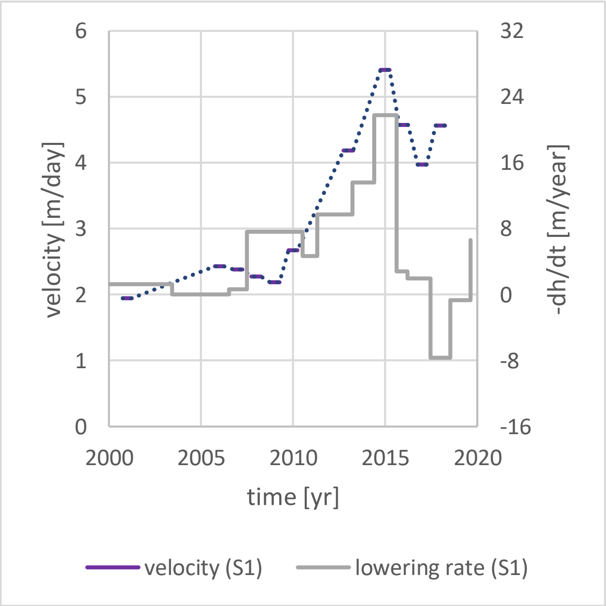

Figure 62: Surface elevation change rate and surface flow velocity from (Joughin et al. 2015) from 2000-2019. The lowering rates are averaged between the timestamps of the EoS DEMs.

Interestingly, the increased velocities observed during winter 2017/18 occur simultaneously (or rather temporally overlapping) with a thickening of sector 1 from 21st August 2017 to 11th July 2018. However, the seasonality of the surface elevation could explain this observation, as the beginning of July is still early summer in the study area and the seasonal surface elevation lowering might not have proceeded much. Also, the disagreement of the curves in the periods 2003-2006 and 2007-2010 is explicable with the low temporal resolution of the underlying dataset. Further, also the quality of the *AsterDEMs* of 2003. 2006 and 2010 might negatively influence the correlation.

6.3.4. Seasonality Pattern

The seasonal pattern of surface elevation change at Eqip Sermia occurs combined with a seasonal front position variation, which is typical for marine-terminating outlet glaciers (e.g. Howat et al. 2010; Moon et al. 2014). Also, seasonal surface elevation changes have been linked to seasonal surface flow velocity variations (Joughin et al. 2012; Bevan et al. 2015). Lüthi et al. (2016) have show seasonal velocity variations at Eqip Sermia, with a speedup of 10 percent at the start of the melting season.

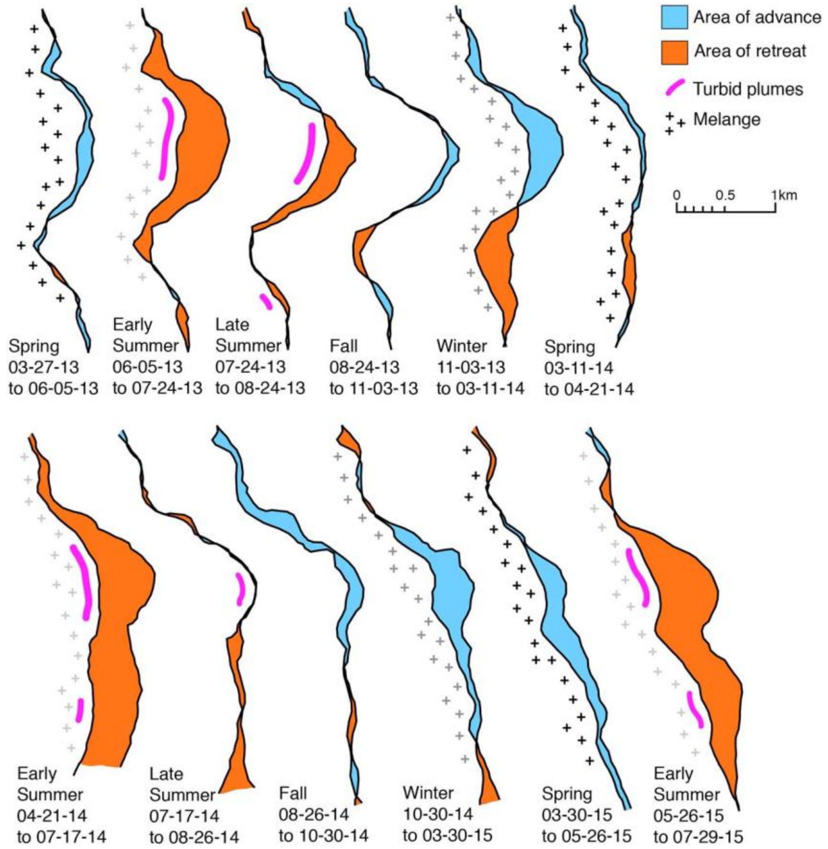

Figure 63: Seasonal front change pattern at Eqip Sermia from spring 2013 until spring 2015. Areas of advance (blue) and retreat (orange) are complemented with the positions of meltwater plumes and presence of ice mélange. Figure from Fried et al. (2018: 1600).

The seasonal length changes of Eqip Sermia are of larger magnitude after the large retreat 2011-2014 in comparison to those before. However, in the current configuration, especially in the years 2013-2016, relatively large embayments were eroded into front during the melt season. According to Fried et al. (2018), the formation of such embayments is linked to submarine melt induced by the meltwater plume and marks a typical pattern occurring at fronts of relatively shallow grounded marine-terminating outlet glaciers (figure 63). The period of the formation and disappearance of large embayments also temporally correlates with the largest seasonal length changes of Eqip Sermia. Further, Fried et al. (2018) identified a correlation of the front position and the presence of ice-mélange. Thus, the seasonal retreat and readvance at Eqip Sermia probably is largely driven by processes at the front rather than the flow velocities.

Kehrl et al. (2017) found that the seasonal velocity changes are related to dynamic feedbacks following seasonal front position changes rather than seasonal meltwater-related lubrication at the glacier bed. Accordingly, the presence of ice-mélange during winter and inhibited meltwater driven submarine melting permit the glacier front to advance and thicken. In spring, the breakup of the sea ice and the onset of the melt season induce the frontal retreat, which in response causes the glacier to accelerate and thin. (Kehrl et al. 2017) Thus, the timing of the seasonal surface elevation change is expected to be slightly shifted to that of the length change, resulting in a seasonal elevation-length-hysteresis. Unfortunately, in this study, a detailed analysis of the timing of the seasonal surface elevation changes is not possible due to limited temporal resolution of elevation datasets.

For Eqip Sermia, a magnitude of the seasonal surface elevation change of 10-15 metres is determined. This number, however, has to be interpreted with care, as the applied method is highly sensitive to the timing of the available elevation data. The values are relatively small in comparison with other (larger) glaciers. For instance, Kehrl et al. (2017) and Joughin et al. (2020) measured seasonal surface elevation changes of several dozen up to 100 metres at *Helheim*- and *Kangerlussuaq*-glacier as well as *Jakobshavn Isbræ*. However, the flow velocities of the glaciers investigated in those studies are much higher than those of Eqip Sermia. The magnitude of seasonal surface elevation change is expected to depend on flow velocities, as this dependency is known for the frontal winter advance (Joughin et al. 2008b; Brough et al. 2019; Kehrl et al. 2017). Further, this gives and additional explanation for the temporal changes of the length variability at Eqip Sermia in the context of recent velocity changes.

6.3.5. Dynamic Retreat

As shown in the previous chapters, Eqip Sermia underwent large changes in the recent past, most pronounced during the last two decades. Notably, the concurrent occurrence of front retreat, ice flow acceleration and thinning is omnipresent. Simultaneous velocity change, surface elevation change and length change is observed both on the long-term (years to decades) as well as inter-annually.

As discussed above, a change of the climatic conditions starting in the 1990s seems to have triggered the following changes at Eqip Sermia. However, the subsequent trigger-reaction cascade is difficult to assess in the scope of this study, as supposed driving mechanisms seem to interfere strongly with each other and observed changes are often overlain both spatially and temporally.

The climate conditions have been warming and thus favouring enhanced surface melt and subglacial meltwater discharge, increasing plume-driven submarine melting and a general warming of ocean temperatures. Also, the onset of the (spatially heterogeneous) front retreat slightly precedes the first notions of surface elevation change. Therefore, it is likely that the dynamic retreat at Eqip Sermia is initiated by changes of the conditions at the front. Temperature increase and frontal retreat are followed by a lowering of the surface elevation that can be observed behind the most affected sectors of the front. Further, during the same period, a distinct acceleration of surface flow velocities is documented.

However, the analysis of the available dataset for the period with the largest change rates of surface elevation, velocity and front position does not allow for a temporal distinction of the observed changes. Nevertheless, the fact that both velocity and surface elevation dramatically changed during the retreat period at Eqip Sermia clearly shows that the retreat was highly dynamic. The strong spatial heterogeneity and temporal intermittency of the front retreat of Eqip Sermia indicates that the bathymetry and subglacial topography are an important control over the retreat dynamics at Eqip Sermia.

6.3.6. Temporal Pattern on Low-Dynamic Margins

The above presented interpretations indicate a strong correlation of flow velocities on the temporal patterns of surface elevation change. In contrast to the high-dynamic centre of Eqip Sermia, the marginal areas are characterised by very low flow velocities. Accordingly, the observed temporal patterns of surface elevation change in these areas are different (see chapter 5.3.6). According to time-lapse imagery (Moreau, personal communication, Lüthi et al. 2016) and literature (Reeh 1991), the accumulation is very small in the study area, and thus largely negligible. Neglecting the flow dynamics too, thus assuming that they do not influence the surface elevation change, it can be expected that the surface elevation change on the investigated margins can be explained solely by the SMB.

Backward modelling of the surface elevation in the low-dynamic margins and a comparison with the observed surface elevation change allows for an assessment of the evolution of the dynamics in the respective areas. Exemplarily for all three low-dynamic margins, figure 64 shows the observed surface

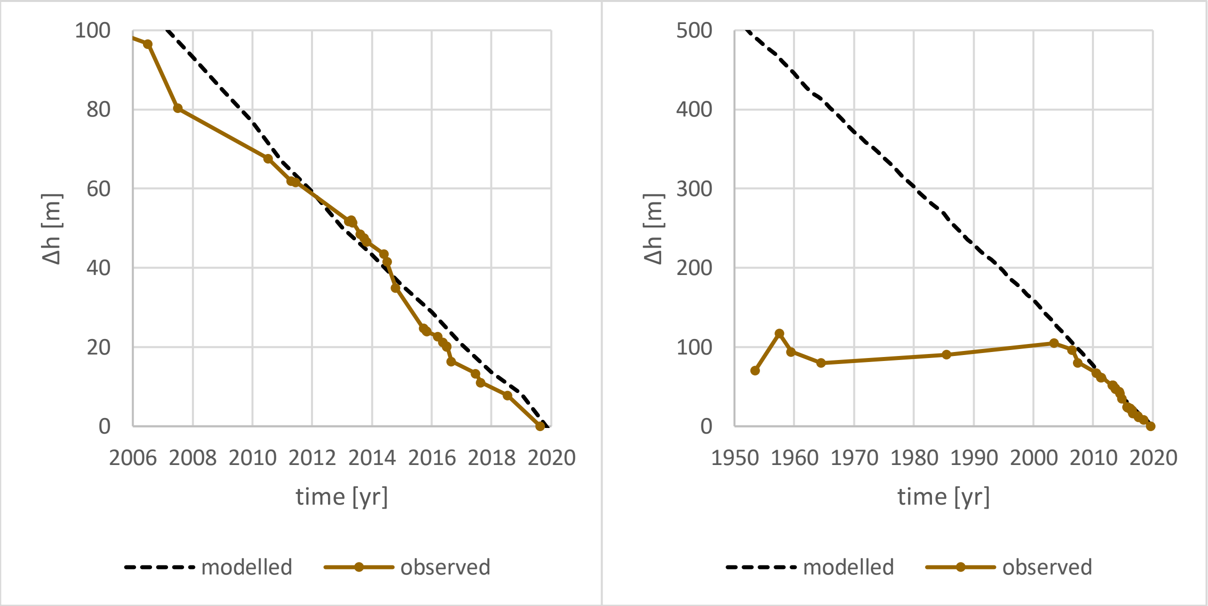

Figure 64: Observed surface lowering and modelled surface evolution based on modelled annual melt rates. Left: 2006-2019; right: 1950-2019. The elevation difference is calculated relative to the surface elevation of DR190820*.*

elevaton and the in-situ modelled surface elevation (according to the model presented in chapter 5.6.1), assuming that the surface elevation is only controlled by surface melt. The modelled surface elevation agrees well with the observations from 2010-2019. The measured surface lowering is steady and nearly linear except for a seasonal pattern (figure 64: left). Going back in time, the two graphs start to deviate before 2010 until they completely diverge in 2003 (figure 64: right). Before 2003, the observed surface elevation at Eqip Sermia seems be controlled by flow dynamics rather than surface melt, as the pattern follows the general surface elevation change of Eqip Sermia. This iresult indicates that around 2003, a drastic change with implications on the dynamics occurred, after which the surface elevation is largely controlled by surface melt.

Two mechanism are thinkable; (1) either the margin was dynamically detached from the fast-flowing centre by the lowering between 2003 to 2010, or (2) the dynamic adjustment of the surface elevation is slow and thus the adjustment following the large lowering in the centre of Eqip Sermia is still ongoing. The first mechanism is supported by the fact that the rate of surface lowering is steady and almost constant, with increased lowering during summer and almost stable surface elevation during winter. However, the modelled melt rates at the other two investigated low-dynamic margins are slightly larger than the observed surface lowering (table 11). Assuming that the modelled values are true, this would indicate (unrealistic) accumulation rates of 1-2 metres per year or ongoing dynamic surface elevation control (through ice-recharge) despite very slow flow velocities.

Table 11: Modelled annual surface melt rates, observed surface elevation change rates and residuals for the low-dynamic margins from 2010-2019. The residual marks the difference between the modelled and the (adjusted) observed values.

area	elevation 20.08.2019 [m]	**modelled** **2010-2019 [m/yr]**	**observed** **2010-2019 [m/yr]**	**adjusted** **2010-2019 [m/yr]**	**residual** **2010-2019 [m/yr]**
right margin, S1	*204*	-7.9	-8.3	-6.75	1.15
left margin, S3	*393*	-6.3	-5.6		0.7
ice-saddle, S2	*348*	-6.6	-4.2		2.4

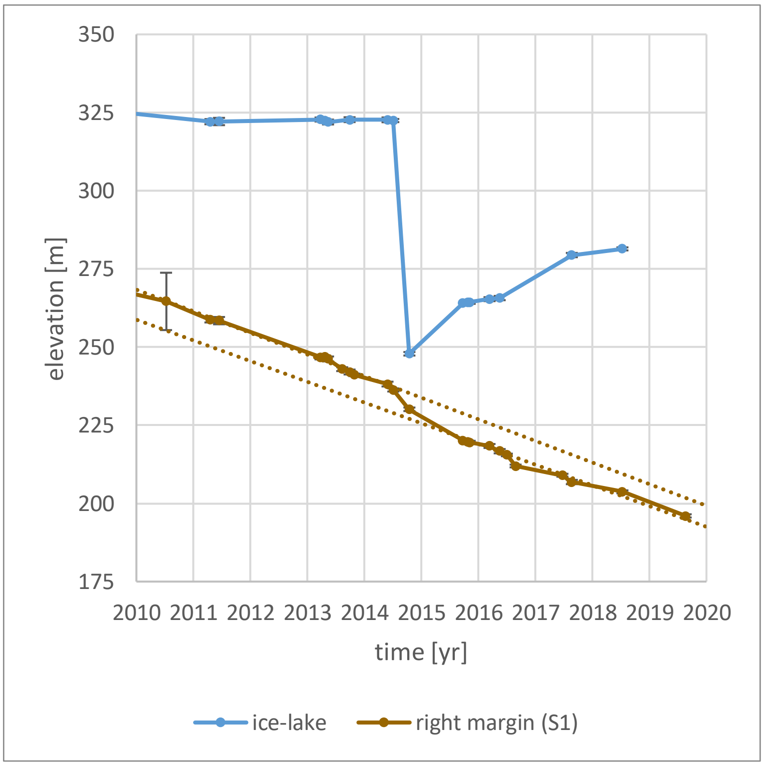

Figure 65: Surface elevation change of the right margin in sector 1 and water level change of the ice-lake. The dotted lines mark the trendlines for the surface elevation change on the margin for the periods 2010-2014 and 2015-2019, respectively.

In contrast, the average surface elevation lowering rate observed at the right margin in sector 1 exceeds the modelled melt rate. However, if assessed in more detail, a *step change* in the otherwise nearly constantly lowering surface elevation is observable (figure 65). This *step change* occurs between July and October 2014 and thus in the same time with the rapid drainage of the ice-lake water level. The observed average change rate between the respective two timestamps yields -22 metres per year. The subsequent interval frames the time from October 2014 to September 2015, with an average change rate of ca. -11 metres per year, which is still clearly larger than the modelled melt during summer 2015 (-6.8 m/yr). Accordingly, it can be assumed that the ice-lake drainage dynamically affected the right margin in sector 1 and that accordingly a dynamic connection between the low-dynamic margin and the high-dynamic centre of Eqip Sermia persists. Neglecting the period from July to October 2014, the rate of surface lowering yields -6.9 (before) and -6.6 metres per year (after), which is again slightly less than the modelled surface melt. The observed step change by itself accounts for approximately 8 metres of surface lowering. The residual differences between the modelled and (adjusted) observed annual surface elevation lowering rates could be attributed to either dynamic ice recharge, winter accumulation or modelling uncertainties. If they only result from ice recharge, the difference is relative to the magnitude of dynamics. Accordingly, the dynamics would be largest at the ice-saddle and smaller on the other two margins, which seems reasonable.

The detailed analysis of the surface elevation change on the low-dynamic margins reveals that the temporal pattern is different from that in the high-dynamic centre of Eqip Sermia. Due to the fact that the lowering rates are almost steady on the margins, they can largely be explained by surface melt.

Accordingly, their behaviour in recent years is similar to the adjacent land-terminating margins of the GrIS (Schudel 2019). Further information is presented in chapter 6.4.3. The identified differences of temporal patterns on the margins and in the high-dynamic centre emphasise the importance of the flow velocity as a main determinant for the surface elevation change at Eqip Sermia.

6.3.7. Temperature Lapse Rate and Melt Rate

The temperature lapse rate (-0.0072°C/m) is determined site specifically for the left margin in sector 3 (Walter 2016). A comparison of the reconstructed temperature series of *AWS-ICE* and *Swiss Camp* resulted in an average JJA temperature lapse rate of -0.104°C/m, which is clearly larger than the lapse rate used for the surface melt calculation on the low-dynamic margins. This indicates that a microclimate influences the measured temperatures at one or both of the monitoring stations. *AWS-ICE* is located on the moraine next to ice margin, whereas the *Swiss Camp* is located in the ice sheet interior. Among other factors, lacking low-albedo surfaces at *Swiss Camp* supposedly result in a cooling effect on the climatic conditions in comparison to *AWS-ICE*, which can explain the negative difference of the measured to the site-specific lapse rate. The conditions between *AWS-ICE* and the investigated ice-margins are probably similar, as they all are both influenced by (cooling) Eqip Sermia and (warming) adjacent land surfaces.

The surface melt rate accounts for the site-specific characteristic ice surface properties such as e.g. albedo, which influence the near-surface energy balance (Walter 2016). The melt rate extrapolation is based on the assumption that the surface properties on all targeted margins are comparable. As no in-situ measurements of the right margin in sector 1 and the ice-saddle are available, no adjustment of the surface-melt rate is made. A visual check on the high-resolution orthomosaic from the drone campaign 11th July 2018 confirms that the brightness in all three areas is roughly identical. Although the albedo is known to vary among the seasons (Banwell et al. 2012), a constant melt rate is assumed.

A comparison of the elevation dependent melt rates with values from literature reveals that the values obtained in this study are realistic, but however, at the larger end of the scale. An analysis by Reeh (1991) yields melt rates of ca. -6 metres per year at sea level for *Paakitsoq* (69.5° N). The values by Machguth et al. (2016) for comparable latitude are even lower (-3 to -4 metres per year at 400 metres a.s.l.). Modelling results from the regional climate model *RACMO* suggest an average melt at Eqip Sermia in an elevation comparable to that of the ice-saddle of -3.5 metres per year from 2010 to 2018 (Noël et al. 2015).

The terminus of Eqip Sermia is located in a valley enclosed by relatively large landmasses including large and steep south-exposed slopes to the north, which can potentially contribute to a warmer microclimate. However, if the melt rates modelled for this study are too large, lower values would result in smaller residuals to the observations. This would result in an even stronger correlation of the surface elevations on the margins with the modelled surface melt.

6.4. Regional Context

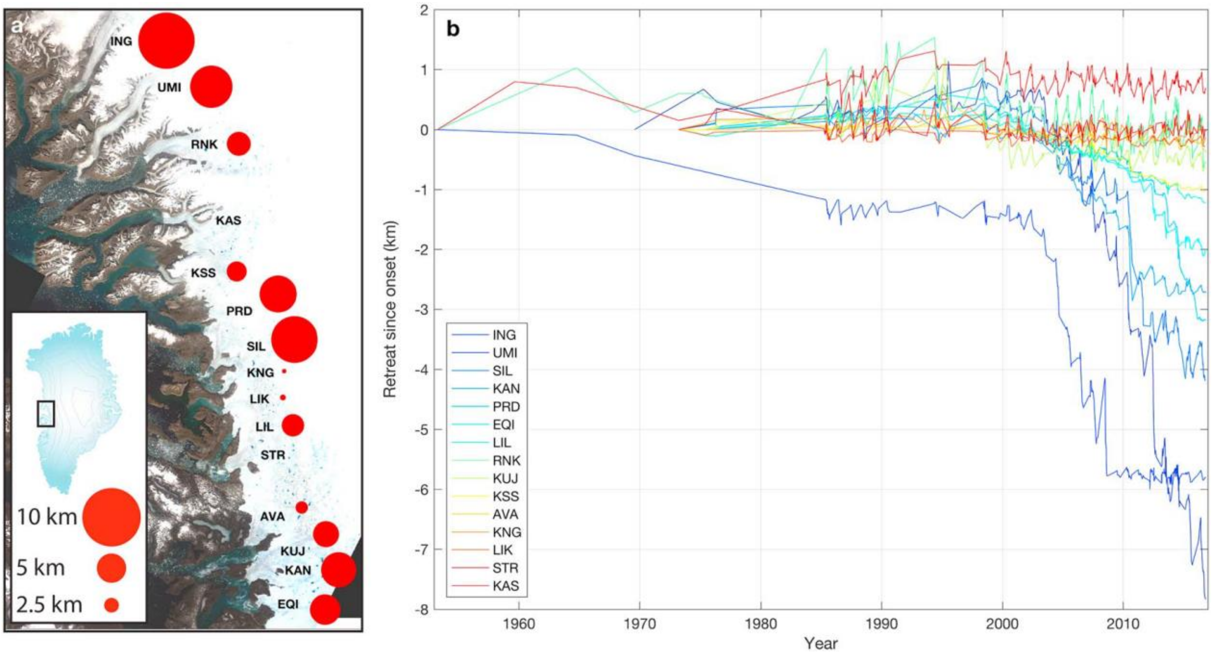

Figure 66: Length changes of different marine-terminating outlet glaciers in central Western Greenland. Ordered by total retreat (right), Eqip Sermia (EQI) is rough average among other glaciers of the region. Figure from Catania et al. (2018: 2026).

The dynamic pattern of acceleration, thinning and retreat at Eqip Sermia at the beginning of the 21st century agrees well with observations from all over Greenland. The increase of flow velocities and inherently mass-flux due to dynamic retreat of marine-terminating outlet glaciers has considerable negative effects on the mass change of the GrIS. (Rignot & Kanagaratnam 2006; Pritchard et al. 2009) Further description of mass loss is presented in chapter 6.4.2. Eqip Sermia stands exemplarily for the general trend of dynamic retreat and mass loss among the marine-terminating outlet glaciers in Western Greenland. Recent studies assessing the entire region show that length changes (Catania et al. 2018, figure 66) and mass loss (Felikson et al. 2017, figure 67) at Eqip Sermia (EQI) are comparable in magnitude to other marine-terminating outlet glaciers in the area.

However, dynamic mass loss and length changes show high variability even within regions, which indicates that glacier-specific factors are important controls on the sensitivity of marine-terminating outlet glaciers (Moon et al. 2012, Catania et al. 2018). While after drastic retreat Eqip Sermia has stabilised recently, e.g. neighbouring *Kangilerngata Sermia* (KAN) has retreated into a deeper section of the fjord and is expected to continue retreating rapidly during the coming years (Kane et al. 2016). *Store Glacier* (STR) on the other hand shows a significant mass gain from 1985 to 2016 (Felikson et al. 2017), while its front is stabilised by a sill (Morlighem et al. 2016). Further, Khazendar et al. (2019) showed that *Jakobshavn Isbræ* (JAK) started to decelerate and thicken again (in response to regionally cooling ocean temperatures) in 2016 after two decades of continuous retreat. However, according to Felikson et al. (2017), among all variability, numerous glaciers have experienced mass loss through dynamic retreat during the past decades.

6.4.1. Dynamic Retreat and Morphologic Control

Dynamic retreat includes thinning and acceleration as a dynamic reaction of the glacier to loss of backstress at the front. In order to rebuild force balance after a front geometry change, the glacier accelerates, which leads to the formation of lateral and longitudinal stress gradients. Inherently, the longitudinal stretching is causing a lowering of the surface elevation. Thinning can induce acceleration and increased calving and thus retreat due to a reduction of the effective pressure at the glacier bed. (Howat et al. 2005)

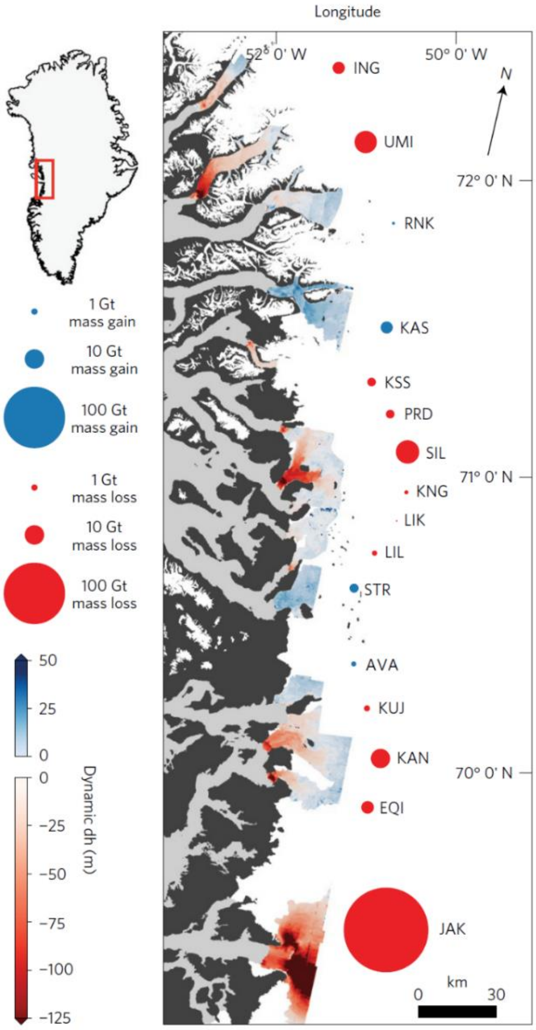

Figure 67: Dynamic surface elevation change and mass loss of different marine-terminating outlet glaciers in central Western Greenland. By dynamic mass loss, Eqip Sermia (EQI) is rough average among other glaciers of the region. Note the large variability of mass loss within the same region. Figure from Felikson et al. (2017: 367).

In certain environments including deepening bedrock further inland, the theoretically self-sustaining cycle of dynamic retreat leads to very large frontal retreat rates (e.g. Catania et al. 2018, Hill et al. 2018). The front of Eqip Sermia showed typical patterns of dynamic retreat before 2014 and most prominently between 2011 and 2014, when the protruding front, its tip located on a shallow zone in the fjord, suddenly retreated through a minor overdeepening (Lüthi et al. 2016; Morlighem et al. 2017). However, the current situation at Eqip Sermia is slightly different. The average depth of the grounding line at Eqip Sermia is only 25 metres below sea level (Catania et al. 2018). When the front of Eqip Sermia retreated onto prograde slope again (at the approximate current front position), the dynamic retreat of was stopped. On bedrock with prograde slope, a further retreat increases the effective pressure at the bed due to decreasing water depth, which results in a negative feedback. Further, after front geometry adjustment, the surface elevation stabilised and the glacier decelerated. A similar behaviour on slightly larger scale showed e.g. *Umiamiko Isbræ* (UMI) which retreated rapidly through an overdeepening from 2004-2009, until the front reached prograde slope again (Catania et al. 2018). The glacier front retreated 4 kilometres within 6 years and a temporary speedup by factor 2.5 was recorded (Catania et al. 2018).

The strong morphologic control at Eqip Sermia thus is not a unique. However, the fact that the front of Eqip Sermia has been located in relatively shallow water for more than 100 years by now is extraordinary and explains the relatively few and small front position changes during the investigated period. By its own measures, the rapid changes of Eqip Sermia at the onset of the 21st century are unprecedented in record history. Currently, the front position of Eqip Sermia seems to be relatively stable. However, in case of further retreat in the future, this would change dramatically, as the bedrock beyond the front of Eqip Sermia is strongly overdeepened many kilometres inland (Morlighem et al. 2017).

6.4.2. Mass Loss & Sea-Level Rise

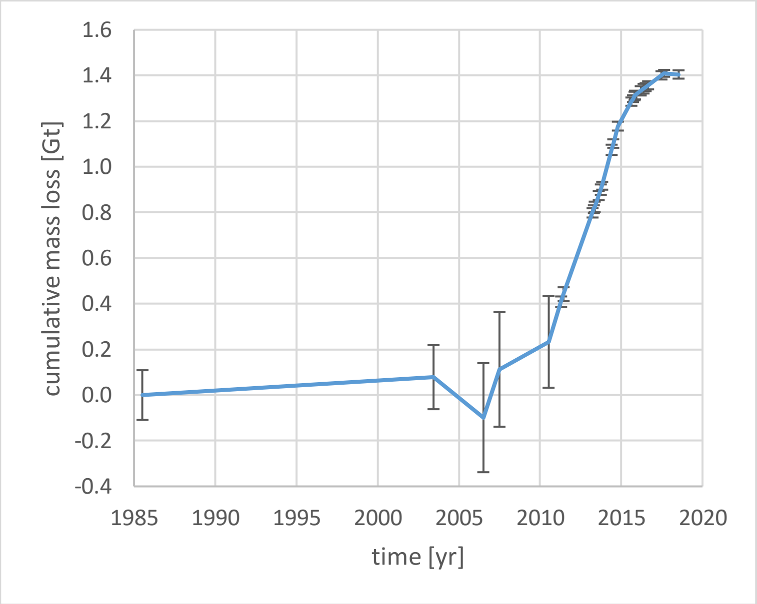

Figure 68: Cumulative mass loss in Gt of Eqip Sermia in sectors 1, 2 and 3 from 1985 to 2018. Note that therefore these numbers do not include the loss of ice in the area, where Eqip Sermia retreated.

An assessment of the cumulative mass change at Eqip Sermia shows that the surface lowering related mass loss in the sectors 1-3 of the terminus, excluding the margins, yields 1.41 Gt (SMB and dynamic loss combined) from 1985 to 2017 (figure 68). The mass loss related to surface lowering in sectors 1-3 is substantially dynamic, as the (modelled) surface melt rate on the terminus only increased by ca. -0.8 metres per year from the stable period (1912-2003) to 2004-2019 (table 10). Accordingly, the recent change of the SMB accounts for 10-15 metres on the terminus from 2004-2019, whereas the total surface lowering in the same area and period was ca. 60 metres (figure 37). Thus, dynamic mass loss accounts for ca. 80 percent of the total mass loss in sectors 1-3 of Eqip Sermia between 1985 and 2017. In 2014, the portion of dynamic mass peaked at ca. 95 percent when (at an elevation of 300 metres) the surface melt rate was modelled to exceed the long term stable trend of 1912-2003 by 0.53 metres while the observed surface lowering rate was larger than 12 metres per year (from October 2013 to October 2014). From October 2014 to November 2015, according to the deviation of the modelled surface melt from the long-term stable trend, the surface elevation should have increased by 0.46 metres, while a surface elevation lowering rate of 5.9 metres per year was observed. These numbers show that the portion of dynamic surface elevation change is not long-term stable and can show strong inter-annual variability, or in other words, that the SMB is negligible on short-term time scales.

The total mass loss of Eqip Sermia through dynamic thinning has been estimated to 4.15 Gt from 1985 to 2016 (Felikson et al. 2017). Of course, a large part of this number is caused by the loss of a considerable section of the terminus, which explains the large discrepancy to the numbers presented above.

The total mass loss at Eqip Sermia is relatively small compared to the largest glaciers of Greenland inherently also the GrIS. However, the dimensions of the GrIS and the magnitude and pace of ongoing changes result in a significant contribution of the ongoing changes in Greenland to global sea level rise (e.g. Shepherd et al. 2020). Felikson et al. (2017) show that the dynamic mass loss of *Jakobshavn Isbræ* between 1985 and 2016 exceeded 100 Gt (equal to ca. 3 Gt/yr). On the large scale, between 1992 and 2018, the GrIS lost almost 4000 Gt of ice, where melt driven mass loss and dynamic mass loss each account for ca. 50 percent. Thus, Eqip Sermia is above average, with a higher dynamic mass loss contribution in percentage. This may be partly explicable by the highly dynamic retreat between 2011 and 2014 and the installation of a new geometry (incl. high front), which favours persistent dynamic speedup.

A recent assessment by Shepherd et al. (2020) shows that in 2011 the annual mass loss of the GrIS yielded 345 Gt, which was the maximum during the recent episode of climate warming and contributed ca. 1mm to global sea level rise. Between 2013 and 2017, the values lowered to an annual mean 220 Gt. The values have lowered in response to large-scale shifts of climatic conditions (namely the North Atlantic Oscillation). The total contribution to sea level rise of the GrIS from 1992 to 2018 yields ca. 11 millimetres. (Shepherd et al. 2020) According to the IPCC of 2013, the GrIS related sea level rise contribution by the end of the century will be 7-13cm, as the currently measured values follow the high-end scenario (Church et al. 2013; Shepherd et al. 2020).

6.4.3. Land-Terminating GrIS Margins

The findings of this study show that the surface elevation changes at Eqip Sermia are largely different from respective results on low-dynamic ice bodies such as the land-terminating GrIS margins. This is in agreement with results from a study by Sole et al. (2008), according to which the thinning on marine-terminating outlet glaciers is resulting from a change of a control mechanism. They further stated that at the same time the increased surface lowering on land-terminating ice margins are fully explainable by deviations of ablation rates from the long-term average. Further, Schudel (2019) investigated surface elevation changes at the land-terminating ice margin *Nunap Kigdlinga*, adjacent to Eqip Sermia, in detail. He concluded that surface elevation changes are largely reproducible through temperature-based backward modelling of the SMB, which is not the case for high-dynamic Eqip Sermia.

Interestingly, also the recent surface elevation changes on the low-dynamic margins of Eqip Sermia are largely explainable by surface melt. As the study area of Schudel (2019) is characterised by very low surface flow velocities in the range of 15-20 metres per year, this is a clear indication that the flow velocities are a very important control of surface elevation change in the fast-flowing centre of Eqip Sermia.

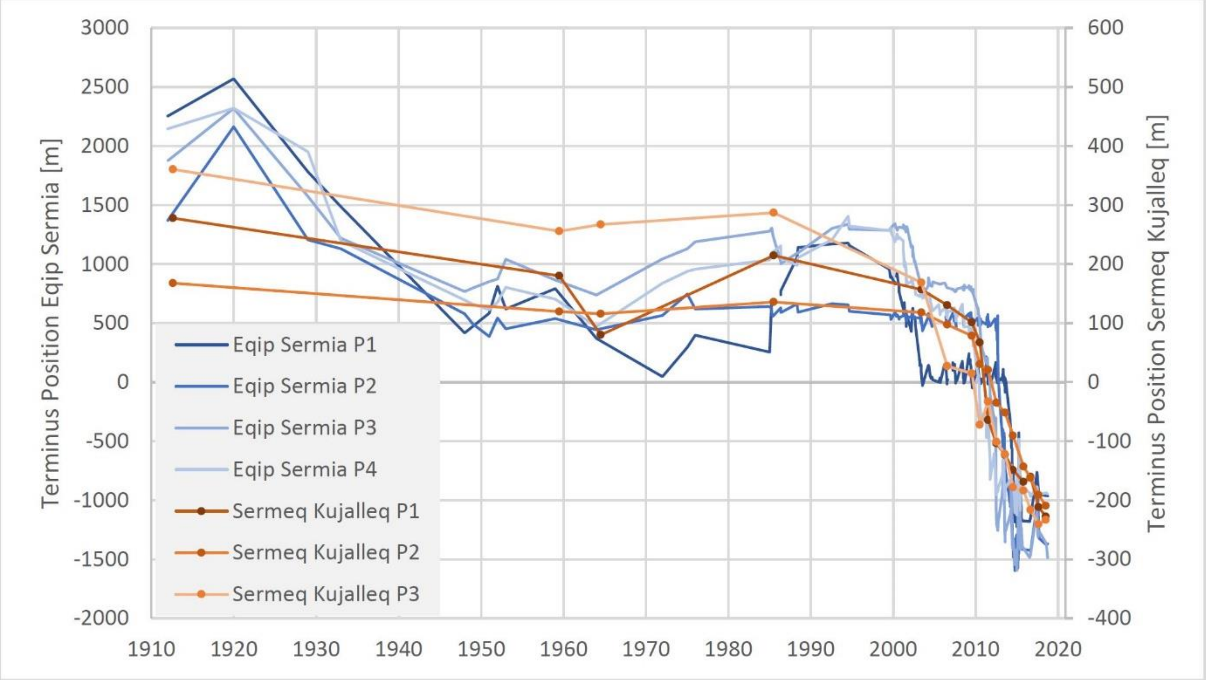

Figure 69: Length change at Eqip Sermia (Lüthi et al. 2016) and Sermeq Kujalleq (Schudel 2019). Sermeq Kujalleq is located few kilometres south of Eqip Sermia and its glacier lobe is land-terminating. Figure from Schudel (2019: 90).

Further, Schudel (2019) showed that the length change of the lobe of the land-terminating outlet glacier *Sermeq Kujalleq*, also adjacent to Eqip Sermia, is largely synchronous to that of Eqip Sermia (figure 69). Noteworthy are the different magnitudes, which are 5x larger at Eqip Sermia. Qualitatively, this result is comparable with the comparison of the cumulative PD and the surface elevation change at

Eqip Sermia (figure 60), as the length of Eqip Sermia correlates with the surface elevation and the surface elevation of *Nunap Kigdlinga* is controlled by the atmospheric conditions (i.e. SMB).

The main differences between the surface evolution at high-dynamic Eqip Sermia and *Nunap Kigdlinga/Sermeq Kujalleq* are the two following: (1) Eqip Sermia shows phases of increasing surface elevation on the long-term and short-term time scale whereas the surface lowering at the low dynamic margins is mostly steady, and (2) the magnitude of surface elevation changes (and length changes) at Eqip Sermia is generally larger, only with similar values at the tip of *Sermeq Kujalleq*.

6.4.4. Drainage of Marginal Ice-Lake

As already mentioned, the ice-lake located to the north of the terminus of Eqip Sermia has drained within very short time. This incident is a good example to show what further implications can come with surface lowering of glaciers.

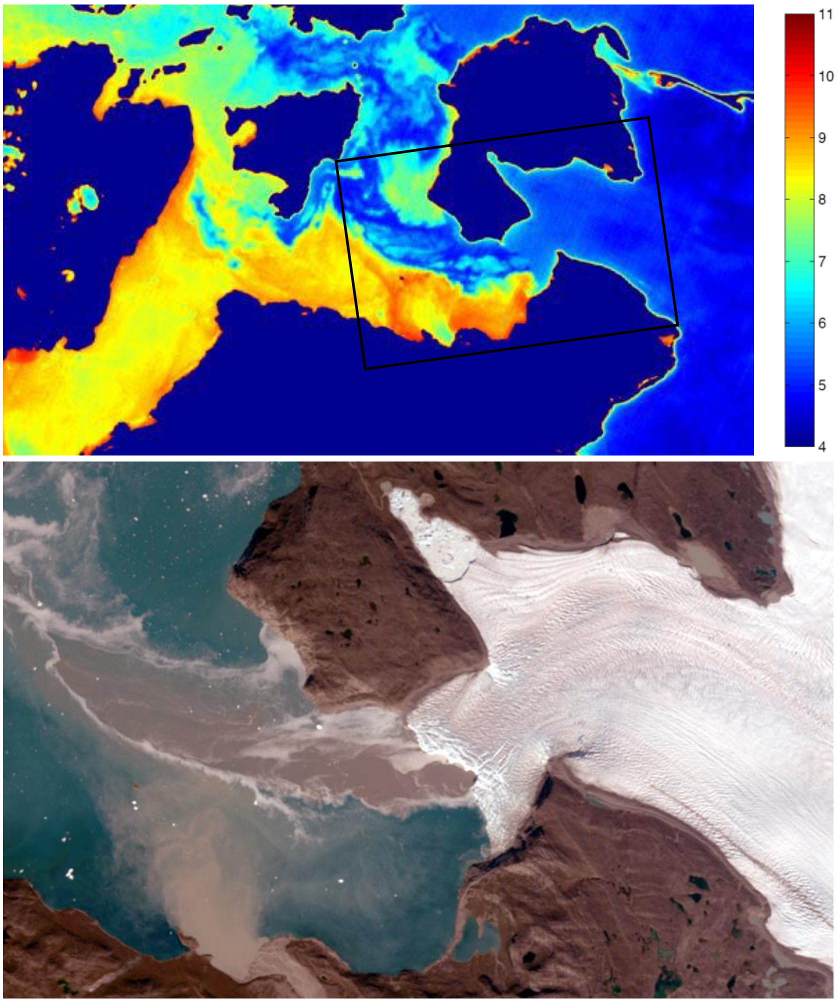

Figure 70: Comparison of (top) ocean surface temperatures and (bottom) optical satellite imagery. Both scenes are dated to 11th August 2014. The black rectangle in the upper image indicates the extent of the RGB image. Figure adapted from Vieli et al. (2018, POLAR2018).

On the long-term, the ice-lake drainage was triggered by the continuous thinning and related mass loss of the damming Eqip Sermia. Further, Vieli et al. (2018) found an extraordinary precipitation event occurring in the area from 9.-11. August 2014 to be a possible additional short-term trigger of the lake drainage. Satellite measurements of the sea surface temperature in the fjord suggest that the extensive plume, that formed during the lake drainage event, was the driver of a pronounced rise of sea surface temperature in the southern part of the fjord through turbulent advection (figure 70) (Vieli et al. 2018). The effects of this warm-water advance might have had further implications on the submarine melt at the front of Eqip Sermia. However, the short-term changes on the terminus and at the front are not assessable in the scope of this study, as the temporal resolution of the elevation (and velocity) data is insufficient.

Based on a comparison of *AD140704* and *AD141015*, the drainage volume of the ice-lake is estimated to ca. 80 mio. m^3 (which is roughly comparable to the volume of *Sihlsee* in Switzerland). If the ice-lake drained completely within ca. 2 days, resulting in a 2-day average discharge was 460 m^3/s. If such an event would affect inhabited areas, the resulting consequences are potentially catastrophic. On the small scale, the rerouting of the outlet of the ice-lake and subsequent lowering of the water level caused the former creek to the north to dry out, what affects the local ecosystem.

Subsequent to the rapid drainage, the stepwise (seasonal) water-level rise indicates that the subglacial outlet has been closed shortly after the event. By October 2015, the lake-volume increased again by 9 mio. m^3 and in August 2017, the lake volume was already ca. 20 mio. m^3 larger than in October 2014. Thus, if the subglacial drainage remains closed, within roughly 10 years after the drainage (ca. 2024), the lake volume will reach its former water level. However, if the surface elevation in the damming ice-saddle area continues to lower, the next catastrophic lake-drainage event is due even before. Then again, a sudden intermediate lowering of the increase rate of the water level before the lake is refilled completely would hint at the reactivation of a subglacial discharge.

6.5. Uncertainties, Challenges and Limitations

6.5.1. DEM Acquisition Methods

All DEMs used in this study are derived from optical imagery, with elevation extraction based on photogrammetry. The *GimpDEM* additionally includes laser altimetry derived elevation information, as it is georeferenced to *ICEsat* data. The different DEMs are derived from drone imagery (drone DEMs 2016-2019), aerial imagery from manned reconnaissance flights (SFM DEMs 1953-1964 and *AeroDEM*) and satellite imagery (*ArcticDEMs*, *GimpDEM* and *AsterDEMs*). In general, the spatial resolution of the DEMs decreases with increasing elevation of the data acquisition. The *ArcticDEMs* are an exception as these DEMs are derived from (commercial) ultra-high resolution optical imagery. The AsterDEMs are derived from stereo-pairs of images with a resolution of 15 metres, which is a possible explanation for their relatively large uncertainties in comparison to the other satellite DEMs.

All DEMs except for the *GimpDEM* are snapshots with a single-day timestamp. The *GimpDEM* on the other hand is a composite of data from 2003 to 2009 with a nominal timestamp of 2007, which is a potential source of uncertainty. However, the *GimpDEM* has been identified to agree well with a CReSIS surface elevation profile of 2008 (see figure 77, appendix I.) and thus the uncertainty of the assigned timestamp is small.

6.5.2. Spatial Resolution

In many cases, it is advantageous to have elevation data of very high spatial resolution. In case of surface elevation change analysis at Eqip Sermia, the surface roughness is very large due to crevasses and séracs. If high-resolution DEMs are directly compared, this causes a lot of noise which complicates the interpretation. However, the high-resolution DEMs allow for a very accurate co-registration. Nevertheless, it can be stated that for surface elevation change of magnitudes like on the terminus of Eqip Sermia, the spatial resolution of the (newer) datasets imposes no limitations.

The issue of different original resolution ranging from 0.17 to 30 metres is assessed by interpolation-free aggregation of all DEMs to the same resolution before comparing. Downscaling after the co-registration was tied to snap grids in order to prevent the introduction of elevation biases. Further surface smoothing resulted in the point time series to represent the average elevation of the original resolution DEM in an area of 150x150 metres (figure 71). However, this method at least preserves if not increases the vertical accuracy of the original data.

Thus, after adjusting the spatial resolution, the only difference with effect on the comparability of DEMs with different acquisition methods is the elevation accuracy.

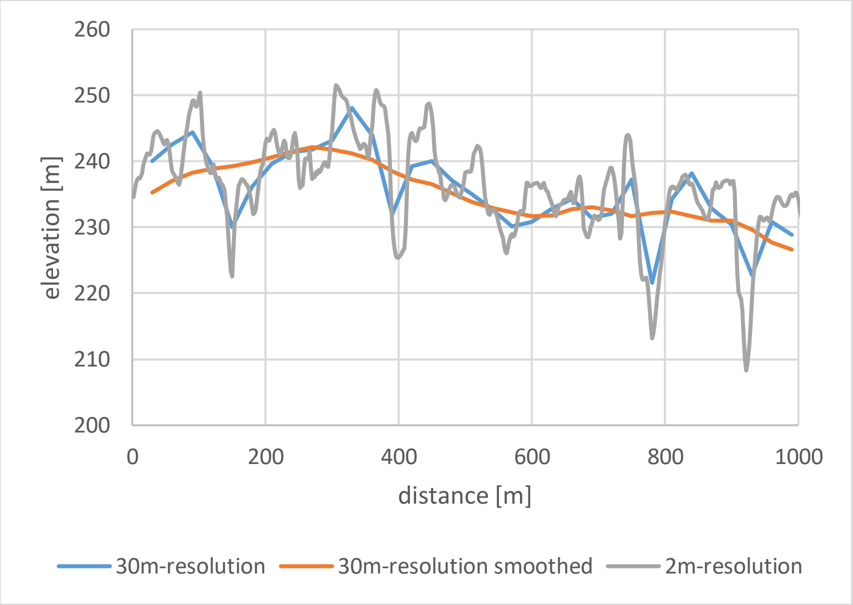

Figure 71: Comparison of surface structure of DEMs with (no or) different post-processing before analysis. The upscaling was done by aggregation with assigning the mean of the parent cells to the aggregated cell. The smoothing was done by applying a 5x5 (=150x150m) filter, assigning the focal mean of the neighbourhood to the target cell. The values were extracted from a straight profile with 1km length across a heavily crevassed section of sector 1 in DR180711*.*

6.5.3. Vertical Accuracy

The vertical accuracy strongly varies with the underlying data acquisition method. While the drone DEMs, the *Arctic DEMs*, the *AeroDEM* and the *GimpDEM* are relatively accurate, the SFM DEMs and also the *AsterDEMs* include major quality issues. With the magnitudes of change at Eqip Sermia, the vertical accuracy of the newer DEMs (i.e. drone DEMs and *ArcticDEMs*) not limiting the surface elevation change analysis.

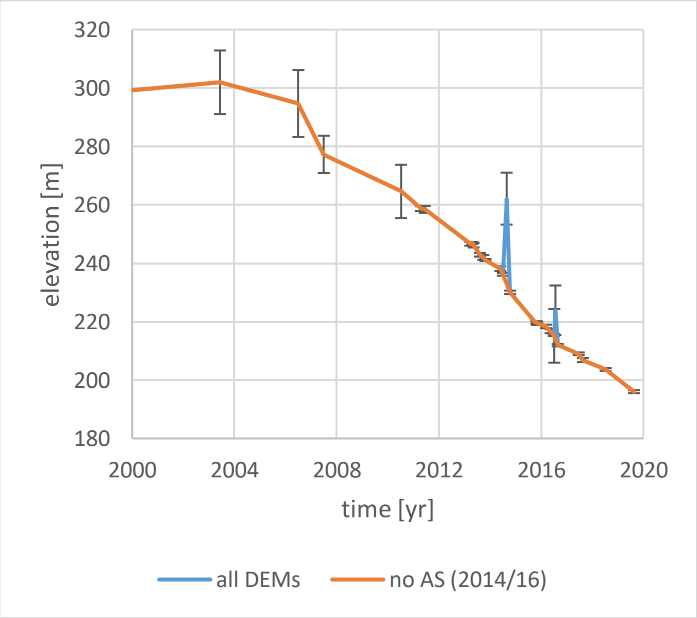

Figure 72: Profile with and without AsterDEM *snapshots from 2014 and 2016. Note that especially for* AS140826 *the deviance of the value from the surface evolution trend is much larger than the given uncertainty range of the DEM.*

However, even after co-registration, the *AsterDEMs* show considerable quality issues on ice-surfaces and the elevation values often deviate strongly from those with comparable timestamp. This becomes most apparent with point time series. Figure 72 shows that the deviation of *AS140826* from the expected trend is clearly larger than the uncertainty and therefore, the value of the *AsterDEM* is classified *unrealistic*. Thus, *AsterDEMs* are only considered during periods where no other high quality DEMs are available (2003, 2006 and 2010). Still, the generally increased uncertainty has to be considered when interpreting results including information from these *AsterDEMs*.

The SFM DEMs are subject to very high vertical errors, including elevation dependent bias and artefacts on glacier- and land surfaces. Among the SFM DEMs, 1953 is by far the best. Thus, information derived from elevation information of the respective DEMs have to be interpreted with care. The SFM DEM of 1959 even shows signs of an elevation dependent bias. However, further assessment is considered out of scope.

Additionally, the historic maps which have been used for the extraction of elevation information are including relatively large uncertainties. They potentially arise from the decision on reference points used for topographic measurements, which include small horizontal and vertical angles. Accordingly, the elevation point included in the surface profile figures rather serve as orientation than as basis for robust interpretations. Additionally, the elevation information of historic maps is measured relative to sea level, which was accounted for with a standard elevation correction by the difference of the geoid to the WGS 84 ellipsoid.

6.5.4. DEM Coverage

The collection of DEMs used in this study in general shows quite good coverage in the terminus area. However, more than ca. 5 kilometres from the front, the number of DEMs with coverage decreases drastically. Only the *AeroDEM* and the *GimpDEM* as well as few *ArcticDEMs* (and the low-quality *AsterDEMs* of 2014/16) fulfil the criteria of sufficient stable terrain necessary for co-registration and at the same time cover larger areas further upstream. Thus, especially the assessment of the upstream propagation of elevation change signals, both on the seasonal and on the long-term trend is strongly limited by coverage.

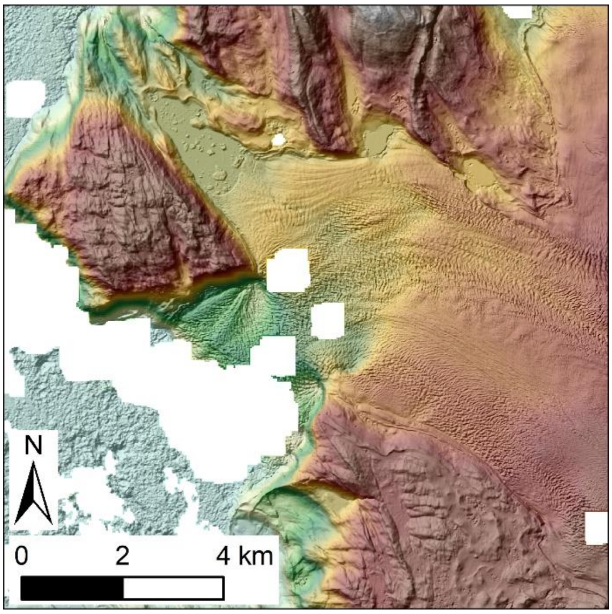

Figure 73: Example of reduced coverage of AD140704 *(coloured DEM and transparent corresponding hillshade) in the lower sectors of the study area. With data from Porter et al. (2018).*

However, the coverage was not only an issue further upstream. Several DEMs also include voids or artefacts in sectors 1-3 (figure 73). These voids are not only important locally but also limit the analysis of sector-averaged surface elevation change. Apart from the voids, the coverage extent of the drone DEMs from 2016, 2017 and 2019 was limited to sector 1. Also the drone DEM of 2019 only covers the lowest 5 kilometres of Eqip Sermia.

The limited spatial coverage of the drone DEMs artificially increases the relative importance of *AD170821*, which should be considered when interpreting respective results. However, this is lesser of an issue, as this snapshot is of high quality.

6.5.5. DEM Timestamps and Comparability

When DEMs with coverage of highly dynamic areas with seasonal surface elevation change patters such as the terminus of Eqip Sermia are compared, it is always important to consider the exact timestamps of the snapshots. Otherwise, observed differences be misinterpreted. Exemplarily, the difference between *AD170821* and *DR180711* is probably affected by seasonality, as the time between 11th July and 21st August is typically characterised by seasonal surface elevation lowering. However, due to the remaining high uncertainties of the timing and magnitude of the seasonal surface elevation oscillation, no correction is possible, to assess such timestamp-related bias.

6.5.6. Temporal Resolution of the Elevation Data

One major limitation of this study is the temporal resolution of the available elevation information, as Eqip Sermia is characterised by high dynamics. Therefore, some processes could only be analysed by a comparison of the states before and after. For example, the lake-drainage event occurring from 10th and 11th August 2014 is mainly assessed with two *ArcticDEMs* from July and October 2014. This temporal resolution does not allow to distinguish between lake-drainage related and other surface elevation changes on the terminus of Eqip Sermia.

The most DEMs per year are available for 2013. However, in 2013, three DEMs show the state of the glacier terminus in spring (March, April and May) and 3 DEMs in autumn (August, September, October). In that year (as in most years), the largest changes occurred at and shortly after the onset of the melting season, which is typically June/July. Even if a DEM with a timestamp during the dynamic period of summer surface lowering is available (e.g. *AD140704*), it is not clear, which processes are going right then, as the DEM only represents a single short moment. Thus, seasonality patterns of changes at the front and in surface elevation are detectable, but not assessable in detail.

Also, an investigation of the dynamic interdependency of processes such as front changes and elevation changes requires very high temporal resolution. Even with the new *ArcticDEM* strips providing high-resolution DEMs every 1-3 months during summer, the temporal resolution remains a limitation of this study. It can be detected that velocity changes and surface elevation changes are occurring simultaneously, but *simultaneously* in this chase means *within the same period*, and thus it remains unclear, which process is followed by which. On the other hand, the ultra-high temporal resolution of drone DEMs is of no use for an analysis of seasonal or long-term elevation change investigation and thus only one DEM per campaign was considered for analysis in this study. Therefore, the collection of DEMs for analysis only included two DEMs for 2017 (1x AD, 1x DR) and one each for 2018 and 2019.

Further, it should be considered that, on the long-term, limitations of the temporal resolution of the DEM availability artificially increase the relative importance of the *SFM530703*, *AE850709* and *AS030609* in figures and interpretations. Thus, the issues observed with the quality of other *AsterDEMs* require a careful interpretation of statements regarding the *AsterDEM* of 2003.

6.5.7. Processing of Drone Imagery

The processing of the drone image series in the photogrammetric software *Pix4Dmapper* was relatively easy. The quality of the input data was perfect as the underlying data acquisition method was designed specifically for this purpose. A large amount of high-resolution images with 80 percent overlapping in both directions and available GPS positions of the images have resulted in very good output quality without further effort. In comparison to other study sites, where low-contrast surfaces can result in dome-/bowl-effects (e.g. Schudel 2019), the heavily crevassed terminus of Eqip Sermia seems to be favourable for DEM generation. However, some artefacts resulted to lower the quality of the orthomosaic and DEM at the calving front of Eqip Sermia (figure 74). These artefacts probably result from a

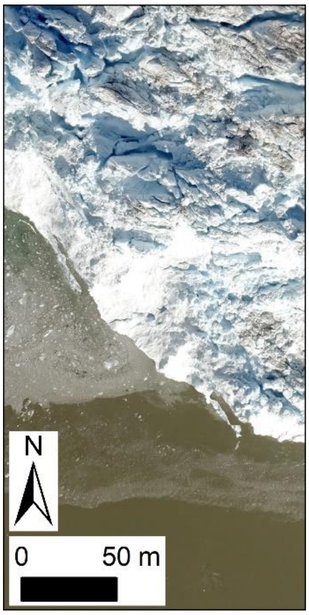

Figure 74: Section of the front of the orthomosaic corresponding to DR190820 *with artefacts.*

combination of very low contrast in the area of the upwelling meltwater plume, from relatively large motion of floating ice at the front (during a 25-minute back-and-forth flight) and from changing geometry through calving during the time of image acquisition. Nevertheless, except from little uncertainties when mapping the front from the resulting orthomosaics, these artefacts did not further influence the quality of the results, as no specific assessment of the front geometry was made in the scope of this study.

Artefacts along the calving front in the generated orthomosaic could be omitted or reduces by unchecking *transparent* in the mosaicking settings. Also, all marine surfaces in the drone images could be masked manually in the *Pix4Dmapper*, which would leave the respective pixels in the images disregarded for the further processing. However, in *Pix4Dmapper*, this is quite unhandy and thus time consuming, considering that several hundred images partly cover sea surface.

6.5.8. Processing of Historic Aerial Imagery

The processing of the historic aerial image series in Agisoft was a big effort due to several issues. On one hand, many images had artefacts, which had to be masked by hand before the start of the processing. Futher, varying extent of the aerial image sequences and the quality of the images required the selection of specific GCPs for each SfM project, as not all GCPs were identifyable in all projects. The manual marking of the GCPs was often challenging because of the dfifferent contrast and resolution of the *master orthomosaic* (*AeroDEM*) and the aerial images (figure 75). In several areas, mostly with steeper terrain, either one or both of the images showed contortions. The production of the *AeroDEM* orthomosaic itself was obviosly also suffering from its own difficulties, which may have translated into the final SFM DEMs.

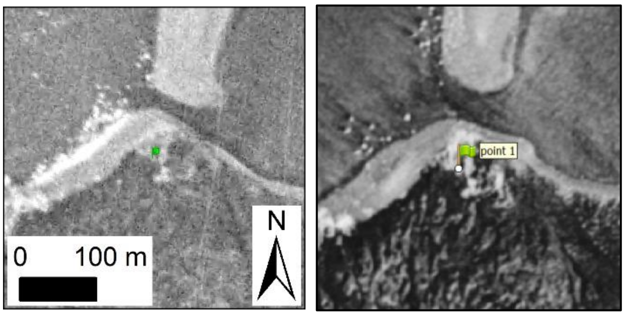

Figure 75: Manual tagging of GCPs in the SfM processing. Left: orthomosaic corresponding to the AeroDEM*; right: orthoimage from the aerial campaign of 1953.*

The aerial images of 1953 resulted in the SFM DEM with the highest quality despite little available photographs and very poor overlapping of 2-3 images (figure 76). On the other hand, the image series from 1957 consists of a relatively large number of photographs, which at first seemes promising. However, the little coverage of stable terrain and partly bad contrast on the glacier surface resulted in major quality issues of the resulting DEM. Further improvements were acquired through adding additional GCPs taken from a preliminary georeferenced single images in *ArcMap*, in order to fix the position of the glacier front at sea level. Nevertheless, the resulting DEM is practically disposable. The SFM DEM of 1959 resulted in an elevation dependent bias, which was not further assessed, and also

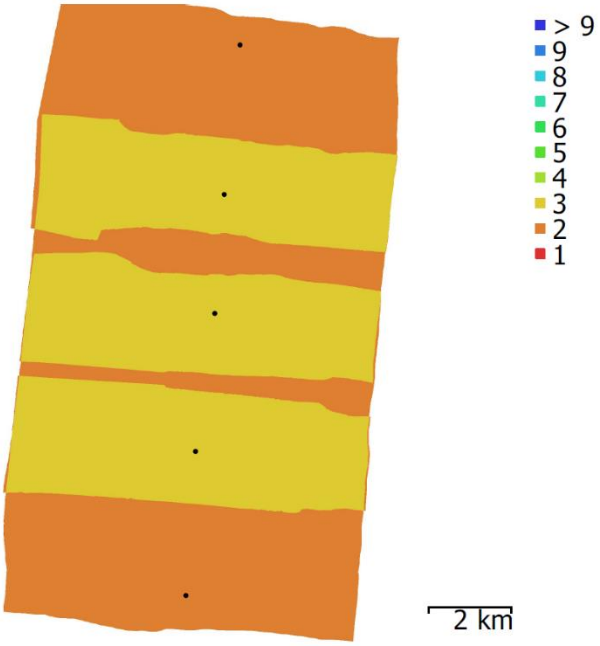

Figure 76: Poor overlapping of 2-3 aerial images for the SfM project SFM530712*. Nevertheless, the output DEM was better than that of the other historic SfM projects.*

the SFM DEM of 1964 includes uncertainties which are location-dependent despite a trial-and-error testing of multiple different GCP configurations.

It can be concluded that SfM technologies are great tools to extract elevation information of historic data. However, the capabilities of the software are limited, and those limits were reached in at least 2 of the SfM projects realised for this study. Refined processing of the DEMs of 1953 and an assessment of the elevation depenednt bias possibly allow further improvements, but were, howver, out of scope for this study. If the DEMs did not show satisiyable quality, at least the resulting orthomosaics could eventually be used for the mapping of the termini.

6.5.9. Placing of Analysis Profiles and Points

The placing of the along- and across-profiles and accordingly the analysis points used for the point time series is somewhat arbitrary. As stated already, the along-profiles are oriented along the flow lines of Eqip Sermia. In a study by Lüthi et al. (2016), four profiles were used to assess the length changes. However, for the purpose of this study it was considered to be important to place at least one profile on the central flow line, to be able to investigate the changes in the most dynamic area of Eqip Sermia. The, the along-profiles were also used to measure the temporal evolution of the front length. For this purpose, it was important, that the central flow line cut through the protruding location of the front in 2012. Whether the central flow line is naturally going through this location is unclear.

The only criteria for the positioning of the other along-profiles is the roughly equal distance to the left and right at the front. As the centre and left profiles converge in sector 2, the distance is not equal anymore. This could result in an additional bias of elevation change detection for all values that are averaged among all three analysis points in sector 2 in comparison to the average values of sector 1 and 3, where the distribution is more equal. As the elevation changes are controlled by the flow velocities (which are getting slower towards the margins), the exact location of the profile and analysis points might influence the results. The uncertainties introduced with the assessment of elevation change in point locations are reduced again by the calculation of 150x150 metre average values per grid cell, before extracting the point elevation values.

Further, the positioning of the across profiles is based on two criteria; (1) the natural structuring of the surface topography of Eqip Sermia should be represented and (2) the intersections with the along-profiles should be located in relatively *unspectacular* locations, as they are used for the extraction of point time series that should be representative for larger areas. For the across-profile and the according analysis points in sector 1, this included, that they should be located as close to the front as possible without being directly affected by the crumbling and disintegration of the ice body of Eqip Sermia in the front. However, as they are placed *on the limit*, a direct influence of the front itself on the observed surface elevation changes is still possible.

6.5.10. Qualitative Approach

This study is mainly focusing on a qualitative analysis of the surface elevation change and related parameters at Eqip Sermia. This approach includes limitations in the assessment of dynamic interplay of mechanisms. If it is detected that different processes such as surface elevation lowering and surface slow speed acceleration supposedly occur within the same period, this approach does not allow for the exact determination whether process one triggered process two, or reversely. However, some observations show a slight temporal shift, which allows for the identification of the trigger-reaction cascade. The qualitative assessment is highly dependent on the temporal resolution of the underlying data.

7. Conclusion & Outlook

7.1. Conclusion

The focus of this study was centred on marine-terminating outlet glacier Eqip Sermia. Surface elevation change and related processes were analysed based on a collection of data from different source and gathered over more than 100 years. Here, the main findings of these investigations are concluded, organised according to the underlying research questions.

- **How did the surface elevation of marine-terminating outlet glacier Eqip Sermia change from 1912 to 2019?**
    - **What spatial patterns of surface elevation change are observable? What is the magnitude? How does the surface geometry change?**

The surface elevation of Eqip Sermia has lowered in the entire terminus area. Surface elevation change is traceable up to more than 20 kilometres upstream from the front. From 1985 to 2016, the total surface elevation change close to the front measured approximately -90 metres, 5 kilometres from the front ca. -55 metres and 15 kilometres upstream ca. -20 metres. Thus, the magnitude of elevation change is decreasing with increasing distance from the front. Subsequent to changes of the front position, the surface elevation changes are largest on the terminus behind the affected retreating sector of the front. Shortly after large geometry changes at the front from 2011 to 2014, the elevation change in the lower sectors closer to the front were larger than further upstream. In the subsequent years, the spatial pattern inverted and the elevation change closer to the front ceased whereas in areas >5 kilometres upstream of the front persistent area-wide lowering can be observed. The low-dynamic ice-margins of Eqip Sermia show mostly continuous elevation lowering rates during the last 10 years. According to the differing magnitudes of surface elevation lowering depending on the distance to the front, the average downglacier surface slope gradient in the lowest 5 kilometres of Eqip Sermia increased by ca. 20 percent from 2006 to 2017, while the ice thickness decreased by ca. 15 percent.

- **What temporal patterns of surface elevation change are observable?**

The surface elevation on the terminus of Eqip Sermia was mostly stable from 1953 to 2003, when the surface elevation started to decrease. The surface elevation change was characterised by increasing lowering rates until October 2014, when the surface elevation lowering close to the front suddenly stopped. This temporal pattern is roughly identical 2.5 kilometres from the front, though the changes occurred at lower rate. 5 kilometres from the front, the surface elevation lowering is persistent at least until 2017, but also at lower rate. Concurrent with the long-term surface elevation change at Eqip Sermia, also a seasonal surface elevation change pattern was identified. The surface elevation is increasing in winter and decreasing in summer. The magnitude of seasonal surface elevation change is ca. 10-15 metres close to the front and decreases further upstream.

- **Is it possible to observe upstream propagation of surface elevation change signals? On what time scales?**

The observation of a stable surface elevation close to the front after October 2014 and simultaneously ongoing surface elevation change in higher elevations is a strong indication for upstream propagation of surface elevation change. After the large geometry changes from 2011 to 2014 and drastic thinning close to the front, the lowering of the surface elevation > 5km from the front is persistent with nearly constant rate at least until July 2018. Two kilometres from the front, the surface elevation lowering continued until 2015, though at lower rate, and eventually ceased. In the area close to the front, the surface elevation was already close to stable between October 2014 and October 2015. These results show that the surface elevation change signal subsequent to large geometry changes at the front is propagating far upstream on a time scale of many years. The short-term seasonal pattern of surface elevation change is traceable up to 5 kilometres from the front, but due to limited temporal coverage, no detailed assessment of the timing necessary for the identification of upstream propagation is possible.

- **Do the observed surface elevation changes correlate with changes of the front position, the flow velocity and climate change?**
  - **What are the driving factors?**

The surface elevation change at Eqip Sermia strongly correlates with the front position change. 1 kilometre of retreat causes a surface elevation lowering of ca. 40 metres. The observed spatial pattern of front retreat demonstrates that the bedrock is an important control of retreat and inherently surface elevation lowering at Eqip Sermia. The current front position is located in a sector with very shallow bedrock, which stabilised Eqip Sermia after the large retreat and related surface elevation lowering from 2011-2014, which was unprecedented in record history.

Further, the elevation change rate correlates well with the observed flow velocity. During the period of increasing surface elevation lowering rates from 2003 to 2014, the velocities increased simultaneously. The stabilisation of the elevation at the front coincides with a deceleration and stabilisation of the flow velocity. The observed spatial patterns indicate that the flow velocity is the main driving factor of inhomogeneous surface elevation change. Geometry-related acceleration from steepening and deceleration form thinning are roughly in balance and thus, the geometry of the glacier front is suspected to be a more important control of recent flow velocity changes. The fastest response of surface elevation to front position change is observed in the sectors with high flow velocities whereas the response time in higher elevations and on the low-dynamic margins is longer.

Ultimately, the temporal pattern of the elevation change is largely correlating with an increase of the occurrence of positive temperatures at the approximate equilibrium line altitude. The temperature rise precedes the surface elevation lowering by ca. 5-10 years, which indicated that the recent climate change triggered the surface elevation change and co-occurring dynamic retreat through an indirect mechanism. The recent surface elevation change on the low-dynamic margins of Eqip Sermia is largely explainable by surface melt.

7.2. Outlook

A further improvement of certain methodologies applied in this study could yield in improved and more robust results. Among others, of course the low quality of the historic SFM DEMs shows room for further improvement. Most promising, with the exception of the relatively good DEM of 1953, would be a further improvement of *SFM590625*. Among the range of different GCP configurations, it could maybe supports the SfM software to add additional GCPs on the glacier surface itself. Such an approach is feasible with the DEM of 1959, as historic measurements of the surface elevation of the same year are available (Bauer 1968a). In addition, the apparent elevation dependent bias of this DEM could be further assessed by the methodology presented by Nuth & Kääb (2011). Without considerable improvements of the capabilities of SfM software, a further assessment of the historic aerial image series of 1957 and 1964 seems futile, at least with the tested *Pix4Dmapper* and *Agisoft Photoscan*.

Further, the methodology of the elevation change analysis on the terminus of Eqip Sermia could be improved. For instance, the analysis points could be replaced (enlarged) by zones to get an even smoother surface elevation change signal. Also, the averaging of the elevations at the three locations per one sector could be replaced by an average per across-profile or even the average elevation change along elevation contours. A more distributed approach for the analysis of elevation change rates along the central flow line of Eqip Sermia could provide further information about the inland propagation of the signal of diffusive thinning after large geometry changes at the front. However, such an approach is also limited by the temporal resolution of the available DEMs. In addition, the strong changes of relative surface elevation of the right margin in sector 1 and the centre of Eqip Sermia raises the question about possible ice-flow perpendicular to the central flow line.

The melt modelling could be further refined by adjusting the temperature lapse rate according to local conditions. Also, the site-specific melt rate could be adjusted, based on the brightness of the orthoimages in the area of interest. The expected resulting improvement could eventually increase the understanding of the (residual) dynamics on the low-dynamic margins. Further, the front geometry could be a target of additional research, as changes of its geometry have been found to have a strong impact on the surface elevation further upstream. Measurements of the inclination of the calving front (as assessed by Lüthi et al. (2016) during a short-time period) could be applied to the entire available dataset. This could include a reprocessing of the drone DEMs with masking of the sea surface in order to avoid artefacts.

Additional fieldwork could include the installation of a long-term monitoring system, which allows for a continuous assessment of the area-wide surface flow velocity. This would fill an important gap that currently limits the assessment of the flow dynamics. Other studies have shown that already the processing of high-resolution time-lapse images can yield in considerably good velocity data (e.g. Ahn & Box 2010). Also, new achievements in UAV technologies are opportune for the monitoring of large areas, even if they are remote (Jouvet et al. 2019). Repeated monitoring on a longer-term (e.g. one entire season) with high frequency and focus on one glacier (e.g. on Eqip Sermia) would allow for a detailed assessment of the evolution of surface elevation, flow velocity and front position.

In the scope of subsequent studies, additional bathymetric data of higher resolution in combination with ocean temperature data could lead to a better understanding of the submarine processes at the calving front and complement recent findings of heterogenic calving activity (Walter at al. 2020). For a further assessment of the dynamic link between surface elevation change and velocity changes as well as changes at the calving front, a detailed modelling approach could help. Modelling of the ice sheet flow can contribute to an improved understanding of the downward propagation of atmosphere controlled SMB changes in the ice sheet interior.

Detailed knowledge about the mechanisms which control the recent developments at Eqip Sermia can contribute to a further understanding of the importance of local control such as bathymetry. This eventually allows for a general improvement of marine-terminating outlet glaciers and better predictability of their further changes and ultimately to the sensitivity of the GrIS towards the recent climate change.

Ultimately, further achievements in satellite technology considering high-resolution mapping of the Earth's surface can be expected. The presentation of the *ArcticDEM* only recently stands exemplarily for the latest achievements in this field.

8. References

Agisoft LLC (2018). Agisoft PhotoScan User Manual – Professional Edition, Version 1.4. Available at: http://www.agisoft.com/pdf/photoscan-pro_1_4_en.pdf [Accessed September 21, 2019].

Ahn, Y. & Box, J.E. (2010). Instruments and Methods: Glacier velocities from time-lapse photos: technique development and first results from the Extreme Ice Survey (EIS) in Greenland. Journal of Glaciology, 56(198), pp. 723-734. (doi: 10.3189/002214310793146313)

Andrews, L.C. et al. (2014). Direct observations of evolving subglacial drainage beneath the Greenland Ice Sheet. *Nature*, 514, 80–83. (doi: 10.1038/nature13796)

Bamber, J.L. et al. (2001). A new, high-resolution digital elevation model of Greenland fully validated with airborne laser altimeter data. *Journal of Geophysical Research B: Solid Earth*, 106(B4), pp.6733–6745. (doi: 10.1029/2000JB900365)

Bamber, J.L. et al. (2007). Rapid response of modern day ice sheets to external forcing. *Earth and Planetary Science Letters*, 257, pp. 1–13. (doi: 10.1016/j.epsl.2007.03.005)

Banwell, A.F. et al. (2012). Calibration and evaluation of a high-resolution surface mass-balance model for Paakitsoq, West Greenland. *Journal of Glaciology*, 58, pp. 1047–1062, (doi: 10.3189/2012JoG12J034)

Bassis, J.N. & Walker, C.C. (2012). Upper and lower limits on the stability of calving glaciers from the yield strength envelope of ice. *Proceedings of the Royal Society A*, 648, pp. 913-931. (doi: 0.1098/rspa.2011.0422)

Bauer, A. (1953). Frontverschiebungen des Gletschers Eqip Sermia, West-Grönland 1912-1953. *Polarforschung*, 23(1/2), pp.234–235.

Bauer, A. (1955). Glaciologie Groenland II. le glacier de l'Eqe. Librairie Scientifique Hermann, ed., Paris: Actualités Scientifiques et Industrielles.

Bauer, A. (1968a). Le Glacier de l'Eqe (Eqip Sermia) – Mouvement et variations du front (1959), Copenhagen: C.A. Reitzels Forlag.

Bauer, A. (1968b). Missions aériennes de reconnaissance au Groenland 1957-1958. Copenhagen: C.A. Reitzels Forlag.

Bauer, A. & Carbonnell, M. (1968). Exploitation des couvertures photographiques aériennes répétées du front des glaciers vêlant dans Disko Bugt et Umanak Fjord, Juin-Juillet 1964. *Meddelelser om Grønland*, 173(5), p.78.

Benn, D.I. & Evans, D.J.A. (2010). Glaciers & Glaciation. 2nd ed., London: Hodder Education. (doi: 10.1017/CBO9781107415324.004)

Bevan, S.L. et al. (2015). Seasonal dynamic thinning at Helheim Glacier. *Earth and Planetary Science Letters*, 415, pp. 47–53. (doi: 10.1016/j.epsl.2015.01.031)

Bevis, M. et al. (2019). Accelerating changes in ice mass within Greenland, and the ice sheet's sensitivity to atmospheric forcing. *PNAS*, 116(6), pp. 1934-1939. (doi: 10.1073/pnas.1806562116)

Bhardwaj, A. et al. (2016). UAVs as remote sensing platform in glaciology: Present applications and future prospects. *Remote Sensing of Environment*, 175, pp.196–204. (doi: 10.1016/j.rse.2015.12.029)

Box, J.E. & Ski, K. (2007). Remote sounding of Greenland supraglacial melt lakes: implications for subglacial hydraulics. *Journal of Glaciology*, 53(181), pp. 257-265. (doi: 10.3189/172756507782202883)

Box, J.E. & Steffen, K. (2000). Greenland Climate Network (GC-NET) – Data Reference. Boulder, CO. Available at: http://cires1.colorado.edu/steffen/gcnet/Gc-net_documentation_Nov_10_2000.pdf [Accessed November 22, 2019]

Brough, S. et al. (2019). Exceptional Retreat of Kangerlussuaq Glacier, East Greenland, Between 2016 and 2018. *Frontiers in Earth Science*, 7(123), pp. 1-11. (doi: 10.3389/feart.2019.00123).

Cappelen, J. (2020). DMI Historical Climate Data Collection 1784-2019. J. Cappelen, ed., Copenhagen, DK. Available at: https://www.dmi.dk/publikationer/ [Accessed March 12, 2020]

Carr, J. R. et al. (2017). Threefold increase in marine-terminating outlet glacier retreat rates across the Atlantic Arctic: 1992–2010. *Annals of Glaciology*, 58(74), pp. 72-91. (doi: 10.1017/aog.2017.3)

Carroll, D. et al. (2015). Modeling Turbulent Subglacial Meltwater Plumes: Implications for Fjord-Scale Buoyancy-Driven Circulation. *Journal of Physical Oceanography*, 45(8), pp. 2169–2185. (doi: 10.1175/JPOD-15-0033.1)

Catania G.A. et al. (2018). Geometric controls on tidewater glacier retreat in central western Greenland. *Journal of Geophysical Research: Earth Surface*, 123, pp. 2024–2038. (doi: 10.1029/2017JF004499)

Catania, G.A. et al. (2020). Future Evolution of Greenland's Marine-Terminating Outlet Glaciers. *Journal of Geophysical Research: Earth Surface*, 125 (2), pp. 1-28. (doi: 10.1029/2018JF004873)

Church, J.A. et al. (2013): Sea Level Change. In: Climate Change 2013: The Physical Science Basis. Contribution of Working Group I to the Fifth Assessment Report of the Intergovernmental Panel on Climate Change [Stocker, T.F. et al. (eds.)]. Cambridge University Press, Cambridge, United Kingdom and New York, NY, USA.

Csatho, B.M. et al. (2014). Laser altimetry reveals complex pattern of Greenland Ice Sheet dynamics. *PNAS*, 111(52), pp. 18478-18483. (doi: 10.1073/pnas.1411680112)

Cuffey, K.M. & Paterson, W.S.B. (2010). The Physics of Glaciers. Fourth edition. Oxford: Elsevier, Butterworth-Heinemann. (doi: 10.3189/002214311796405906)

de Quervain, A. & Mercanton, P.-L. (1925). Résultats scientifiques de l’expédition suisse au Groenland 1912-1913. Copenhagen: Bianco Lunos Bogtrykkeri.

Ekholm, S. (1996). A full coverage, high-resolution, topographic model of Greenland computed from a variety of digital elevation data. *Journal of Geophysical Research*, 101(B10), pp.21961–21972. (doi: 10.1029/96JB01912)

Enderlin, E.M. et al. (2013). High sensitivity of tidewater outlet glacier dynamics to shape. *The Cryosphere*, 7(3), pp. 1007-1015. (doi: 10.5194/tc-7-1007-2013)

European Commission (2015). Copernicus – Europe’s eyes on Earth. Brussels, Belgium. (doi: 10.2873/93104)

Felikson, D. et al. (2017). Inland thinning on the Greenland ice sheet controlled by outlet glacier geometry. *Nature Geoscience*, 10, pp. 366–369 (doi: 10.1038/ngeo2934)

Fried, M.J. et al. (2015). Distributed subglacial discharge drives significant submarine melt at a Greenland tidewater glacier. *Geophysical Research Letters*, 42, 9328–9336. (doi: 10.1002/2015GL065806)

Fried, M.J., et al. (2018). Reconciling drivers of seasonal terminus advance and retreat at 13 central west Greenland tidewater glaciers. *Journal of Geophysical Research: Earth Surface*, 123, pp. 1590–1607. (doi: 10.1029/2018JF004628)

Gogineni, P. (2012). CReSIS Greenland radar data, Lawrence, Kansas, USA. Digital Media. http://data.cresis.ku.edu/.

Google Earth (2020). DigitalGlobe Imagery. Available at: https://google.com/earth/ [Accessed April 15, 2020].

Gregory, J.M. et al. (2004). Threatened loss of the Greenland Ice Sheet. *Nature*, 428(6983) p. 616. (doi: 10.1038/428616a)

Hansen, K. (1968). Glacialgeologiske og sedimentologiske undersøgelser ved Eqe – Vestgrønland. Copenhagen.

Hall, D.K. et al. (2008). Greenland ice sheet surface temperature, melt and mass loss: 2000–06. *Journal of Glaciology*, 54(184), pp. 81-93. (doi: 10.3189/002214308784409170)

Hall, D.K. et al. (2013). Variability in the surface temperature and melt extent of the Greenland ice sheet from MODIS. *Geophysical Research Letters*, 40, pp. 2114–2120. (doi: 10.1002/grl.50240)

Hanna, E. et al. (2011). Greenland Ice Sheet surface mass balance 1870 to 2010 based on Twentieth Century Reanalysis, and links with global climate forcing. *Journal of Geophysical Research Atmospheres*, 116(24), pp.1–20. (doi: 10.1029/2011JD016387)

Hanna, E. et al. (2012). Recent warming in Greenland in a long-term instrumental (1881–2012) climatic context: I. Evaluation of surface air temperature records. *Environmental Research Letters*, 7, pp. 1-15. (doi: 10.1088/1748-9326/7/4/045404)

Hill, E.A. et al. (2018). Dynamic changes in outlet glaciers in northern Greenland from 1948 to 2015. *The Cryosphere*, 12, pp. 3243–3263. (doi: 10.5194/tc-12-3243-2018)

Höhle, J. & Höhle, M. (2009). Accuracy assessment of digital elevation models by means of robust statistical methods. *ISPRS Journal of Photogrammetry and Remote Sensing*, 64(4), pp.398–406. (doi: 10.1016/j.isprsjprs.2009.02.003)

Holtzscherer, J.-J. & Bauer, A. (1954). Contribution à la connaissance de l'inlandsis du Groenland. Paris, F.

Howat, I.M. et al. (2005). Rapid retreat and acceleration of Helheim Glacier, east Greenland. *Geophysical Research Letters*, 32, pp. 1-4. (doi: 10.1029/2005GL024737)

Howat, I.M. et al. (2008). Synchronous retreat and acceleration of southeast Greenland outlet glaciers 2000–06: ice dynamics and coupling to climate. *Journal of Glaciology*, 54(187), pp. 66-660. (doi: 10.3189/002214308786570908)

Howat, I.M. et al. (2010). Seasonal variability in the dynamics of marine-terminating outlet glaciers in Greenland. *Journal of Glaciology*, Vol. 56, No. 198, pp. 601-613. (doi: 10.3189/002214310793146232)

Howat, I.M. et al. (2014). The Greenland Ice Mapping Project (GIMP) land classification and surface elevation data sets. *Cryosphere*, 8(4), pp.1509–1518. (doi: 10.5194/tc-8-1509-2014)

Huss, M. et al. (2008). Determination of the seasonal mass balance of four Alpine glaciers since 1865. *Journal of Geophysical Research: Earth Surface*, 113(F1), pp. 11-11. (doi: 10.1029/2007JF000803)

Håkansson, L. et al. (2014). Slow retreat of a land based sector of the West Greenland Ice Sheet during the Holocene Thermal Maximum: evidence from threshold lakes at Paakitsoq. *Quaternary Science Reviews*, 98, pp.74–83. (doi: 10.1016/j.quascirev.2014.05.016)

Joughin, I. et al. (2008a). Seasonal Speedup Along the Western Flank of the Greenland Ice Sheet. *Science*, 320(5877), pp. 781-783. (doi: 10.1126/science.1153288)

Joughin, I. et al. (2008b). Ice-front variation and tidewater behavior on Helheim and Kangerdlugssuaq Glaciers, Greenland. *Journal of Geophysical Research*, 113, pp. 1-11. (doi: doi:10.1029/2007JF000837)

Joughin, I. et al. (2012). Seasonal to decadal scale variations in the surface velocity of Jakobshavn Isbrae, Greenland: Observation and model-based analysis. *Journal of Geophysical Research*, 117, pp. 1-20. (doi: 10.1029/2011JF002110)

Joughin, I. et al. (2015, updated 2018). MEaSUREs Greenland Ice Sheet Velocity Map from InSAR Data, Version 2 – Greenland Velocity Mosaic 200, velocity magnitude. NASA National Snow and Ice Data Center Distributed Active Archive. Boulder, CO. (doi: 10.5067/OC7B04ZM9G6Q)

Joughin, I. et al. (2020). A decade of variability on Jakobshavn Isbræ: ocean temperatures pace speed through influence on mélange rigidity. *The Cryosphere*, 14, pp. 211–227. doi: 10.5194/tc-14-211-2020)

Jouvet, G. et al. (2019). High-Endurance UAV for Monitoring Calving Glaciers: Application to the Inglefield Bredning and Eqip Sermia, Greenland. *Frontiers in Earth Scien*ce, 7(206), pp. 1-15. (doi: 10.3389/feart.2019.00206)

Kadded, F. & Moreau, L. (2013). Sur les traces de Paul-Emile Victor, relevés topographiques 3d au Groenland. *Revue XYZ*, 137(4), pp. 47–56.

Kane, E. et al. (2016). Measuring short term velocity changes of Kangilerngata Sermia, west Greenland using a Gamma Portable Radar Interferometer. American Geophysical Union, Fall Meeting 2016, abstract #C13C-0831.

Kehrl, L.M. et al. (2017). Seasonal and interannual variabilities in terminus position, glacier velocity, and surface elevation at Helheim and Kangerlussuaq Glaciers from 2008 to 2016, *Journal of Geophysical Research: Earth Surface*, 122, pp. 1635–1652, (doi: 10.1002/2016JF004133)

Khan, S.A. et al. (2014). Glacier dynamics at Helheim and Kangerdlugssuaq glaciers, southeast Greenland, since the Little Ice Age. *The Cryosphere*, 8, pp. 1497–1507. (doi: 10.5194/tc-8-1497-2014)

Khazendar, A. et al. (2019). Interruption of two decades of Jakobshavn Isbrae acceleration and thinning as regional ocean cools. Nature Geoscience, 12, pp. 277–283. (doi: 10.1038/s41561-019-0329-3)

King, M.D. et al. (2018). Seasonal to decadal variability in ice discharge from the Greenland Ice Sheet. *The Cryosphere*, 12, pp. 3813–3825 (doi: 10.5194/tc-12-3813-2018)

Kjeldsen, K.K. et al. (2015). Spatial and temporal distribution of mass loss from the Greenland Ice Sheet since AD 1900. *Nature*, 528(7582), pp.396–400. (doi: 10.1038/nature16183)

Korona, J. et al. (2009). SPIRIT. SPOT 5 stereoscopic survey of Polar Ice: Reference Images and Topographies during the fourth International Polar Year (2007-2009). *ISPRS Journal of Photogrammetry and Remote Sensing*, 64(2), pp.204–212. (doi: 10.1016/j.isprsjprs.2008.10.005)

Korsgaard, N.J. et al. (2016). Data Descriptor: Digital elevation model and orthophotographs of Greenland based on aerial photographs from 1978 – 1987. *Scientific Data*, 3, pp.1–15. (doi: 10.1038/sdata.2016.32)

Korsgaard, N. et al. (2017). AirBase - A database of 160,000 aerial photos of Greenland 1930-1980s. In *Geophysical Research Abstracts*. EGU General Assembly 2017. Vienna.

LeSchack, L.A. (1964). The French Polar Effort and the Expeditions Polaires Francaises. *Arctic*, 17(1), pp.1–14. (doi: 10.14430/arctic3480)

Lloyd, J. et al. (2011). A 100 yr record of ocean temperature control on the stability of Jakobshavn Isbrae, West Greenland. *Geology*, 39, pp. 867-870. (doi: 10.1130/G32076.1)

Lüthi, M.P. et al. (2016). A century of geometry and velocity evolution at Eqip Sermia, West Greenland. *Journal of Glaciology*, 62(234), pp.640–654. (doi: 10.1017/jog.2016.38)

McFadden, E.M. et al. (2011). Changes in the dynamics of marine terminating outlet glaciers in west Greenland (2000–2009), *Journal of Geophysical Research*, 116(F0202) (doi: 10.1029/2010JF001757)

Machguth, H. et al. (2016). Greenland surface mass-balance observations from the ice-sheet ablation area and local glaciers. Journal of Glaciology, 62(235), pp. 861–887. (doi: 10.1017/jog.2016.75)

Mercenier, R. et al. (2019). Calving relation for tidewater glaciers based on detailed stress field analysis. *The Cryosphere*, 12, pp. 721–739. (doi: 10.5194/tc-12-721-2018)

Mernild, S.H. et al. (2011). Greenland ice sheet surface melt extent and trends: 1960–2010. *Journal of Glaciology*, 57(204), pp. 621-628. (doi: 10.3189/002214311797409712)

Midgley, N.G. et al. (2018). Evolution of high-Arctic glacial landforms during deglaciation. *Geomorphology*, 311, pp. 63–75. (doi: 0.1016/j.geomorph.2018.03.027)

Mölg, N. & Bolch, T. (2017). Structure-from-motion using historical aerial images to analyse changes in glacier surface elevation. *Remote Sensing*, 9(10). (doi: 10.3390/rs9101021)

Moon, T. et al. (2012). 21st-Century Evolution of Greenland Outlet Glacier Velocities. *Science*, 336(6081), pp. 576-578. (doi: 10.1126/science.1219985)

Moon, T. et al. (2014). Distinct patterns of season Greenland glacier velocity. *Geophysical Research Letters*, 41, pp. 7209–7216. (doi:10.1002/2014GL061836)

Moon, T. & Joughin, I. (2008). Changes in ice front position on Greenland's outlet glaciers from 1992 to 2007. *Journal of Geophysical Research*, 113, pp. 1-10. (doi: 10.1029/2007JF000927)

Morin, P. et al. (2016). ArcticDEM; A Publically Available, High Resolution Elevation Model of the Arctic. In *Geophysical Research Abstracts*. Vienna.

Morlighem, M. et al. (2016). Modeling of Store Gletscher's calving dynamics, West Greenland, in response to ocean thermal forcing. *Geophysical Research Letters*, 43, pp. 2659–2666. (doi: 10.1002/2016GL067695)

Morlighem, M. et al. (2017). BedMachine v3: Complete Bed Topography and Ocean Bathymetry Mapping of Greenland From Multibeam Echo Sounding Combined With Mass Conservation. *Geophysical Research Letters*, 44(21), p.11051-11061. (doi: 10.1002/2017GL074954)

Mouginot, J. et al. (2019). Forty-six years of Greenland Ice Sheet mass balance from 1972 to 2018. *PNAS*, 116(19), pp. 9239-9244. (doi: 10.1073/pnas.1904242116)

NGA & NSF (2018). Guide: Introduction to ArcticDEM. Available at: https://www.pgc.umn.edu/guides/arcticdem/introduction-to-arcticdem/ [Accessed September 24, 2019].

Noël, B. et al. (2015). Evaluation of the updated regional climate model RACMO2.3: summer snowfall impact on the Greenland Ice Sheet. *The Cryosphere*, 9, pp. 1831–1844. (doi: 10.5194/tc-9-1831-2015)

Noël, B. et al. (2018). Modelling the climate and surface mass balance of polar ice sheets using RACMO2 – Part 1: Greenland (1958–2016). *The Cryosphere*, 12, pp. 811–831. (doi: 10.5194/tc-12-811-2018)

Noh, M.-J. & Howat, I. (2018). Automated stereo-photogrammetric DEM generation at high latitudes: Surface Extraction with TIN-based Search-space Minimization (SETSM) validation and demonstration over glaciated regions. *GIScience & Remote Sensing*, 52(2), pp. 1-20. (doi: 10.1080/15481603.2015.1008621)

Nuth, C. & Kääb (2011). Co-registration and bias corrections of satellite elevation data sets for quantifying glacier thickness change. *Cryosphere*, 5(1), pp.271–290. (doi: 10.5194/tc-5-271-2011)

Pix4D SA Pix4Dmapper 4.1. (2017). User Mannual Pix4D SA. Lausanne, Switzerland. Available at: https://support.pix4d.com/hc/en-us/articles/204272989-Offline-Getting-Started-and-Manual-pdf [Accessed September 10, 2019]

Porter, C. et al. (2018). Arctic DEM V3. (doi: 10.7910/DVN/OHHUKH)

Price, S.F. et al. (2011). Committed sea-level rise for the next century from Greenland ice sheet dynamics during the past decade. *PNAS*, 108(22), pp. 8978–8983. (doi: 10.1073/pnas.1017313108)

Pritchard, H.D. et al. (2009). Extensive dynamic thinning on the margins of the Greenland and Antarctic ice sheets. Nature, 461(7266), pp. 971–975. (doi: 10.1038/nature08471)

Reeh, N. (1991). Parametrization of Melt Rate and Surface Temperature on the Greenland Ice Sheet. *Polarforschung*, 5913, pp. 113-128.

Rignot, E. et al. (2001). Penetration depth of interferometric synthetic aperture radar signals in snow and ice. *Geophysical Research Letters*, 28(18), pp.3501–3504. (doi: 10.1029/2000GL012484)

Rignot, E. & Kanagaratnam, P. (2006). Changes in the Velocity Structure of the Greenland Ice Sheet. *Science*, 311(5763), pp.986–990. (doi: 10.1126/science.1121381)

Rignot, E. et al. (2015). Undercutting of marine-terminating glaciers in West Greenland. *Geophysical Research Letters*, 42(14), pp. 5909-5917. (doi: 10.1002/2015GL064236)

Rohner, C. et al. (2019). Multisensor validation of tidewater glacier flow fields derived from synthetic aperture radar (SAR) intensity tracking. *The Cryosphere*, 13, pp. 2953-2975. (doi: 10.5194/tc-13-2953-2019)

Rossini, M. et al. (2018). Rapid melting dynamics of an alpine glacier with repeated UAV photogrammetry. *Geomorphology*, 304, pp.159–172. (doi: 10.1016/j.geomorph.2017.12.039)

Ruan, R. et al. (2019). Decelerated Greenland Ice Sheet melt driven by positive summer North Atlantic Oscillation. *Journal of Geophysical Research: Atmospheres*, 124, pp. 7633–7646. (doi: 10.1029/2019JD030689)

Ryan, J.C. et al. (2019). Greenland Ice Sheet surface melt amplified by snowline migration and bare ice exposure. *Science Advances*, 5(3), pp. 1-10. (doi: 10.1126/sciadv.aav3738)

Scambos, T.A. & Haran, T. (2002). An image-enhanced DEM of the Greenland ice sheet. *Annals of Glaciology*, 34, pp.291–298. (doi: 10.3189/172756402781817969)

Schudel, S. (2019). Ice Sheet Margin on the Rocks. A Century of Thinning, Retreat and Velocity Measurements at a Land-Terminating Ice Sheet Margin in West Greenland. Master's Thesis. University of Zurich.

Shepherd, A. et al. (2020). Mass balance of the Greenland Ice Sheet from 1992 to 2018. *Nature*, 579, pp. 233–239. (doi: 10.1038/s41586-019-1855-2)

Slater, J.A. et al. (2011). Global Assessment of the New ASTER Global Digital Elevation Model. *Photogrammetric Engineering & Remote Sensing*, 77(4), pp.335–349. (doi: 10.14358/PERS.77.4.335)

Sole, A. et al. (2008). Testing hypotheses of the cause of peripheral thinning of the Greenland Ice Sheet: Is land-terminating ice thinning at anomalously high rates? *Cryosphere*, 2(2), pp. 205–218. (doi: 10.5194/tc-2-205-2008)

Stearns L.A. & Hamilton G.S. (2007). Rapid volume loss from two East Greenland outlet glaciers quantified using repeat stereo satellite imagery. *Geophysical Research Letters*, 34(5). (doi: 10.1029/2006GL028982)

Stober, M. et al. (2015). The geodetic campaign 2014 for studies in mass balance, ice dynamics and validation of satellite data in the Swiss Camp area, West Greenland. *IASC Workshop & Network on Arctic Glaciology*, annual meeting 23-25 March 2015.

Straneo, F. & Heimbach, P. (2013). North Atlantic warming and the retreat of Greenland's outlet glaciers. *Nature*, 504, pp. 34-43. (doi: 10.1038/nature12854).

Tachikawa, T. et al. (2011). Characteristics of ASTER GDEM version 2. *2011 IEEE International Geoscience and Remote Sensing Symposium*, pp.3657–3660. (doi: 10.1109 / IGARSS.2011.6050017)

U.S./Japan ASTER Science Team (2007). ASTER On-Demand L3 DEM and Orthorectified Images, GeoTIF Format. (doi: 10.5067/ASTER/AST14DMO.003)

van Angelen, J.H. et al. (2014). Contemporary (1960–2012) Evolution of the Climate and Surface Mass Balance of the Greenland Ice Sheet. *Surveys in Geophysics*, 35(5), pp. 1155–1174. (doi: 10.1007/s10712-013-9261-z)

van den Broeke, M.R. et al. (2016). On the recent contribution of the Greenland ice sheet to sea level change. *The Cryosphere*, 10, pp. 1933–1946. (doi: 10.5194/tc-10-1933-2016)

Vieli, A. et al. (2004). Short-term velocity variations on Hansbreen, a tidewater glacier in Spitsbergen. *Journal of Glaciology*, 50(170), pp. 389-398. (doi: 10.3189/172756504781829963)

Vieli, A. (2015). Retreat instability of tidewater glaciers and marine ice sheets. Chapter in book: Snow and Ice-Related Hazards, Risks and Disasters, edited by C. Whiteman and W. Haeberli, Elsevier. (doi: 10.1016/B978-0-12-394849-6.00019-6)

Vieli, A. et al. (2018). Marginal Lake Drainage and Implications at a Tidewater Glacier in Greenland, *POLAR2018*, Open Science Conference OSC 19 - 23 June 2018.

Walter, A. (2016). Estimation of Glacier Melt and Discharge of the Eqip Glacier, a Calving Outlet Glacier in Greenland. Master's Thesis. University of Zurich.

Walter, A. et al. (2020). Calving event size measurements and statistics of Eqip Sermia, Greenland, from terrestrial radar interferometry. *The Cryosphere*, 14, pp. 1051–1066. (doi: 10.5194/tc-14-1051-2020)

Zick, W. (1972). Eisbewegungen am Eqip Sermia und im westlichen Randgebiet des grönländischen Inlandeises (EGIG Arbeitsgebiet). *Polarforschung*, pp.24–30.

Zwally, H.J. et al. (2002). Surface melt induced acceleration of Greenland ice sheet flow. *Science*, 297(July), pp.218–222. (doi: 10.1126/science.1072708)

9. Appendix

I. GimpDEM Timestamp Validation

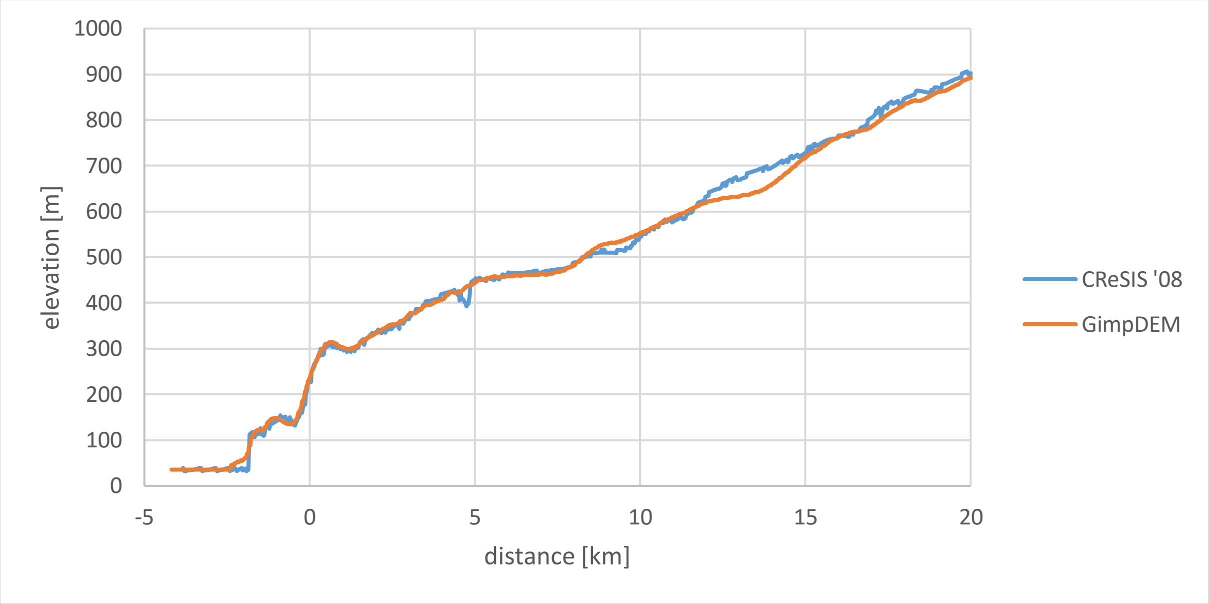

Figure 77: Comparison of GimpDEM elevation (dated to 2007) and CReSIS radar elevation (state of 2008) along the central profile used by Lüthi et al. (2016). With data from Gogineni (2012). Note that especially between km 0 and 8, which accords to the main analysis area of this study, the elevation differences are small.

II. Table of Front Positions

Table 12: Collection of all front positions as well as respective authors and original sources. The date is composed as YYYYMMDD.

year	*date*	**mapped by**	**source**
1912	*19120819*	Lüthi et al. 2016	de Quervain & Mercanton (1925) map
1920		Lüthi et al. 2016	Bauer (1955) map
1929		Lüthi et al. 2016	Bauer (1955) map
1933		Lüthi et al. 2016	Bauer (1955) map
1948		Lüthi et al. 2016	Bauer (1955) map
1949		Lüthi et al. 2016	Bauer (1955) map
1951		Lüthi et al. 2016	Bauer (1955) map
1952		Lüthi et al. 2016	Bauer (1955) map
1953	*19530703*	Roger Honegger	Bauer (1968b) aerial images
1957	*19570712*	Roger Honegger	SDFE aerial images
1959	*19590625*	Roger Honegger	Bauer (1968a) aerial images
1964	*19640712*	Roger Honegger	Bauer & Carbonnell (1968) aerial images
1972		Lüthi et al. 2016	Zick (1972) map
1975		Lüthi et al. 2016	Landsat
1976		Lüthi et al. 2016	Landsat
1985	*19850709*	Roger Honegger	orthomosaic AeroDEM
1986	*19860512*	Lüthi et al. 2016	Landsat
1988	*19880429*	Lüthi et al. 2016	Landsat
1988	*19880609*	Lüthi et al. 2016	Landsat
1992	*19920730*	Lüthi et al. 2016	Landsat
1994	*19940712*	Lüthi et al. 2016	Landsat
1994	*19940829*	Lüthi et al. 2016	Landsat
1999	*19990709*	Lüthi et al. 2016	Landsat
1999	*19990828*	Lüthi et al. 2016	Landsat
1999	*19990918*	Lüthi et al. 2016	Landsat
2000	*20000314*	Lüthi et al. 2016	Landsat
2000	*20000515*	Lüthi et al. 2016	Landsat
2000	*20000616*	Lüthi et al. 2016	Landsat
2000	*20000805*	Lüthi et al. 2016	Landsat
2000	*20000913*	Lüthi et al. 2016	Landsat
2001	*20010315*	Lüthi et al. 2016	Landsat
2001	*20010504*	Lüthi et al. 2016	Landsat
2001	*20010612*	Lüthi et al. 2016	Landsat
2001	*20010707*	Lüthi et al. 2016	Landsat
2001	*20010808*	Lüthi et al. 2016	Landsat
2001	*20010907*	Lüthi et al. 2016	Landsat
2002	*20020304*	Lüthi et al. 2016	Landsat
2002	*20020405*	Lüthi et al. 2016	Landsat
2002	*20020428*	Lüthi et al. 2016	Landsat
2002	*20020606*	Lüthi et al. 2016	Landsat
2002	*20020802*	Lüthi et al. 2016	Landsat
2002	*20020903*	Lüthi et al. 2016	Landsat
2003	*20030323*	Lüthi et al. 2016	Landsat

year	*date*	**mapped by**	**source**
2003	*20030422*	Lüthi et al. 2016	Landsat
2003	*20030524*	Lüthi et al. 2016	Landsat
2003	*20030609*	Roger Honegger	AsterDEM
2003	*20030711*	Lüthi et al. 2016	Landsat
2004	*20040410*	Lüthi et al. 2016	Landsat
2004	*20040519*	Lüthi et al. 2016	Landsat
2004	*20040620*	Lüthi et al. 2016	Landsat
2004	*20040729*	Lüthi et al. 2016	Landsat
2004	*20040915*	Lüthi et al. 2016	Landsat
2004	*20041003*	Lüthi et al. 2016	Landsat
2005	*20050630*	Lüthi et al. 2016	Landsat
2005	*20050826*	Lüthi et al. 2016	Landsat
2005	*20050911*	Lüthi et al. 2016	Landsat
2006	*20060315*	Lüthi et al. 2016	Landsat
2006	*20060502*	Lüthi et al. 2016	Landsat
2006	*20060518*	Lüthi et al. 2016	Landsat
2006	*20060626*	Lüthi et al. 2016	Landsat
2006	*20060703*	Roger Honegger	AsterDEM
2006	*20060806*	Lüthi et al. 2016	Landsat
2007	*20070325*	Lüthi et al. 2016	Landsat
2007	*20070503*	Lüthi et al. 2016	Landsat
2007	*20070604*	Lüthi et al. 2016	Landsat
2007	*20070622*	Lüthi et al. 2016	Landsat
2007	*20070724*	Lüthi et al. 2016	Landsat
2007	*20070825*	Lüthi et al. 2016	Landsat
2007	*20070924*	Lüthi et al. 2016	Landsat
2008	*20080521*	Lüthi et al. 2016	Landsat
2008	*20080622*	Lüthi et al. 2016	Landsat
2008	*20080719*	Lüthi et al. 2016	Landsat
2008	*20080811*	Lüthi et al. 2016	Landsat
2008	*20080921*	Lüthi et al. 2016	Landsat
2009	*20090314*	Lüthi et al. 2016	Landsat
2009	*20090524*	Lüthi et al. 2016	Landsat
2009	*20090618*	Lüthi et al. 2016	Landsat
2009	*20090711*	Lüthi et al. 2016	Landsat
2009	*20090821*	Lüthi et al. 2016	Landsat
2009	*20090915*	Lüthi et al. 2016	Landsat
2009	*20091001*	Lüthi et al. 2016	Landsat
2010	*20100418*	Lüthi et al. 2016	Landsat
2010	*20100527*	Lüthi et al. 2016	Landsat
2010	*20100621*	Lüthi et al. 2016	Landsat
2010	*20100709*	Roger Honegger	AsterDEM
2010	*20100817*	Lüthi et al. 2016	Landsat
2010	*20100925*	Lüthi et al. 2016	Landsat
2010	*20101004*	Lüthi et al. 2016	Landsat
2011	*20110419*	Roger Honegger	ArcticDEM

year	*date*	**mapped by**	**source**
2011	*20110523*	Lüthi et al. 2016	Landsat
2011	*20110613*	Roger Honegger	ArcticDEM
2011	*20110703*	Lüthi et al. 2016	Landsat
2011	*20110818*	Lüthi et al. 2016	Landsat
2011	*20110921*	Lüthi et al. 2016	Landsat
2012	*20120329*	Lüthi et al. 2016	Landsat
2012	*20120518*	Lüthi et al. 2016	Landsat
2012	*20120619*	Lüthi et al. 2016	Landsat
2012	*20120719*	Lüthi et al. 2016	Landsat
2012	*20120820*	Lüthi et al. 2016	Landsat
2012	*20120923*	Lüthi et al. 2016	Landsat
2013	*20130325*	Roger Honegger	ArcticDEM
2013	*20130423*	Roger Honegger	ArcticDEM
2013	*20130512*	Roger Honegger	ArcticDEM
2013	*20130621*	Lüthi et al. 2016	Landsat
2013	*20130722*	Lüthi et al. 2016	Landsat
2013	*20130811*	Roger Honegger	ArcticDEM
2013	*20130927*	Roger Honegger	ArcticDEM
2013	*20131028*	Roger Honegger	ArcticDEM
2014	*20140327*	Lüthi et al. 2016	Landsat
2014	*20140421*	Lüthi et al. 2016	Landsat
2014	*20140528*	Roger Honegger	ArcticDEM
2014	*20140615*	Lüthi et al. 2016	Landsat
2014	*20140704*	Roger Honegger	AsterDEM
2014	*20140719*	Lüthi et al. 2016	Landsat
2014	*20140826*	Roger Honegger	ArcticDEM
2014	*20141015*	Roger Honegger	ArcticDEM
2014	*20141019*	Lüthi et al. 2016	Sentinel-1A
2014	*20141124*	Lüthi et al. 2016	Sentinel-1A
2014	*20141222*	Lüthi et al. 2016	Sentinel-1A
2015	*20150115*	Lüthi et al. 2016	Sentinel-1A
2015	*20150215*	Lüthi et al. 2016	Landsat
2015	*20150216*	Lüthi et al. 2016	Sentinel-1A
2015	*20150316*	Lüthi et al. 2016	Sentinel-1A
2015	*20150417*	Lüthi et al. 2016	Sentinel-1A
2015	*20150515*	Lüthi et al. 2016	Sentinel-1A
2015	*20150620*	Lüthi et al. 2016	Landsat
2015	*20150715*	Lüthi et al. 2016	Landsat
2015	*20150823*	Lüthi et al. 2016	Landsat
2015	*20150921*	Roger Honegger	ArcticDEM
2015	*20151024*	Roger Honegger	ArcticDEM
2015	*20151105*	Roger Honegger	ArcticDEM
2016	*20160311*	Roger Honegger	ArcticDEM
2016	*20160515*	Roger Honegger	ArcticDEM
2016	*20160630*	Roger Honegger	drone orthomosaic
2016	*20160702*	Roger Honegger	drone orthomosaic

year	*date*	**mapped by**	**source**
2016	*20160707*	Roger Honegger	AsterDEM
2016	*20160723*	Roger Honegger	AsterDEM
2016	*20160821*	Roger Honegger	drone orthomosaic
2016	*20160825*	Roger Honegger	drone orthomosaic
2017	*20170527*	Rohner (personal communication, Rohner et al. 2019	Sentinel-2
2017	*20170612*	Rohner (personal communication, Rohner et al. 2019	Sentinel-2
2017	*20170616*	Roger Honegger	drone orthomosaic
2017	*20170620*	Roger Honegger	drone orthomosaic
2017	*20170622*	Roger Honegger	drone orthomosaic
2017	*20170721*	Rohner (personal communication, Rohner et al. 2019	Sentinel-2
2017	*20170821*	Roger Honegger	ArcticDEM
2018	*20180706*	Roger Honegger	drone orthomosaic (Jouvet et al. 2019)
2018	*20180708*	Roger Honegger	drone orthomosaic (Jouvet et al. 2019)
2018	*20180711*	Roger Honegger	drone orthomosaic (Jouvet et al. 2019)
2018	*20180719*	Rohner (personal communication, Rohner et al. 2019	Sentinel-2
2018	*20180816*	Rohner (personal communication, Rohner et al. 2019	Sentinel-2
2018	*20181011*	Rohner (personal communication, Rohner et al. 2019	Sentinel-2
2019	*20190227*	Rohner (personal communication, Rohner et al. 2019	Sentinel-2
2019	*20190311*	Rohner (personal communication, Rohner et al. 2019	Sentinel-2
2019	*20190428*	Rohner (personal communication, Rohner et al. 2019	Sentinel-2
2019	*20190528*	Rohner (personal communication, Rohner et al. 2019	Sentinel-2
2019	*20190624*	Rohner (personal communication, Rohner et al. 2019	Sentinel-2
2019	*20190724*	Rohner (personal communication, Rohner et al. 2019	Sentinel-2
2019	*20190818*	Roger Honegger	drone orthomosaic
2019	*20190820*	Roger Honegger	drone orthomosaic
2019	*20190823*	Rohner (personal communication, Rohner et al. 2019	Sentinel-2
2019	*20190919*	Rohner (personal communication, Rohner et al. 2019	Sentinel-2
2019	*20191026*	Rohner (personal communication, Rohner et al. 2019	Sentinel-2

III. Table of Co-Registration Parameters

Table 13: Quality measures Δh and STDV of all used DEMs before and after co-registration. In alphabetical order. In addition, the number or iterations and the total translation vectors applied to the slave DEMs are given. Note that AD130325 *and* AD160515 *are mosaicked each from two single ArcticDEM strips (N: north, S: south) with the same acquisition date. They were co-registered separately and mosaicked after. (*):* master DEM*.*

DEM name		**Δh of stable terrain [m]**		**# iterations**	**Translation vectors [m]**		
		Mean	**STDV**		**Δx**	**Δy**	**Δz**
AD110419	*before*	-1.41	2.46	2			
	after	-0.06	2.47		-1.5	-1.5	1.5
AD1100613	*before (N)*	0.32	1.59	1			
	before (S)	0.33	7.07	1			
	final	0.01	5.03		-2.7/-1.3	0.4/1.1	-0.2/-0.5
AD130325	*before*	4.55	2.13	2			
	final	-0.02	1.21		-6.1	-1.7	-4.2
AD130423	*before*	0.41	0.88	1			
	final	0.00	0.70		1.9	0.2	-0.5
AD130512	*before*	2.32	2.90	2			
	final	0.11	2.90		-0.7	-0.5	-2.3
AD130811	*before*	0.96	1.14	1			
	final	-0.04	1.14		0.0	0.0	-1.0
AD130927	*before*	1.26	1.61	1			
	final	-0.03	1.43		-0.9	-3.0	-1.2
AD131028	*before*	7.67	1.31	2			
	final	0.02	1.62		0.2	1.5	-7.7
AD140528	*before*	2.43	3.01	3			
	final	-0.02	2.78		3.7	-1.9	-2.4
AD140704	*before*	0.39	0.88	2			
	final	-0.01	0.88		0.3	0.6	-0.4
AD141015	*before*	-0.48	1.80	3			
	final	-0.01	1.00		-4.4	-1.7	0.7
AD150815	*before*	3.71	0.95	2			
	final	0.02	0.79		0.9	2.4	-3.8
*AD150921**	*final*	0	0	0	0	0	0
AD151024	*before*	0.97	1.57	1			
	final	-0.02	0.89		-3.9	-2.3	-0.8
AD151105	*before*	1.30	1.17	4			
	final	-0.01	0.85		3.5	0.9	-1.4
AD160311	*before*	2.83	1.55	2			
	final	-0.03	1.10		-1.8	-3.2	-2.6
AD160515	*before (N)*	-0.99	1.34	1			
	before (S)	-0.13	1.69	1			
	final	-0.02	1.23		2.5/3.2	-1.8/-1.9	1.0/-0.6
AD170821	*before*	2.19	1.59	2			
	final	0.05	1.35		-2.9	-0.8	-2.1
AE850709	*before*	0.85	6.46	1			
	final	0.05	6.46		-2.4	-8.1	-0.8

DEM name		Δh of stable terrain [m]		# iterations	Translation vectors [m]		
		Mean	**STDV**		**Δx**	**Δy**	**Δz**
AS030609	*before*	-44.02	16.78	5			
	final	0.12	14.32		-30.7	14.1	43.9
AS060703	*before*	-42.15	14.12	3			
	final	0.06	12.88		-13.1	-22.7	43.7
AS100709	*before*	-45.81	11.66	4			
	final	0.61	9.15		-38.8	-10.4	46.6
AS140826	*before*	-43.75	9.27	3			
	final	-0.35	9.27		-10.0	-0.8	43.4
AS160707	*before*	-53.02	11.90	2			
	final	0.16	9.73		-19.8	23.3	51.8
AS160723	*before*	-66.15	12.15	3			
	final	0.10	9.66		-16.2	-9.1	66.4
DR160630	*before*	-2.21	1.54	2			
	final	-0.01	1.54		0.1	-0.7	2.2
DR160702	*before*	-2.35	1.51	2			
	final	-0.05	1.51		0.2	0.0	2.3
DR160821	*before*	-2.10	1.46	3			
	final	0.00	1.46		0.8	-0.2	2.1
DR160823	*before*	-2.00	0.93	2			
	final	0.00	0.93		0.1	-1.5	2.1
DR160825	*before*	-2.15	1.48	2			
	final	0.01	1.54		0.8	-1.3	2.1
DR170616	*before*	-1.98	1.59	3			
	final	0.02	1.59		-1.3	0.2	2.0
DR170620	*before*	-2.36	1.95	2			
	final	0.02	2.00		0.3	-2.3	2.3
DR170622	*before*	-2.06	1.54	2			
	final	-0.04	1.58		0.7	-2.2	2.0
DR180706	*before*	-1.63	1.38	2			
	final	0.00	1.38		1.2	-1.4	1.6
DR180708	*before*	-1.84	1.20	3			
	final	-0.03	1.22		0.1	-1.7	1.8
DR180711	*before*	-1.82	1.20	3			
	final	-0.01	1.22		0.4	-1.5	1.8
DR190818	*before*	-2.10	1.48	3			
	final	0.00	1.48		0.2	-0.3	2.1
DR190820	*before*	-2.15	1.50	3			
	final	0.02	1.58		0.6	-1.5	2.1
GD07comp	*before*	-6.32	8.83	1			
	final	0.37	8.13		17.0	3.2	6.4
SFM530703	*before*	4.89	20.57	2			
	final	0.04	20.21		11.4	-7.8	-4.0
SFM570712	*before*	-5.07	28.16	1			
	final	-0.55	26.97		37.1	-1.4	5.6

DEM name		**Δh of stable terrain [m]**		**# iterations**	**Translation vectors [m]**		
		Mean	**STDV**		**Δx**	**Δy**	**Δz**
SFM590625	*before*	-31.29	38.71	4			
	final	0.01	36.57		-47.3	68.3	28.2
SFM640712	*before*	7.51	20.14	1			
	final	-0.06	18.19		1.0	31.7	8.5

IV. Overview Map Including Analysis Points in Sector 4

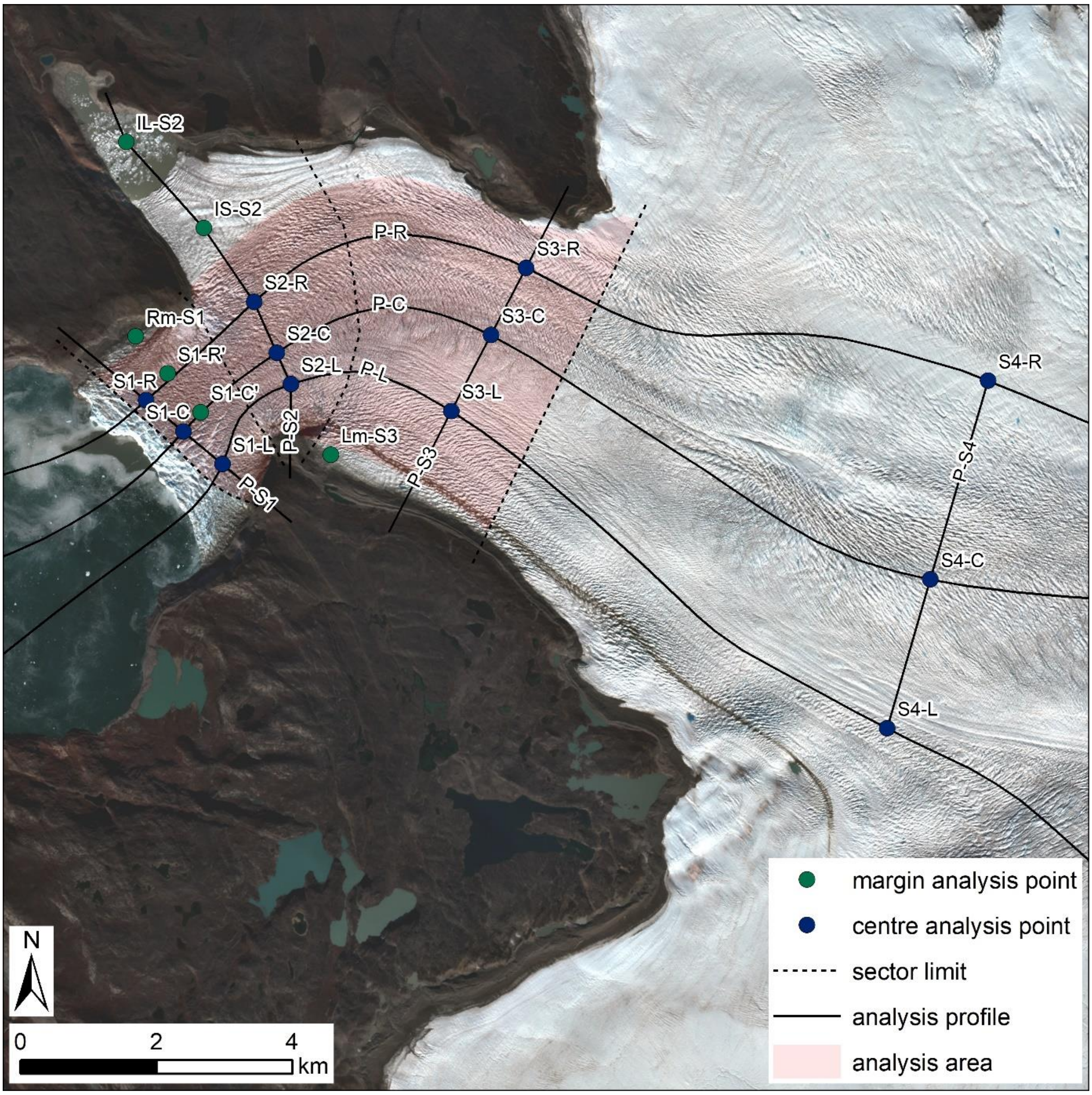

Figure 78: Analysis profiles, centre analysis points, margin analysis points and analysis area used for the investigation of surface eleva-tion change and related parameters. The full versions of the abbreviated names in the figure are given in the text. In addition, the sector margins are included. Background: Sentinel-2B, 30th August 2019, European Commission (2015).

V. Table of Quality Measures of Co-Registered DEMs

Table 14: Quality measures for all DEMs on stable terrain relative to the master DEM. In chronological order. The grey entries were disregarded for the analysis due to quality issues (AS) or redundancy (DR). (*): master DEM.

DEM name	**mean**	**STDV**	**NMAD**	**median**	**68.3%-quantile**	**95.2%-quantile**
SFM530703	0.04	20.21	15.33	-1.44	15.02	32.44
SFM570712	-0.55	26.97	20.39	1.10	20.74	55.02
SFM590625	0.01	36.57	31.00	3.57	35.06	78.45
SFM640712	-0.06	18.19	18.45	2.80	18.31	36.42
AE850709	0.05	6.46	4.93	0.31	5.13	12.78
AS030609	0.12	14.32	10.91	-0.23	11.03	24.82
AS060703	0.06	12.88	11.47	-0.08	11.78	25.48
GD07comp	0.37	8.13	6.39	0.90	6.45	13.94
AS100709	0.61	9.15	9.17	0.66	9.01	17.38
AD110419	-0.06	2.47	0.82	-0.10	0.81	2.03
AD110613	0.01	5.03	1.17	-0.12	1.21	2.81
AD130325	-0.02	1.21	0.64	-0.04	0.64	1.43
AD130423	0.00	0.70	0.37	-0.03	0.38	1.05
AD130512	0.11	2.90	0.78	0.03	0.81	2.66
AD130811	-0.04	1.14	0.61	-0.07	0.62	1.27
AD130927	-0.03	1.43	0.78	-0.12	0.79	1.68
AD131028	0.02	1.62	0.40	-0.01	0.41	1.01
AD140528	-0.02	2.78	0.76	-0.11	0.78	2.87
AD140704	-0.01	0.88	0.50	0.01	0.50	1.19
AS140826	-0.35	9.27	8.90	-0.41	8.89	18.01
AD141015	-0.01	1.00	0.56	0.07	0.58	1.54
AD150815	0.02	0.79	0.47	0.03	0.48	1.03
*AD150921**	0	0	0	0	0	0
AD151024	-0.02	0.89	0.50	-0.03	0.53	1.26
AD151105	-0.01	0.85	0.54	-0.06	0.54	1.32
AD160311	-0.03	1.10	0.63	-0.05	0.65	1.69
AD160515	-0.02	1.23	0.68	0.01	0.70	1.65
DR160630	-0.01	1.54	0.41	0.03	0.41	0.93
DR160702	-0.05	1.51	0.42	-0.02	0.43	0.95
AS160707	*0.16*	*9.73*	*9.18*	*0.55*	*9.18*	*18.83*
AS160723	*0.10*	*9.66*	*8.48*	*0.15*	*8.61*	*18.99*
DR160821	0.00	1.46	0.44	0.09	0.46	1.02
DR160823	0.00	0.93	0.41	0.00	0.42	1.01
DR160825	0.01	1.54	0.43	0.10	0.44	1.03
DR170616	0.02	1.59	0.54	0.04	0.57	1.31
DR170620	0.02	2.00	0.53	0.11	0.54	1.26
DR170622	-0.04	1.58	0.47	0.00	0.49	1.25
AD170821	0.05	1.35	0.69	0.02	0.69	1.66
DR180706	0.00	1.38	0.50	0.08	0.50	1.11
DR180708	-0.03	1.22	0.45	0.00	0.46	1.15
DR180711	-0.01	1.22	0.48	0.01	0.49	1.20
DR190818	0.00	1.48	0.47	0.04	0.49	1.08
DR190820	0.02	1.58	0.51	0.10	0.52	1.11

VI. Additional Along- and Across-Profiles

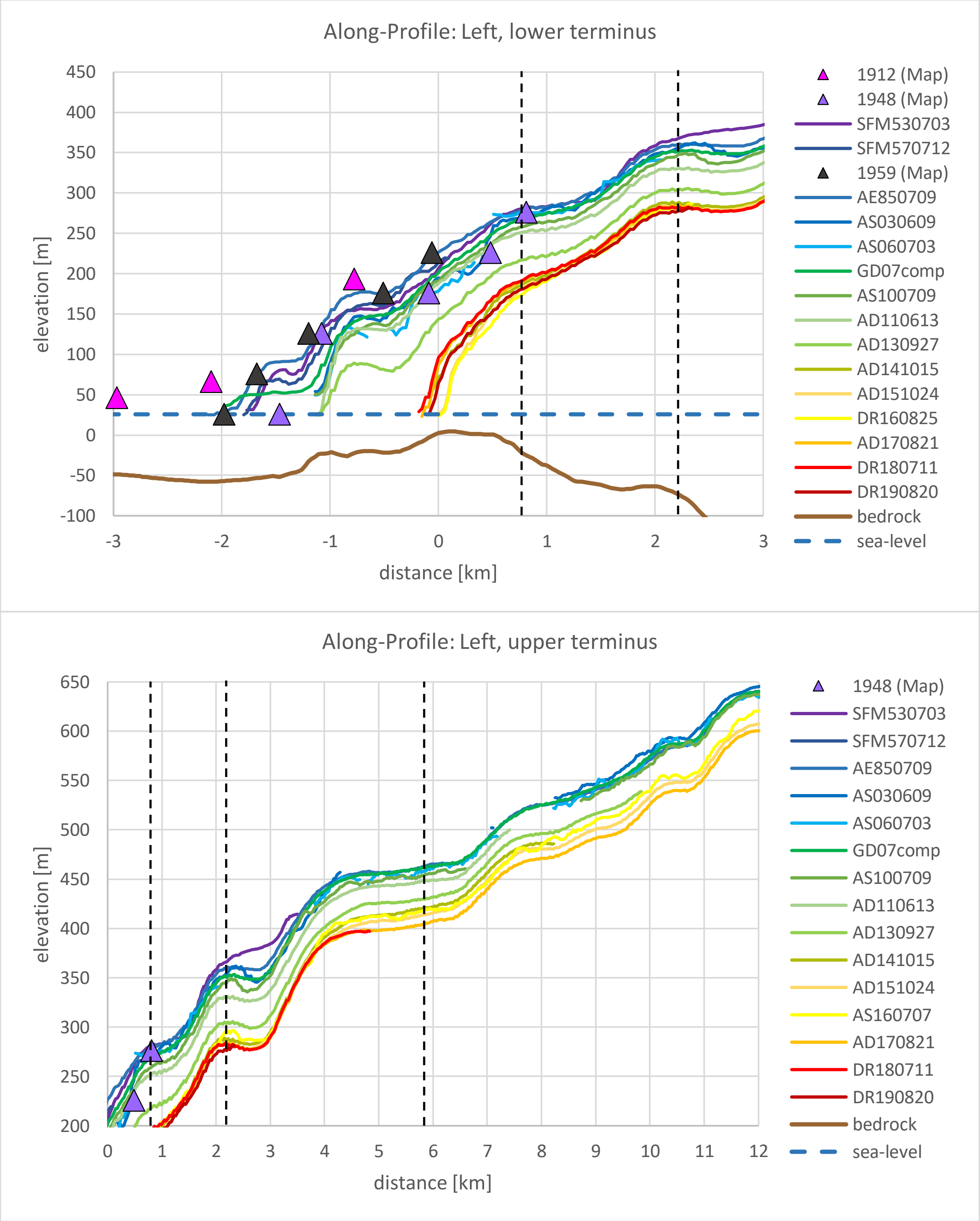

Figure 79: Surface geometry of the left along-profile; top: lower section (km -3 – 3) and bottom: upper terminus (km 0 – 12). Note that not all DEMs are represented. After 2010, (if available) one DEM per year is included. Further excluded due to quality issues are the profiles resulting from the SFM DEMs of 1959 and 1964. Triangles represent elevations of contours and bench-marks of historic maps. The distance reference (0 km) is the front of 20th August 2019. The bedrock elevation is extracted from the BedMachine v3 *by Morlighem et al. (2017). The vertical black dashed lines indicate the location, where the analysis points* S1-L, S2-L *and* S3-L *are located, respectively, where the across-profiles* P-S1, P-S2 *and* P-S3 *intersect.*

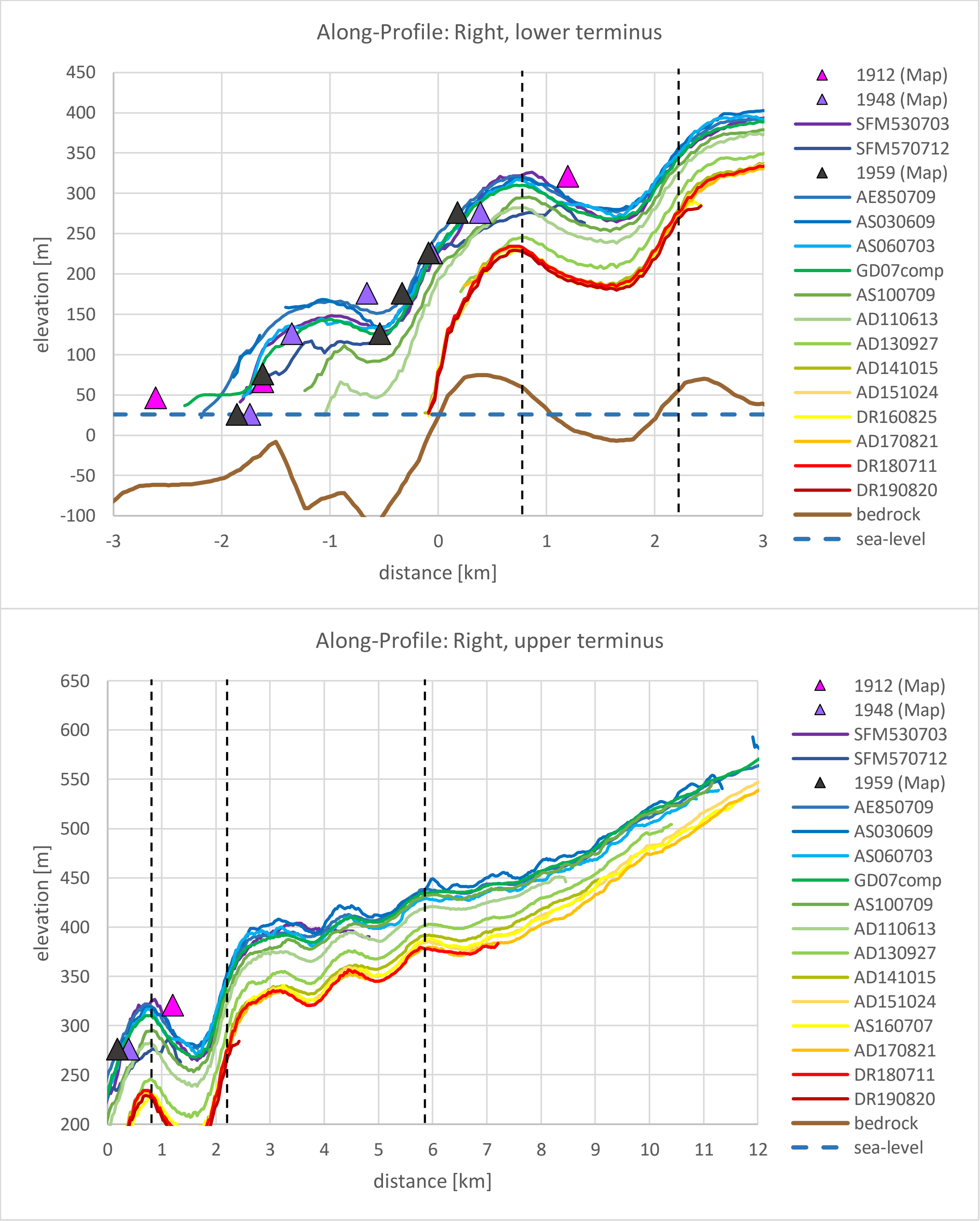

Figure 80: Surface geometry of the left along-profile; top: lower section (km -3 – 3) and bottom: upper terminus (km 0 – 12). Note that not all DEMs are represented. After 2010, (if available) one DEM per year is included. Further excluded due to quality issues are the profiles resulting from the SFM DEMs of 1959 and 1964. Triangles represent elevations of contours and benchmarks of historic maps. The distance reference (0 km) is the front of 20th August 2019. The bedrock elevation is extracted from the BedMachine v3 *by Morlighem et al. (2017). The vertical black dashed lines indicate the location, where the analysis points* S1-R, S2-R *and* S3-R *are located, respectively, where the across-profiles* P-S1, P-S2 *and* P-S3 *intersect.*

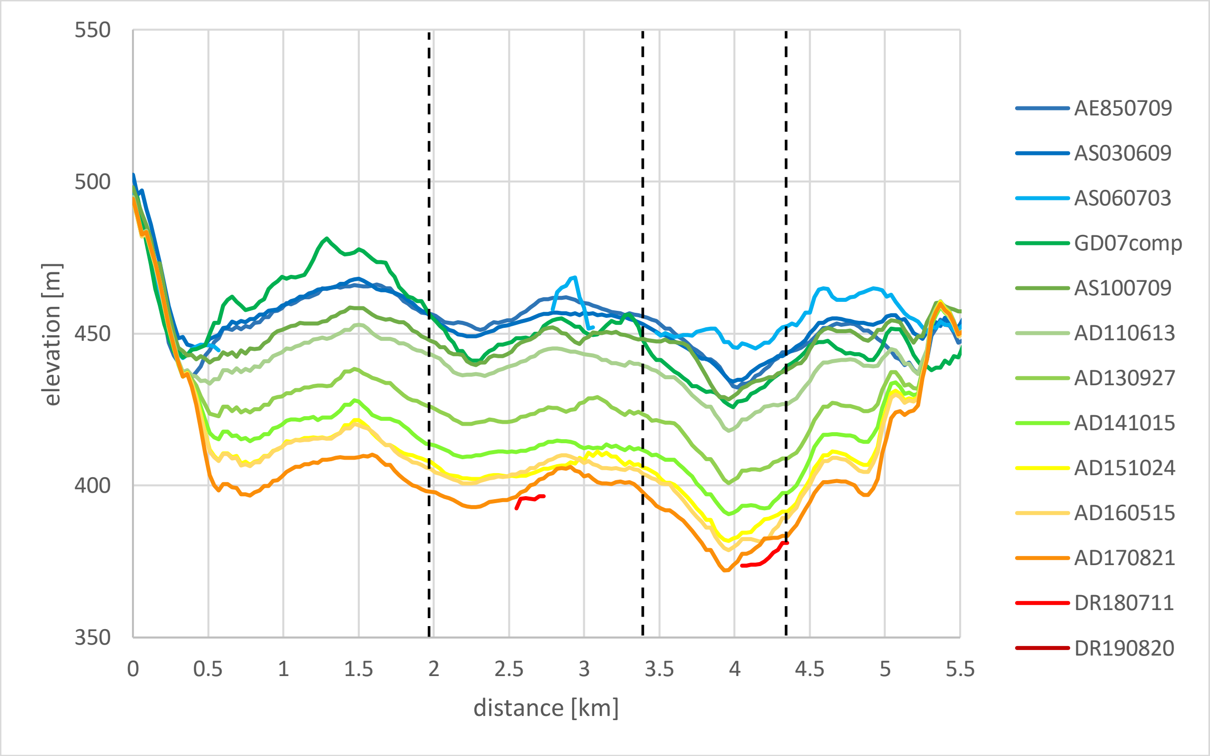

Figure 81: Across-profile through sector 3 (P-S3). Note that not all DEMs are represented. After 2010, (if available) one DEM per year is included. Further excluded due to quality issues or lack of coverage are the profiles resulting from the SFM DEMs. The distance is measured along the profile from orographic left to right (south to north). The vertical black dashed lines indicate the location, where the analysis points S2-L, S2-C and S2-R are located, respectively, where the along-profiles P-L, P-C and P-R intersect.

VII. End-of-Season Surface Elevation Change and Seasonality in Sector 3

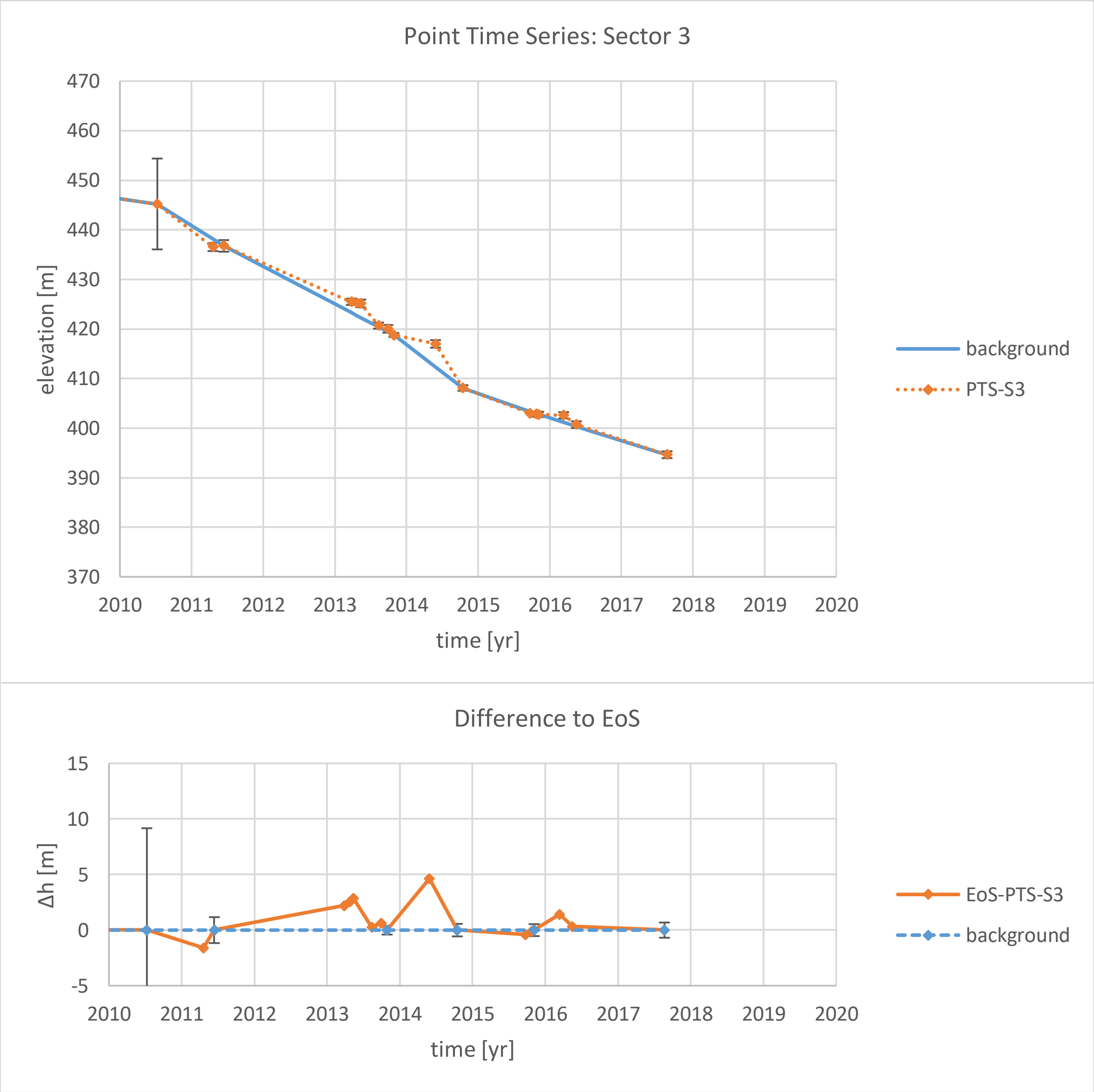

Figure 82: Background surface elevation change and seasonal pattern in sector 3. The values are averaged among the three analysis points in the sector. The reference DEMs for the background change determination are given in table 8. Note that the temporal coverage before 2013 and after 2017 is not high enough for the detection of a seasonal pattern.

VIII. Flow Velocities Along the Central Flow Line

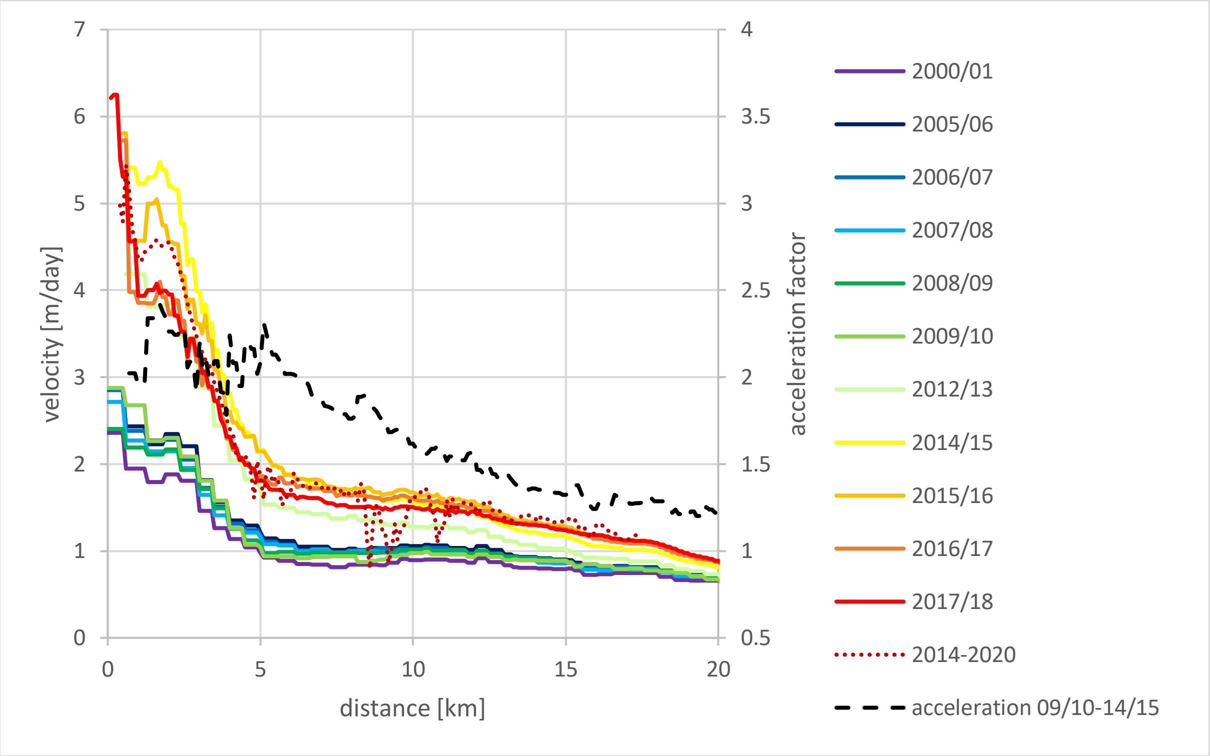

Figure 83: Flow velocities along the central flow line. Solid lines: winter average flow velocities from Joughin et al. (2015). Dotted line: 5-year average between October 2014 and January 2020 from Rohner (personal communication, Rohner et al. 2019). Dashed black line: Velocity increase from winter 2009/10 to winter 2014/15. The temporal evolution of the flow velocities is visualised in figure 56.

Personal Declaration

I hereby declare that the submitted thesis is the result of my own, independent work. All external sources are explicitly acknowledged in the thesis.

Roger Honegger

Dürnten, 30th April 2020